UNIVERSITY OF SOUTHAMPTON

FACULTY OF ENGINEERING, SCIENCE & MATHEMATICS

Institute of Sound and Vibration Research

DECENTRALISED VELOCITY FEEDBACK CONTROL FOR THIN HOMOGENEOUS AND LIGHTWEIGHT SANDWICH PANELS

by

Jens Rohlfing

Thesis for the degree of Doctor of Philosophy

October 2009

UNIVERSITY OF SOUTHAMPTON

ABSTRACT

FACULTY OF ENGINEERING, SIENCE AND MATHEMATICS
INSTITUTE OF SOUND AND VIBRATION RESEARCH

Doctor of Philosophy

DECENTRALISED VELOCITY FEEDBACK CONTROL FOR THIN HOMOGENEOUS AND LIGHTWEIGHT SANDWICH PANELS

by Jens Rohlfing

This thesis presents theoretical and experimental studies on decentralised velocity feedback control for thin homogeneous and lightweight sandwich panels. This research is motivated by the increasing interest in lightweight design for fuel efficient transportation vehicles. Lightweight sandwich panels are very appealing due to their high stiffness to weight ratio but also exhibit undesirable sound transmission properties which could cause problems with vehicle interior noise. The aim of this work is to assess the performance of decentralised velocity feedback control on lightweight sandwich panels.

The first part of this thesis presents the theoretical model used to predict the structural response, sound radiation and sound transmission through active panels with decentralised velocity feedback loops. The model is then used in simulation studies on the intrinsic limitation of decentralised feedback control for thin homogeneous and sandwich active panels under distributed deterministic and stochastic excitations in the whole audio frequency range. The results suggest that decentralised velocity feedback control on lightweight sandwich panels is more efficient and can be applied over wider range of audio frequencies than for conventional thin homogeneous panels.

The second part of this thesis presents experimental and simulation studies on a control system with five decentralised control units with proof-mass electrodynamic actuators, installed on conventional aluminium panel and a honeycomb sandwich panel. This study provides insight in the open and closed-loop response of the control units and gives a good understanding of the interaction between the panels and the control system. The results suggest that a practical control system that implements decentralised velocity feedback can offset some of the undesired sound transmission properties of lightweight sandwich structures by efficiently reducing structural vibration and sound power radiation in the mid audio frequency range.

Contents

List of Figures

List of Tables

Declaration of Authorship

I, Jens Rohlfing, declare that this thesis entitled ”Decentralised Velocity Feedback Control for Thin Homogeneous and Lightweight Sandwich Panels” and the work presented in it are my own. I confirm that:

1. This work was done wholly while in candidature for a research degree at this University;
2. Where any part of this thesis has previously been submitted for a degree or any other qualification at this University or any other institution, this has been clearly stated;
3. Where I have consulted the published work of others, this is always clearly attributed;
4. Where I have quoted from the work of others, the source is always given. With the exception of such quotations, this thesis is entirely my own work;
5. I have acknowledged all main sources of help;
6. Where the thesis is based on work done by myself jointly with others, I have made clear exactly what was done by others and what I have contributed myself;
7. Parts of this work have been published as:

    - J. Rohlfing and P. Gardonio, ”Experimental studies on decentralized velocity feedback control on thin aluminium and honeycomb sandwich panels”, Proceedings of Active 2009 conference, Ottawa, Canada, 20-22 August 2009.
    - J. Rohlfing and P. Gardonio, ”Homogeneous and sandwich active panels under deterministic and stochastic excitation”, *Journal of the Acoustical Society of America*, 125(6), p.3696-3706, 2009.
    - J. Rohlfing and P. Gardonio, ”Comparison of homogeneous and sandwich panels with decentralised velocity feedback control units”, Proceedings of Noise and Vibration: Emerging Methods NOVEM 2009 conference, Oxford, UK, 5-8 April 2009, p.020 - 1-12.
    - J. Rohlfing and P. Gardonio, ”Comparison of Active Structural Acoustic Control on Homogeneous and Composite Sandwich Panels under deterministic and Stochastic Excitation”, ISVR Technical Memorandum 984. 2009.
    - D.J. Thompson, P. Gardonio and J. Rohlfing, ”Can a transmission coefficient be greater than unity?”, *Applied Acoustics*, 70(5), 2009, p.681-688.
    - J. Rohlfing and P. Gardonio, ”Active panels under stochastic excitation”, Proceedings of ISMA 2008, International Conference on Noise and Vibration Engineering, 2008, p.63-77.
    - J. Rohlfing and P. Gardonio, ”Active control of sound transmission through panels with flexible boundaries under deterministic and stochastic excitation”, ISVR Technical Memorandum 977. 2007.

Signed: ....., Date: .....

Acknowledgement

This thesis the result of my research activities at the institute of Sound and Vibration Research (ISVR), University of Southampton. At this point I would like to sincerely thank all the institutions, organisations and individuals that contributed towards my work with their advice, practical and/or financial support, their experience and their encouragement.

First and foremost I express my deep and sincere gratitude to my supervisor Prof. Paolo Gardonio for his guidance, encouragement and continuous support throughout my Ph.D. research. I have greatly benefited from his experience and his advice. The assistance and advice of my co-supervisor Prof. David Thompson is also acknowledged with sincere thankfulness. Special thanks are also due to Dr. Ken Frampton, who contributed by giving constructive advice.

Special thanks goes to the ISVR for providing me with the opportunity to conduct my work in this renowned institution with its inspiring research environment and also to the Signal Processing and Control Group (SPCG).

I am particularly grateful to the staff and fellow Ph.D. students at the ISVR and SPCG (Cristóbal González Díaz, Michelle Zilletti, Neven Alujević, Olie Baumann, Yohko Aoki and many others) for inspiring discussions, for their suggestions, advice and practical help.

Special thanks goes to the ISVR technical support team, to Dennis White for building the aluminium test frame used in the sound transmission chamber experiments and also to Antony Wood, Andy Westerman and Nigel Davies for their practical help and advice for the refurbishment of the control actuators and the modifications to the sound transmission suite.

Special thanks also go to the ISVR Dynamics group for giving me access to the laser vibrometer measurement equipment and to Dr. Armando Vavalle from GKN Aerospace Ltd. for his cooperation and for providing the honeycomb test panel used in the experimental studies.

Financial support for this research project was provided by a Marie Curie Early Stage Training (MC EST) fellowship, within the research and training network ”European Doctorate in Sound and Vibration Studies (EDSVS)” and is greatfully acknowledged.

Last but not least I would like to thank all my friends that saw me through these three years and also my parents Friedrich and Doris Rohlfing who always encouraged me to take my own decisions and offered their unconditional support for whatever my plans turned out to be.

Thank you all.

Nomenclature

Symbol	Description	Unit
Latin Letters:		
a	Modal displacement	
c	Wave speed	m/s
c_2	Damping coefficient (Actuator suspension)	Ns/m
d	Distance between the sandwich faceplate neutral axes	m
f_1	Frequency	Hz
f_2	Force	N
h	Thickness (panel)	m
j	Imaginary unit defined as: $j = \sqrt{-1}$	
k_1	Wavenumber	rad/m
k_2	Stiffness (Actuator suspension)	N/m
l	Length	m
m	Mass	kg
p	Acoustic pressure	N/m^2
t	Time	s
w	Transverse displacement	m
x	x-coordinate (plate axis)	m
y	y-coordinate (plate axis)	m
z	z-coordinate (perpendicular to plate)	m
A	Surface area (panel or panel element)	m^2
D	Flexural rigidity or bending stiffness	Nm^2
E_1	Young's modulus of elasticity	N/m^2
E_2	Kinetic energy	J
F	Modal force or generalised force	N
G	Receptance (Appendix A only)	m/N
H	Frequency response function (general)	
I_1	Second moment of area	m^4
I_2	Current	A
L_1	Correlation length	m
L_2	Electric inductance (Actuator voice coil)	H
M	Mass (total / modal / elemental)	kg

N	Total number (modes / elements / primary forces)	
P	Power	W
R_1	Distance between two points on the panel	
R_2	Element of radiation matrix	
R_3	Resistance (electrical)	Ω
S	Spectral density	
T_1	Time period	s
T_2	Transmission index	dB
TL	Transmission loss index	dB
U_1	Speed	m/s
U_2	Voltage	m/s
Y	Mobility	m/(Ns)
Z	Impedance	Ns/m
$\mathbf{A}$	Power transfer matrix	
$\mathbf{F}$	Force matrix (modal and elemental)	
$\mathbf{G}$	Mobility matrix including velocity feedback control	

Greek Letters:

η	Loss factor	
θ	Angle of incidence angle relative to surface normal	rad or deg
ν	Poisson's ratio	
ρ	Mass density (equivalent to m''')	kg/m^3
ϕ	Natural modes or modeshapes	
φ	Angle of incidence relative to x axis	rad or deg
ω	Angular frequency ($2\pi f$)	rad/s
Φ_1	Power spectrum	
Φ_2	Voice coil coefficient	N/A
$\mathbf{\Omega}$	Matrix of modal resonant terms	

Subscripts

0	Property of air
a	Specific to actuator voice coil motor
b	Bending
c_1	Control (element / force)
c_2	Critical
c_3	Specific to the sandwich core
$conv$	Convection
dyn	Dynamic (modes)
e_1	Plate element (element centre point)
e_2	Electric (Chapter 4 and Appendix C only)
f	Specific to sandwich faceplate
i	Index (plate elements)

in	Input
j	Index (plate elements)
m	Mode order x-direction
n	Mode order y-direction
p_1	Primary point excitation
p_2	Plate
r	Index (modes)
rad	Radiation
res	Residual (modes)
s_1	Index (modes)
s_2	Corresponding to shear
s_3	Specific to actuator suspension
ADF	Specific to acoustic diffuse field
TBL	Specific to turbulent boundary layer

Mathematical:

X	Real value X
$\tilde{X}$	Complex value X
$Re\{\tilde{X}\}$	Real part of X
$Im\{\tilde{X}\}$	Imaginary part of X
$\hat{X}$	Peak value X
$\tilde{X}^*$	Complex conjugate of X
$E\left[\tilde{X}^*\tilde{X}\right]$	Expectation of $\left[\tilde{X}^*\tilde{X}\right]$ for infinite sampling length
$\mathbf{var}\left[X\right]$	variance of X
X^n	X to the power of n
$\exp(X)$	e to the power of X
X'	First spatial derivative of X
X''	Second spatial derivative of X ...
$\dot{X}$	First derivative of X in respect to time
d	Differential operator
$\mathbf{X}$	Matrix X
$\mathbf{X}^{-1}$	Inverse of matrix $\mathbf{X}$
$\mathbf{X}^T$	Non conjugate transpose of matrix $\mathbf{X}$
$\mathbf{X}^H$	Complex conjugate transpose of matrix $\mathbf{X}$
$\mathbf{I}$	Identity matrix
$\sec(X)$	Secant of X; equals $\frac{1}{cos(X)}$

Chapter 1

Introduction

1.1 Motivation

The decline of fossil fuel stock and global warming are forcing industries for air and surface civil transportation to reconsider their strategies for the forthcoming generation of vehicles. Besides ongoing long term efforts in developing efficient propulsion systems that run on renewable energy, in the short term, weight reduction is a key factor to diminish fuel consumption and thus CO_2 emissions of vehicles.

Aircraft and car manufacturers have already started to investigate innovative lightweight designs for the fuselage of aircraft and the body of cars. To improve the fuel consumption efficiency and yet retain structural strength, new designs of aircraft fuselage and automobile bodywork involve stiff and lightweight panels, which unfortunately have undesired acoustic properties and efficiently transmit noise generated by external sources (i.e. jet noise or reciprocating engine noise), by aerodynamic sources (e.g. turbulent boundary layer pressure fields on aircraft skins or on car bodyworks) and by structure-borne paths (e.g. engine induced vibrations or road induced vibrations) [1, 2, 3, 4].

In particular the airframe of the new generation of aircraft involves an increasingly higher proportion of lightweight composite materials made from carbon fibres. Car manufacturers have also begun to consider lightweight constructions, e.g. aluminium and carbon fibre car bodies, and the use of stiff lightweight sandwich panels made from low cost materials such as plastic or even paper for the core layer. The use of these new materials has a direct impact on the structure-borne and air-borne sound transmission phenomena.

Passive treatments, such as stiffening, mass or damping treatments, can be used to reduce

the undesired effects in the dynamic response of lightweight structures although, in many cases, in order to be effective at low audio frequencies, they tend to be bulky and introduce extra mass, which interferes with the new weight requirements for those vehicles [5, 6, 7]. Active control systems enable the design of lightweight smart panels that could satisfy both the requirements for low weight and low vehicle interior noise levels.

This thesis presents a comprehensive study on the vibration and sound transmission characteristics of smart panels with decentralized velocity feedback control units. The passive and active control properties for an aluminium panel and a honeycomb panel are investigated in theoretical and experimental studies in order to assess the feasibility and advantages of lightweight smart structures against conventional structures. The theoretical and practical studies consider both deterministic and stochastic disturbances, such as acoustic diffuse field and turbulent boundary layer aerodynamic excitations. Both the theoretical and experimental work consider a wide audio frequency range to assess the effectiveness of the smart panels in the low frequency range where the response of the panels is dominated by discrete resonant modes and in the mid to high audio frequency range where acoustic and convective coincidence phenomena occur.

1.2 Technical background

1.2.1 Interior noise in vehicles

This section provides a brief introduction to the main sources and transmission mechanisms that produce interior noise in transportation vehicles. More details about the mechanisms of noise generation analysed here can be found in References [1, 2].

Turbulent boundary layer (TBL) induced noise: The airflow over the outer surface of moving vehicles can generate high levels of turbulent boundary layer (TBL) induced noise. This is quite often the most significant source of interior noise for high travel speeds. For all types of high-speed vehicle such as aircraft, high-speed trains and cars the airflow over the outer surface is characterized by a turbulent boundary layer that generates a fluctuating pressure field over the outer skin surface which excites the cabin partition structure. The nature of these fluctuations is random both in the time and spatial domains. The pressure field is convective in the direction of the airflow, where the convective speed is a function of

the free air flow speed over the surface. The pressure fluctuations can be characterized by pressure frequency spectra with characteristic wavenumbers in stream and span wise directions. Convective coincidence occurs at frequencies where the phase of the boundary layer induced pressure fluctuations matches the phase of the transverse vibration of the vehicle‘s outer skin in the stream wise direction. These phenomena result in efficient vibration excitation of the cabin walls which then radiate sound into the cabin to generate an acoustic field that is perceived as interior noise. A comprehensive review of research on the wavenumber-frequency spectrum prior to 1996 is given by Bull [8] and more recently Hwang et al. [9] reviewed and compared semi-empirical models that calculate the turbulent boundary layer wall pressure frequency spectra for various models published from the late 1960s to 2004.

Propeller noise: Propeller noise is specific to aircraft and is generated by the periodic interactions between the air and the rotating propeller blades. The noise produced by propellers can be considered to be deterministic because the generated interior sound field is well correlated to the rotational speed of the propellers. Stochastic broad band contributions to the noise spectrum are generated by boundary layer turbulence in the airflow over the blade surface; however these contributions are less important. The characteristics of propeller noise are influenced by many factors: the power produced by the propeller, the blade tip speed, the number of blades, the blade shape and the angle of attack which determines uniformity of the airflow into the propeller. The frequency spectrum of propeller noise is dominated by distinctive tones. The lowest tone is determined by the blade passing frequency and the higher ones are higher harmonics of this. The highest excitation levels on the outside of the fuselage skin occur in the plane of the propellers. The blade passing frequency can occur at very low frequencies particularly for large rotors as those of helicopters.

Engine noise: In aircraft, jet engine noise is mainly generated by the turbulent flow of high-speed and high temperature jet gases in the engines and their mixing with the airflow behind the engine. The generated disturbance is stochastic and broad-band with a small convective pattern in the direction of motion. Jet noise mainly affects the aircraft cabin section behind the engines and is particularly strong during flight manoeuvers such as take-off, climb, thrust reversing and landing. Jet mixing noise is efficiently reduced for high-bypass jet engines that operate with higher flow volumes but reduced flow speed. However, the inlet compressor of this type of jet engine generates tonal fan buzz saw noise, which is radiated towards the front part of the aircraft.

In some cases sound radiation from the engine cage outer surface could also affect the noise levels inside the cabin. In the same way noise form reciprocating combustion engines in cars is directly transmitted into the passenger compartment via the bulk head panels. The noise from reciprocating engines is characterized by both deterministic tonal components and stochastic broad-band contributions [1].

Structure borne noise: Reciprocating engines and jet engines are directly mounted to the vehicle structure. Particularly aircraft engines are mounted to the wings or airframe using rigid mounts for safety, reliability and durability reasons. The levels of structural excitation can be very large particularly when the moving components of the engines, power train and propulsion system rotate with unbalance. In particular the vibration of a helicopter gearbox and main rotor generates intense structural excitations at low frequencies which are transmitted to the helicopter cabin via rigid struts and largely contribute to the helicopter interior noise levels. For propeller aircraft the front and tail wings are also excited by the wakes detached from the propeller blades. For surface transportation vehicles a further source of structure-borne sound originates from tyre-road or wheel-rail interaction which is transmitted into the vehicle structure via the suspension system. Theses types of sources for interior noise are referred to as structure-borne noise because the noise originates from structurally transmitted excitation of the cabin structure. The characteristics of structure-borne-noise depend on the specific generation mechanism so that it may be dominated by deterministic tonal components but may also have stochastic broad-band contributions. In general structure-borne noise is best controlled directly at the source or in the transmission path in close proximity to the source. Note that most structure-borne noise sources such as engines, tyre-road and wheel-rail interactions are also sources of airborne noise where the dominance of the air-borne and structure-borne contribution towards interior noise level varies with frequency [1].

Other sources of interior noise: There are many other sources of interior noise in vehicles. For example tonal aerodynamic noise generated by elements that stick out of the main vehicle body and disturb the passing airflow e.g. sensors, antennae, side mirrors. Noise can also be generated from the operation of hydraulic or pneumatic systems that are used to position flaps, release landing gear and control braking mechanisms. Another contribution to interior noise in vehicles is generated by the operation of air conditioning systems that provide fresh air supply to the passengers.

The interior noise sources for transportation vehicles discussed above can be categorized into two groups: those that predominantly produce deterministic tonal disturbance and those that produce stochastic broad-band disturbances. As described in the following section, the source characteristics determine which control strategies are appropriate for specific applications.

1.2.2 Active control approaches

In this section a brief review of some existing active approaches for the global control of interior noise levels is presented [4]. The aim is to briefly outline recent progress and the current state of research, development and practical application of active control systems, and also to point out the strength and weaknesses of existing control technologies compared with smart panels for the reduction of structural vibration and sound transmission. Initially the control strategies may be divided into active and semi-active approaches.

Semi-active approaches aim to improve the performance of passive devices by adapting the physical properties of a passive control treatment to the changes in the excitation characteristics and in the dynamic response of the structure under control. Tuned passive devices such as arrays of vibration neutralisers, tunable vibration absorbers (TVA), or arrays of Helmholtz resonators can be used to control vibration and radiated noise from aircraft fuselages or car body sections. However these devices are only particularly suited for the control of tonal disturbances unless a very large number of units are used, which can be randomly tuned to cover a wider frequency range [6, 7]. Semi-active approaches allow the tuning frequency of an 'active tunable vibration absorber' (ATVA) to be continuously matched to the dominant tonal component of the primary disturbance. For example, for the control of aircraft interior noise, ATVAs have been tuned to minimize a cost function that estimates the sound level in an aircraft cabin. The absorbers are therefore effectively tuned to rearrange the fuselage vibration to minimise the sound radiation rather than the overall vibration level [10]. However, the principal function of the ATVAs in this semi-active control strategy remains passive rather than active.

The development of purely active control systems for the control of interior noise has gone through a development cycle considering different control strategies [4]. With respect to the objectives in this thesis the control strategies can be subdivided into two principal groups.

The first group of systems implements a centralised feed-forward control strategy for the direct control of the global sound field. This approach has been implemented as 'active noise control' (ANC) and 'active noise and vibration control' (ANVC) systems. ANC systems are implemented using a set of loudspeakers that are driven by a multi-channel feed-forward controller to produce a secondary acoustic field that destructively interferes with the acoustic sound field in the cabin produced by the primary noise sources [11]. ANVC systems are implemented using structural actuator transducers in order actively to alter the vibration of the fuselage skin in order to minimise the overall interior sound levels in the cabin [12].

ANC systems use exclusively acoustic error sensors (microphones), whereas for ANVC systems both acoustic and structural sensors are employed. In both cases the signals from the error sensors are used to define a global cost function and the centralised feed-forward controller drives the actuators in order to minimise the overall interior noise level in the cabin [11]. Significant global reduction of the overall interior noise levels can be achieved for low frequencies where the acoustic wavelength is long or of similar length as the cabin interior dimensions such that the acoustic field is dominated by a small number of discrete acoustic modes. As frequency increases the acoustic wavelength reduces and the acoustic field inside the cabin is formed by an increasing number of overlapping modes. Global control at high frequencies therefore requires more complex control systems with unfeasibly high numbers of error sensors and actuators. For a feed-forward strategy it is also necessary to obtain a causal and well-correlated reference signal to the primary disturbance, such as for example the rotational speed of a propeller rotor shaft. If the dominating primary excitation is stochastic and broad-band, such as those induced by jet noise and turbulent boundary layers, it is rather difficult to obtain a correlated reference signal since a large array of sensors should be used and the time advance of the measured signal would be very short. Therefore it would be particularly challenging to build a causal controller [13].

This first group of control systems allows efficient control of the sound field in a confined acoustic space, such as the interior of an aircraft cabin or the passenger compartment of a car, if the interior noise is dominated by a tonal deterministic disturbance for which a well correlated control signal is available. Drawbacks of these approaches are the rather complex architecture of the centralised controller particular when a large number of actuators and sensors are employed. Also the amount of wiring required for data and power cables for these centralised systems introduces considerable additional weight and additional installation and maintenance costs.

As an alternative the second group of control systems implement control exclusively employing structural sensor and actuator pairs on the fuselage skin or the trim panels. This strategy alters and reduces the structural vibration and sound radiation from the fuselage panels and hence reduces the overall fuselage vibration and noise transmission into the cabin interior. Both feed-forward and feedback strategies have been investigated [14].

In contrast to feed-forward strategies, no reference signal is required for feedback control approaches. Therefore feedback control systems are better suited to control stochastic primary excitations with broad-band excitation spectra. Depending on the sensor and actuator arrangements feedback control approaches can be classified into single input single output (SISO) feedback control strategy via a single distributed actuator-sensor pair and decentralised multi-input multi-output (MIMO) feedback control via a large number of localised actuator-sensor pairs. Also hybrid approaches with modular distributed MIMO feedback strategies have been investigated where the signals of a group of local sensors is used to create the input signals to a group of local actuators [15, 16].

With decentralised feedback architectures a rather large number of control units can be used so that the frequency range over which the control system is effective can be extended to higher frequencies. This is because the systems are modular and can be integrated with the panel so that no extensive wiring and no complex central controller unit is required. Also the modal density for the panel structures is increasing with a much lower rate (it is constant for thin homogeneous panels) than the modal density of a three dimensional sound field and thus for a given number of control units, larger control effects would be produced than with decentralised acoustic systems. The principal issue of decentralised feedback control strategies is the stability of feedback loops with practical sensor-actuator pairs. In particular undesired cross-coupling effects within larger arrays of practical feedback control units may lead to instabilities even for low control gains.

Centralised ANC feed-forward control systems have been successfully implemented, mainly with application to commercial aircraft. Control systems that directly act on the fuselage skin or inner trim panel promise solutions to a wide range of practical problems. However, this type of systems has not yet reached the stage of development for use in commercial applications. In recent years much research effort has been put towards the investigation of modular systems with local sensor-actuator pairs with distributed and decentralised feedback control strategies. As result a number of practical demonstrators in the form of smart panels were produced. The next section focuses on a review of some of the important steps

in the development of these smart panels.

1.2.3 ASAC and AVC for smart panels

In this section some important steps in the development of smart panels with 'active vibration control' (AVC) and 'active structural acoustic control' (ASAC) systems are reviewed in order to provide a comprehensive overview of the smart panel technology that leads to the specific scope and objectives of this thesis.

About twenty years ago researchers started to investigate the possibility of reducing the response and sound radiation of thin structures using vibration control systems where sensors and actuators are embedded in the structure itself [17, 18, 19]. At the beginning feedforward controllers were developed, which are set to minimise the total sound power radiated by the structure. This early work led to the formulation of the sound radiation problem in terms of so called "radiation modes" [20], which, in contrast to structural modes, radiate sound independently [17, 18, 19]. In this way it has been possible to identify vibration control strategies that lead to the reduction of the sound radiation. As a result this control approach was named 'active structural acoustic control' (ASAC) [17].

In order to detect and excite radiation modes precisely, distributed transducers should be used. This has led to the development of smart structures with thin distributed piezoelectric transducers whose electrodes could be shaped in such a way that they detect or act upon the specific structural modes to be controlled [21]. In general, below the acoustic critical frequency the first radiation mode is by far the most efficient radiator [19]. Moreover, for frequencies such that the acoustic wavelength is larger than the dimensions of the thin structure, the first radiation mode corresponds to the net volumetric displacement of the structure [22]. As a result, a simple single channel control system could be implemented with a distributed and matched piezoelectric sensor-actuator pair embedded in the structure itself. The close location of the sensor and actuator transducers also allows the implementation of feedback control, which would enable the control of frequency broad-band random disturbances that affect interior noise in vehicles [18, 19, 22, 23]. Practical demonstrators have been developed but research in this type of control system has come to a halt due to unresolved issues with control stability related to undesired in-plane coupling effects between sensor and actuator piezoelectric sensors.

Recent research work has shown that decentralised MIMO feedback 'active vibration con-

trol' (AVC) may provide a simple and effective alternative approach for the control of broad-band vibration and sound radiation by structures, particularly in the low frequency range where the response of the panels is dominated by well-separated resonant modes. With these systems multiple actuators and sensors are arranged in closely spaced pairs, ideally collocated, so that simple local feedback control loops can be implemented around each pair. If the sensors and actuators are chosen such that the sensor and actuator output signals form power conjugated pairs, e.g. transverse velocity and transverse force, then a single feedback loop and also an array of such local control loops, can be shown to be unconditionally stable [24, 25]. This is true even for large changes in the response of the structure or the failure of individual control units.

Over the recent few years there has been some controversy whether decentralised AVC approaches can perform as well as approaches implementing centralised or distributed control. A comparative study has shown that decentralised AVC control systems can perform as well as centralised and distributed control strategies if the objective is to achieve broad-band reductions in structural vibration and sound radiation [26]. Centralised and distributed AVC strategies were shown to be more efficient if the objective is to control a narrow band of frequencies. Hence, for the control of structures excited by broad-band stochastic excitation, both approaches are expected to show similar performance. In fact if the centralised controller is set to minimise the overall vibration of a panel due to a broad-band excitation, the off-diagonal terms of the fully populated control matrix vanish so that the control signals are dominated by the output of the collocated sensor and hence decentralised control is implemented.

The decentralised AVC approach has the advantage of being relatively simple and modular. The simplest type of local control is velocity feedback with a collocated force actuator, which is physically equivalent to adding a point damper to the system [19]. For structures with a low modal density, where the response at any one frequency is dominated by a single mode, adding "point dampers" can be very effective, both in terms of controlling structural response and sound radiation. This strategy has recently been successfully adopted in the control of sound radiation and transmission by thin structures. In this case two-dimensional arrays of decentralised velocity feedback control units have been used to generate active damping in the structure [27, 28, 29, 30, 31, 32, 33, 34]. Also decentralised velocity feedback control has been used to control the sound transmission through a double panel by controlling the relative velocity between the source panel and the radiating panel [35, 36].

The principal open problem in AVC strategies is the design of stable control units with dual and collocated senor-actuator pairs which produce power conjugated outputs, i.e. transverse force and transverse velocity. In practice the sensing and actuation transducers that could be embedded in lightweight panels are characterised by stability issues introduced by the electrodynamic responses of the transducers [19, 37].

1.2.4 Sensors and actuator for decentralised AVC

This section provides a brief review of recent research work on various practical sensor and actuator configurations for decentralised velocity feedback control on thin panels with reference to stability issues.

Strain actuators and sensors: Flexural vibration on thin panels can be generated by strain transducers that are rigidly bonded to the surface. Normally piezoelectric strain transducers are used which are composed of thin piezoelectric laminas polarised along the thickness and with thin metal electrodes on the opposite faces. When a driving voltage is applied to the transducers, an electric field is generated across the piezoelectric material and because of the piezoelectric effect the transducer deforms in the plane of the lamina and also in the transverse direction, although the latter is comparatively small [19, 38]. When these piezoelectric actuators are bound to a thin panel, an in-plane stress field is generated, which causes the panel to bend, twist and stretch. Complex distributions of the stress field can be produced by shaping the electrodes or shading the poling of the piezoelectric lamina according to specific spatial functions [19, 38]. In reverse, piezoelectric patches can also be used as sensors where the piezoelectric effect produces a voltage output proportional to the transverse and in-plane vibration of the panel structure. Large distributed sensor-actuator pairs could be used to sense and control volumetric radiation modes with a SISO feedback ASAC strategy [39]. However, due to undesired in-plane coupling of the distributed sensor and actuator patches this type of sensor-actuator arrangement gives poor control stability. Therefore small piezoelectric patches that produce comparatively low in-plane deformation amplitude are used as actuators for decentralised MIMO feedback AVC approaches. For example, small square piezoelectric patches with seismic accelerometer sensors in their centres that are distributed over the surface of a panel implement AVC by producing localised bending moments [19]. Triangular shaped transducers with accelerometer sensors located at their tip, that are arranged along the periphery of a panel with clamped edges, can also be

employed to produce localised control excitation [31, 32]. Hong and Elliott [40, 41] investigated decentralised feedback AVC with square piezoelectric-actuator accelerometer-sensor pairs specifically for the control of sound radiation from honeycomb sandwich structures.

Stability issues with localised piezoelectric-actuator and accelerometer-sensor pairs occur at relatively high frequency. This is due to two main reasons. Firstly with increasing frequency the piezoelectric patches couple more efficiently with the bending waves of the panel and secondly the lightly damped resonance of the seismic accelerometers which cause a 180° phase shift in the open loop response function [19]. Also at high frequencies the non-duality and non-perfect collocation of the sensor-actuator pairs results in further phase lag in the feedback open loop response functions. An improvement of the control performance could be achieved by employing low-pass filters and appropriate compensators. For sandwich panels local coupling effects between the sensors and actuators allows for higher gain margins. However, relatively poor global performance is achieved because of localization of reduction around the position of the sensor-actuator pair [41].

Electrodynamic proof-mass actuators: One way to generate a 'sky-hook' transverse force excitation on structures is to use electrodynamic voice coil actuators which react off a resiliently suspended proof mass [19]. For example Paulitsch et al. [42, 43, 44] developed a compact lightweight proof-mass electrodynamic actuator and produced a prototype specifically designed for feedback AVC purposes. The prototype consists of an electrodynamic linear motor with the voice coil assembly fixed to the base of the actuator and the permanent magnet, which forms part of the proof-mass, suspended from the base via three soft circular springs. González Díaz et al. [33, 34, 45] produced four identical control units and developed a five channel decentralised velocity feedback AVC system. Collocated feedback loops are formed using seismic accelerometer sensors which are mounted in the footprint of the actuators on the opposite side of the panel.

The main stability issue for feedback loops with proof-mass electrodynamic-actuator and accelerometer-sensor pairs occurs around the actuator fundamental resonance frequency which causes an 180° phase shift in the open loop frequency response function [19]. An important factor for the gain margin is the ratio between the resonance frequencies of the first volumetric bending mode of the panel and the fundamental resonance of the actuator. Supposing the fundamental actuator resonance is sufficiently damped, a high frequency ratio (low actuator resonance frequency and high panel volumetric mode resonance) allows for

a high gain margin. This has motivated the feasibility study presented in this thesis, where the stability and performance of this control approach is contrasted for conventional thin homogeneous and stiff lightweight sandwich panels.

In this section some recent research work on various practical sensor and actuator configurations for decentralised velocity feedback control on thin panels has been reviewed with particular emphasis on inherent limitations for control stability. All practical sensor-actuator arrangements reviewed are only conditionally stable since sensors and actuators are not perfectly dual and collocated [24]. Out of the configurations reviewed, the system employing velocity feedback loops with proof-mass electrodynamic actuators seems to be the most promising for the implementation of decentralised AVC on stiff lightweight panels.

1.2.5 Lightweight sandwich panels

It is well known that lightweight composite panels, and stiff lightweight sandwich panels in particular, have undesirable sound transmission properties [19] and that the design of structures made from these panels must be carefully optimised to obtain acceptable sound transmission loss properties.

There are two main effects that cause problems with sound transmission through structures constructed with lightweight sandwich panels. Firstly, the partitions have a lower mass per unit area. This results in a reduction of the transmission loss in the frequency range were the sound transmission is mass-controlled [19].

Secondly the high stiffness-to-weight ratio of lightweight sandwich structures generates relatively long transverse wavelengths than those observed for conventional thin homogeneous panels. As a result acoustic and convective coincidence effects shift down in frequency. For example the acoustic critical frequency [19] for conventional thin aluminium panels (thickness less than 2 mm) occurs at the upper end of the audio frequency range and is not an issue for most practical noise control applications. For a stiff lightweight sandwich panel, the acoustic critical frequency shifts down into the mid audio frequency range. Around the acoustic critical frequency the panels radiate and transmit sound efficiently so that a partition constructed from sandwich panels may transmit more sound over a wide range of audio frequencies even if it has the same mass per unit area as a conventional construction.

In summary, stiff lightweight sandwich structures are very appealing for the design and construction of lightweight vehicles. However these panels have undesirable sound trans-

mission properties that are difficult to address with passive measures without diminishing the desired weight benefit. However the dynamic properties of lightweight sandwich panels may enable the use of decentralised feedback AVC systems in order to control the interior noise in future generations of lightweight vehicles.

1.3 Scope and Objectives

This thesis presents a theoretical and experimental study on AVC with decentralised velocity feedback loops for thin homogeneous and lightweight sandwich panels.

The general aim of this work is to provide an initial study on the feasibility of a lightweight structure with velocity feedback control using small lightweight proof-mass electrodynamic actuator units that can operate both at low and mid audio frequencies.

The specific objectives of this thesis can be summarised as follows:

1. To investigate the intrinsic limitations of decentralised velocity feedback control via ideal sensor-actuator pairs for thin homogeneous and sandwich panels under distributed deterministic and stochastic excitation in the whole audio frequency range.
2. The analysis of the stability requirements and performance of a single control unit with reference to its open-loop and closed-loop base impedance.
3. The investigation of the stability and performance of a practical vibration control system, comprising five proof-mass electrodynamic-actuator accelerometer-sensor pairs, on a thin homogeneous aluminium panel and a honeycomb sandwich panel.

The first objective is addressed with a simulation study on decentralised velocity feedback control via ideal sensor actuator pairs on

- a thin homogeneous panel and
- a sandwich panel with equal static stiffness but four times lower mass per unit area.

Both panels are subjected to

- deterministic acoustic plane wave (APW) excitation and
- stochastic excitations, i.e.
  - Acoustic diffuse field (ADF)
  - Turbulent boundary layer (TBL)

For the second objective the open loop and closed loop base response of one control unit is investigated both theoretically and experimentally taking into account the sensor, actuator and controller components. The aim is to characterise the control unit in terms of the impedance function it exerts on the structure where it is mounted. Also, the intention is to provide a physical interpretation of a) the control effects that can be generated by the control unit and b) the intrinsic stability limits of the feedback loop.

For the third objective the study focuses on the practical implementation of velocity feedback control via a set of five proof-mass electrodynamic actuators with accelerometer sensors at their footprints. The control system is installed on

- a thin homogeneous aluminium panel and
- a honeycomb sandwich panel with equal weight but significantly higher static stiffness.

The smart panels have been installed in a sound transmission suite. The control stability of the system is analysed with respect to the open loop frequency response functions of the control loops and in terms of eigenvalues analysis of the control systems' open loop transfer function matrix. The control performance is assessed in terms of reductions in panel kinetic energy and radiated, i.e. transmitted, sound power.

The smart panels are subjected to

- a point force excitation via an electrodynamic shaker and
- an acoustic excitation produced by a loudspeaker.

The experimental measurements have been compared with simulation results from a fully coupled model of the panels with the five proof-mass inertial actuators used in the experimental study.

1.4 Structure and Organisation

This thesis is organised in six chapters.

Chapter 1 provides a brief introduction on motivation and technical background for active vibration control for two-dimensional structures. Also the objectives and structure of this dissertation are outlined and the original contributions of this research are highlighted.

Chapter 2 introduces a general, element-based model, for the structural response and radiated sound power of passive and active panels with feedback control. The expressions for discrete and distributed deterministic transverse excitation, and distributed stochastic transverse excitation are reviewed. In addition

- Appendix A summarises the expressions used to derive the natural frequencies, natural modes and point and transfer mobilities of thin homogeneous isotropic panels.
- Appendix B gives the formulations for panel kinetic energy and radiated sound power for deterministic and stochastic excitations which are derived from first principles.

Chapter 3 presents the simulation studies on decentralised velocity feedback control via ideal sensor-actuator pairs for different types of distributed deterministic and stochastic excitation. Section 3.1 introduces the basic model used to capture the dynamic characteristics of a sandwich panel within the general model framework. The characteristic differences between the structural response of thin homogeneous and sandwich panels are discussed with respect to the real wavenumber solutions of the governing equations. Resulting problems for interior noise are discussed with respect to excitation and radiation coincidence effects. In this study both panels have equal static stiffness but the sandwich panel has a four times lower mass per unit area. The simulated response and radiated sound power of the two panels with and without feedback control are presented for acoustic plane wave (APW) excitation for different angles of incidence and for stochastic acoustic diffuse field (ADF) and turbulent boundary layer (TBL) excitation.

Chapter 4 describes experimental and simulation studies on the open and closed loop base impedance of a practical control unit consisting of proof-mass electrodynamic-actuator accelerometer-sensor pair and realistic integrator and amplifier controller circuits. In addition

- Appendix C provides the derivation of the open and closed loop base impedance for current and voltage driven control units.

Chapter 5 discusses the results of the transmission chamber experimental studies on a thin aluminium panel and a honeycomb sandwich panel with a control system consisting of five decentralised control units with proof-mass electrodynamic-actuator accelerometer-sensor pairs. The experimental results for the two panels are contrasted with respect to the control stability and the measured responses and radiated sound power for shaker and loudspeaker excitation. The experimental results are also compared with the corresponding simulation

results for the model implementing the practical feedback control model described in Chapter 4. In addition

- Appendix D provides background information on the experimental studies on the structural parameters of the anisotropic honeycomb test panel, and
- Appendix E provides further background information on the transmission chamber experimental set-up.

Chapter 6 summarises the findings of this thesis and also presents suggestions for future work.

1.5 Contributions

The original contributions of this thesis can be organised in three groups.

1. Modelling: The first group of contributions concerns the development of a general two port model for the structural response, sound radiation and sound transmission through panels equipped with decentralised velocity feedback control units. The model is based on an elemental approach, which enables the formulation in a consistent framework of the following physical effects:

- Discrete and distributed deterministic transverse excitation (e.g. point forces and acoustic plane waves)
- Distributed stochastic transverse excitation (e.g. rain on the roof, acoustic diffuse field and Turbulent Boundary Layer)
- Passive and active effects of open/closed loop control units

The passive and active effects of the decentralised control units are modelled in terms of their open and closed loop base impedances. This has enabled the investigation and physical interpretation of decentralised feedback control in terms of the impedance effect the control units produce on the structure at the mounting location.

The model can be easily extended to capture other physical effects such as for example fluid loading and flexible boundaries as reported in Reference [46].

2. Simulation studies on idealised control loops: The second group of contributions concerns the theoretical study of decentralised velocity feedback control with idealised velocity

sensor and force actuator pairs on a homogeneous aluminium panel and a lightweight sandwich panel with significantly different dynamic responses.

This study introduces a comprehensive analysis on how the control performance of decentralised velocity feedback control depends on

- the frequency range where the response of the panels are characterised by well separated resonance peaks of low order modes;
- the frequency range where the acoustic and convective excitation coincidence effects occur and
- the frequency range where sound radiation coincidence occurs.

3. Simulation and experimental work on a practical control set up: The third group of contributions is focused on the implementation of modular control units on a homogeneous aluminium panel and a honeycomb sandwich panel. Each control unit is formed by a proof-mass electrodynamic actuator with an accelerometer sensor at its footprint.

At first the behaviour (control stability and performance) of a feedback control unit has been investigated both theoretically and experimentally with respect to its base impedance, thus independently from the coupled response with the structure.

Secondly the performances of a set of five control units mounted on the two panels have been investigated. The feasibility of velocity feedback control over low and mid audio frequency bands for stiff lightweight smart structures compared to more flexible standard homogeneous panels has been verified.

Chapter 2

Modelling sound transmission through passive and active panels using the elemental approach

This chapter introduces a general model for the structural response and radiated sound power of passive and active panels with feedback control loops, which is based on an elemental approach. The expressions for point and distributed deterministic transverse excitation (e.g. point forces and acoustic plane wave), and distributed stochastic transverse excitation (e.g. Turbulent Boundary Layer (TBL) aerodynamic pressure fluctuations and Acoustic Diffuse Field (ADF)) are reviewed. The numerical simulation results for the transmission coefficient for acoustic plane wave excitation are validated by comparison with results from approximate analytic solutions. Also experimental validations have been obtained for point force and acoustic excitation considering the test panels discussed in Chapter 5. The aim of this chapter is to introduce the models used to generate the simulation results presented in Chapters 3 and 5 of this thesis.

Elliott and Johnson [20, 22] predict the spatially averaged response and the total sound power radiation from a panel using the so called 'elemental approach' [19]. In 2004 Gardonio and Elliott [23] presented a theoretical study using this approach to predict and compare the sound transmission through different types of smart panels with active feedback control systems. With the elemental approach the surface of the panel is subdivided into a uniform grid of elements. The time-averaged panel kinetic energy and the time-averaged total sound power radiated by the panel is derived in terms of the panel velocity at the element centre

positions. Thus the spatial integrals in the expressions for the kinetic energy and sound power radiation are replaced by sums over the grid of elements.

Following the work presented in References [20, 22, 23], this chapter first describes the element-based modelling approach for the structural vibration and sound radiation by passive thin rectangular panels with a given set of point force excitations. Then the formulation is expanded in such a way as to consider distributed deterministic excitation, i.e. Acoustic Plane Wave excitation (APW) and distributed stochastic excitation, i.e. Acoustic Diffuse Field (ADF) and Turbulent Boundary Layer excitation (TBL).

The effect of multichannel feedback control with point actuator and sensor transducers is also integrated in the elemental model. The elemental and feedback control models are cast into a matrix formulation that can be graphically represented in terms of a two-port block diagram with a multi-channel feedback loop.

This chapter presents the principal steps and equations of the model. A detailed summary of the expressions used in the formulation are given in Appendices A and B. In particular:

- Appendix A summarises the expressions used to derive the the natural frequencies, natural modes and point and transfer mobilities of thin homogeneous isotropic panels.
- Appendix B gives the formulations for panel kinetic energy and radiated sound power for deterministic and stochastic excitations which are derived from first principles.

In this study the point and transfer mobility functions between the locations on the panel are derived from finite modal expansion formulations which are given in Appendix A. The particular model problem studied in this thesis is shown in Figure 2.1 and resembles a rectangular panel mounted in an infinite baffle. The geometry and physical properties for the homogeneous aluminium panel considered for the simulation studies in this chapter and Chapter 3 are given in Table 2.1 and represents a typical panel in an aircraft fuselage.

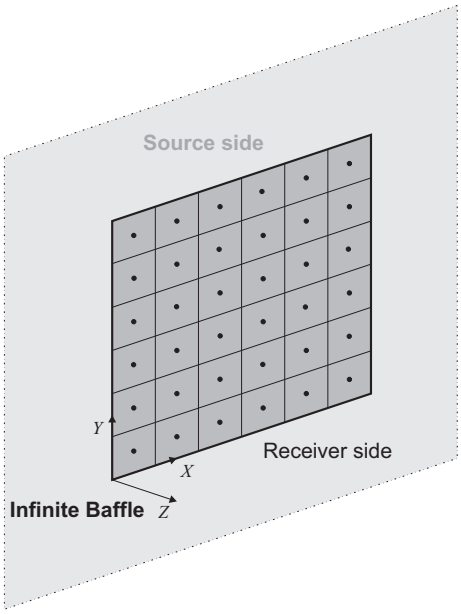

Figure 2.1: Model problem: rectangular panel in an infinite baffle, where the panel is subdivided in a uniform grid of elements.

Table 2.1: Geometry and physical parameters of the aluminium panel used in the simulation studies.

Parameter	Symbol	Value	Unit
x-dimension	l_x	278	mm
y-dimension	l_y	247	mm
Thickness	h	1.6	mm
Mass density	ρ	2720	kg m^{-3}
Young's modulus	E	70	GPa
Poisson's ratio	ν	0.33	–
Modal loss factor	η	0.02	–

2.1 Panel response to point and distributed excitations

In this section the formulations for the passive response of a panel excited by point forces and distributed deterministic disturbances are introduced. At first the formulation for the response of a single panel element is considered, which is then cast into a matrix expression for the determination of the overall panel response and sound radiation considering the contributions from all panel elements.

2.1.1 Deterministic excitation

Point force excitation

As shown in Figure 2.2, in this subsection the response at the centres of the panel elements due to a set of point forces is determined.

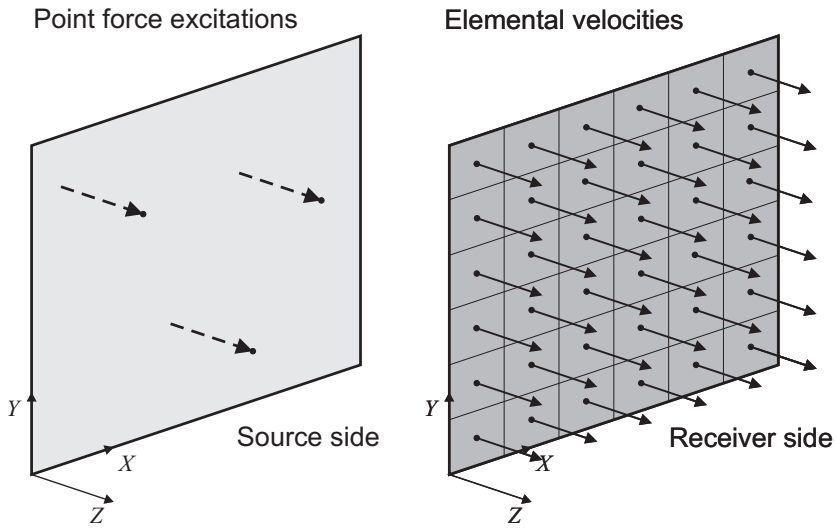

Figure 2.2: Panel model with point force excitation.

The steady-state response of the panel elements is expressed assuming time-harmonic excitation of the form $Re\{\exp(j\omega t)\}$ where ω is the angular frequency and $j = \sqrt{-1}$. For brevity the time-harmonic term $\exp(j\omega t)$ will be omitted in the formulation which will be given in complex form. Therefore, the time-harmonic velocity $\dot{w}(t) = Re\{\tilde{\dot{w}}(\omega)\exp(j\omega t)\}$ and force $F(t) = Re\{\tilde{F}(\omega)\exp(j\omega t)\}$ will be replaced by the frequency-dependent complex velocity and force phasors $\tilde{\dot{w}}(\omega)$ and $\tilde{F}(\omega)$. Throughout the thesis $\tilde{}$ will be used to identify complex, frequency-dependent functions.

Assuming the system is linear, the velocity at the centre of the e-th element due to N_p point forces can be determined from the following summation.

$$\tilde{\dot{w}}_e(\omega) = \sum_{p=1}^{N_p} \tilde{Y}_{e,p}(\omega)\tilde{F}_p(\omega), \tag{2.1}$$

where $\tilde{Y}_{ep}$ are the transfer mobilities between the primary excitation forces at the excitation position p and the velocity at the centre of the element e. As shown schematically by the block diagram in Figure 2.3, the set of N_e elemental velocities due to N_p point forces can

be determined with the following matrix expression,

$$\tilde{\dot{\mathbf{w}}}_e(\omega) = \tilde{\mathbf{Y}}_{ep}(\omega)\tilde{\mathbf{F}}_p(\omega), \tag{2.2}$$

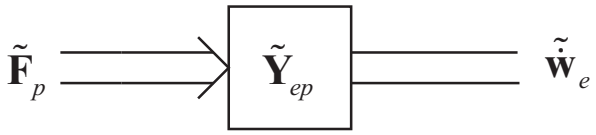

Figure 2.3: Block diagram for passive response of a panel elements to a discrete primary excitation.

where $\tilde{\dot{\mathbf{w}}}_e$ is a $[N_e \times 1]$ vector containing the elemental velocities

$$\tilde{\dot{\mathbf{w}}}_e(\omega) = \left\{ \begin{array}{c} \tilde{\dot{w}}_{e1}(\omega) \\ \tilde{\dot{w}}_{e2}(\omega) \\ \vdots \\ \tilde{\dot{w}}_{eN_e}(\omega) \end{array} \right\} \tag{2.3}$$

and $\tilde{\mathbf{F}}_p(\omega)$ is the $[N_p \times 1]$ vector of discrete primary excitation forces,

$$\tilde{\mathbf{F}}_p(\omega) = \left\{ \begin{array}{c} \tilde{F}_{p1}(\omega) \\ \tilde{F}_{p2}(\omega) \\ \vdots \\ \tilde{F}_{pN_p}(\omega) \end{array} \right\}. \tag{2.4}$$

The $[N_e \times N_p]$ mobility matrix $\tilde{\mathbf{Y}}_{ep}(\omega)$ contains the transfer mobilities between the centres of the panel elements and the primary excitation locations. The formulation presented above is general and not restricted to thin rectangular plates. Thus it can be used for other structures such as curved shells provided expressions for the structural point and transfer mobilities are available, i.e. expressions for the natural frequency and modes of the structure. In this study the response of the panel is described using thin plate theory. The expressions given in Appendix A for the natural frequencies and natural modes of thin rectangular plates are taken from references [47, 48].

The total number of elements N_e is given by the product of the number of elements along the x and y-axis $N_{ex} \times N_{ey}$. The number of elements along each axis depends on the shortest bending wavelength of the panel at the highest frequency of interest. At least two elements per wavelength are needed to describe the panel motion uniquely, i.e. to avoid

spatial aliasing. For adequate spatial sampling, at very least three elements per wavelength are used in this study. A convergence study on the element resolution with respect to the estimated panel total kinetic energy is presented in Reference [46].

Distributed deterministic excitation

As shown in Figure 2.4 a distributed disturbance is represented by equivalent discrete forces acting on the element centres.

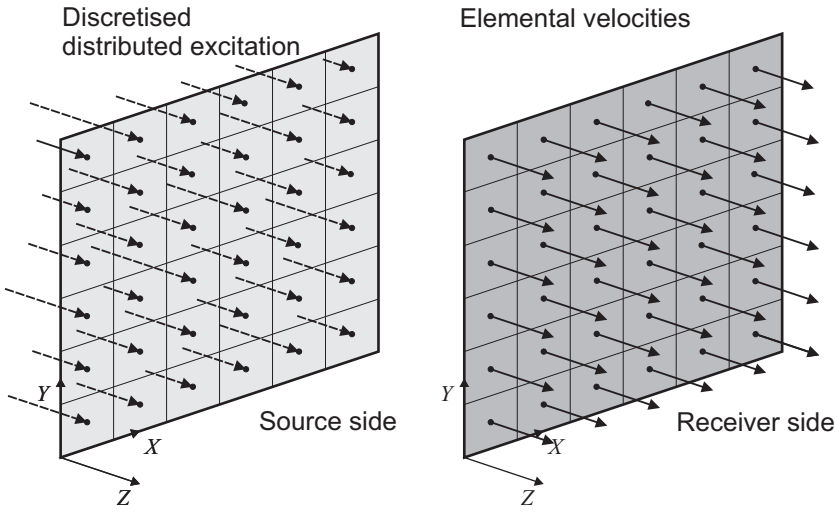

Figure 2.4: Panel model discretised distributed excitation.

Thus the set of N_e elemental velocities can be derived with the matrix expression in Equation (2.2), where the terms $\tilde{\mathbf{F}}_p$ and $\tilde{\mathbf{Y}}_{ep}(\omega)$ are replaced by the $[N_e \times 1]$ vector of element excitation forces $\tilde{\mathbf{F}}_e(\omega)$ and the $[N_e \times N_e]$ matrix of element point and transfer mobilities $\tilde{\mathbf{Y}}_{ee}(\omega)$ so that

$$\tilde{\dot{\mathbf{w}}}_e(\omega) = \tilde{\mathbf{Y}}_{ee}(\omega)\tilde{\mathbf{F}}_e(\omega). \tag{2.5}$$

As an example of a deterministic disturbance, an Acoustic Plane Wave (APW) excitation is considered. The wave is defined by its sound pressure amplitude and by the angles of incidence θ (taken from the normal to the panel surface) and the angle φ (given in the (x, y)-plane, measured from the x-axis) as shown in Figure 2.5.

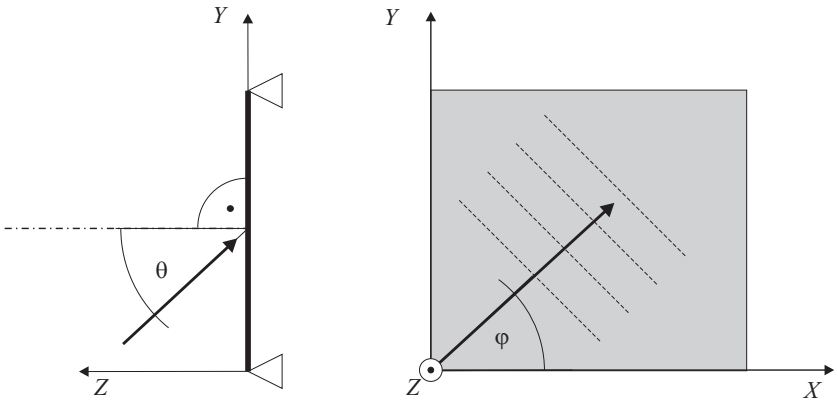

Figure 2.5: Angle of incidence for acoustic plane wave.

Assuming time-harmonic pressure fluctuations, the incident sound pressure $p(x, y, t)$ acting on the source side of the panel is given as

$$p(x, y, t) = Re\{\hat{p}(\omega)e^{j(\omega t - k_x x - k_y y)}\}, \tag{2.6}$$

where $\hat{p}(\omega)$ is the pressure amplitude of the incident wave. The wavenumbers in the x and y directions, k_x and k_y, are given by

$$k_x(\omega) = k_0(\omega)\sin\theta\cos\varphi, \tag{2.7}$$

$$k_y(\omega) = k_0(\omega)\sin\theta\sin\varphi, \tag{2.8}$$

where $k_0(\omega) = \omega/c_0$ is the wavenumber of sound in the surrounding fluid. The fluid properties of air used throughout the simulation studies are given in Table 2.2 below. The pressure amplitude $\hat{p}(\omega)$ is set to unity. The angle of incidence φ is set to 45° while different values for the angle θ are considered.

Table 2.2: Acoustical parameters of air

Parameter	Symbol	Value	Unit
Speed of sound	c_0	343	m/s
Density	ρ_0	1.21	kg/m^3
Specific impedance	$Z_0 = c_0\rho_0$	415	Ns/m^3

In order to predict the response due to a plane wave excitation, the panel needs to be subdivided into an appropriate number of equally spaced and sized elements. The minimum

element resolution is determined by the shortest wavelength at the maximum frequency considered in the simulation. Below the acoustic critical frequency [19] the acoustic wavelength is longer than the bending wavelength on the panel, thus the minimum element resolution is determined by the bending wavelength on the panel. Above the acoustic critical frequency the acoustic wavelength is shorter than the bending wave length on the panel; thus the minimum element resolution is given by the acoustic wavelength at the maximum frequency considered in the simulation.

In order to characterise the pressure field produced by an acoustic plane wave at any angle of incidence and to sample the excitation of the bending structural modes of a panel, ideally at least four elements per shortest acoustic or structural wavelength should be used [46]. Increasing the element resolution yields more accurate results. However a simulation study on the effect of resolution has shown that an increase of the element resolution above four elements per shortest wavelength only marginally affects the results at the upper end of the observed frequency range but produces a considerable increase of the computation time.

The elements of the vector $\tilde{\mathbf{F}}_e(\omega)$ for APW excitation are given by

$$\tilde{F}_{e_i}(\omega) = 2A_e\hat{p}(\omega)e^{-j(k_x x_i + k_y y_i)}, \tag{2.9}$$

where A_e is the area of a single element and the factor 2 accounts for the assumption of blocked pressure on the panel surface [19]. The resulting $[N_e \times 1]$ vector of complex forces is then used as the excitation term in Equation (2.5).

Panel kinetic energy

The response of the panel is assessed in terms of its total kinetic energy, which gives an indicator for the spatially averaged vibration and also of the near field sound radiation. For harmonic excitations, the time-averaged kinetic energy of a thin rectangular panel with uniform mass per unit area is given by [19]

$$E(\omega) = \frac{\rho h}{4} \int_0^{l_x} \int_0^{l_y} \left|\tilde{\dot{w}}(x, y, \omega)\right|^2 \, dx \, dy, \tag{2.10}$$

where the additional factor 1/2 arises from the conversion from peak to RMS values. In the elemental approach the surface integral in Equation (2.10) is replaced by a sum over the

element velocities [19]. Utilizing matrix algebra this summation can be calculated from the inner Hermitian product of the element velocity vectors. This yields the total kinetic energy as [see Appendix B, Equations (B.21) to (B.32)]

$$E(\omega) = \frac{M_e}{4} \ \tilde{\dot{\mathbf{w}}}_e^H(\omega)\tilde{\dot{\mathbf{w}}}_e(\omega), \tag{2.11}$$

where ^{H} denotes the Hermitian transpose and M_e is the mass of an individual element. Substituting Equation (2.5) into Equation (2.11) gives the total kinetic energy with reference in terms of the vector of elemental forces

$$E(\omega) = \frac{M_e}{4} \ \tilde{\mathbf{F}}_e^H(\omega) \left(\tilde{\mathbf{Y}}_{ee}^H(\omega)\tilde{\mathbf{Y}}_{ee}(\omega)\right) \tilde{\mathbf{F}}_e(\omega). \tag{2.12}$$

Figure 2.6 shows the spectrum of the kinetic energy of a simply supported aluminium panel normalised to the pressure amplitude of a plane acoustic wave incident at an angle θ=45° and φ=45° in the frequency range between 50 Hz and 20 kHz. The panel dimensions and material properties are summarised in Table 2.1.

At frequencies below 1500 Hz, the response of the panel is characterised by well-separated resonances which are controlled by low-order resonant modes. Above 1500 Hz the response is increasingly controlled by overlapping clusters of modes and rolls off following a mass law. Between 10 and 20 kHz there is a wide-band peak due to the acoustic coincidence effect. In fact the acoustic coincidence for the θ=45° plane wave occurs around 15 kHz.

Radiated sound power

The sound radiated by the panel is expressed in terms of the total sound power radiated which gives an indication of the far field, spatially-averaged, sound radiation. The time-averaged total sound power radiated on one side of the panel is given by [19]

$$P(\omega) = \frac{1}{2} \int_0^{l_x} \int_0^{l_y} Re\left\{\tilde{\dot{w}}^*(x,y,\omega)\, \tilde{p}(x,y,\omega)\right\} dx\, dy, \tag{2.13}$$

where * denotes the complex conjugate and the factor 1/2 arises from the conversion from peak to RMS values. Considering radiation into free space, for an ideally planar panel, the Rayleigh integral [19] is used to rewrite the acoustic pressure on the surface in terms of the

surface velocities and radiation impedance. Utilising matrix algebra Equation (2.13) can be cast in the form [see Appendix B, Equations (B.33) to (B.41)]

$$P(\omega) = \tilde{\dot{\mathbf{w}}}_e^H(\omega)\mathbf{R}_{rad}(\omega)\tilde{\dot{\mathbf{w}}}_e(\omega), \tag{2.14}$$

Substituting Equation (2.5) into Equation (2.14) gives the total sound power radiated in terms of the vector of the elemental forces

$$P(\omega) = \tilde{\mathbf{F}}_e^H(\omega)\tilde{\mathbf{Y}}_{ee}^H(\omega)\mathbf{R}_{rad}(\omega)\tilde{\mathbf{Y}}_{ee}(\omega)\tilde{\mathbf{F}}_e(\omega), \tag{2.15}$$

where $\mathbf{R}_{rad}(\omega)$ in Equations (2.14) and (2.15) is the $[N_e \times N_e]$ radiation matrix with the elements [see Appendix B, Equations (B.43) to (B.46)]

$$R_{rad_{i,j}} = \frac{\omega^2 \rho_0 A_e^2}{4\pi c_0} \frac{\sin(k_0 R_{i,j})}{k_0 R_{i,j}}. \tag{2.16}$$

In this equation k_0 is the acoustic wavenumber on the receiving side of the panel and $R_{i,j} = \sqrt{(x_i - x_j)^2 + (y_i - y_j)^2}$ is the distance between the centres of the elements i and j. The distance $R_{i,i}$ is zero, thus the radiation terms $R_{rad_{i,i}}$ on the main diagonal of the radiation matrix are undefined. However, using L' Hôpital's rule [49] it is found that

$$\lim_{R \to 0} \frac{\sin(k_0 R)}{k_0 R} = \lim_{R \to 0} \frac{k_0 \cos(k_0 R)}{k_0} = 1. \tag{2.17}$$

Figure 2.6 also shows the spectrum of the total sound power radiated by the panel considered above in the frequency range between 50 Hz and 20 kHz for plane acoustic wave excitation incident at an angle θ=45° and angle φ=45°, normalized to an acoustic pressure amplitude of 1 Pascal. At low frequencies the spectrum of the radiated sound power is dominated by the response of the principal panel mode. The resonance peaks of low order modes with low radiation efficiency (even, symmetric panel modes) are small compared with those of modes with higher radiation efficiency (odd, asymmetric panel modes). As found for the vibration response of the panel, above 1500 Hz the total sound power radiated is characterised by overlapping clusters of modes and rolls off following a mass law. However, in this case, the sound power starts to rise again from about 5 kHz since the sound radiation becomes increasingly effective above the acoustic critical frequency, which for this panel is at about 7.5 kHz. Moreover, between 10 kHz and 20 kHz there is a wide frequency band peak due to the coincidence effect of the acoustic wave incident at θ=45°.

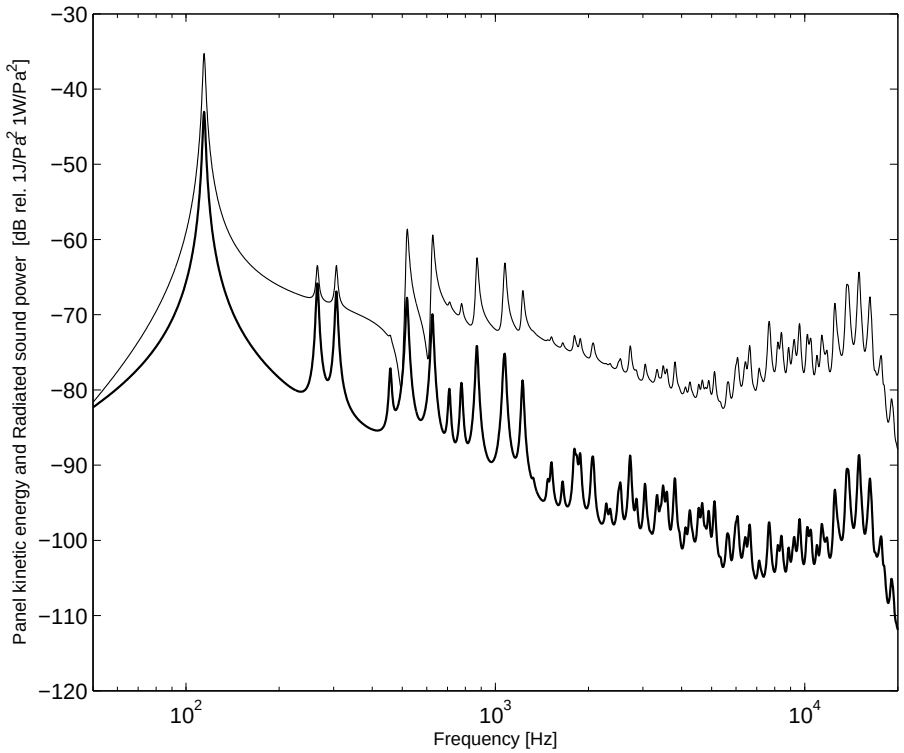

Figure 2.6: Panel kinetic energy ($solid$) and radiated sound power ($faint$) normalized to the pressure amplitude of a plane wave incident at an angle θ=45° and angle φ=45° for the panel with pinned boundary conditions specified in Table 2.1.

Sound transmission

The sound transmission coefficient τ is definer [19] as the ratio between the radiated sound power in the far field of the radiating side of the panel P_{rad} and the sound power of the incident plane wave on the source side of the panel P_{in}.

$$\tau(\omega) = \frac{P_{rad}(\omega)}{P_{in}(\omega)}. \tag{2.18}$$

Note that the definition of the transmission coefficient τ considers only the component of the power in an infinitely extended incident plane wave P_{in} incident on the panel area and not the total power on the source side of the panel, which is determined by the interaction of the incident, reflected and back-radiated acoustic waves over the area of the panel. The power in the incident acoustic plane wave is given by [50, 23]

$$P_{in}(\omega) = \hat{p}^2(\omega)\frac{A_p \cos(\theta)}{2\rho_0 c_0}. \tag{2.19}$$

As for most acoustical quantities it is convenient to express the transmission coefficient τ in logarithmic terms to give the sound transmission index in decibels

$$T(\omega) = 10\log_{10}\left(\tau(\omega)\right). \tag{2.20}$$

The sound transmission loss or sound reduction index in decibels is calculated from the reciprocal of the transmission coefficient and is expressed as follows:

$$TL(\omega) = 10\log_{10}\left(\frac{1}{\tau(\omega)}\right). \tag{2.21}$$

Approximate solutions for the sound transmission coefficient are widely discussed in the literature. In Reference [5] Fahy discusses an approximate formulation that allows the transmission coefficient to be evaluated for infinite thin panels due to plane wave excitations depending on the out-of-plane incidence angle θ

$$\tau(\theta) = \frac{\left(\frac{2Z_0}{\omega m''}\right)^2 \sec^2(\theta)}{\left[\left(\frac{2Z_0}{\omega m''}\right)\sec^2(\theta) + \eta\left(\frac{k_0}{k_b}\right)^4 \sin^4(\theta)\right]^2 + \left[1 - \left(\frac{k_0}{k_b}\right)^4 \sin^4(\theta)\right]^2}, \tag{2.22}$$

where k_b is the bending wavenumber, m'' is the mass per unit area of the panel and η is the damping loss factor. Fahy [51] also gives an approximation for the sound transmission coefficient through a thin unbounded panel mounted upon a viscously damped elastic suspension. This is a first order approximation for the fundamental mode of a large finite panel. The formulation is derived for an acoustic plane wave excitation normal to the surface ($\theta = 0$). For non-identical media on both sides of the panel, the transmission coefficient τ_0 is given as

$$\tau_0 = \frac{4n}{\left[\frac{\omega m'' - \frac{s}{\omega}}{Z_2}\right]^2 + \left(\frac{\omega_{1,1} m'' \eta}{Z_2} + n + 1\right)^2}, \tag{2.23}$$

where n is the ratio between the specific impedance of the fluid on the source side Z_1 and the specific impedance of the fluid on the receiving side of the panel Z_2 so that $n = Z_1/Z_2 = \rho_1 c_1/\rho_2 c_2$ and s is the stiffness per unit area at the fundamental panel bending mode given by $s = m''\omega_{1,1}^2$. In the case that the fluid on both sides of the panel is air, the sound transmission coefficient well above the first natural frequency of the panel $\omega_{1,1}$ can be approximated as [51]

$$\tau_0 = \left(\frac{2Z_0}{\omega m''}\right)^2. \tag{2.24}$$

This indicates that the transmission coefficient is dropping by 6 dB per frequency doubling i.e. 20 dB per decade and is known as the 'mass law'.

Figures 2.7 and 2.8 show the sound transmission index predicted using the elemental approach and the approximate solutions from Equations (2.22) and (2.23). The results for an acoustic plane wave incident at an angle θ=0° (normal to the panel) in Figure 2.7 show that at low frequencies, up to 800 Hz, the modal response of the panel controls the transmission coefficient and the agreement is poor between the elemental approach and the analytical approximations. Above 800 Hz the results from the elemental approach and both the results for $\tau(\theta = 0)$ from Equation (2.22) and τ_0 from Equation (2.23) are in good agreement up to about 5000 Hz. Above 5000 Hz the transmission index predicted from the elemental approach is higher due to acoustic radiation coincidence effects which are not captured in the analytical solutions. These coincidence effects are further discussed in Chapter 3.

Figure 2.8 shows the results for an acoustic plane wave incident at an angle θ=45° and φ=45°. At low frequencies, up to 1000 Hz, the modal response controls the transmission coefficient. Again poor agreement is found between the elemental approach and the analytical approximations. Above 1000 Hz the results from the elemental approach and the results for $\tau(\theta = 45°)$ from Equation (2.22) converge asymptotically up to about 5000 Hz. Above 5000 Hz the transmission loss predicted from the elemental approach exhibits radiation coincidence effects and excitation coincidence effects. The radiation coincidence effects are not captured in the analytical solutions from Equation (2.22). However the formulation in Equation (2.22) captures the excitation coincidence effect due the projection of the incident plane wave, which occurs around 15 kHz. In this coincidence frequency region both the analytical and the numerical results from the elemental approach are in good agreement, which validates the numerical results. Excitation and acoustic radiation coincidence effects are further discussed in Chapter 3.

It is interesting to note that, at the fundamental natural frequency of the panel, the elemental approach predicts transmission coefficients higher than zero. This effect is investigated in Reference [52]. In effect the resonant panel is excited by an sound field that is large than its own surface. Due to the existence of a panel resonance with low impedance, energy is attracted by diffraction from the incident sound field well beyond the immediate surface of the panel. Further discussion on the modelling of the structural response and the radiated and transmitted sound power through fluid loaded panel with flexible boundaries is provided in Reference [46].

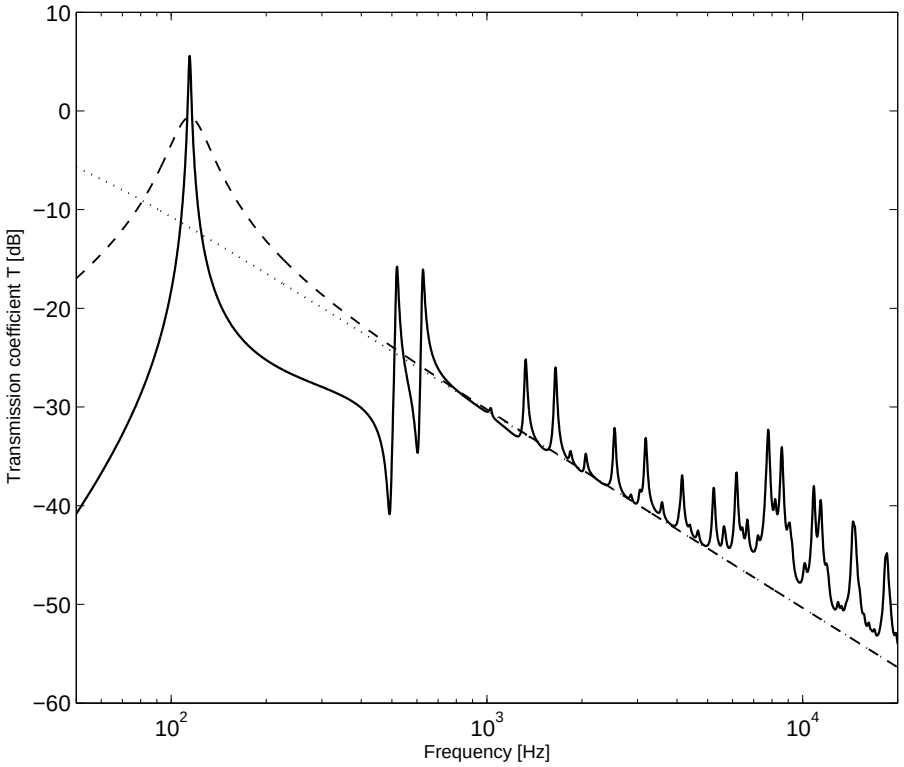

Figure 2.7: Transmission coefficient for an acoustic plane wave excitation incident at an angle θ=0° and φ=45° for the panel with pinned boundary conditions specified in Table 2.1. Elemental approach ($solid$), approximate analytical result $\tau(\theta = 0°)$ ($dotted$) and τ_0 ($dashed$).

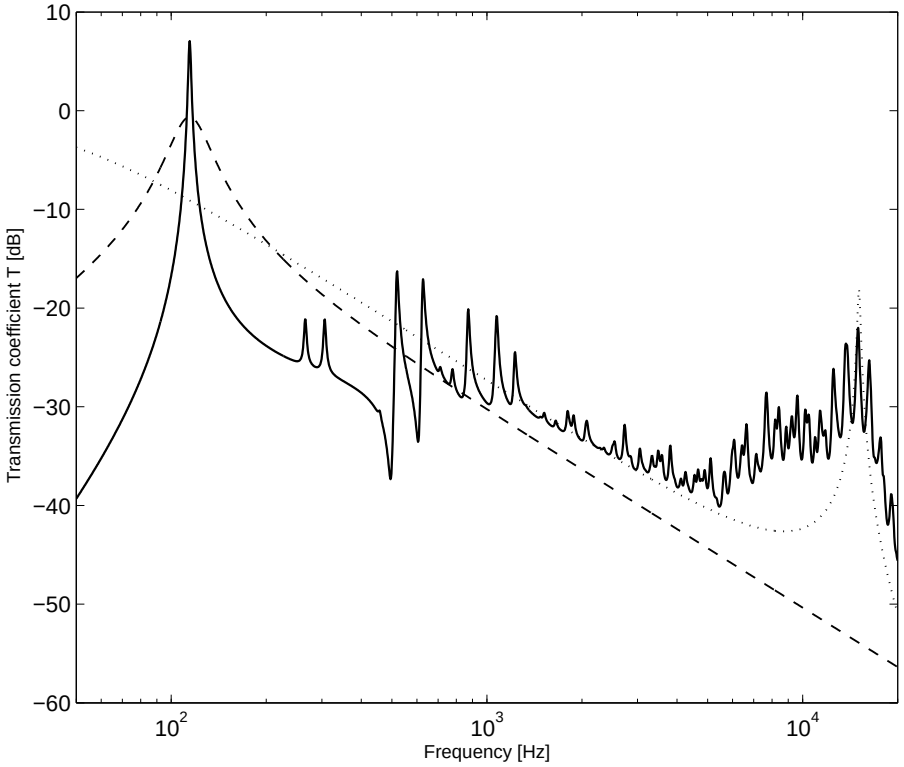

Figure 2.8: Transmission coefficient for an acoustic plane wave excitation incident at an angle θ=45° and φ=45° for the panel with pinned boundary conditions specified in Table 2.1. Elemental approach ($solid$), approximate analytical result $\tau(\theta = 45°)$ ($dotted$) and τ_0 ($dashed$).

2.1.2 Stochastic excitation

For many practical vibro-acoustic problems, the excitation is not deterministic. For instance acoustic diffuse sound fields (ADF) or turbulent boundary layer (TBL) pressure fields, produced by the interaction of a turbulent flow of fluid and a structure, are often encountered in vehicles such as aircraft, high speed trains and cars. Analytical formulations for the statistical properties of the excitation fields produced by ADF and TBL are available. These formulations describe disturbances in terms of power spectral density and spatial correlation functions. The response and sound radiation induced by such random excitation fields are also expressed in terms of power spectral densities. In particular the response is expressed in terms of the power spectral density for the total kinetic energy, which for a panel structure, is given by [see Appendix B, Equations (B.47) to (B.49)]

$$S_E(\omega) = \frac{\rho h}{2} \int_0^{l_x} \int_0^{l_y} \lim_{T\to\infty} E\left[\frac{1}{T}\tilde{\dot{w}}^*(x,y,\omega)\tilde{\dot{w}}(x,y,\omega)\right] dx\, dy, \tag{2.25}$$

where $\tilde{\dot{w}}$ is the finite Fourier transfor of $\dot{w}(t)$. Considering the matrix formulation for the elemental approach, Equation (2.25) can be reformulated to give [see Appendix B, Equations (B.49) to (B.62)]

$$S_E(\omega) = \frac{M_e}{2}\ trace\left(\tilde{\mathbf{Y}}_{ee}^H\, \tilde{\mathbf{S}}_{f_e f_e}(\omega)\, \tilde{\mathbf{Y}}_{ee}\right). \tag{2.26}$$

where $\tilde{\mathbf{S}}_{f_e f_e}$ is the $[N_e \times N_e]$ matrix of cross-spectral densities between the forces acting on the centres of panel elements. The matrix of cross-spectral densities of the elemental excitation due to a disturbance which is stochastic over time and space has the form

$$\tilde{\mathbf{S}}_{f_e f_e}(\omega) = A_e^2\, \Psi(\omega)\, \tilde{\mathbf{C}}_{ee}(\omega), \tag{2.27}$$

where A_e is the area of an element, $\Psi(\omega)$ is the time-averaged power spectrum of the disturbance per unit area and $\tilde{\mathbf{C}}_{ee}$ is the $[N_e \times N_e]$ spatial cross-correlation matrix of the excitation disturbance calculated at the element centre locations. The sound radiation is expressed in terms of the power spectral density of the sound power radiated into an infinite half-space on the receiving side of the panel, which is given by

$$S_P(\omega) = Re\left\{ \int_0^{l_x} \int_0^{l_y} \lim_{T\to\infty} E\left[\frac{1}{T}\tilde{\dot{w}}^*(x,y,\omega)\tilde{p}(x,y,0,\omega)\right] dx\, dy \right\}. \tag{2.28}$$

Considering the elemental formulation, Equation (2.28) can be reformulated to give [see Appendix B, Equations (B.63) to (B.71)]

$$S_P(\omega) = 2\, trace\left[\left(\tilde{\mathbf{Y}}_{ee}^H \tilde{\mathbf{S}}_{f_e f_e} \tilde{\mathbf{Y}}_{ee}\right) \mathbf{R}_{rad}\right], \tag{2.29}$$

where $\mathbf{R}_{rad}$ is the element radiation matrix with the elements defined in Equation (2.16).

2.1.3 Acoustic diffuse field

The acoustic diffuse field (ADF) is a widely used model to describe the excitation from a reverberant sound field which is produced by random acoustic plane waves incident to a surface for all angles. The cross-spectral density for an acoustic diffuse field excitation has been discussed by Shorter and Langley [53]. The power spectral density of an acoustic diffuse field is given by

$$\Psi_{ADF}(\omega) = 4E\left[\tilde{p}\,\tilde{p}^*\right] = 4\langle\overline{\tilde{p}^2}\rangle \tag{2.30}$$

where $\langle\overline{\tilde{p}^2}\rangle$ denotes the farfield mean square pressure. The factor of 4 arises from the pressure doubling at a rigid surface (and from the relationship between the pressure magnitude and mean square value). The spatial correlation function for an acoustic diffuse field on the surface of a rigid infinite plane is given by [53]

$$C_{ADF_{i,j}}(\omega) = \frac{\sin\left(k_0\, R_{i,j}\right)}{k_0\, R_{i,j}}, \tag{2.31}$$

where k_0 is the acoustic wavenumber on the source side of the panel and $R_{i,j}$ is the distance between the centres of the elements i and j. It is interesting to note that the correlation function for an ADF disturbance has the same spatial characteristics as the radiation matrix defined in Equation (2.16).

2.1.4 Turbulent boundary layer

Turbulent boundary layer (TBL) disturbance models are widely used to describe the excitation produced on a surface by a turbulent fluid flow. Models for the spatial correlation of TBL disturbances have been discussed in References [54] and [55]. The most common expression for TBL cross spectral density is given by Corcos [56]. The parameters that define the model of the spatial correlation of a fully developed TBL on the panels considered in this study, are given in Table 2.3, where the flow speed is chosen to represent typical aircraft cruising speeds. The flow direction is assumed parallel to the y-axis. The spatial correlation function in the x-direction (span-wise) and y-direction (stream-wise) is given by

$$\tilde{C}_{TBL_{i,j}}(\omega) = \exp\left(-\frac{|R_{x_{i,j}}|}{L_x(\omega)}\right)\exp\left(-\frac{|R_{y_{i,j}}|}{L_y(\omega)}\right)\exp\left(\frac{-j\omega R_{y_{i,j}}}{U_c}\right), \tag{2.32}$$

where $|R_{x_{i,j}}| = |x_i - x_j|$ and $|R_{y_{i,j}}| = |y_i - y_j|$ are the distances between the centres of element i and j in the x- and y-directions and L_x and L_y are the correlation lengths in x and y, given by

$$L_x(\omega) = \frac{\alpha_x U_{conv}}{\omega}, \tag{2.33}$$

$$L_y(\omega) = \frac{\alpha_y U_{conv}}{\omega}, \tag{2.34}$$

where α_x and α_y are empirical constants taken from [54, 55] and U_{conv} is the convection velocity. The convection velocity is a function of frequency [56, 57], but can be approximated as a fixed fraction of the free flow velocity. Since this hypothesis is equivalent to assuming that the cross-correlation function is independent of the boundary layer thickness, it overestimates the correlation length at very low frequency. Comprehensive reviews on TBL excitation models and research on the wavenumber-frequency spectrum are given by Bull [8], by Cousin [57] and more resent by Hwang et al. [9]. In general, the power spectral density of the surface pressure fluctuations due to a turbulent boundary layer decreases with increasing frequency. The results presented in this thesis do not reflect this dependency but only compare the panel response to different disturbances with respect to their frequency-dependent spatial correlation.

Table 2.3: Parameters for the turbulent boundary layer disturbance.

Parameter	Symbol	Value	Unit
Free-stream velocity	U_∞	225	m/s
Convection velocity	U_{conv}	0.6 $\times U_\infty$	m/s
Empirical constant [1]	α_x	1.2	–
Empirical constant [1]	α_y	8	–

[1] taken from Ref. [54]

2.1.5 Element resolution

The required element grid density depends on (a) the disturbance characteristics, (b) the flexural response of the panel and (c) the radiation properties of the panels, which are given by the radiation matrix. For frequencies below the convective and acoustic coincidence frequencies the bending wavelength is shorter than the acoustic wavelength; thus the required mesh density is determined by the bending wavelength $\lambda_b = c_b(f)/f$ on the panels. For frequencies above the acoustic coincidence frequency, it is the acoustic wavelength that is shorter than the bending wavelength on the panel; therefore the element density is determined by the acoustic wavelength $\lambda_0 = c_0/f$. For TBL disturbance, the element density in the stream-wise direction for frequencies above the convective coincidence is determined by the convective wavelength $\lambda_{conv} = U_{conv}/f$. In the span-wise x-direction the correlation function in Equation (2.32) is exponentially decaying, thus a low resolution of the element grid in x-direction results in an overestimation of the structural response but does not change its general characteristics. In general at least two elements per shortest wavelength are required to avoid spatial aliasing. Numerical convergence studies showed that four elements per shortest wavelength, at the highest frequency of interest, ensures convergence at high frequencies and accurate predictions for the entire observed frequency range [46].

2.2 Decentralised velocity feedback control

This section introduces the formulations for decentralized multi-input multi-output (MIMO) feedback loops with idealized feedback forces and point velocity sensors as shown in Figure 2.9. The formulations are cast in the framework of element matrix expressions introduced in previous sections. The formulations are developed considering a distributed excitation. The feedback loops discussed are unconditionally stable if perfectly collocated feedback force and velocity sensor pairs are considered [24].

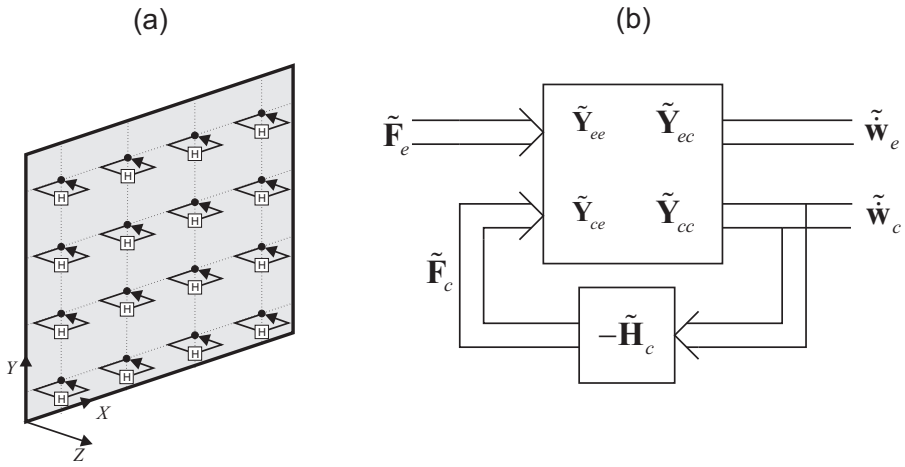

Figure 2.9: Schematic of panel model. (a) Panel with 16 discrete decentralised velocity feedback loops and (b) "two port" block diagram of the panel model with decentralised MIMO feedback control.

As shown in Figure 2.9(a), the decentralised feedback control system is formed by a 4×4 grid of velocity feedback loops using collocated point velocity sensors and point force actuators. The closed loop response of the panel can be modelled with the two ports block diagram in Figure 2.9 (b). Assuming the system is linear this indicates that the response at both the element centres and the control positions result from the linear superposition of the vibration induced by the primary excitation, produced by the pressure field over the surface on the source side of the panel, and the secondary excitation produced by the control point forces, which depend on the control velocities via the feedback control gains. Thus the velocity response at the centres of the panel elements is given by

$$\tilde{\dot{\mathbf{w}}}_e = \tilde{\mathbf{Y}}_{ee}\tilde{\mathbf{F}}_e + \tilde{\mathbf{Y}}_{ec}\tilde{\mathbf{F}}_c, \tag{2.35}$$

where $\tilde{\mathbf{F}}_c$ is the $[N_c \times 1]$ vector of feedback control forces

$$\tilde{\mathbf{F}}_c(\omega) = \left\{ \begin{array}{c} \tilde{F}_{c_1}(\omega) \\ \tilde{F}_{c_2}(\omega) \\ \vdots \\ \tilde{F}_{c_{N_c}}(\omega) \end{array} \right\}. \tag{2.36}$$

and $\tilde{\mathbf{Y}}_{ec}$ is the $[N_e \times N_c]$ matrix of transfer mobilities between the control locations an the centres of the panel elements. As for the $\tilde{\mathbf{Y}}_{ee}$ matrix, the mobility functions in the $\tilde{\mathbf{Y}}_{ec}$ matrix are derived using the finite modal summation formula given in Appendix A. As shown in the block diagram in Figure 2.9(b), for direct velocity feedback control, the vector

of control forces is given by

$$\tilde{\mathbf{F}}_c = -\tilde{\mathbf{H}}_c \tilde{\dot{\mathbf{w}}}_c, \tag{2.37}$$

where $\tilde{\mathbf{H}}_c$ is the $[N_c \times N_c]$ diagonal matrix of control gains and $\tilde{\dot{\mathbf{w}}}_c$ is the $[N_c \times 1]$ vector of velocity sensor outputs at the control locations

$$\tilde{\dot{\mathbf{w}}}_c(\omega) = \left\{ \begin{array}{c} \tilde{\dot{w}}_{c1}(\omega) \\ \tilde{\dot{w}}_{c2}(\omega) \\ \vdots \\ \tilde{\dot{w}}_{cN_c}(\omega) \end{array} \right\}. \tag{2.38}$$

According to the "two port" block diagram in Figure 2.9(b), the vector of control point velocities is given by

$$\tilde{\dot{\mathbf{w}}}_c = \tilde{\mathbf{Y}}_{ce} \tilde{\mathbf{F}}_e + \tilde{\mathbf{Y}}_{cc} \tilde{\mathbf{F}}_c, \tag{2.39}$$

where $\tilde{\mathbf{Y}}_{cc}$ is the $[N_c \times N_c]$ matrix of point and transfer mobilities between the control locations and $\tilde{\mathbf{Y}}_{ce}$ is the $[N_c \times N_e]$ matrix of transfer mobilities between the centres of the panel elements and the control locations. Substituting Equation (2.37) into Equation (2.39) gives

$$\tilde{\dot{\mathbf{w}}}_c = \tilde{\mathbf{Y}}_{ce} \tilde{\mathbf{F}}_e - \tilde{\mathbf{Y}}_{cc} \tilde{\mathbf{H}}_c \tilde{\dot{\mathbf{w}}}_c \tag{2.40}$$

An explicit formulation for $\tilde{\dot{\mathbf{w}}}_c$ can hence be derived as

$$\tilde{\dot{\mathbf{w}}}_c = \left(\mathbf{I}_c + \tilde{\mathbf{Y}}_{cc} \tilde{\mathbf{H}}_c \right)^{-1} \tilde{\mathbf{Y}}_{ce} \tilde{\mathbf{F}}_e, \tag{2.41}$$

where $\mathbf{I}_c$ is a $[N_c \times N_c]$ unit matrix. The control force $\tilde{\mathbf{F}}_c$ in Equation (2.37) can subsequently be found as

$$\tilde{\mathbf{F}}_c = -\tilde{\mathbf{H}}_c \left(\mathbf{I}_c + \tilde{\mathbf{Y}}_{cc} \tilde{\mathbf{H}}_c \right)^{-1} \tilde{\mathbf{Y}}_{ce} \tilde{\mathbf{F}}_e. \tag{2.42}$$

Substituting Equation (2.42) into Equation (2.35) and rearranging for $\tilde{\dot{\mathbf{w}}}_e$ finally gives the

vector of element velocities as

$$\tilde{\dot{\mathbf{w}}}_e = \left[\tilde{\mathbf{Y}}_{ee} - \tilde{\mathbf{Y}}_{ec}\tilde{\mathbf{H}}_c\left(\mathbf{I}_c + \tilde{\mathbf{Y}}_{cc}\tilde{\mathbf{H}}_c\right)^{-1}\tilde{\mathbf{Y}}_{ce}\right]\tilde{\mathbf{F}}_e = \tilde{\mathbf{G}}_{ee}\tilde{\mathbf{F}}_e, \tag{2.43}$$

where $\tilde{\mathbf{G}}_{ee} = \tilde{\mathbf{Y}}_{ee} - \tilde{\mathbf{Y}}_{ec}\tilde{\mathbf{H}}_c(\mathbf{I}_c + \tilde{\mathbf{Y}}_{cc}\tilde{\mathbf{H}}_c)^{-1}\tilde{\mathbf{Y}}_{ce}$ is the panel element mobility matrix with active control. Thus, when an active panel is considered, the spectrum (or power spectral density) of the total kinetic energy and total sound power radiated can be derived respectively from Equations (2.12) or (2.26) and Equations (2.15) or (2.29) by simply replacing the matrix $\tilde{\mathbf{Y}}_{ee}$ with $\tilde{\mathbf{G}}_{ee}$.

2.3 Summary

In this chapter an element-based approach for the modelling of structural response and radiated sound power for passive panels and active panels with decentralised feedback control has been introduced. The expressions for transverse point force and distributed deterministic excitations, and transverse distributed stochastic excitations have been reviewed to provide background information for the models used to generate the simulation results presented in Chapters 3 and 5.

Preliminary simulation results have shown that the transmission coefficient of a baffled passive panel derived with the elemental approach is in good agreement with the corresponding analytical solutions in the frequency range for which the analytical results are valid.

The next chapter discusses the structural response and sound radiation of baffled panels due to APW excitations at different angles and stochastic ADF and TBL excitations in further detail and also contrasts the response and radiated sound power for a thin homogeneous aluminium panel with those of a lightweight sandwich panel.

Chapter 3

Comparison between thin homogeneous and lightweight sandwich passive and active panels

This chapter presents the results of a simulation study considering a thin homogeneous active panel and a lightweight sandwich active panel for different types of distributed deterministic and stochastic excitations. The objectives of this simulation work are twofold. Firstly, to investigate and contrast the structural response and the sound radiation in the audio frequency range produced by homogeneous and lightweight sandwich panels subject to deterministic and stochastic distributed excitations. Secondly, to study and compare the control effects produced by an array of idealized velocity feedback control loops on homogeneous and lightweight sandwich panels.

The elemental approach introduced in Chapter 2 is used to predict the structural response and sound radiation of the two smart panels excited by (a) an Acoustic Plane Wave (APW) at different angles of incidence, (b) a stochastic Acoustic Diffuse Field (ADF) and (c) a Turbulent Boundary Layer (TBL). The first panel is made of aluminium while the second is a composite sandwich panel with equivalent static stiffness but four times lower mass per unit area. As shown in Figure 2.9, the panels are equipped with sixteen decentralised velocity feedback control loops using idealized point force actuators and collocated idealized velocity sensors [27, 23]. In this way the intrinsic limits of decentralised feedback control are investigated independently from the electrodynamic response of the control units.

- Section 3.1 specifies the models used to capture the dynamic characteristics of the thin homogeneous and the lightweight sandwich panels.
- Section 3.2 discusses the characteristic differences between the structural response of these two panels are with respect to (a) the real wavenumber solutions of the governing equations, (b) modal density, (c) modal overlap factor and (d) both excitation and radiation coincidence effects.
- Section 3.3 presents the results from simulation studies on the panels without control in order to contrast the structural response and sound radiated by the two panels under the different distributed excitations.
- Section 3.4 then presents the results from simulations studies on the two panels with 16 ideal velocity feedback loops. The control performance for the two smart panels is discussed with respect to modal density, structural point mobility function and control position and also with respect to excitation and radiation acoustic coincidence effects.

3.1 Panel models

This section introduces the dynamic models considered for the modelling of the thin homogeneous and the lightweight sandwich panel considered in this simulation study. The sandwich panel is designed to have a four times lower mass per unit area than the thin homogeneous panel which is modelled using the material properties of aluminium. The panel parameters of both panels are chosen to yield an equivalent static panel stiffness.

3.1.1 Thin homogeneous panel

The rectangular aluminium panel has been modelled as a thin homogeneous and isotropic panel with all sides simply supported. The mass-normalised mode shapes [47] are given by [see Appendix 2, Section A.2]

$$\phi_r(x,y) = 2\sin\left(\frac{m_r\,\pi x}{l_x}\right)\sin\left(\frac{n_r\,\pi y}{l_y}\right), \tag{3.1}$$

where and m_r and n_r are the mode orders of mode r in the x- and y-direction of the panel. The natural frequencies are given by

$$\omega_r = \sqrt{\frac{D}{m''}}\left[\left(\frac{m_r\,\pi}{l_x}\right)^2 + \left(\frac{n_r\,\pi}{l_y}\right)^2\right], \tag{3.2}$$

where $m'' = \rho h$ is the panel mass per unit area and $D = Eh^3/12(1-\nu^2)$ is the bending. Also E is the Young's modulus of elasticity and ν is the Poisson's ratio of the panel material. The panel geometry and material properties of the aluminium panel considered in the theoretical simulation studies are given in Table 2.1 of Chapter 2.

3.1.2 Sandwich panel

The dynamic response of the sandwich panel is modelled using a basic theory [19, 58] which considers pure bending of the cross-section and the faceplates and pure transverse shear of the core. The panel is assumed to have the same material properties in the x- and y-directions. The relationship between the transverse wavenumber k and the wavenumbers corresponding to pure bending and to pure shear of a sandwich panel is given by

$$1 + \left(\frac{k_s}{k_b}\right)^2\left(\frac{k}{k_b}\right)^2 - \left(\frac{k}{k_b}\right)^4 - \left(\frac{k_b}{k_{bf}}\right)^4\left(\frac{k_s}{k_b}\right)^2\left(\frac{k}{k_b}\right)^6 = 0, \tag{3.3}$$

where k_s is the shear wavenumber in the absence of transverse bending forces, k_b is the overall cross-section bending wavenumber in the absence of shear distortion and k_{bf} is the bending wavenumber for faceplate bending alone. These wavenumbers are given as

$$\text{(a)}\ k_s^2 = \frac{m''\omega^2}{G\,d}, \qquad \text{(b)}\ k_b^4 = \frac{m''\omega^2}{D_1}, \qquad \text{(c)}\ k_{bf}^4 = \frac{m''\omega^2}{2\,D_2}, \tag{3.4}$$

where m'' is the total panel mass per unit area and G is the transverse core shear modulus. As shown in Figure 3.1, d is the distance between the faceplate neutral axes, which assuming that d is much larger than the thickness of the faceplates is also used to represent the core thickness. D_1 is the bending stiffness of the cross-section and D_2 is the bending stiffness of an individual faceplate. These flexural stiffness terms are given by

$$\text{(a)}\ D_1 = \frac{Ed^2h_f}{2\,(1-\nu^2)}, \qquad \text{(b)}\ D_2 = \frac{Eh_f^3}{12\,(1-\nu^2)}. \tag{3.5}$$

where $h_f << d$ is the faceplate thickness. The physical parameters used to model the composite sandwich panel are given in Table 3.1. The parameters are chosen to yield a

panel with equal static stiffness but a four times lower mass per unit area than that of the homogeneous 1.6 mm thick aluminium panel specified in Table 2.1. Equation (3.3) has one real and two imaginary pairs of axi-symmetric solutions. For simplicity the sandwich panel is assumed to have the same mode shapes as a corresponding thin simply supported panel given in Equation (3.1) and that (a) the equivalent flexural rigidity D, (b) wavenumber at resonance k_r and (c) natural frequencies ω_r are given by

$$\text{(a) } D = \frac{\omega^2 m''}{k^4}, \quad \text{(b) } k_r = \sqrt{\left(\frac{m_r \pi}{l_x}\right) + \left(\frac{n_r \pi}{l_y}\right)}, \quad \text{(c) } \omega_r = \sqrt{\frac{k_r^4 \frac{D_1}{m''} + k_r^6 \frac{2D_2 D_1}{G\,d\,m''}}{1 + k_r^2 \frac{D_1}{G\,d}}}, \tag{3.6}$$

where the wavenumber k in Equation (3.6)(a) corresponds to the real wavenumber solution of Equation (3.3), which corresponds to travelling waves. The imaginary wavenumber solutions to Equation (3.3) correspond to decaying near field waves, which are neglected. The highest mode order of interest is calculated using the equivalent flexural rigidity at the highest frequency of interest. The acoustic coincidence frequency is found by reformulating Equation (3.3) as an implicit function in ω_c. Setting $\omega = \omega_c$ and $k = k_c = \omega_c / c_0$ Equation (3.3) results in the following relationship

$$\omega_c^4 \left(\frac{2D_2 D_1}{G\,d\,m'' c_0^6}\right) + \left(\frac{D_1}{m'' c_0^4} - \frac{D_1}{G\,d\,c_0^2}\right) - 1 = 0. \tag{3.7}$$

This basic model captures the principal characteristics of a sandwich panel and is thought to be suitable for an initial comparison between the structural response and radiated sound power of thin homogeneous and sandwich active panels. A more complex model, considering near field waves and the cross-section dynamics of the sandwich structure, may be needed for more detailed investigations. In particular, the near field wave effect could play an important role in the stability of the feedback control loops when realistic sensor and actuator transducers are considered.

Table 3.1: Cross section geometry and physical properties for the composite sandwich panel.

Parameter	Symbol	Value	Unit
Thickness of face-plate	h_f	0.3	mm
Core depth	d	3.0	mm
Mass density face-plates	ρ_f	1000	kg m^{-3}
Mass density core	ρ_c	180	kg m^{-3}
Panel mass per unit area[1]	m''	1.086	kg m^{-2}
Young's modulus face plates	E	17.7	GPa
Poisson's ratio	ν	0.33	–
Shear modulus core	G	80	MPa
Loss factor	η	0.02	–

[1] $m'' = 2h_f\rho_f + (d - h_f)\rho_c$

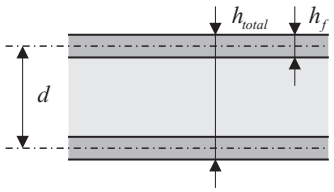

Figure 3.1: Sketch of sandwich panel cross section geometry.

3.1.3 Element resolution and mode range

As discussed in Chapter 2 the required panel element resolution depends on

- the flexural response of the panels as described in subsections 3.1.1 and 3.1.2 above,
- the radiation properties of the panels, which are given by the radiation matrix as defined in Chapter 2, Equation (2.16) and
- the disturbance characteristics, given in Chapter 2, Sections 2.1.1, 2.1.3 and 2.1.4.

Table 3.2 summarizes the frequency range, element distribution and criteria used to define the element grid density in the prediction models.

Table 3.2: Frequency range and element grid definition.

Excitation	maximum frequency	No. of elements x	No. of elements y	Total No. of elements	Criterion x	Criterion y
APW	20 kHz	57	51	2907	$\Delta_x \leq \lambda_0/3.5$	$\Delta_y \leq \lambda_0/3.5$
ADF	12 kHz	39	35	1365	$\Delta_x \leq \lambda_0/4$	$\Delta_y \leq \lambda_0/4$
TBL	12 kHz	35	77	2695	$\Delta_x \leq \lambda_0/3.5$	$\Delta_y \leq \lambda_{conv}/3.5$

In this study modes with natural frequency up to twice the observed frequency range were considered in the model of the panels, i.e. up to 40 kHz for APW excitation and up to 24 kHz for ADF and TBL excitation. All modes were considered dynamically with stiffness damping and mass parts (see Appendix A). For the APW excitation the total number of modes are 527 for the aluminium panel and 1425 for the sandwich panel. For the ADF and TBL excitation the total number of modes considered are 313 for the aluminium panel and 558 for the sandwich panel.

3.2 Panel characteristics

The most significant difference between the thin homogeneous and sandwich panels is the frequency dependence of the propagating transverse wavenumbers. For thin homogeneous panels the transverse wavenumber increases with $\sqrt{\omega}$ for all frequencies. The transverse wavenumber of a sandwich structure has distinct 'low', 'mid' and 'high' frequency behaviour. At low frequencies the transverse wavenumber is dominated by the cross-section bending and increases with $\sqrt{\omega}$. With increasing frequency the transverse response is increasingly dominated by non-dispersive shear wave distortion due to the sandwich core material. In the shear-controlled region the transverse wavenumber is controlled by the core shear and hence increases in proportion to ω. At high frequencies the rate of increase of the transverse wavenumber is limited by the wavenumber k_{bf} which corresponds to pure faceplate bending so that a $\sqrt{\omega}$ dependence again occurs.

The structural response and sound radiation of panels are strongly affected by the coincidence phenomena [19]. Acoustic coincidence occurs in the frequency range between the acoustic critical frequency where the acoustic wavelength matches the transverse structural wavelength and about twice the acoustic critical frequency where the projected wavelength of a plane acoustic wave incident at an angle of θ=45° matches the structural transverse wavelength.

At acoustic coincidence structural modes are efficiently excited by acoustic fields and also radiate sound very efficiently. The three wavenumber frequency bands described above play an important role for the forced structural response and sound radiation of a sandwich panel. In particular it is the magnitude of the non-dispersive shear wavenumber that determines the bandwidth and extent of the coincidence effect. As shown in Figure 3.2 three cases may be considered [19].

a) If the shear wavenumber $k_s = \omega\sqrt{m''/(Gd)}$ is higher than acoustic wavenumber $k_0 = \omega/c_0$ then acoustic coincidence does not occur until very high frequencies where eventually $k_{bf} = k_0$.

b) If the shear wavenumber k_s is similar or in the extreme case equals the acoustic wavenumber k_0 then acoustic coincidence occurs over a wide frequency band so that, potentially, a large number of modes are efficiently excited at resonance and also efficiently radiate sound.

c) If the shear wavenumber k_s is much lower then the acoustic wavenumber then acoustic coincidence occurs at relatively low frequencies where $k_b = k_0$. In this case too sound radiation from the sandwich panel will be higher than that from a corresponding homogeneous panel since the wavenumber curves intersect at a small angle so that the panel transverse and acoustic wavenumber remain in close proximity over a wider range of frequencies.

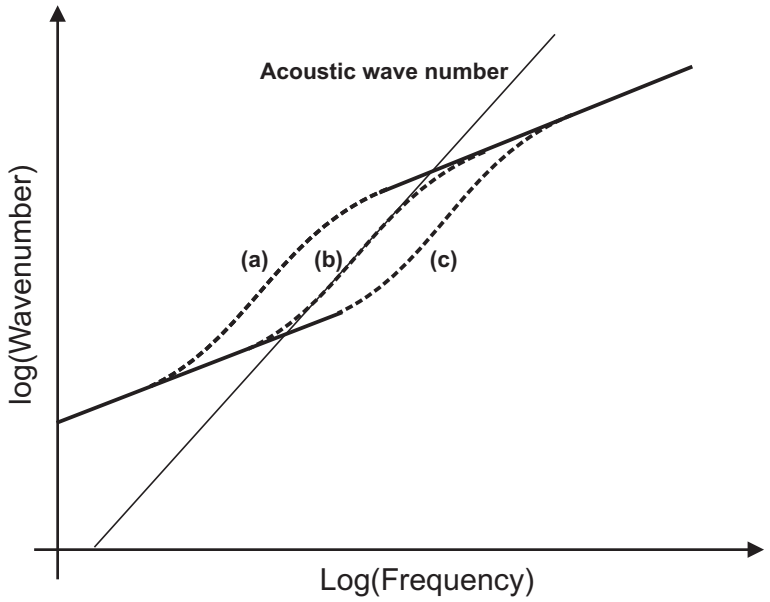

Figure 3.2: Schematic graph of sandwich panel transverse wavenumbers for three different cases of core shear stiffness, (a) $k_s > k_0$, (b) $k_s \approx k_0$ and (c) $k_s < k_0$.

Additionally to acoustic coincidence effects convective coincidence occurs for TBL excitation when the transverse wavenumber in the direction of the air flow on the panel equals the convective wavenumber of the turbulent boundary layer.

3.2.1 Wavenumbers and coincidence frequencies

Figure 3.3 shows the positive propagating bending wavenumber as a function of frequency for (a) the aluminium panel and (b) the composite sandwich panel considered in this simulation study. The circles represent the modal wavenumber components along the x- and y-directions. The wavenumber components satisfy the relationship $k_n = \sqrt{k_{x,n}^2 + k_{y,n}^2}$. The convective and acoustic wavenumber are given by $k_{conv} = \omega / U_{conv}$ and $k_0 = \omega / c_0$ respectively.

At frequencies below 11 kHz the transverse wavenumber of the composite sandwich panel, shown in Figure 3.3(b), is lower than that for the aluminium panel, shown in Figure 3.3(a). As discussed above, the transverse wavenumber of the aluminium panel is increasing proportional to $\sqrt{\omega}$ over the entire frequency range. At low frequencies the transverse wavenumber of the sandwich panel is also increasing proportional to $\sqrt{\omega}$. In this frequency range the transverse wavenumber of both panels at a given frequency is proportional to $\sqrt[4]{m''/D}$. Both panels have equal static stiffness but the aluminium panel has a four times higher mass per unit area. Thus, for low frequencies the bending wavenumbers for the aluminium panel are $\sqrt{2}$ higher than those for the composite sandwich panel. With increasing frequency the non-dispersive transverse shear distortion of the core layer results in a more rapid increase in the transverse wavenumber of the sandwich panel which becomes proportional to ω for high frequencies. The limiting effect due to faceplate bending at high frequencies falls outside the observed frequency range. At about 11 kHz both panel models have similar wavenumbers.

The lower wavenumbers on the composite sandwich panel at low frequencies result in lower coincidence frequencies than for the aluminium panel. For the aluminium panel the acoustic critical frequency occurs at about 7.5 kHz. For the composite sandwich panel the acoustic critical frequency occurs at about 5.5 kHz. Efficient radiation modes that resonate around coincidence produce high structural response and sound radiation effects. Thus, according to the wavenumber plots in Figure 3.3, the composite sandwich panel is likely to radiate sound more efficiently than the aluminium panel for a wider range of audio frequencies.

For thin aluminium panels, the effect of acoustic coincidence often is not a problem for practical engineering applications since it occurs at the upper end of the audio frequency range where the structural response has already rolled off due to the mass effect and due to effective passive treatments. For lightweight sandwich structures the coincidence frequency

potentially occurs in the mid audio frequency range where the response of the panel is still controlled by discrete clusters of modes. This might cause an undesired increase in sound radiation, since at low and mid audio frequencies the response of the panel has not rolled off due to the mass effect and passive control measures may not work so effectively.

Assuming the TBL excitation with the parameters defined in Table 2.3, the convective coincidence frequency for the aluminium and composite sandwich panels occurs at 1169 Hz and 609 Hz respectively. This is representative for a fully developed TBL on the outside of an aircraft fuselage at a cruising speed of about 810 km/h. Due to the low coincidence frequency and the directionality of the disturbance field, only a few structural modes of the composite sandwich panel resonate in the vicinity of the convective coincidence frequency. This indicates a potential for active structural control which tends to be particularly effective at controlling low frequency resonances. The effect of the convective coincidence is discussed in more detail in Section 3.3. The acoustic critical and coincidence frequencies and the convective coincidence frequency for the two panels are summarised in Table 3.3.

It should be noted that the convective coincidence directly depends on the free flow velocity. The convective coincidence therefore shifts towards higher frequencies for increasing flow speeds and towards lower frequencies for decreasing flow speeds. Hence the convective coincidence effects may occur over a relatively wide low to mid audio frequency range during a typical operation cycle of an aircraft.

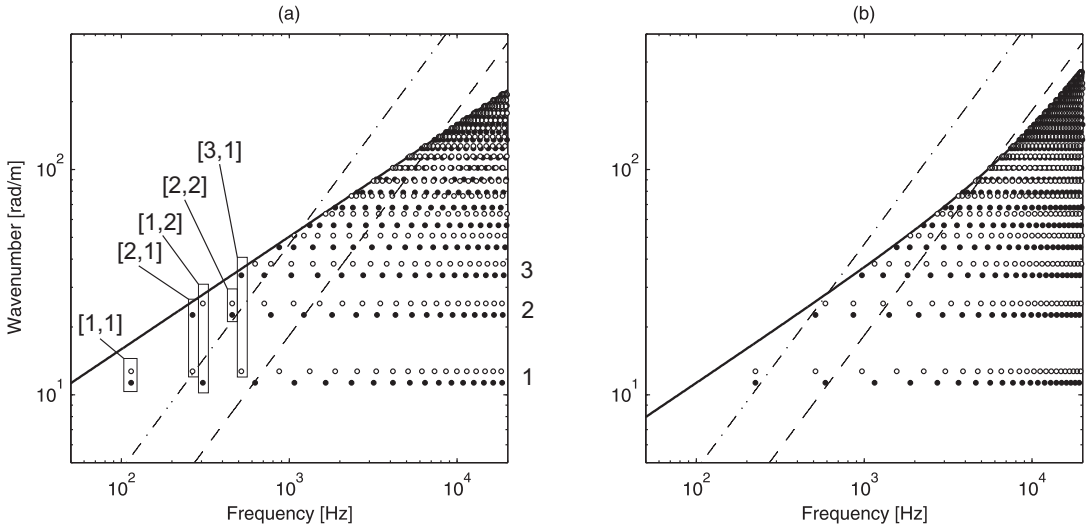

Figure 3.3: Propagating transverse wavenumber ($solid$) of the (a) aluminium and (b) composite sandwich panel; acoustic wavenumber ($dashed$) and convective wavenumber ($dash-dotted$). Wavenumber components of structural modes in span-wise x-direction ($black\,circles$) and in stream-wise y-direction ($white\,circles$).

Table 3.3: Coincidence frequencies.

Panel	Acoustic critical frequency [Hz]	Excitation coincidence frequency [Hz] for APW θ=45°	Convective coincidence frequency [Hz] for TBL disturbance
Aluminium	7,544	15,087	1,169
Sandwich	5,489	190,663	609

3.2.2 Modal density and modal overlap

As shown in Figure 2.6, at low frequencies the response of the aluminium panel and radiated sound power of the aluminium panel is characterised by well-separated resonances which are controlled by low order resonant modes. With increasing frequency, the panel response and radiated sound power are increasingly controlled by overlapping clusters of modes. A statistical measure to describe the distribution of natural frequencies in the frequency domain is the so-called 'modal density'. One definition of this quantity at any frequency is "the inverse of the expected (or averaged) interval between neighbouring natural frequencies $local$ to that frequency" [19]. If the modal density is given as $n(f)$ it is defined as "the number of natural frequencies per Hz". For bending waves on thin homogeneous panels the modal density is constant with frequency and given by Craik [59] as

$$n(f) = \frac{A_p}{2}\sqrt{\frac{m''}{D}} \tag{3.8}$$

where A_p is the panel surface area, m'' is the panel mass per unit area and D is the bending stiffness. For high frequencies this expression represents an expected value of the modal density for a population of grossly similar panels with slight differences in aspect ratios and boundary conditions. For a sandwich panel the modal density is limited by three asymptotes related to cross-section bending, core shear, and face plate bending:

$$\text{(a) } n(f) = \frac{A_p}{2}\sqrt{\frac{m''}{D_1}} \qquad \text{(b) } n(f) = 2\pi f A_p \frac{m''}{G_c d} \qquad \text{(c) } n(f) = \frac{A_p}{2}\sqrt{\frac{m''}{2D_2}} \tag{3.9}$$

Clarkson and Ranky [60] have derived an explicit expression for the modal density of sandwich panels. The notations in the formulations given by Clarkson and Ranky [60] have been adapted to the notations for the sandwich panel parameters defined in Section 3.1 to give

$$n(f) = \frac{\pi m'' A_p f}{gD1} \left(1 + \frac{m''\omega^2 + 2g^2 D_1}{\sqrt{\left(m''\omega^2\right)^2 + 4m'' \left(g\omega\right)^2 D_1}} \right), \tag{3.10}$$

where the parameter g is given as

$$g = \frac{2G_c}{d\, E\, h_f}. \tag{3.11}$$

It should be noted that Equation (3.10) neglects the limiting case of pure faceplate bending which would result in a constant modal density asymptote at high frequencies. As shown in Figure 3.4 this is not an issue for the sandwich panel considered in this simulation study since even at the upper end of the observed frequency range the structural response and hence the modal density is clearly shear-controlled. The modal density curves shown in Figure 3.4 are derived from Equations (3.8) to (3.11) while the and lines and circles represents the specific density of the natural modes of the panels considered in this simulation study, which for each natural frequency have been calculated from

$$n(f_1) = \left(f_1 + \frac{f_2 - f_1}{2} \right)^{-1} \text{ and } n(f_r) = \left(\frac{f_{r+1} - f_{r-1}}{2} \right)^{-1} \tag{3.12}$$

where f_r is the r-th natural frequency of the panels. The modal density of the aluminium panel, shown in Figure 3.4(a), is constant with frequency and has a value of 0.0137 [per Hz]. For low frequencies the modal density of the composite sandwich panel shown in Figure 3.4(b) has a lower modal density than the aluminium panel. With increasing frequency the modal density rises and reaches the same value as for the aluminium panel at about 6150 Hz. In this frequency range the structural response of the sandwich panel is shear controlled and the modal density increases linearly with frequency. Both the asymptotic limit in Equation (3.9) and the results from Equation (3.10) are in generally good agreement with the specific density of modes for the panels estimated from Equation (3.12). The high variation between the modal density and the specific frequency spacing between natural modes of the panels illustrates that the modal density is a statistical parameter which is only valid for the average over either an assemble of similar panels or the average over an assemble of neighbouring modes in a wider frequency band.

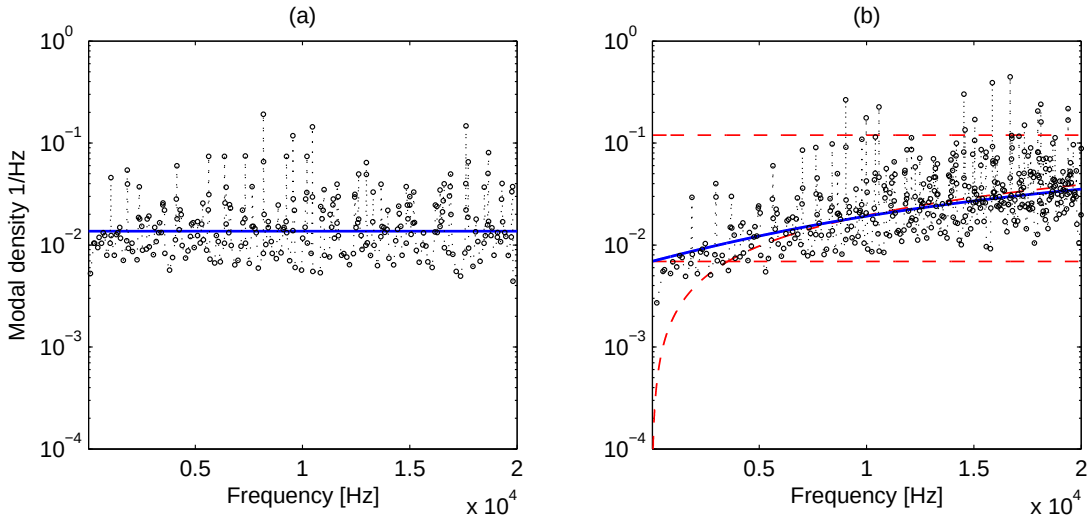

Figure 3.4: Statistical and numerical modal density for (a) the homogeneous aluminium panel and (b) the composite sandwich panel. Numerical results ($circles - dotted$), statistical results ($solid$) and asymptotic limits for the sandwich panel ($faint - dashed$).

The modal overlap factor gives the ratio of the half-power bandwidth to the local average interval between natural frequencies [19] and is given by

$$M(f) = f\eta n(f) \tag{3.13}$$

where f is the frequency in Hz, η is the material loss factor and $n(f)$ is the modal density. For modal overlap factors below unity the response of a structure is characterised by well-separated resonant modes with narrow peaks at their natural frequencies which are separated by broad troughs. As M approaches unity, the individual modal responses begin to overlap and, as it increases beyond unity, neighbouring modes combine to form broad overlapping clusters of modes separated by narrow dips. The modal overlap factor therefore plays a major role in the analysis of high frequency response based on probabilistic models such as Statistical Energy Analysis (SEA) [19, 59].

Velocity feedback control systems introduce active damping effects on a panel, which are particularly effective at resonance frequencies. Thus the modal overlap factor is of great importance in this study since it provides an indication of the frequency band where the response of a structure is controlled by individual resonant modes and thus active damping could be efficiently employed to reduce the response and sound radiation of the structure.

The modal overlap factor for the aluminium panel in Figure 3.5 is increasing linearly with frequency and exceeds unity for frequencies above 3623 Hz. At low frequencies the modal overlap factor for the composite sandwich panel in Figure 3.5 is lower than that of the

aluminium panel and exceeds unity at a higher frequency of about 4500 Hz. For frequencies above 1000 Hz the response of the sandwich panel is increasingly influenced by shear effects which results in a more rapidly rising modal overlap. In the shear controlled frequency region the modal overlap increases proportional to ω^2.

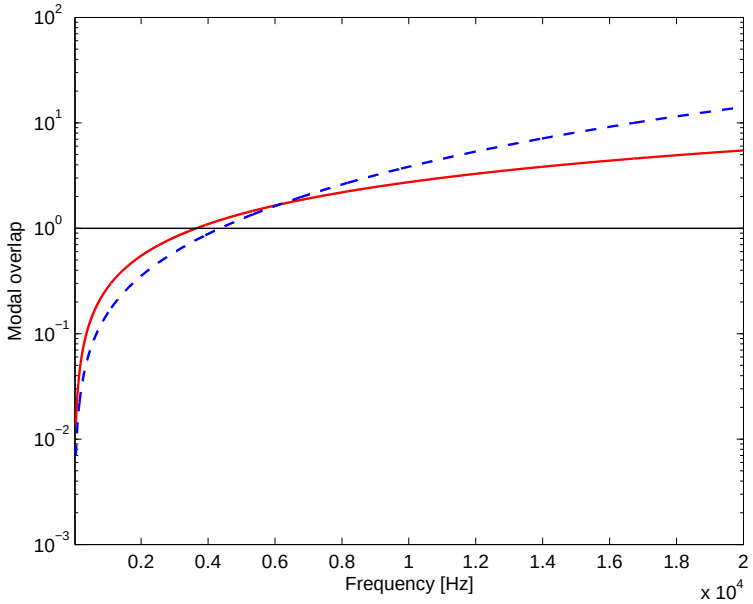

Figure 3.5: Modal overlap factor for the homogeneous aluminium panel ($solid$) and the composite sandwich panel ($dashed$).

The results for the modal density and modal overlap indicate that the response of the sandwich panel is controlled by individual resonant modes over a wider range of low and mid audio frequencies than the aluminium panel. This implies that the response of the composite sandwich panel can be efficiently controlled by means of active velocity feedback control over a wider range of audio frequencies.

With control systems comprising evenly spaced discrete velocity feedback loops not all modes can be efficiently controlled and the frequency range over which control effects are guaranteed is a function of the total number of discrete feedback loops and the frequency dependent total mode count. The statistical mode count is given by integral of the modal density in the interval between 0 Hz and the observation frequency, while for specific systems the mode count is simply given by the number of natural modes with resonance frequencies below the observation frequency. Due to the lower modal density and hence lower mode count of the sandwich panel, control effects due to a finite number of velocity feedback loops are expected to extend to higher frequencies than for the aluminium panel.

3.3 Structural response and sound radiation

At first the structural response and sound radiation of the aluminium panel and the composite sandwich panel due to deterministic and stochastic disturbances are investigated without active control. Significant differences in the panel response and sound radiation are observed for different types of disturbances. The structural response of the panels is assessed in terms of the panel kinetic energy which also gives an indication of the acoustic field in the close proximity of the panel. The sound transmission through the panels is assessed in terms of the far field radiated sound power for a unit pressure amplitude of the pressure fluctuation on the source side of the panel. Since radiation losses and fluid loading effects have been neglected, the spectrum of panel kinetic energy only depends on the characteristics of the disturbance and the panel structural response. The spectra of the radiated sound power also include the radiation characteristics of the panels.

3.3.1 Acoustic plane wave

Figure 3.6 shows the frequency spectrum of panel kinetic energy (left hand side) and radiated sound power (right hand side) of the aluminium panel ($solid$) line and composite sandwich panel ($faint$) line for a plane wave excitation. Three different angles of incidence are considered: θ=0° (normal incidence), θ=45° and θ=90° (grazing incidence). The in-plane excitation angle is $\varphi = 45°$ for all cases, where relevant.

APW with θ = 0° (normal incidence):

Figure 3.6(a) and (b) show the structural response and radiated sound power for both panels due to a plane wave excitation at normal incidence. Even structural modes are not excited. This is because the excitation field is uniform over the surface of the panel. Odd modes however are efficiently excited. Since the plane wave is incident normal to the panel surface no excitation coincidence effects are present in the kinetic energy and radiated sound power spectra. Above the first few resonances of the panel, the kinetic energy follows the mass law [19] and rolls off at a rate of 6 dB per octave, i.e. 20 dB per decade. In this mass-controlled frequency band the panel kinetic energy of the composite sandwich panel is about 6 dB higher than that of the aluminium panel. This is because the aluminium panel has a four times higher mass per unit area. Corresponding low order resonant modes for the two panels have a similar response magnitude but are shifted in frequency by a factor of 2.

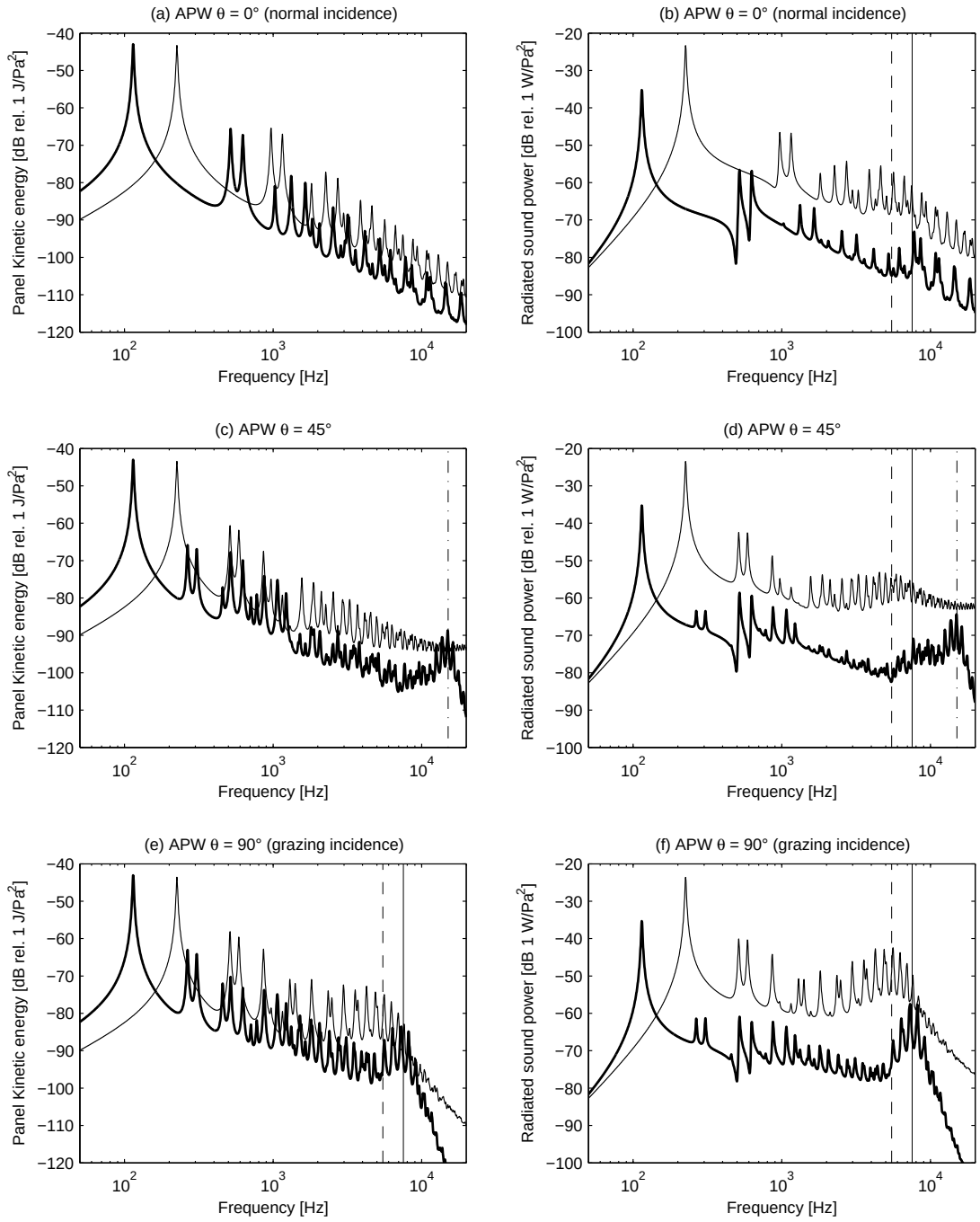

Figure 3.6: Panel kinetic energy and radiated sound power of the 1.6 mm aluminium panel ($solid$) and the composite sandwich panel with equivalent static bending stiffness ($faint$) for a acoustic plane wave incident at θ = 0°, 45° and 90°. Vertical lines mark the acoustical critical frequency of the aluminium panel ($solid$), composite sandwich panel ($dashed$) and the θ = 45° excitation coincidence frequency for the aluminium panel ($dash - dotted$).

The radiated sound power for the two panels is the same at frequencies well below the first panel resonance. This is because the radiated sound power in this frequency band is determined by the static bending stiffness which is equal for both panels. Above the first panel resonance, the radiated sound powers are mass-controlled up to frequencies close to the acoustic critical frequencies [19] of the two panels. In the mass-controlled region, the radiated sound power of the composite sandwich panel is 12 dB higher than that of the

aluminium panel. The radiated sound power of the aluminium panel follows the mass law up to 5 kHz. Around the acoustic critical frequency at about 7.5 kHz, the radiated sound power increases because of the acoustic coincidence effect in the radiation properties of the panel [19]. The radiated sound power of the composite sandwich panel follows the mass law only up to 2 kHz. Around the critical frequency at bout 5.5 kHz the radiated sound power increases because of the radiation acoustic coincidence effect. Around 5.5 kHz, the radiated sound power spectra of the composite sandwich panel is more than 20 dB higher than that of the aluminium panel.

The radiation acoustic coincidence frequency range for the composite sandwich panel is wider than that for the aluminium panel. This is due to the transition from bending to shear response which produces acoustic coincidence conditions over an extended frequency band. This effect can be visualised in the wavenumber plots of Figure 3.3. The lines for the acoustic wavenumber and the flexural wavenumber for the aluminium panel intersect at a rather wide angle at the critical frequency. In contrast the acoustic wavenumber and the transverse wavenumber lines for the composite sandwich panel intersect at a more shallow angle and remain in close proximity to each other above the critical frequency so that the radiation acoustic coincidence effect extends over a wider frequency band. It is also interesting to note that, at low frequencies, the spectra of the radiated sound power of the aluminium panel are characterised by resonance and anti-resonance effects. This occurs between two structural resonances that interfere destructively, causing a cancellation of the modal contributions to the radiated sound power.

APW with θ = 45°

Figure 3.6(c) and (d) show the panel response and radiated sound power for a plane wave incident at an angle θ=45°. In this case all structural modes are efficiently excited. Above the first resonance frequency, the structural response of the aluminium panel follows the mass law up to about 10 kHz. Around this frequency the spectrum of the panel kinetic energy shows a wide frequency band crest composed of a series of resonance peaks. This is because the projection of the acoustic excitation wave onto the panel surface for an angle θ=45° is $\sqrt{2}$ longer than the acoustic wavelength. Thus, since the bending wavenumber is proportional to $\sqrt{\omega}$ an excitation coincidence effect occurs at twice the critical frequency, that is about 15 kHz. Around this coincidence frequency the response of the panel is dominated by resonances of efficiently excited modes whose responses are controlled by structural damp-

ing. Above this coincidence frequency the panel response is stiffness and mass controlled and rolls off rapidly at a rate of 36 dB per octave.

The structural response of the composite sandwich panel does not exhibit this excitation coincidence effect, which occurs at 190 kHz and is therefore outside the observed frequency range. This is because the structural wavenumber of the sandwich panel in the shear transition region is higher than the projected wavenumber of the acoustic excitation $\omega/(\sqrt{2}c_0)$. The response of the composite sandwich panel at high frequencies exhibits mass-controlled behaviour. However the roll off rate is lower than 6 dB per octave.

The radiated sound power of the aluminium panel is mass-controlled up to 5 kHz. Above 5 kHz the radiated sound power spectra of the aluminium panel shows the combined effect of the radiation acoustic coincidence around the acoustic critical frequency at 7.5 kHz, and the excitation coincidence at 15 kHz. The radiated sound power spectra of the composite sandwich panel exhibits these radiation and excitation acoustic coincidence effects in the frequency range between 2 and 10 kHz. At 5.5 kHz the radiated sound power of the composite sandwich panel is about 25 dB higher than that of the aluminium panel.

In comparison to the kinetic energy spectra, below the critical frequency, some resonant peaks are significantly reduced in the spectrum of the radiated sound power. This is because the surface pressure fluctuations caused by even modes counteract each other and are not efficiently radiated into the far field [19].

APW with θ = 90°

Figure 3.6(e) and (f) show the panel response and radiated sound power for a plane wave incident at an angle θ=90° (grazing incidence). At this angle the plane wave excites all structural modes. For grazing incidence both the excitation acoustic coincidence and the radiation acoustic coincidence occur at the critical frequency. This is because the wavelength of the acoustic excitation projects directly onto the panel surface. The response of the panels around the critical frequency is dominated by discrete efficiently excited modes whose responses are controlled by structural damping. Above the critical frequency the panel response is stiffness and mass controlled and rolls off rapidly. The response of the aluminium panel rolls off at a rate of 36 dB per octave. The response of the composite sandwich panel rolls off at a lower rate of about 16 dB per octave. This difference is caused by the shear distortion in the transverse wavenumber of the sandwich panel which results in a decrease

of the transverse stiffness and thus results in an increase of the modal density.

The spectra of the radiated sound power for frequencies up to 1 kHz are very similar to those for the plane wave incident at θ=45°. For higher frequencies, both panels show the overlaying acoustic coincidence effect in the excitation and the radiation characteristics. Around critical frequency, the sound power spectra is dominated by individual efficiently radiating resonant modes. Above coincidence the radiated sound power of both panels rolls off rapidly with frequency. Around the acoustic critical frequency of the composite sandwich panel at 5.5 kHz the radiated sound power of the sandwich panel exceeds that of the aluminium panel by about 30 dB. Also in this case, below the critical frequencies the amplitudes of the resonance peak of even modes are rather small because of their low radiation efficiency.

3.3.2 Stochastic disturbances

Figure 3.7 shows the predicted panel kinetic energy (left hand side) and radiated sound power (right hand side) of the aluminium panel ($solid$) line and composite sandwich panel ($faint$) line for acoustic diffuse field (top row) and turbulent boundary layer (bottom row) disturbances. The spectra are normalised to the power spectral densities of equivalent acoustic plane wave with a pressure amplitude of 1 Pa at all frequencies.

For very low frequency the correlation function for ADF and TBL excitations tend to unity and the wavelength of an acoustic plane wave becomes large compared to the panel dimensions. Therefore all disturbance types show very similar normalised response levels at low frequencies. Differences in the response spectra at higher frequencies are due to the spatial excitation characteristics with respect to structural response of the panels.

Acoustic diffuse field

Figures 3.7(a) and (b) show the structural response and radiated sound power of the aluminium panel and the composite sandwich panel for an acoustic diffuse field disturbance. Compared with Figure 3.6(c) and (d) it can be seen that the low frequency structural response and radiated sound power of both panels up to 1 kHz is very similar to the response to an acoustic plane wave with incidence angles θ = 45° and φ = 45°.

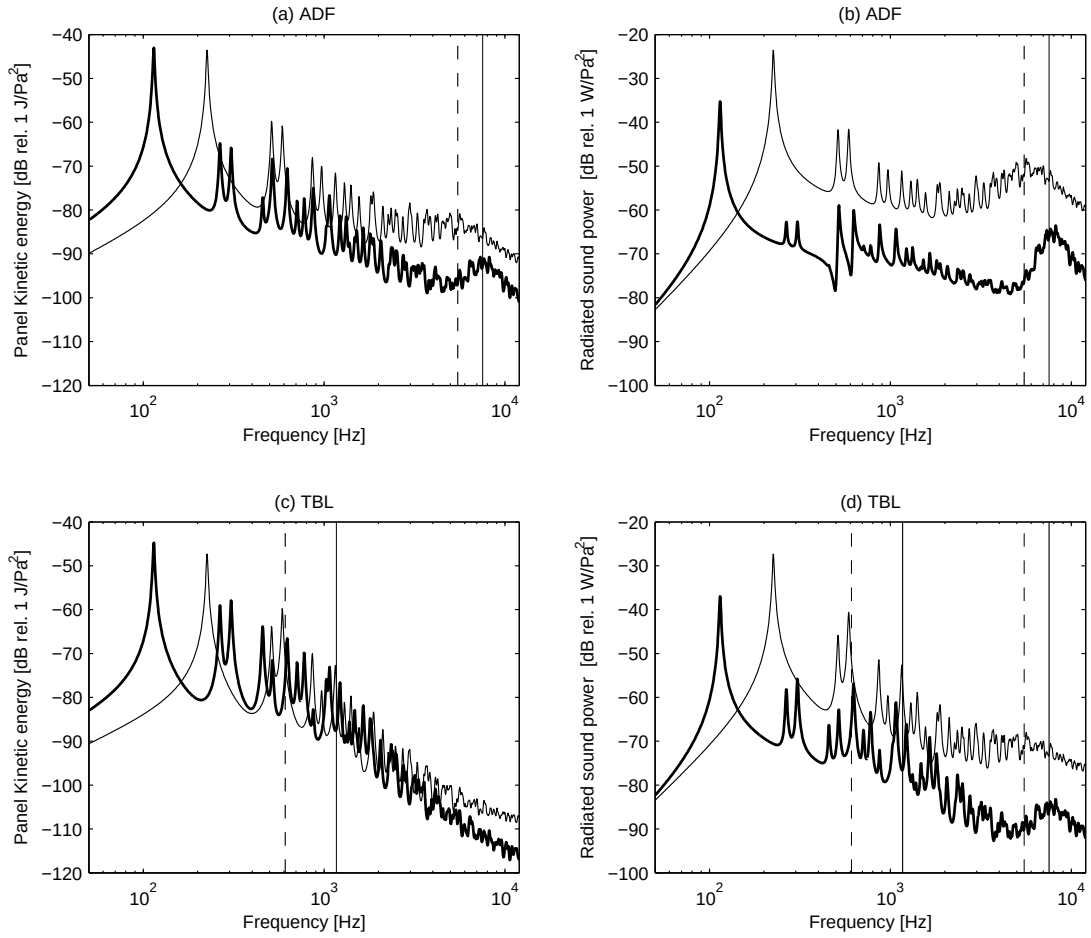

Figure 3.7: Panel kinetic energy and radiated sound power for the 1.6 mm aluminium panel ($solid$) and the composite sandwich panel with equivalent static bending stiffness ($faint$) for ADF and TBL stochastic disturbances. Vertical lines mark the acoustical critical frequencies and aerodynamic coincidence frequencies of the aluminium panel ($solid$) and the composite sandwich panel ($dashed$).

Figure 3.7(a) shows that, at higher frequencies the structural response of the aluminium and composite sandwich panel are characterised by the excitation acoustic coincidence effect, which, for diffuse acoustic excitation, occurs around the acoustic critical frequencies at 7.5 kHz for the aluminium panel and 5.5 kHz for the composite sandwich panel. The panel response in the coincidence region is characterised by resonating modes, but the response of individual modes is less pronounced than for the cases of APW excitation shown in Figure 3.6. Above the coincidence region the kinetic energy spectrum of both panels rolls off at a lower rate than for the cases of APW excitation. These differences in the response spectra can also be explained by the fact that the ADF excitation is formed by acoustic waves at arbitrary random angles of incidence. Figure 3.7(b) shows the spectrum of the radiated sound power of the panels for an acoustic diffuse field disturbance. As for the acoustic plane wave excitation at grazing angle in Figure 3.6(e), the spectrum of radiated sound power in Figure 3.7(b) shows the combined effect of acoustic excitation coincidence and radiation coincidence, which cause a considerable increase of radiated sound power around the acoustic critical frequency.

Turbulent boundary layer

Figures 3.7(c) and (d) show the structural response and radiated sound power of both panels for the TBL disturbance. In the frequency range below 2 kHz the response of both panels is dominated by resonances of low order modes. For the aluminium panel the convective coincidence occurs at 1169 Hz, while for the composite sandwich panel it occurs at 609 Hz. The panel response therefore depends on how efficiently specific modes are excited by the TBL disturbance. Above the convective coincidence region, the response of the aluminium panel drops off at a rate of 9 dB per octave. The roll off rate for the composite sandwich panel is slightly lower. This is due to the increasing modal density.

In order to discuss the response of low order structural modes to TBL disturbance it is necessary to recall the properties of the correlation function for the TBL disturbance in Equation (2.32). Since the correlation function for the TBL in the x-direction (span-wise) is characterised by a monotonically decaying exponential function, there are no coincidence effects along the x-direction of the panels. Therefore only structural modes with a modal wavenumber component in the y-direction which is close to the convective wavenumber are characterised by a coincidence effect.

Table 3.4 gives the panel modes that are efficiently excited by coincidence with the TBL downstream convective field. Bold mode orders indicate efficiently radiating modes, modes in brackets indicate a group of modes that cannot be distinguished as individual resonance peaks in Figure 3.7(c) and (d) and the dashed horizontal lines mark the convective coincidence frequency. The comparison between the two panels shows that for the aluminium panel more modes are efficiently excited by the TBL disturbance than for the composite sandwich panel. A comparison of the results in Table 3.4 with Figure 3.3 shows that efficiently excited modes indeed have a wavenumber component in the y-direction (stream-wise) that is close to the convective wavenumber.

The radiated sound power spectrum in Figure 3.7(d) shows that odd order modes radiate sound efficiently. Although even modes generally have a low radiation efficiently, the even (2,4) mode of the aluminium panel and the (1,2) mode of the composite sandwich panel also show high resonant peaks in the radiated sound power spectra in Figure 3.7(d). Comparison with Figure 3.3 shows that both modes have a wavenumber component in the x-direction which is close to the acoustic wavenumber, which results in a high radiation efficiency.

Table 3.4: Modes efficiently excited by TBL.

Aluminium panel			Composite sandwich panel		
Mode number	Frequency [Hz]	mode order (n_x, n_y)	Mode number	frequency [Hz]	mode order (n_x, n_y)
1	114	**(1,1)**	1	225	**(1,1)**
2	266	(2,1)	3	588	**(1,2)**
3	306	(1,2)	- - - - - - -	609	- - - - - - -
4	457	(2,2)	4	862	(2,2)
6	626	**(1,3)**	6	1155	**(1,3)**
7	710	(3,2)			
8	777	(2,3)			
10	1029	**(3,3)**			
11	1063	(4,2)			
12	1073	(1,4)			
- - - - - - -	1169	- - - - - - -			
13	1224	**(2,4)**			
16	1477	(3,4)			
18	1648	**(1,5)**			
19	1800	(2,5)			
26	2351	(1,6)			

3.4 Decentralised velocity feedback control

In this section the structural response and sound radiation of the aluminium panel and the composite sandwich panel with active structural control for deterministic and stochastic distributed disturbances are considered. As shown in Figure 2.9(b) and Figure 3.8, the panels are fitted with 16 decentralised ideal velocity feedback control loops.

Figures 3.9 and 3.10 show the structural response and total radiated sound power for the aluminium panel (left hand side) and the composite panel (right hand side) with feedback gains in the range from 5 to 80. As discussed by Gardonio and Elliott [23], velocity feedback control introduces active damping. This allows the response of modes at resonance to be controlled. Away from resonance frequencies, active damping is not effective. For low feedback gains, the resonant peaks are initially rounded and anti-resonances in the radiated sound power spectra disappear. For increasing feedback gains, new resonance peaks start to develop. For the composite sandwich panel this occurs for control gains above 20 and for the aluminium panel for gains above 40. This difference relates to the structural impedances of the panels. Only with high feedback control gains are the resonances of low order modes completely cancelled by the sixteen feedback loops. In the high frequency region, the control is limited by the large number of modes that contribute to the response at each frequency.

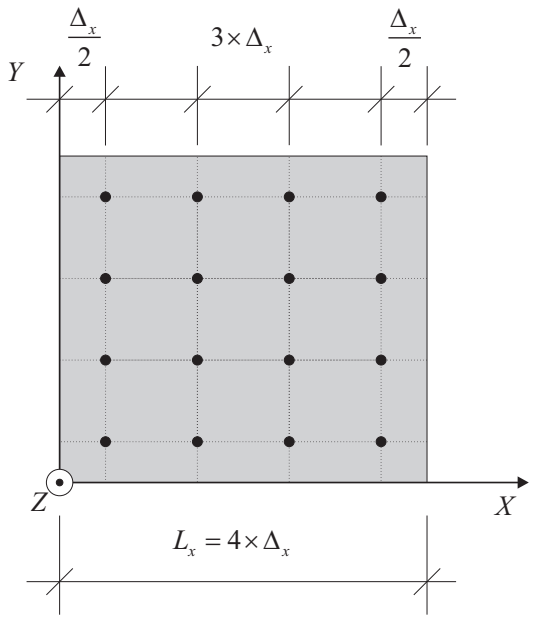

Figure 3.8: Spatial distribution of control loops across the panel.

For all disturbances, the controllable frequency range for the composite sandwich panel extends to higher frequencies than for the aluminium panel. This is predominantly due to the lower modal density [19] on the composite sandwich panel but also due to the lower convective and acoustic coincidence frequencies. At coincidence, the response of the panels is dominated by the response of discrete resonant modes. These resonances can be effectively reduced by means of active velocity feedback. As shown in Figure 3.9 considerable reductions in the structural response of the aluminium panel can be achieved up to about 1.5 kHz for the APW (θ=45°), up to 2 kHz for the ADF and up to 3 kHz for TBL disturbance. For the composite sandwich panel, considerable reductions of the response can be achieved for frequencies up to twice as high. As shown in Figure 3.10 considerable reductions in radiated sound power of the aluminium panel can be achieved up to 1 kHz for the APW (θ=45°) and ADF disturbances, while for the TBL disturbance considerable reductions are achieved up to 3 kHz. As found for the kinetic energy, for the composite sandwich panel considerable reductions of the radiated sound power can be obtained for frequencies up to twice as high as for the aluminium panel.

The predicted control performance for the structural response and radiated sound power for the TBL disturbance is much higher than those for acoustic excitations. This is because the kinetic energy and radiated sound power spectra are dominated by a smaller number of resonant modes for which the k_y structural wavenumber coincides with the convective wavenumber of the TBL disturbance. The response and sound power radiation for APW and ADF disturbances are instead characterized by a large number of resonant modes, for

which either the k_x or k_y structural wavenumbers components coincide with the acoustic wavenumber. Thus a large number of feedback control units would be required to obtain the same bandwidth as for the TBL excitation.

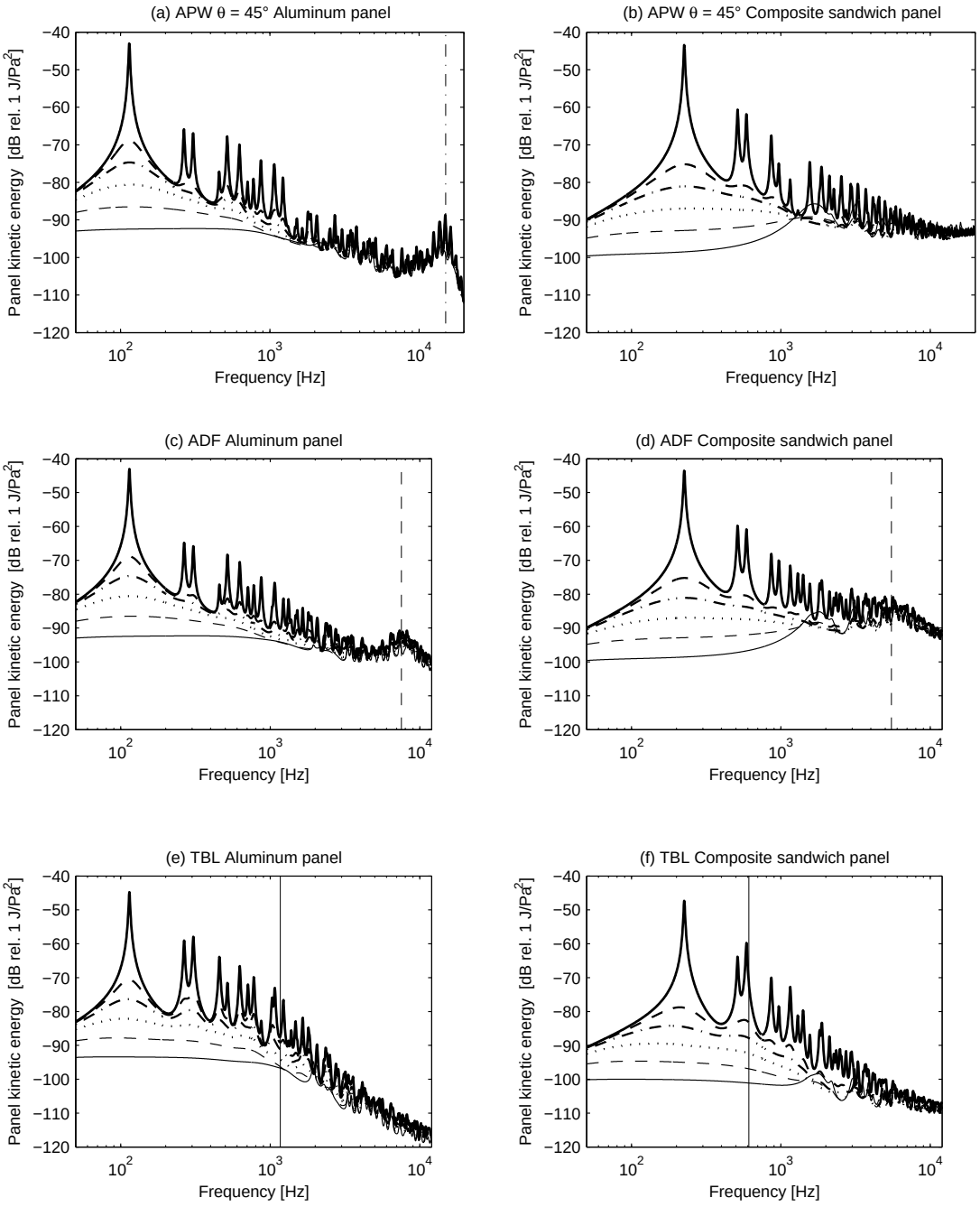

Figure 3.9: Kinetic energy of a 1.6 mm aluminium panel (left column) and a composite sandwich panel with equivalent static bending stiffness (right column) with 16 discrete idealized velocity feedback loops for APW (θ=45°) excitation and ADF and TBL stochastic disturbances. Passive panel ($solid$), feedback gain of 5 ($dashed$), 10 ($dash-dotted$), 20 ($dotted$), 40 ($faint$) and 80 ($faint-dashed$). Vertical lines mark the acoustical critical frequency ($dashed$) and convective coincidence frequency ($solid$).

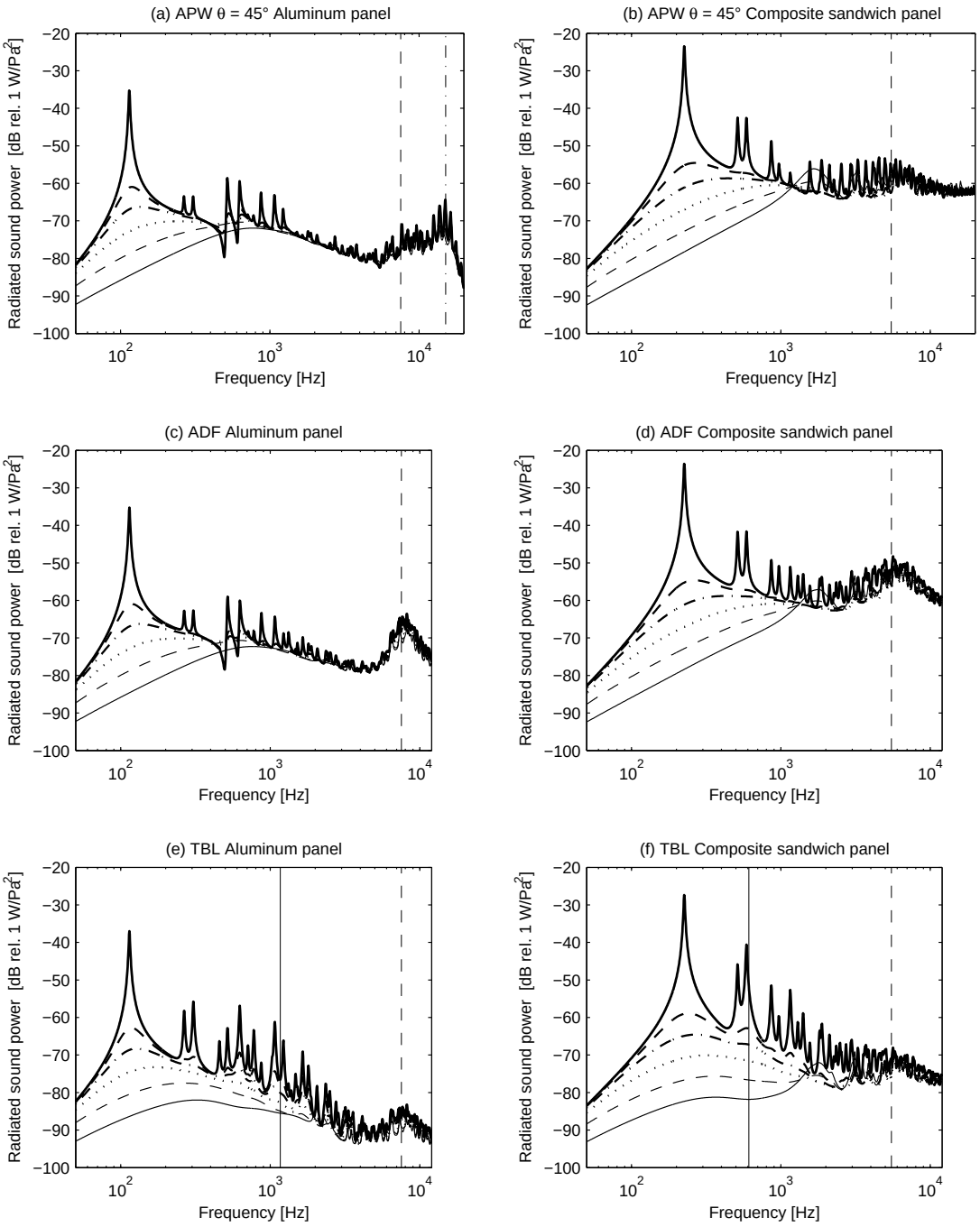

Figure 3.10: Radiated sound power from a 1.6 mm Aluminium panel (left column) and the composite sandwich panel with equivalent static bending stiffness (right column) with 16 discrete idealized velocity feedback loops for APW (θ=45°) excitation and ADF and TBL stochastic disturbances. Passive panel ($solid$), feedback gain of 5 ($dashed$), 10 ($dash-dotted$), 20 (dotted), 40 ($faint$) and 80 ($faint-dashed$). Vertical lines mark the acoustical critical frequency ($dashed$) and convective coincidence frequency ($solid$).

Figure 3.11 shows the spectrum of the radiated sound power of the aluminium panel excited by an ADF disturbance from Figure 3.10(c) on a linear frequency scale. The vertical line marks the acoustical critical frequency at 7.5 kHz. It is shown that, in the coincidence region around 7.5 kHz, with a feedback gain of 80 significant reductions of up to 7 dB can be achieved. This is because the panel response and radiated sound power around acoustic coincidence is dominated by the damping-controlled response of those resonant modes that

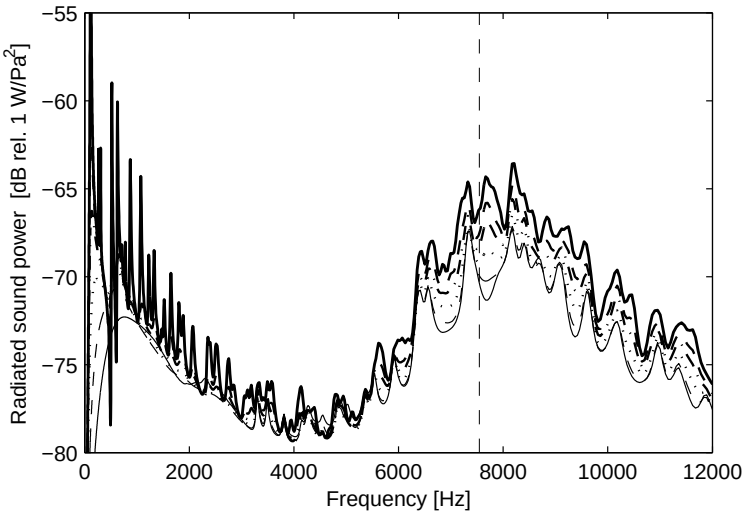

Figure 3.11: Radiated sound power from the 1.6 mm aluminium panel with 16 discrete idealized velocity feedback loops for a ADF disturbance and with a feedback gain of 5 ($dashed$), 10 ($dash - dotted$), 20 ($dotted$), 40 ($faint$) and 80 ($faint - dashed$). The vertical line marks the acoustical critical frequency ($dashed$).

are efficiently excited by the coincident acoustic field.

At these high frequencies, the bending wavelength on the panel is shorter than the distances between the control loops. One may therefore expect that the control performance for single modes will depend on the spatial distribution of the control units with respect to the shape of the modes. However, for stochastic disturbances a wide range of structural modes is excited at coincidence so that some reductions may still be expected for even distributions of the control loops. Reductions of the response and radiated sound power in the coincidence region of thin aluminium panels may not be of practical interest because this effect occurs at the upper end of the audio frequency range and can be efficiently controlled by means of passive damping treatments. For composite sandwich panels the coincidence occurs at much lower frequencies and affects low order modes. In this case decentralised velocity feedback control is thought to be a promising control approach.

Figure 3.12 shows the reductions of both panels kinetic energy (left hand side) and radiated sound power (right hand side) for a feedback gain of 20. The graphs are plotted against wavenumber. Setting the spectra scale to the wavenumber corresponds to a normalisation of the stiffness to mass ratio of the two panels. The difference in the response is then given by the square root of the mass ratio. Since the aluminium panel is four times heavier than the composite panel, the control effort for similar reductions of the response of equal order modes is twice as high. For all disturbance cases the control reductions obtained for low order modes of the composite sandwich panel are significantly higher than those for corresponding modes of the aluminium panel. As shown in Figures 3.12(b) and (d), for the

acoustic disturbances, considerably higher reductions in the radiated sound power of the composite sandwich panel are achieved for modes resonating around the acoustic critical wavenumber of the composite sandwich panel at 100 rad/m.

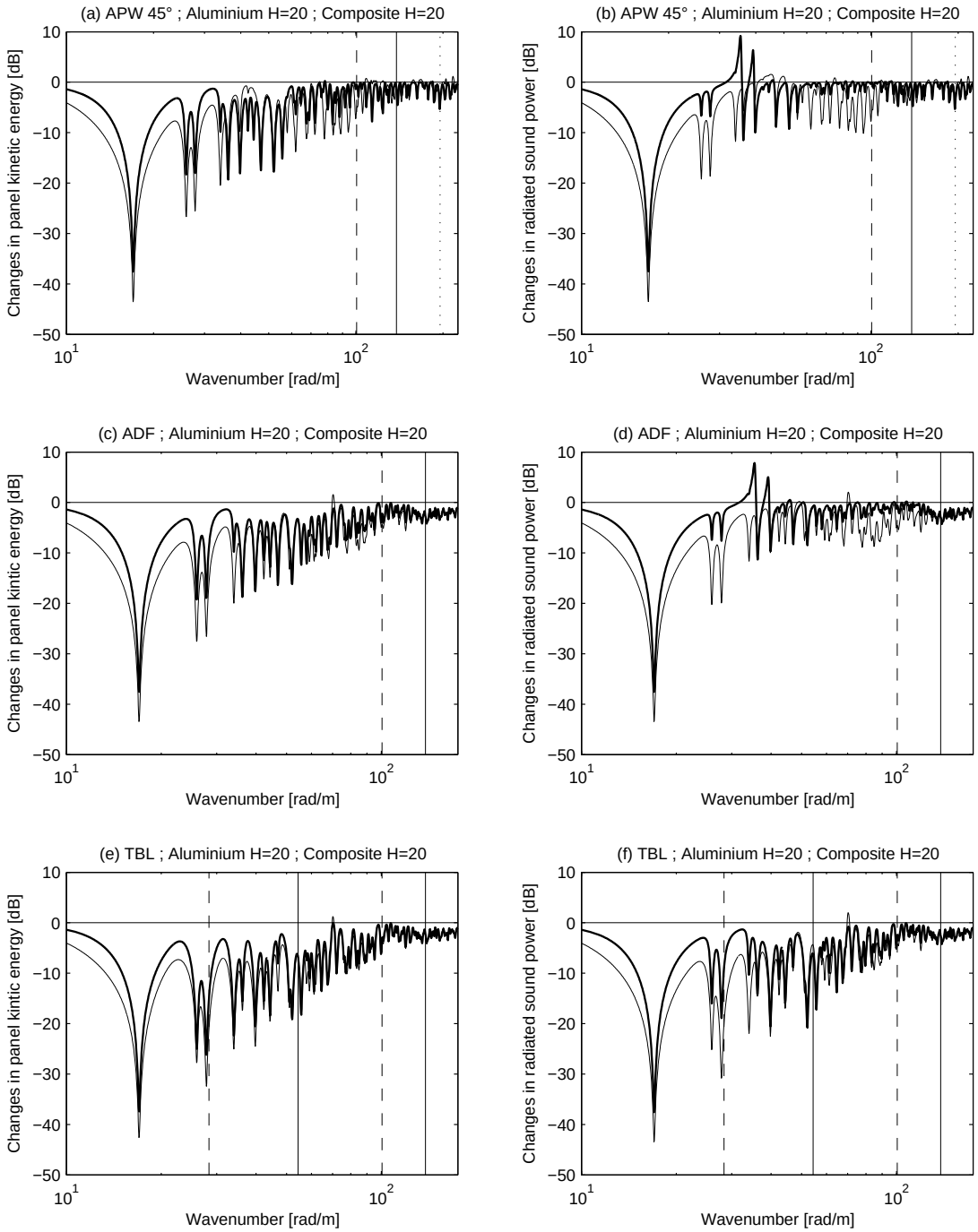

Figure 3.12: Changes in panel kinetic energy and radiated sound power plotted over the structural wavenumber, for a 1.6 mm aluminium panel with feedback gain of 20 ($solid$) and the composite sandwich panel with feedback gain of 20 ($faint$) with 16 discrete idealized velocity feedback loops for APW (θ = 45°) ADF and TBL disturbance. Vertical lines mark the acoustical critical ($dashed$) and convective coincidence frequency ($solid$).

Figure 3.13 shows the reduction of the the A-weighted panel kinetic energy (left hand side) and total sound power radiated (right hand side) averaged in the frequency band between 20 Hz and 12 kHz. This is thought to be a fair approach to assess the overall control performance of the two panels over this wide range of audio frequencies, although the considered forcing spectra are flat. The achieved reductions in the panel kinetic energy are generally higher than those for the radiated sound power. This is because the reductions in all resonant structural modes are reflected in the overall reductions in panel kinetic energy but only reductions in efficiently radiating modes affect the overall reduction in radiated sound power.

Considering the acoustic (APW and ADF) disturbance cases, for low feedback gains higher reductions are achieved for the smart composite sandwich panel than for the smart homogeneous aluminium panel. Optimal control performance for the composite sandwich panel is achieved for a feedback gain of 20. As shown in Figures 3.9 and 3.10, for higher feedback gains new resonance behaviour starts to develop which diminishes the overall control performance. For higher feedback gains the predicted reductions for the aluminium panel are higher than those for the composite sandwich panel; for the kinetic energy this is for gains above 40 and for the radiated sound power this is for gains above 80. The greatest reductions for the aluminium panel are achieved for a feedback gain of 80. The better control performance for the composite sandwich panel is due to the control of the efficiently radiating modes in the mid audio frequency range.

In the case of the TBL excitation significant reductions in the structural response and radiated sound power are predicted for both panels. This is because the TBL excitation excites predominantly low order structural modes whose wavenumber in the y-direction coincides with that of the stream-wise convective field. These modes can be efficiently controlled with decentralised velocity feedback loops. The high response of low order modes shifts the optimal control gain for both panels towards higher values.

The predicted reductions for the composite sandwich panel are up to 10 dB higher than those of the aluminium panel. This is partly because only a small number of low order structural modes of the composite sandwich panel are efficiently excited by the TBL (see Table 3.4), and because for equal feedback gains the response of low order structural modes of the composite sandwich panel are controlled more effectively than those of the aluminium panel (see Figure 3.12).

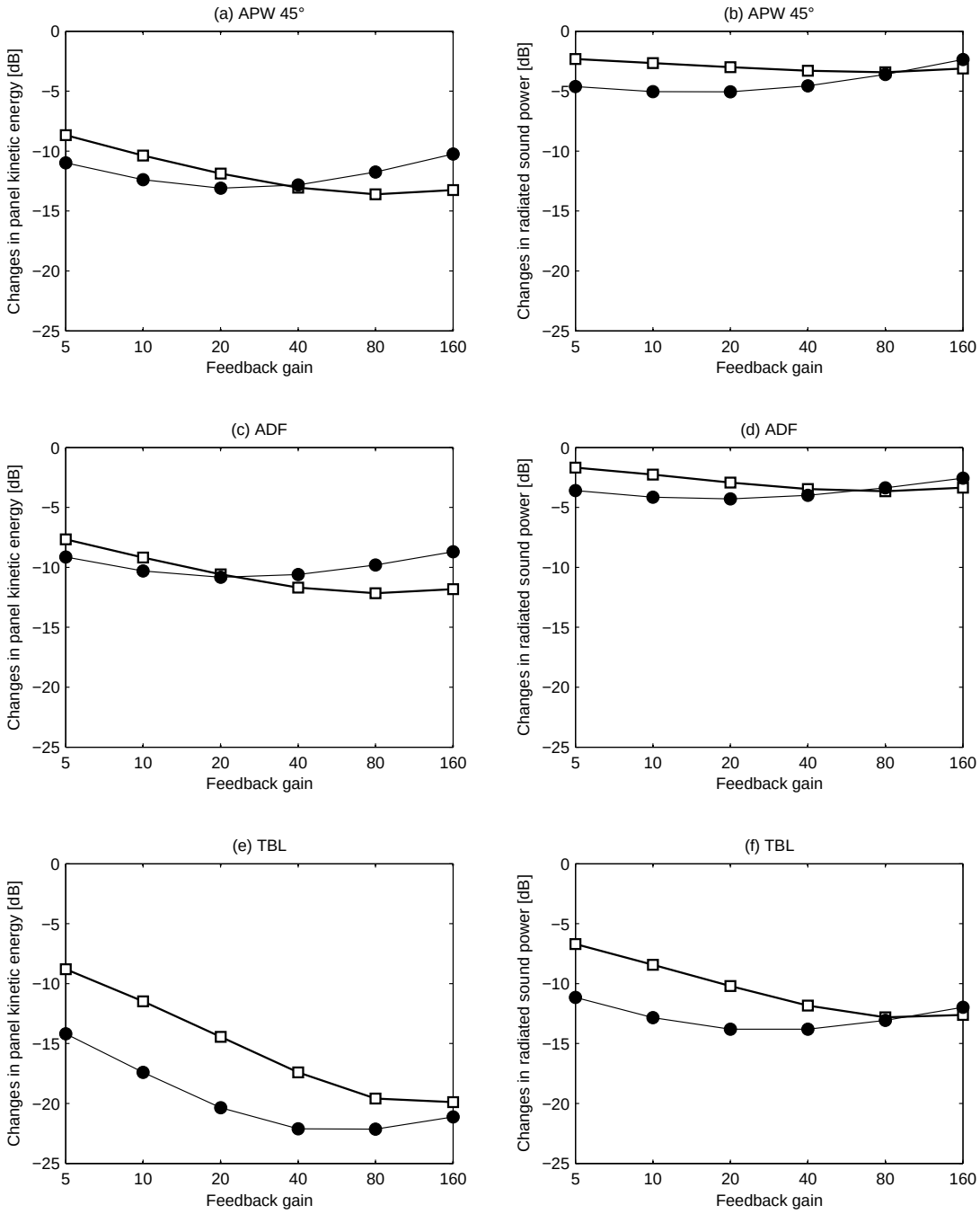

Figure 3.13: Overall reductions in A-weighted panel kinetic energy and radiated sound power for the panels with 16 discrete idealized velocity feedback loops. Aluminium panel ($solid\,line$ / $blanc\,sqares$), composite sandwich panel ($faint\,line$ / $black\,circles$) for a APW (θ = 45°), ADF and TBL disturbance.

In practice it is difficult realise high feedback gains because control systems are often only conditionally stable and can also cause control spill-over effects at low or high frequencies, depending on the type of actuator. The lower optimal feedback gain for the composite sandwich panel may therefore be beneficial for practical applications. Currently active control systems are mainly considered for low frequency noise applications up to 1 kHz. The results of this study indicate that for stiff lightweight sandwich panels it might be possible to extend the operative frequency range of active control systems up to mid audio frequencies.

In this case active control systems could balance the poor sound transmission properties of lightweight sandwich structures to an extent that would justify the additional expense and additional installed mass of an active control system. This may lead to a new design approach for vehicles where the use of active vibration control systems is considered at the design stage and the choice of the geometry and material of the structure is not only based on structural and operational constraints. Such an approach would also have to take into account the benefits and drawbacks of active vibration control systems.

3.5 Summary

This Chapter presented the results of a simulation study considering a thin homogeneous panel and a lightweight sandwich panel for different types of distributed deterministic and stochastic excitations with and without active control. The objectives were twofold. Firstly, to investigate and contrast the structural response and the sound radiation in the audio frequency range produced by homogeneous and lightweight sandwich panels subject to deterministic and stochastic distributed excitations. Secondly, to study and compare the control effects produced by an array of idealized velocity feedback control loops on homogeneous and lightweight sandwich panels.

Due to the low modal density and lower convective and acoustic coincidence frequencies the response of the composite sandwich panel is dominated by discrete resonant modes over a wide range of audio frequencies. This indicates a high potential for the application of active damping treatments to reduce the panel kinetic energy and radiated sound power.

It has been demonstrated that for low feedback gains decentralised velocity feedback control produces better control performance on the lightweight sandwich panel than on the homogeneous aluminium panel. This is particularly the case for TBL excitation where the structural response is dominated by low order resonant modes. Discrete velocity feedback is efficient in controlling the resonant response of low order resonant modes and also in controlling the response of individual modes resonating at acoustic coincidence in the mid and high audio frequency range.

These results suggest that decentralised velocity feedback control is efficient in reducing the structural response and radiated sound power of a lightweight sandwich panel in the low and mid audio frequency range. In this case active control systems could balance the poor sound transmission properties of lightweight sandwich structures to an extent that would

justify the additional expense and additional installed mass of an active control system.

In this simulation study basic structural models and ideal velocity sensor actuator pairs have been considered. The following chapters present the results from theoretical and experimental studies considering an active vibration control system with practical actuator-sensor pairs on aluminium and honeycomb sandwich test panels.

Chapter 4

Open and closed-loop base impedance of proof-mass electrodynamic actuators

This chapter presents the results from simulation and experimental studies on the open and closed loop base response of a practical control unit. As shown in Figure 4.1 the control unit comprises a proof-mass electrodynamic-actuator accelerometer-sensor pair and a controller with integrator and amplifier electronic circuits. The first prototype of this control unit was developed by Paulitsch et al. [42, 43, 44]. González Díaz et al. [33, 34] then produced four more identical control units and developed a five channel decentralised velocity feedback analogue controller.

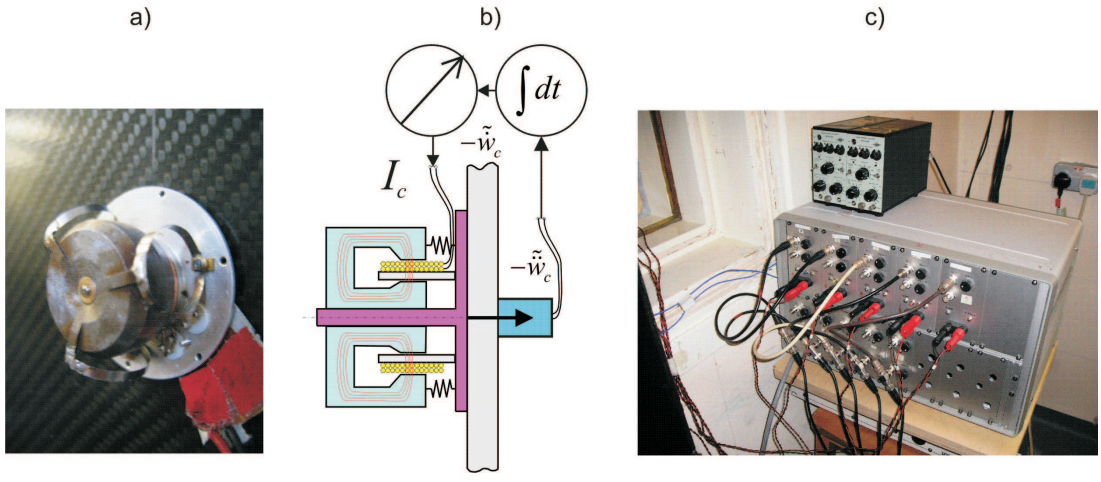

Figure 4.1: (a) actuator unit mounted on panel, (b) control unit schematics and (c) five channel feedback controller.

The proof mass electro-dynamic actuator is used to generate a ‘sky-hook’ force excitation on the structure where they are mounted. The inertial actuation mechanism is obtained by fixing the coil assembly to the base of the actuator on which the permanent magnet is

mounted via three soft circular springs and acts as a proof-mass. For frequencies above the fundamental resonance frequency of the actuator ($f_{res} \approx 1/2\pi\sqrt{k_s/m_2}$ = 23.2 Hz for the actuator used in this study) the magnitude of the generated blocked force per unit input current is frequency independent. Therefore this type of actuator can be used as a 'sky-hook' force actuator provided its fundamental resonance frequency is well below that of the structure under control [19]. As shown in Figure 4.1(b) the input signal to the control actuator is generated by measuring the acceleration at the footprint of the control actuator base on the opposite side of the panel using an piezoelectric inertial accelerometer. An analogue controller is then used to integrate and amplify the acceleration signal to generate a velocity proportional input signal to the control actuator. Although the controller is assumed to produce an ideal output current, the response of the control unit for both current- and voltage-driven actuators are investigated in this study.

In contrast to previous work [33, 34], the experimental and simulation studies presented in this chapter aim to describe the control units in terms of their open and closed-loop base impedances that are exerted to the structure where they are mounted. In this way it is possible to provide a straight-forward physical interpretation for both the stability and control effect produced by the control units.

For this study the five actuators have been fully refurbished. Particular attention has been given to the fabrication of new circular springs and the mounting of the suspension magnet on the guiding stinger so that elastic and damping non-linear effects are minimised.

This chapter is organised in three main sections.

- Section 4.1 presents results from experimental and simulation studies on the actuator blocked force response. A Monte Carlo simulation is used to fit the parameters of a lumped parameter electromechanical model of the actuators to experimental results.
- Section 4.2 presents experimental results on the open and closed loop response of a representative control unit.
- Section 4.3 presents simulation results that provide physical interpretation of the control unit closed loop response considering both ideal and practical frequency response functions of the controller.

In addition, Appendix C provides the derivation of the formulations for the open and closed loop base impedance of control units with current and voltage driven proof-mass electrodynamic actuators.

4.1 Actuator blocked force frequency response function

This Section presents results from the experimental and simulation studies on the blocked force response function of the five electrodynamic proof-mass control actuators. A Monte Carlo simulation is used to fit the parameters of a lumped parameter electromechanical model of the actuators to experimental results.

As shown in Figure 4.2, the blocked force response functions are measured using a B&K type 8001 impedance head which is directly attached to a block of steel with a mass of 8.5 kg. All bonds are realized using thin layers of adhesive wax. The actuators are driven with a white noise signal in the frequency range from 0 Hz to 25600 Hz. The blocked force response functions are measured in terms of the transfer function between the force measured by the impedance head and the voltage across the voice coil of the actuator.

Figure 4.2: Set-up for blocked force measurement.

The Bode diagram in Figure 4.3 shows the measured blocked force response function for all five actuators and the mean of these five responses. The maxima of the response functions occur at the actuator fundamental resonance frequency at about 25 Hz. The results indicate that for all actuators this fundamental resonance is heavily damped. For frequencies below this resonance, the blocked force drops rapidly with decreasing frequency. For frequencies above the actuator resonance, up to about 250 Hz, the magnitude of the blocked force remains approximately constant while above 250 Hz it rolls off under the effect of coil inductance.

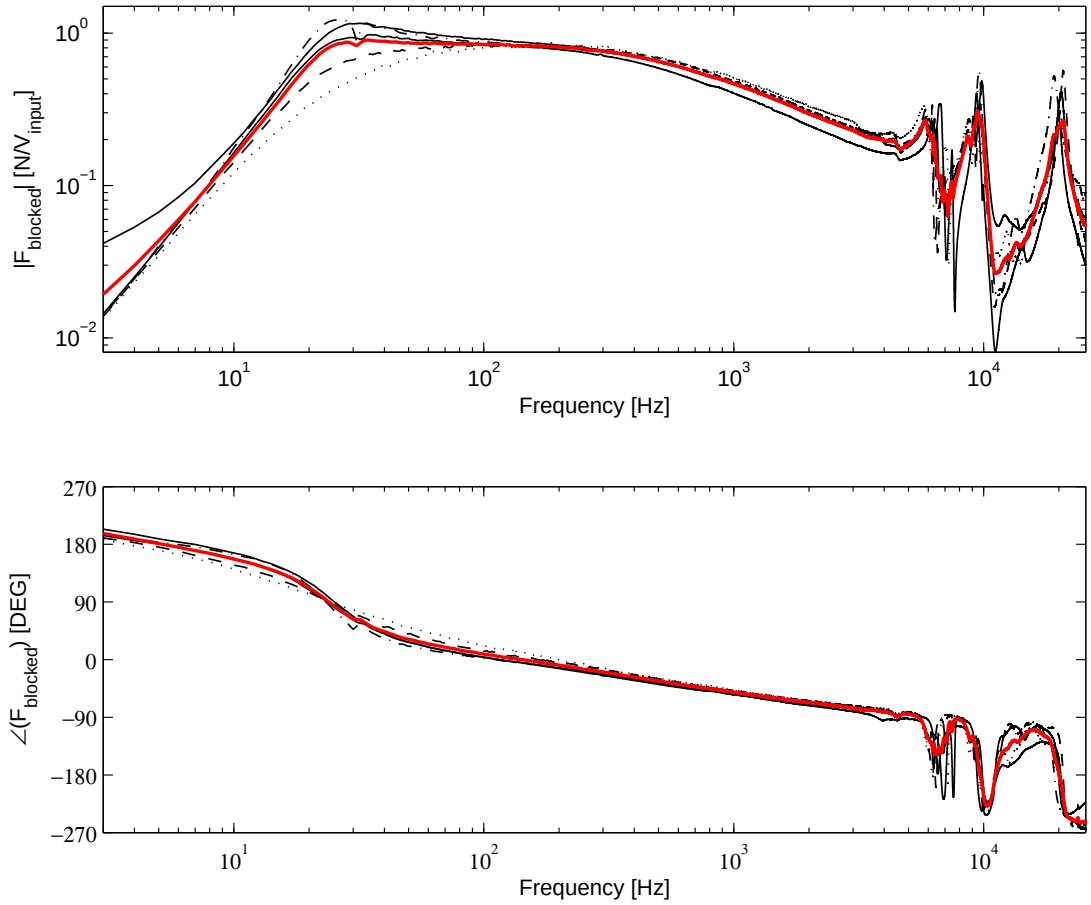

Figure 4.3: Measured blocked force per unit input voltage for all five actuators ($faint - black$), average blocked force for per input voltage ($solid - red$).

At low frequencies the phase is about 180°, which indicates that the blocked force at the base of the actuator is out of phase with the driving electric signal. However around the actuator fundamental resonance there is a 180° phase shift such that above this resonance frequency the blocked force is in phase with the driving signal. However, above 250 Hz there is a gradually increasing phase lag due to the electrical inductance of the coil.

The comparison between the blocked force response function of the different actuators shows a good overall agreement. Around the actuator resonance frequency, the blocked force response functions are dominated by internal damping of the actuators which appears to rather different for each unit.

For frequencies above 5000 Hz the response functions of all actuators show a series of three resonance peaks and anti-resonance troughs, which are due to the mounting resonances of the measurement set-up that can be described as a series of three mass spring systems (i.e. the impedance head mass on wax layer, actuator bases mass on wax layer and actuator proof-mass suspended on the circular springs).

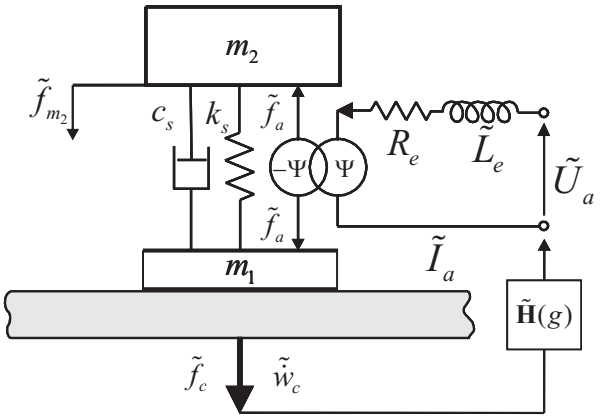

Figure 4.4: Actuator schematics.

Model of actuator blocked force response

As shown schematically in Figure 4.4 the blocked force of a voltage-driven electrodynamic proof-mass actuator can be modelled as

$$\frac{\tilde{F}_c}{\tilde{U}_a} = \frac{\Psi}{\tilde{Z}_e}\left(1 - \frac{\tilde{Z}_s + \frac{\Psi^2}{\tilde{Z}_e}}{\tilde{Z}_{m_2} + \tilde{Z}_s + \frac{\Psi^2}{\tilde{Z}_e}}\right), \tag{4.1}$$

where $\tilde{U}_a$ is the voltage across the actuator voice coil, Ψ is the voice coil coefficient and $\tilde{Z}_e = R_e + j\omega L_e$ is the electrical impedance of the voice coil. Also $\tilde{Z}_s = c_s + k_s/(j\omega)$ and $\tilde{Z}_{m_2} = j\omega m_2$ are the actuator suspension and proof-mass impedances. This formulation includes all mechanical and electrodynamic parameters of the actuator. The corresponding formulation for the blocked force produced by a current-driven electrodynamic proof-mass actuator is independent of the electrical impedance of the voice coil and is given by

$$\frac{\tilde{F}_c}{\tilde{I}_a} = \Psi\left(1 - \frac{\tilde{Z}_s}{\tilde{Z}_{m_2} + \tilde{Z}_s}\right), \tag{4.2}$$

where $\tilde{I}_a$ is the current through the actuator voice coil. The expressions are derived in Appendix C.

A Monte Carlo simulation is used to fit the model parameters in Equation (4.1) to the representative mean blocked force per unit input voltage response function in Figure 4.3 in order to minimise the sum of the squared errors in the frequency range between 10 Hz and 2000 Hz. The resulting simulation results for the blocked force response functions from Equations (4.1) and (4.2) are shown in Figure 4.5. Note that the mechanical model of the

actuator assumes a rigid connection between the blocking mass and the base of the actuator. Hence the effects of mounting resonances due to the spring-damper-mass effects of the thin bonding layer of adhesive wax and the actuator resonant mass-spring-damper-mass system are not captured in this model, but the agreement up to 2 kHz is good.

A comparison between the predicted blocked force response function for the voltage-driven actuator from Equation (4.1) and that for the current-driven actuator from Equation (4.2) show that the blocked force for 1 A current is greater than the blocked force for 1 V voltage. Also above the actuator fundamental resonance, the magnitude and phase of the blocked force per unit current is constant with frequency while the magnitude and phase of the control force per unit voltage drops for increasing frequency because of the frequency-dependent electrical impedance of the voice coil.

The estimated parameters used to model the actuators are summarised in Table 4.1, where the values in $italic$ font are estimated using the Monte Carlo simulation and the values in $bold$ font are measured average masses of the control unit components which are assumed to be known with high accuracy. The estimated actuator parameters and the model parameters previously considered by Paulitsch [42] and González Díaz [45], which are also given in Table 4.1 are in good agreement for the assumed actuator base and proof masses. However, the estimated spring stiffness is a factor of 3.8 to 5.9 times higher than the ones previously considered. Also the estimated coil electrical conductance is a factor of 2 smaller. The coil resistance used in Reference [45] is an order of magnitude higher than that considered in Reference [42] and that estimated as in this study. These discrepancies are due to two principal factors: first the actuators used in this study have been fully refurbished and the suspension spring and coil windings replaced; second the parameters used in References [42] and [45] have been derived from static and simple dynamic analysis (i.e. static deflection and natural frequency) rather than the Monte Carlo best fit procedure used here.

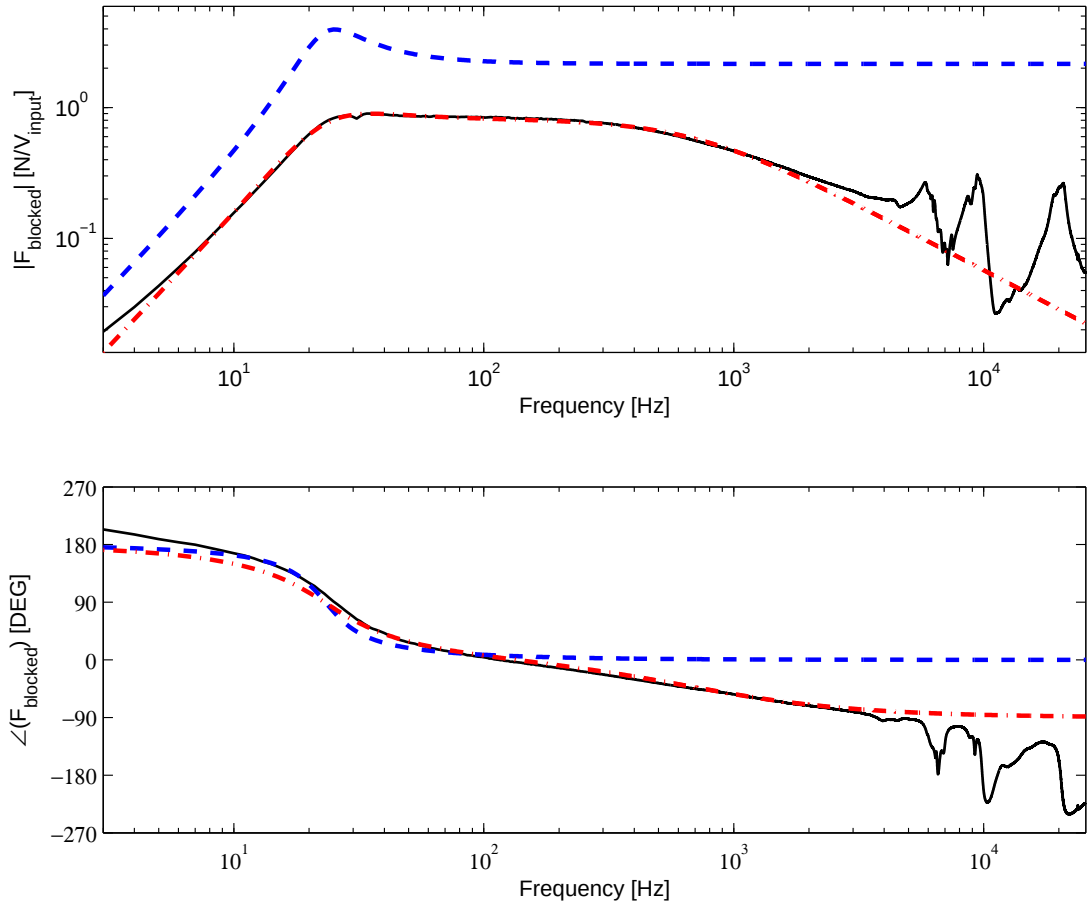

Figure 4.5: Measured average blocked force per input voltage ($solid - black$), predicted blocked force for per input voltage ($dash - dotted - red$) and predicted blocked force per input current ($dashed - blue$).

Table 4.1: Parameters for control actuator model.

Parameter	Symbol	Values			Units
		This study	Ref. [42]	Ref. [45]	
Base mass	m_1	**11+2**	10	8	g
Proof mass	m_2	**24**	20.3	22	g
Suspension stiffness	k_a	*511*	135	86.85	Nm^{-1}
Suspension damping coefficient	c_a	*1.99*	1	2.76	Nsm^{-1}
Coil electrical resistance	R_e	*2.7*	1.8	20	Ω
Coil electrical inductance	L_e	*0.0006*	0.0014	0.002	H
Voice coil coefficient	Ψ	*2.16*	2.5	2.6	$\mathrm{N\,A}^{-1}$

4.2 Experimental studies on the control unit response

This section presents the results from experimental studies on the open and closed loop base impedance of a representative control unit. For the open loop base impedance the actuator is passive while for the closed loop base impedance the feedback control system is activated.

4.2.1 Open loop base impedance

As shown in Figure 4.6(a), in the set-up for the open loop response measurements the actuator was mounted horizontally on a B&K type 8001 impedance head which was rigidly coupled to an LDS 201 electrodynamic shaker. The bond between the actuator and impedance head was realised using a thin layer of adhesive wax. As shown in Figure 4.6(b) and (c) the same set-up was also used to measure the impedance of two lumped masses, where a 11 gram lumped mass represents the base mass of the actuator units including the voice coil and a 35 gram lumped mass represents the total mass of the actuator. The base mass of the actuator when mounted on a panel also includes the weight of the accelerometer sensor which is about 2 grams. The mass of the impedance head below the force gauge is 2.2 grams and the B&K mounting stud has a mass of about 1.2 grams. The slight differences in the base masses are assumed to be negligible for the purpose of this study and no mass correction has been applied in the data post processing. The primary shaker was driven with a white noise signal in the frequency range from 0 Hz to 25600 Hz. The apparent mass of the actuator base for different excitation levels was measured as the transfer function between the force and acceleration output of the impedance head, which was post-processed to yield the actuator open loop base impedance.

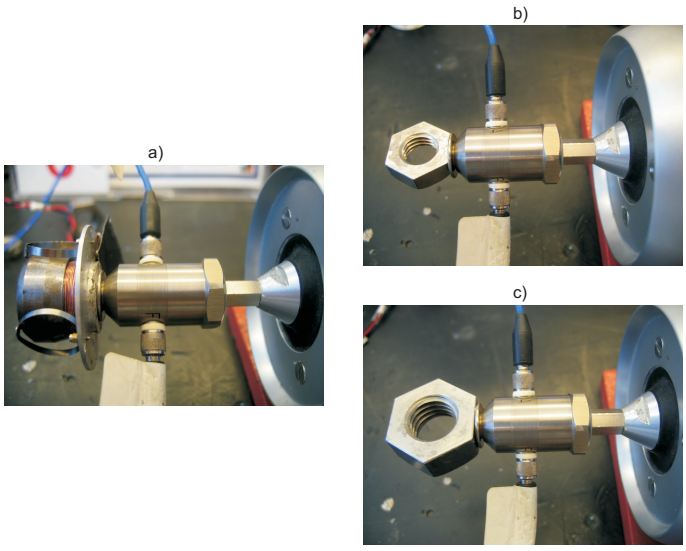

Figure 4.6: Set-up for passive base impedance measurements; a) passive actuator b) equivalent base mass; c) equivalent total mass.

The Bode diagram in Figure 4.7 shows the modulus and phase of the open-loop actuator base impedance of a representative control actuator for various excitation levels. Also the measured impedances of the equivalent base and total lumped masses are presented as references. For low frequencies the magnitude and phase of the base impedance of the actuator unit corresponds to that of the equivalent total lumped mass of the actuator. This is because

below the actuator resonance the base and proof masses of the actuator move in phase. For high frequencies the actuator base impedance converges to that of the equivalent base mass because the base and proof masses are effectively decoupled well above the actuator fundamental resonance.

In the transition region around and above the actuator fundamental resonance the open loop actuator base impedance is controlled by internal damping and has a considerable positive real part. This indicates that in this frequency band the actuator dissipates power from the structure were it is mounted. The measured open loop base impedance of the actuator indicate that in this transition region the response is non-linear and depends on the excitation level. For low excitation levels the actuator base impedance produces damping effects over a wide frequency range up to 3000 Hz. As the excitation level increases the transition region between total mass and base mass behaviour shifts towards lower frequencies, and the transition occurs over a narrower frequency band.

As discussed in Section 4.1, each actuator has a different amount of internal damping, which results in a high variance in the actuator responses in this transition region. During the experiments it was also found that the dynamic response of the actuators in the damping-controlled frequency region had a low reproducibility and varied considerably when units were tested again after remounting on the impedance head or after making minor adjustments of the springs.

For frequencies above 5000 Hz the actuator base impedance exhibits a series of two resonance peaks and an anti-resonance dip. In this frequency range, the reference impedances of two lumped masses both exhibit a distinct resonance which is due to the mass-spring-damper system induced by the wax mounting and the corresponding mass. A comparison between the frequency response functions of these two lumped masses and the actuator suggests that the higher frequency resonance and anti-resonance behaviour of the actuator base impedance is due to the wax mounting conditions which results in a two degree-of-freedom resonant system.

Figure 4.8 shows the Nyquist plot of the open loop base impedances, where Figure 4.8(a) shows locus of the base impedance over the entire observed frequency range while Figure 4.8(b) magnifies the region around the origin. Over almost the entire observed frequency range the locus of the actuator base impedance is real positive. This is also seen from the phase in Figure 4.7, which lies between $\pm 90^{\circ}$. Thus the open loop actuator resonant system is unconditionally stable, as one would expected for a passive system.

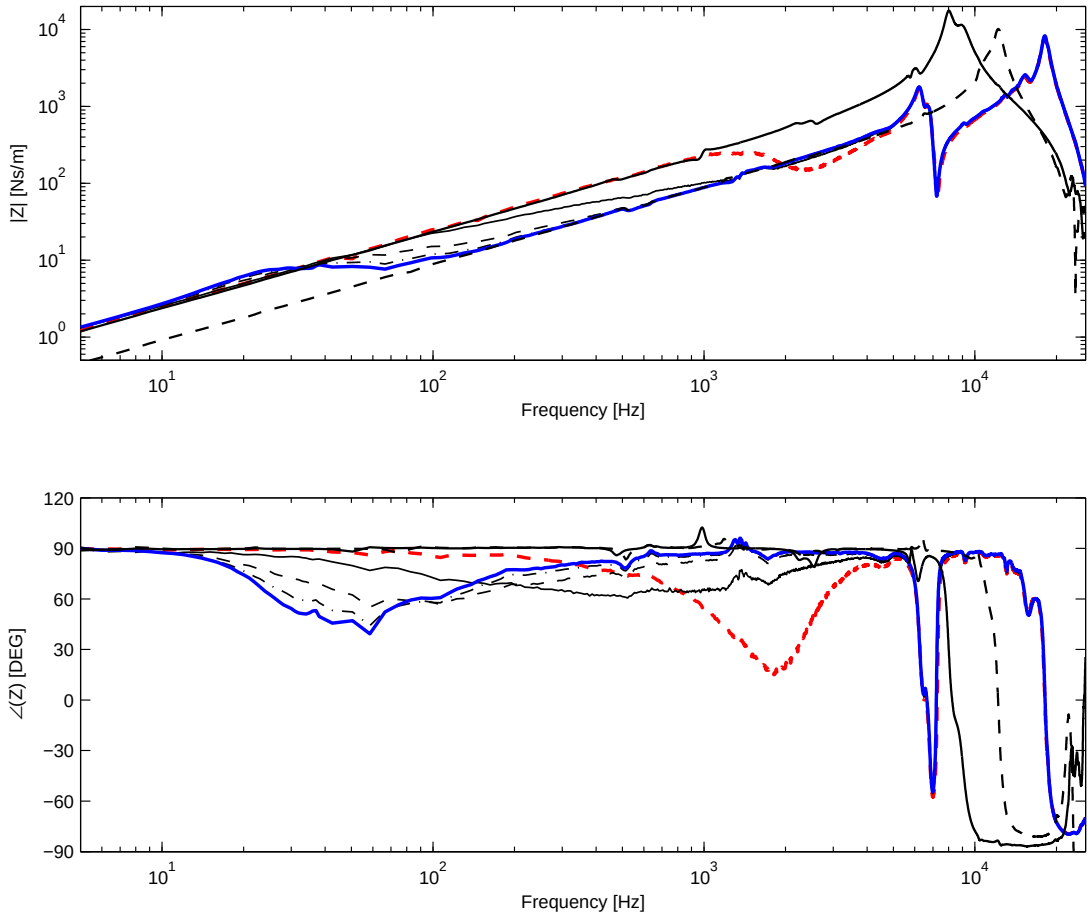

Figure 4.7: Bode diagram of the measured open loop base impedances of a representative actuator for different levels of base excitation: minimal level ($dashed - red$), intermediate levels ($faint - black - lines$)and maximal level ($solid - blue$); for reference: impedance of 35 gram lumped mass ($solid - black$) and 11 gram lumped mass ($dashed - black$).

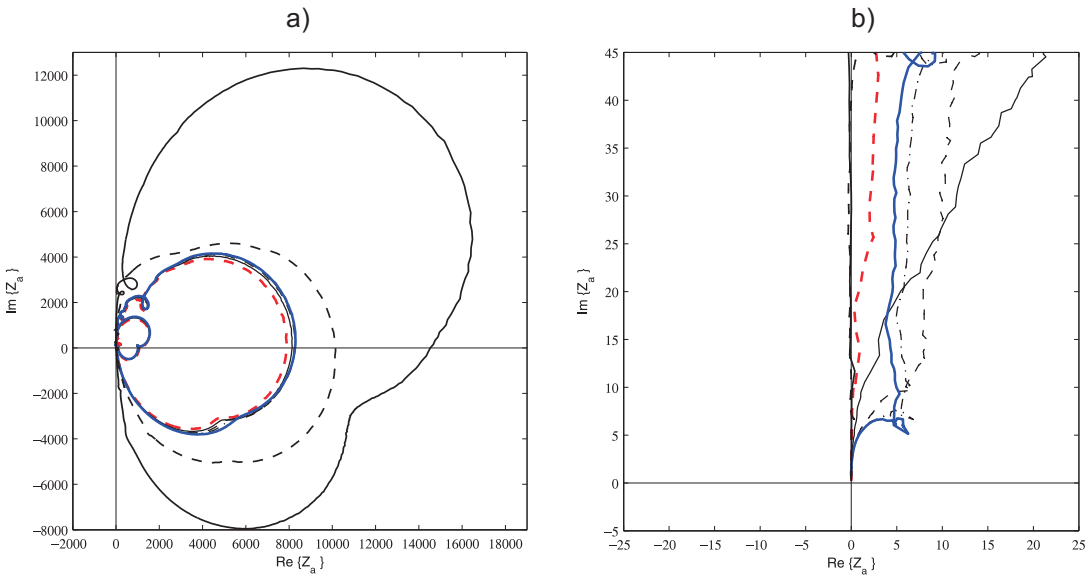

Figure 4.8: Nyquist diagram of the measured open loop base impedances of a representative actuator for different levels of base excitation; (a) for the entire frequency range investigated and (b) magnifying the region around the origin. Minimal level ($dashed - red$), intermediate levels ($faint - black - lines$), maximal level ($solid - blue$); 35 gram lumped mass ($solid - black$)and 11 gram lumped mass ($dashed - black$).

4.2.2 Closed loop base impedance

As for the measurement of the open loop base impedance (passive actuator response), in the set-up for the measurement of the closed loop base impedance (feedback control activated), the actuator was mounted horizontally on a B&K type 8001 impedance head which was rigidly coupled to an LDS 201 electrodynamic shaker. As shown in Figure 4.9, the feedback control loop was installed by adding a PCB type A352C67 accelerometer to the actuator base. The PCB accelerometer signal was fed into a PCB type 481A03 signal conditioner and then into channel 1 of the feedback controller, which consists of an integrator and an amplifier unit. The bonds between the actuator and the impedance head and between the actuator and the PCB accelerometer were realised using a thin layer of adhesive wax. This set-up closely represents the control units when mounted on a panel except that, in the control set-up, the accelerometer would be mounted in the centre of the actuator footprint on the opposite side of the panel.

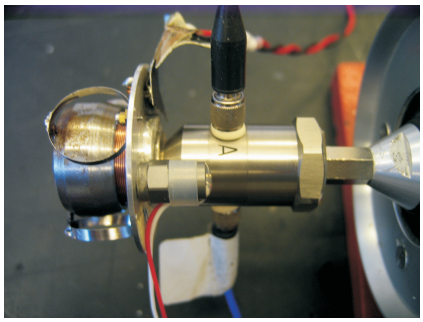

Figure 4.9: Set-up for active base impedance measurement.

The shaker was driven with a white noise signal in the frequency range from 0 Hz to 25600 Hz. The applied excitation level falls in the upper range of excitation levels used in the investigation of the open loop base impedance in Section 4.2.1. The apparent mass of the control unit base is measured as the transfer function between the force and acceleration output of the impedance head and post-processed to yield the control unit open loop base impedance. The mass of the impedance head below the force gauge transducer, the mass of the mounting stud and the mass of the control accelerometer add to the base mass of the actuator. For the purpose of this study, however, these mass effects are assumed to be negligible.

The Bode diagram in Figure 4.10 shows the magnitude and phase of the open and the closed loop base impedance of a representative control unit for a range of feedback control gains. Also the measured impedances of the equivalent base and total lumped masses are presented as references. Considering first the magnitude of the base impedance it can be seen that for

frequencies below 10 Hz the actuator base response corresponds to that of the lumped total mass of the actuator as before. For increasing feedback gains the impedance shows a dip just below 20 Hz followed by a sharp rise at the actuator resonance at about 25 Hz. Between 25 and 500 Hz the response for higher feedback gains is relatively flat. Above 500 Hz the magnitude of the base response for all feedback gains converges towards the impedance of the actuator base mass as before.

At frequencies above 5000 Hz, as discussed with respect to the open loop base impedance in Figure 4.7, the response of the control units is characterised by resonance peaks and anti-resonances troughs due to the mounting conditions. Additional resonances for the closed loop actuator set-up are introduced by rocking motions due to mass of the PCB control accelerometer which is attached to the actuator asymmetrically.

Focusing now on the phase, it can be seen that for frequencies below 10 Hz the phase is 90° for all feedback gains, which corresponds to the impedance of a pure mass. At about 20 Hz the phase of the active base impedance changes rapidly. For all feedback gains the phase initially drops below 90°. Around the actuator fundamental resonance, for low feedback gains, the phase then increases rapidly and then falls below 90° for frequencies above 40 Hz. In contrast, for higher feedback gains the phase further drops rapidly by 360° and falls below -270° for frequencies above 40 Hz. Above 40 Hz the closed loop response of the control units has a phase between 90° and 0°, i.e. -360° and -270°, which indicates that the control unit base impedance has a considerable positive real part and behaves like a damper. With further increase in frequency the phase of the control unit response converges to 90° or -270°, which indicates an increasingly mass-like behaviour. At higher frequencies phase changes occur due to the mounting resonance and anti-resonance behaviour.

The locus of the closed loop control unit base impedance, shown in the Nyquist plots in Figure 4.11 is positive real for all frequencies except those around the actuator fundamental resonance in the frequency range between about 20 Hz and 40 Hz. In this frequency band the locus for the closed loop base impedances form a circle in the left half-plane of the Nyquist plots. This indicates that the closed loop control unit injects power into the structure, it is mounted to, rather than absorbing power from it. The behaviour around the actuator fundamental resonance indicates that the feedback loops are only conditionally stable up to a maximal feedback gain. The maximal feedback gain that guarantees stability for the feedback loop also depends on the impedance of the structures that the control units are mounted to.

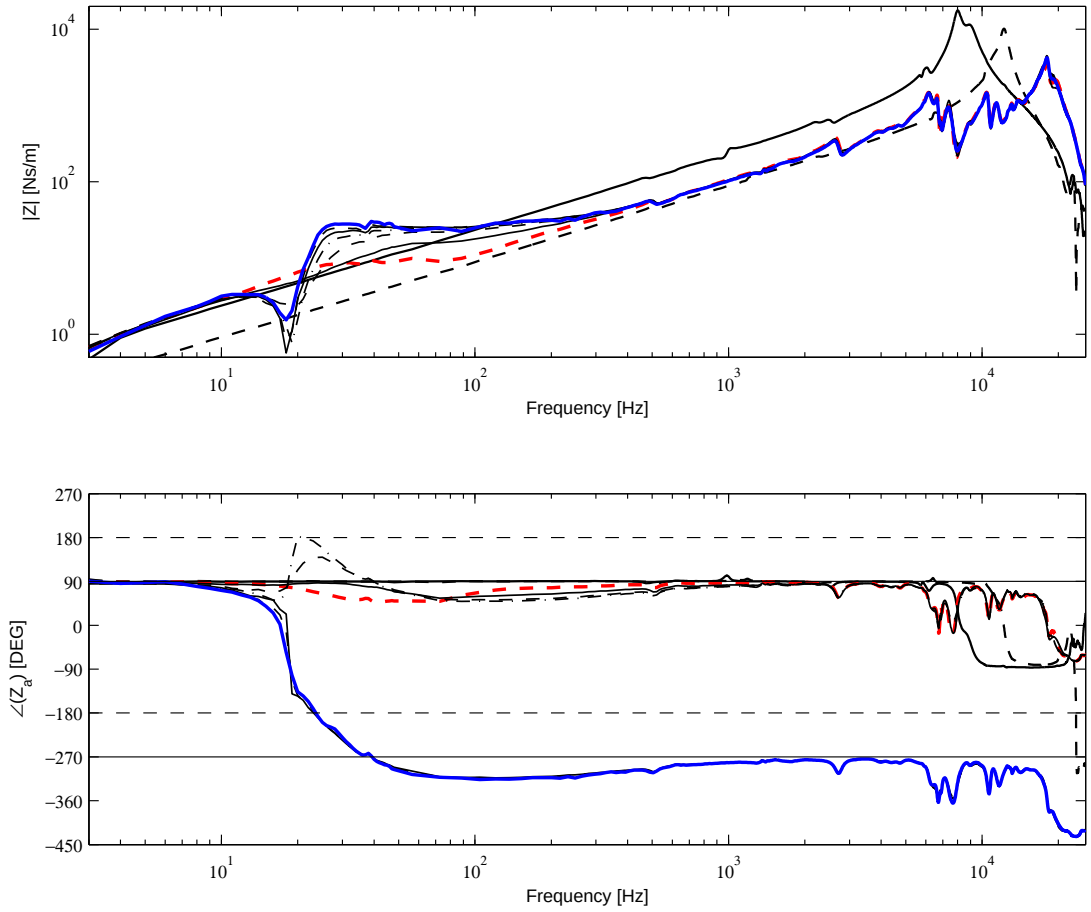

Figure 4.10: Bode diagram with the measured open and closed loop base impedance for a representative actuator unit with attached accelerometer sensor for a range of feedback gains; open loop ($dash - red$), intermediate gains ($faint - black - lines$), closed loop maximal gain ($solid - blue$); for reference: impedance of 35 gram lumped mass ($solid - black$) and 11 gram lumped mass ($dashed - black$).

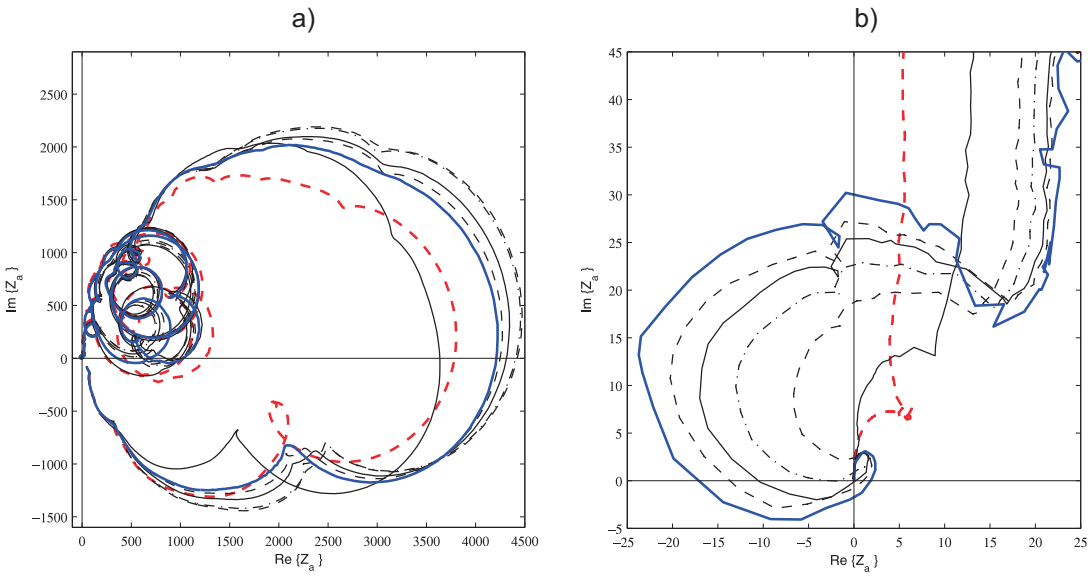

Figure 4.11: Nyquist diagram with the measured open and closed loop base impedance for a representative actuator unit with attached accelerometer sensor, (a) for the entire observed frequency range and (b) magnifying the region around the origin; open loop ($dash - red$),intermediate gains ($faint - black - lines$), closed loop maximal gain ($solid - blue$)

4.2.3 Sensor-actuator open loop response function

During the experimental study on the closed loop base impedance of the control units only relatively small feedback gains could be applied before the control loops became unstable. In order to investigate the stability of the feedback control units the open-loop frequency response function (OL-FRF) between the input to the control board that drives the corresponding actuator and the control accelerometer output has been investigated. The principal set-up is the same as that shown in Figure 4.9 except that for this measurement the primary shaker is passive and it is only the control actuator that drives the system. To guarantee stability the OL-FRF must not encircle the Nyquist instability point at (-1,0j) [13].

Figure 4.12 shows the OL-FRF for the feedback control unit mounted on the shaker as shown in Figure 4.9. At about 30 Hz the magnitude of the OL-FRF in Figure 4.12(a) shows a single repose maxima this indicates that both the control unit and the shaker fundamental resonances are in close proximity and that both are heavily damped. An analysis of the shaker dynamic response showed that the fundamental resonance of the shaker with mounted impedance head and total actuator mass is 30 Hz. Considering the impedance head and actuator base mass this increases to 35 Hz.

The close proximity of the control actuator and shaker resonance peaks results in a high magnitude of the OL-FRF around the actuator fundamental resonance frequency. This produces a large circle in the left half-plane of the Nyquist plot of the OL-FRF, shown in Figure 4.12(b). This sets a stringent limit for the applicable feedback gain. Also at frequencies above 3000 Hz the phase of the OL-FRF tends to fall below -540°, which results in low magnitude circles on the left half-plane of the Nyquist plot. This effect is assumed to be caused by out of phase motion of the actuator base and PCB control accelerometer as an result of mounting resonances, which further limits the stability of the feedback loop, although in practise the relatively low magnitude of these loops implies they are unlikely to be critical.

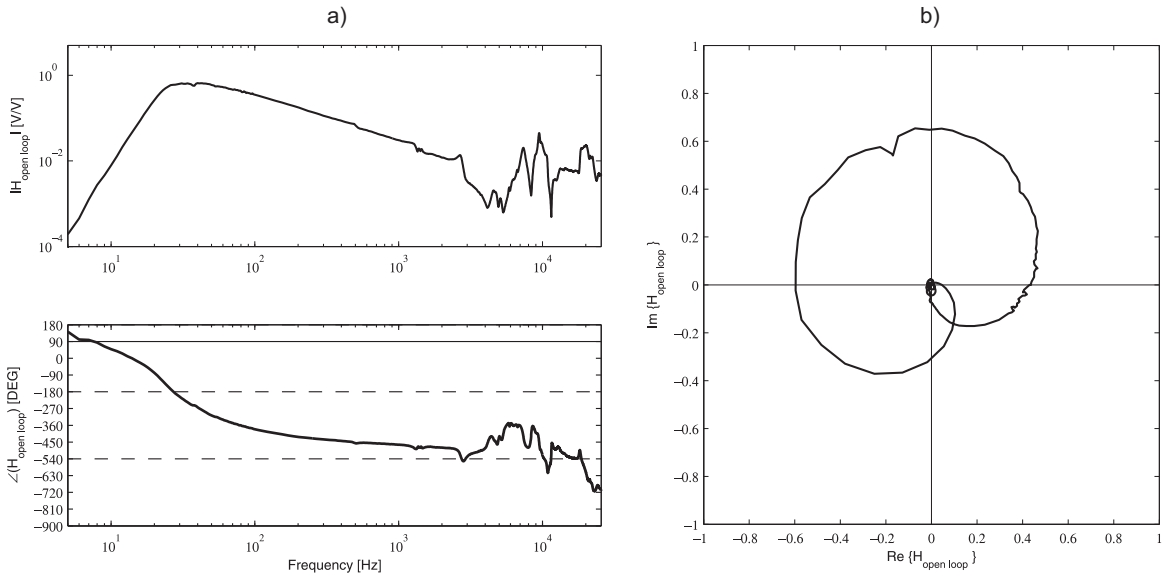

Figure 4.12: Bode (a) and Nyquist (b) plots of the OL-FRF for feedback control unit mounted on a shaker.

In this experimental set-up the control accelerometer is directly attached to the base of the actuator. For the implementation on the panels, the actuators and control accelerometers are separately mounted on the source and receiving sides of the panel. This may introduce additional dynamic effects at higher frequencies, especially for a sandwich panel, which are not considered in this experimental set-up. However, as discussed in Chapter 5, it is found that similar mounting resonance effects arise which produce high frequency spill-over effects and also impose high frequency stability limits for the control units when mounted on two test panels.

An uncertain factor in the measured OL-FRF is the difference between the output impedance of the accelerometer signal conditioner and the output impedance of the analyser signal generator. This may have an effect on the output current per input voltage of the controller board. This has so far been assumed to be a minor issue but should be further investigated to yield a better understanding of the dynamic interaction of all electric circuits in the control loop.

4.3 Physical interpretation of the control unit response

This section presents the results of simulation studies on the open and closed loop control unit base impedance for the cases of current and voltage-driven actuators considering both ideal and practical controller frequency response functions (FRF). The study aims to give a physical interpretation of the control units closed loop base impedance which was determined experimentally in Section 4.2.2. Considering the lumped parameter model depicted in Figure 4.4, the closed loop base impedance of a control unit with current-driven electrodynamic proof-mass actuator is given by

$$\tilde{Z}_{a_I} = \tilde{Z}_s + \tilde{Z}_{m_1} - \frac{\tilde{Z}_s^2}{\tilde{Z}_{m_2} + \tilde{Z}_s} + \tilde{C} g \Psi \left(1 - \frac{\tilde{Z}_s}{\tilde{Z}_{m_2} + \tilde{Z}_s} \right), \tag{4.3}$$

where g is the applied feedback gain, $\tilde{C}$ is the gain-normalised controller FRF, and Ψ is the voice coil coefficient. Also $\tilde{Z}_s = c_s + k_s/(j\omega)$, $\tilde{Z}_{m_1} = j\omega m_1$ and $\tilde{Z}_{m_2} = j\omega m_2$ are the actuator suspension, base mass and proof mass impedances as before. The corresponding formulation for the base impedance of a closed loop voltage-driven electrodynamic proof-mass actuator is given by

$$\tilde{Z}_{a_U} = \tilde{Z}_s + \tilde{Z}_{m_1} + \frac{\Psi^2}{\tilde{Z}_e} - \frac{\left(\tilde{Z}_s + \frac{\Psi^2}{\tilde{Z}_e} \right)^2}{\tilde{Z}_{m_2} + \tilde{Z}_s + \frac{\Psi^2}{\tilde{Z}_e}} + \frac{\tilde{C} g \Psi}{\tilde{Z}_e} \left(1 - \frac{\tilde{Z}_s + \frac{\Psi^2}{\tilde{Z}_e}}{\tilde{Z}_{m_2} + \tilde{Z}_s + \frac{\Psi^2}{\tilde{Z}_e}} \right), \tag{4.4}$$

where $\tilde{Z}_e = R_e + j\omega L_e$ is the electrical impedance of the voice coil. The parameters used to model the actuators were summarised in Table 4.1. These expressions are derived in Appendix C.

4.3.1 Ideal controller response

Considering first the results for a frequency-independent controller FRF with unit gain, Figures 4.13 and 4.14 show the Bode and Nyquist plots of the predicted open and closed loop base impedance for a current-driven actuator with feedback gains g between 0.1 and 250. Comparison with Figures 4.10 and 4.11 shows a generally good agreement with the measured base impedance response functions. However, even for high feedback gains the predicted impedance functions do not exhibit the 360° phase shift around the actuator fundamental resonance. Also, for frequencies below the actuator fundamental resonance, the predicted impedance functions show an increase in magnitude and a positive phase shift of up to 90° relative to the passive system, which is not observed in the measured base impedances.

Figures 4.15 and 4.16 show the Bode and Nyquist plots of the predicted closed loop base impedances for a voltage-driven actuator with feedback gains between 0.1 and 250. These results are quite similar to the results for a current-driven actuator. As discussed in Section 4.1, the actuator blocked force for 1 A input current is higher than the blocked force for 1 V input voltage. Also, above the actuator fundamental resonance, the magnitude and phase of the control force per unit current is constant with frequency while the magnitude and phase of the control force per unit voltage drops with increasing frequency because of the frequency-dependent electrical impedance of the voice coil. Hence, for the same feedback gain the magnitude of the base impedance of the control unit with voltage-driven actuator tends to be lower than that for the control unit with current-controlled actuator. Also, above the actuator fundamental resonance the magnitude and phase of the base impedance for control units with voltage-driven actuators falls with increasing frequency. For high feedback gains, the phase of the base impedance for the control unit with voltage-driven actuator falls below $0°$ and in the frequency range between 1000 and 2000 Hz the magnitude of the closed loop base impedance drops below that of the actuator base mass. For higher frequencies the closed loop control unit base impedance converges towards the impedance of the actuator base mass which increases in proportion to ω.

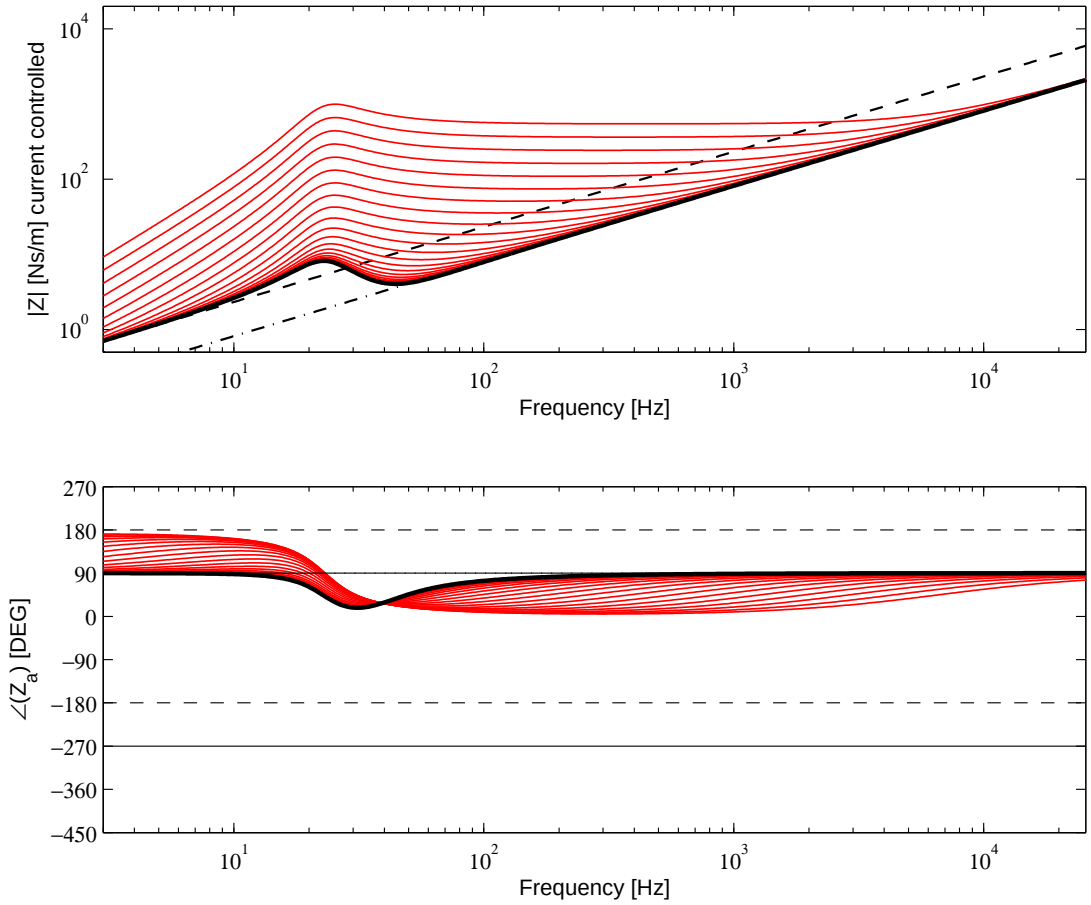

Figure 4.13: Predicted base impedance for closed loop, current controlled actuator for an ideal controller response; 0 feedback gain ($solid$), feedback gains between 0.1 and 250 ($faint$), 35 gram lumped mass ($dashed$) and 11 gram lumped mass ($dash-dotted$).

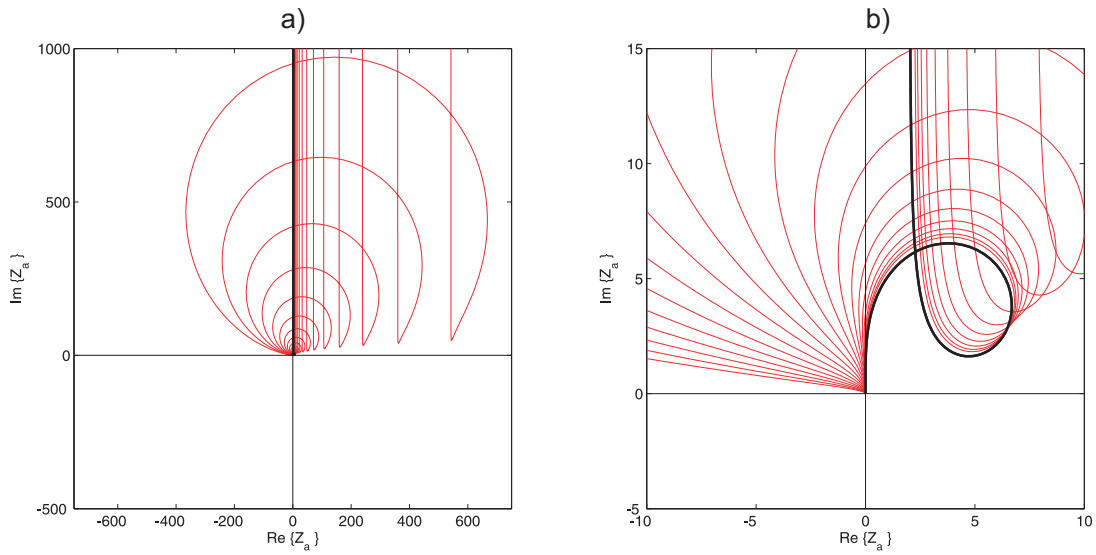

Figure 4.14: Nyquist diagrams of the predicted base impedance for closed loop, current controlled actuator for an ideal controller response; 0 feedback gain ($solid$), feedback gains between 0.1 and 250 ($faint$).

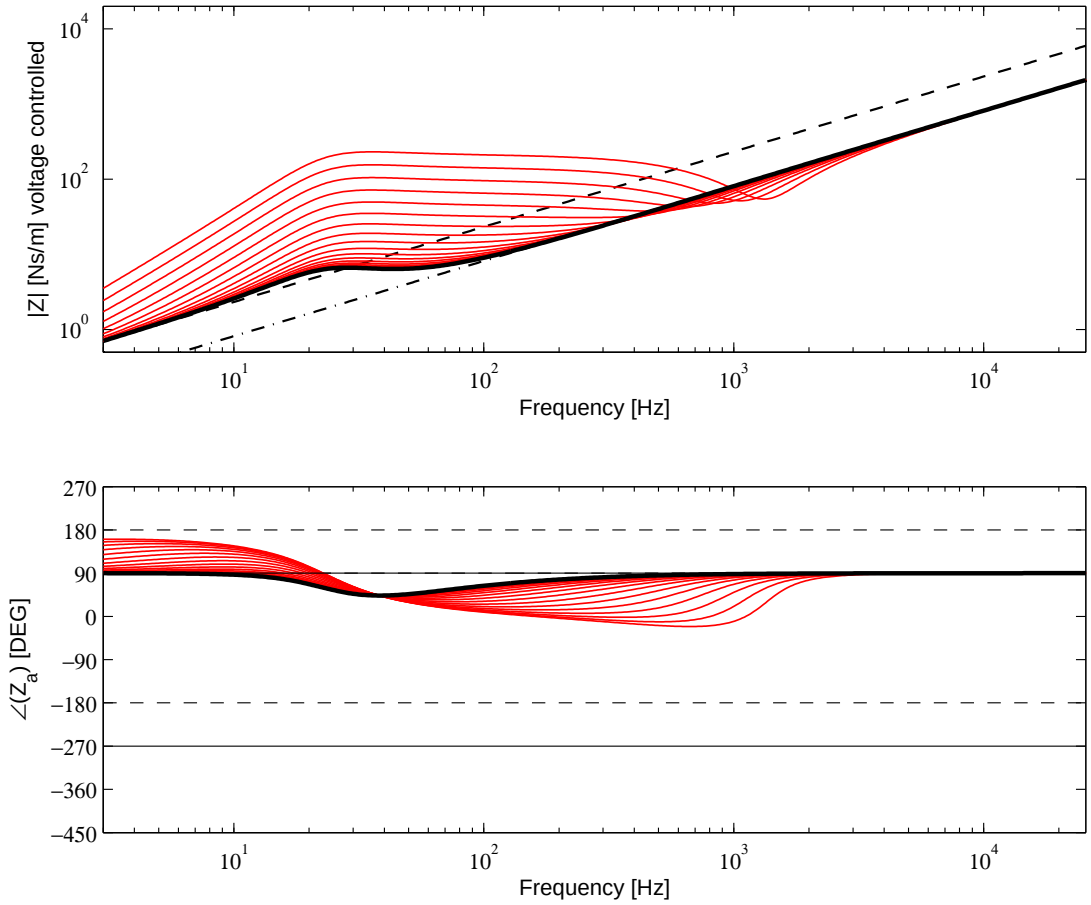

Figure 4.15: Predicted base impedance for closed loop, voltage controlled actuator for an ideal controller response; 0 feedback gain ($solid$), feedback gains between 0.1 and 250 ($faint$), 35 gram lumped mass ($dashed$) and 11 gram lumped mass ($dash-dotted$).

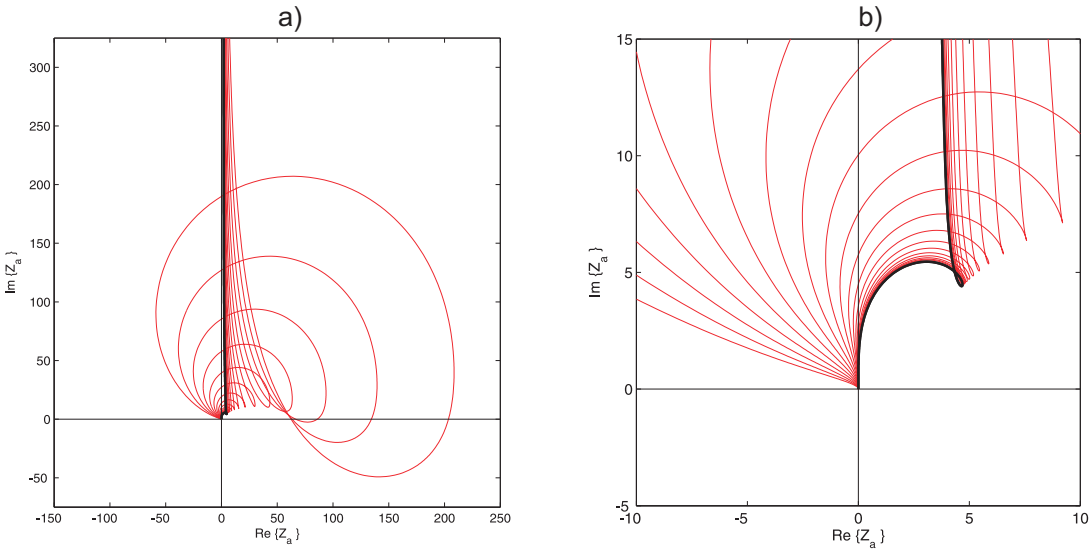

Figure 4.16: Nyquist diagrams of the predicted base impedance for closed loop, voltage controlled actuator for an ideal controller response; 0 feedback gain ($solid$), feedback gains between 0.1 and 250 ($faint$).

4.3.2 Practical controller response

A practical feedback controller does not exhibit an ideal flat frequency response, which therefore affects the spectrum of the resulting closed loop base impedance of the control unit. Each channel of the practical controller used in the experimental studies presented in Chapter 5, Section 5.3, consists of an integrator and an amplifier unit with analogue electronic circuits.

Measurements of the frequency response function of the controller boards showed that the integrator circuit can be readily modelled as the combination of a second order high pass filter for DC decoupling and a first order low pass filter which implements integration. To replicate the measured frequency responses both filters are modelled with a corner frequency of 14.5 Hz. The amplifier FRF was found to have the characteristics of a first order band-pass filter and has been modelled with upper and lower corner frequencies of 5 Hz and 9000 Hz respectively.

Figure 4.17 shows the predicted magnitude and phase of the controller FRF, where the dashed line represents the resulting FRF arising from a combination of integrator and amplifier FRFs and the solid line represents the same controller response function corrected by an ideal integration term. The corrected controller FRF represents the controller response with respect to an ideal velocity sensor as assumed in the formulations for the closed loop control unit base impedances in Equations (4.3) and (4.4).

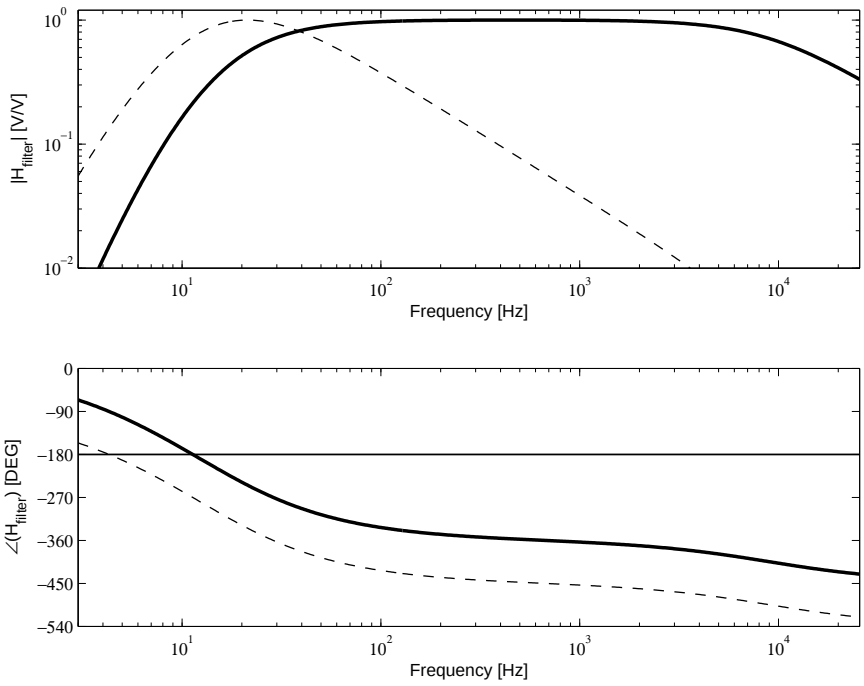

Figure 4.17: Controller frequency response function; as implemented in the electric circuits ($dashed$) and corrected by an ideal integration term ($solid$).

It should be noted that this model does not consider the response characteristics of the accelerometer sensor, which at high frequencies is characterised by a sharp peak around the accelerometer internal resonance. This resonance occurs at very high frequencies where the closed loop base impedance of the actuator is dominated by the passive impedance of the actuator base mass and mounting resonance effects. It is therefore assumed that the accelerometer output signal is ideally flat in the frequency range over which the response of the control units could become unstable.

Figures 4.18 and 4.19 show the predicted closed loop base impedance for a current-driven actuator with feedback gains between 0.1 and 250, considering the practical controller FRF shown in Figure 4.17. Comparison with the measured closed loop base impedance in Figures 4.10 and 4.11 shows a very good general agreement between measured and predicted results.

Around 20 Hz the predicted base impedance of the control unit with practical controller FRF captures the 360° phase shift and the corresponding dip in magnitude of the impedance, which is observed in the measured results in Figure 4.10. This phase shift is due to the rapid change in phase of the controller FRF which results from the combined responses of the integrator and amplifier FRF functions. Well below the actuator fundamental resonance, in contrast to the base impedance with the flat controller FRF, no positive phase change is predicted while the increase in magnitude is more gradual. This is due to the third order low pass filer characteristics of the controller FRF at very low frequencies. For high frequencies, the closed loop base impedance tends to decrease slightly with increasing frequency which is due to the low pass filter characteristics of the controller FRF which has a corner frequency of 9000 Hz.

Figures 4.20 and 4.21 show the predicted closed loop base impedance for a voltage-driven control unit with feedback gains between 0.1 and 250 considering the practical controller FRF shown in Figure 4.17. As for the predicted impedances with ideal flat controller response, the base impedance for voltage and current control give similar results. However, the results in the Nyquist diagram in Figure 4.21(a) indicate that for frequencies above 2000 Hz, for high feedback gains the locus of the base impedance migrates into the left half plane, i.e. the phase of the base impedance for voltage-control rises slightly above -270°. This results in a base impedance with a small negative real part which indicates the possibility of control instability and control spillover problems at high frequencies.

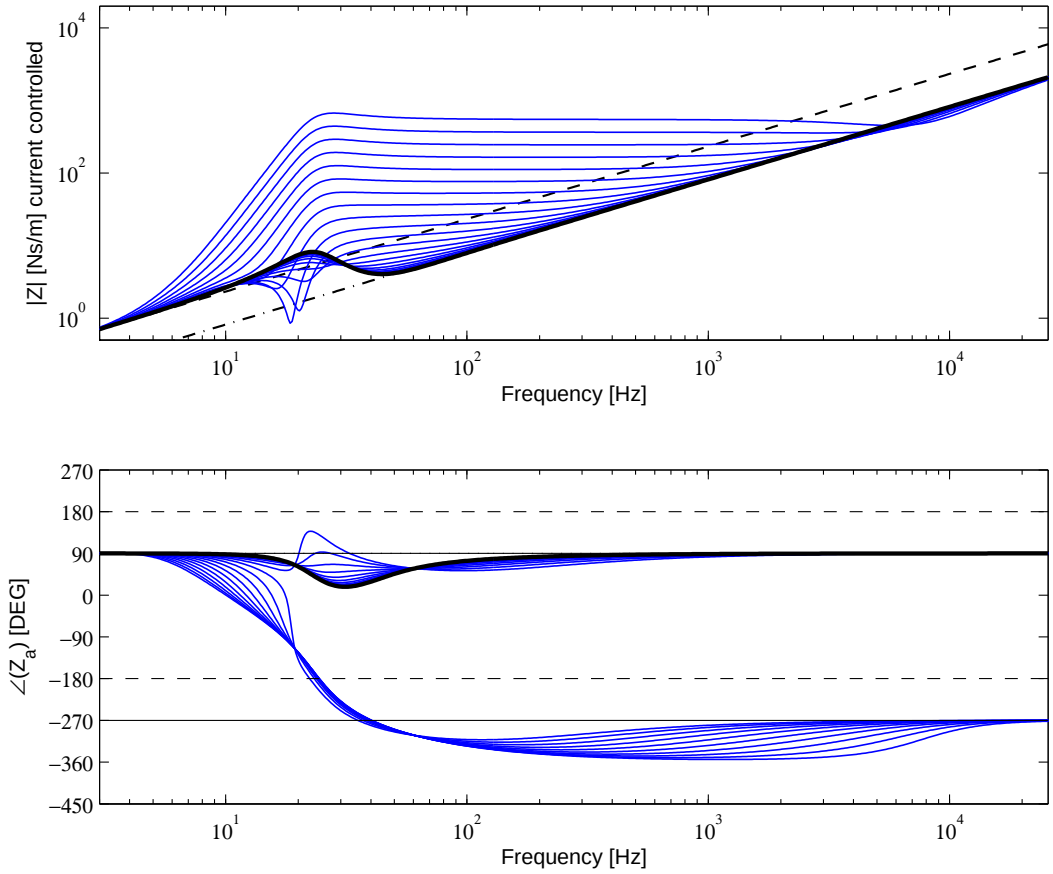

Figure 4.18: Predicted base impedance for closed loop, current controlled actuator for a practical controller response; 0 feedback gain ($solid$), feedback gains between 0.1 and 250 ($faint$), 35 gram lumped mass ($dashed$) and 11 gram lumped mass ($dash-dotted$).

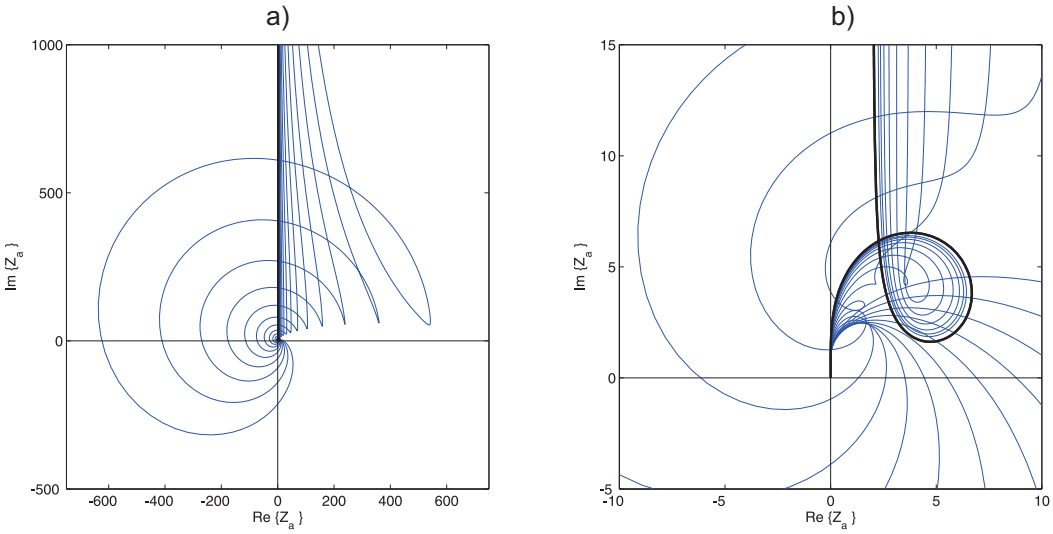

Figure 4.19: Nyquist diagrams of the predicted base impedance for closed loop, current controlled actuator for feedback for a practical controller response; 0 feedback gain ($solid$), feedback gains between 0.1 and 250 ($faint$).

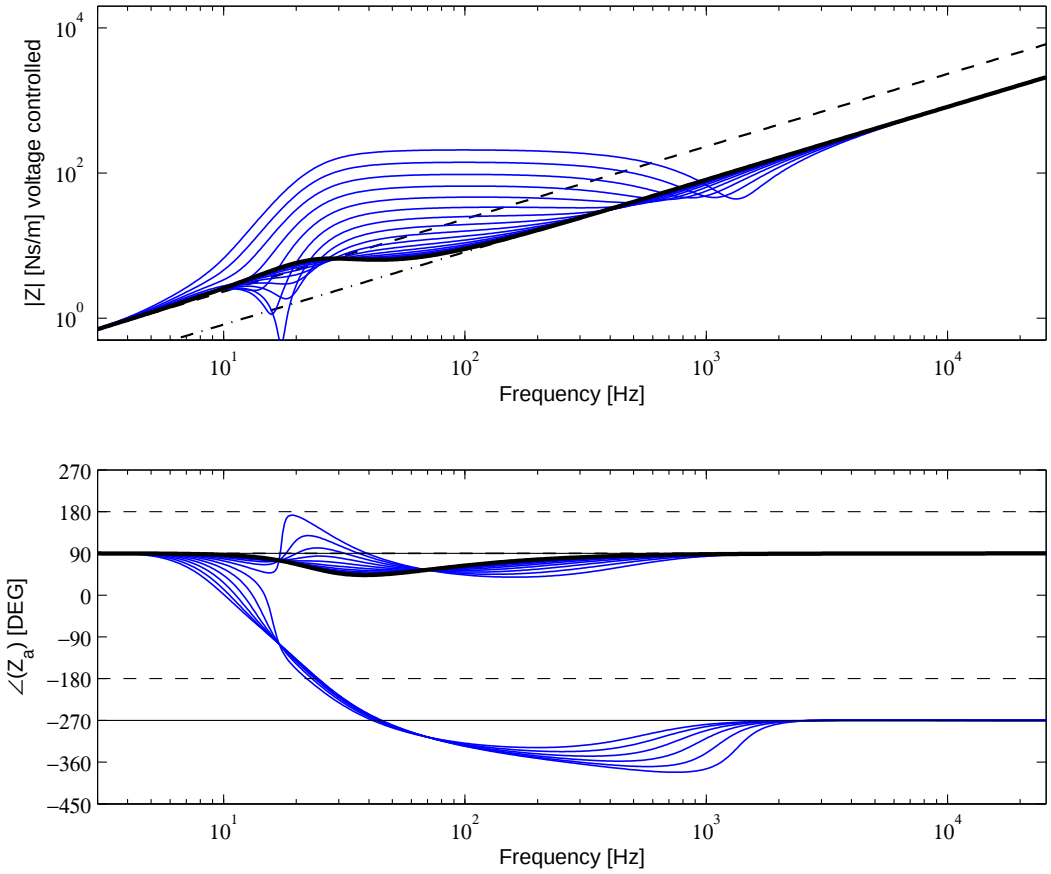

Figure 4.20: Predicted base impedance for closed loop, voltage controlled actuator for a practical controller response; 0 feedback gain ($solid$), feedback gains between 0.1 and 250 ($faint$), 35 gram lumped mass ($dashed$) and 11 gram lumped mass ($dash-dotted$).

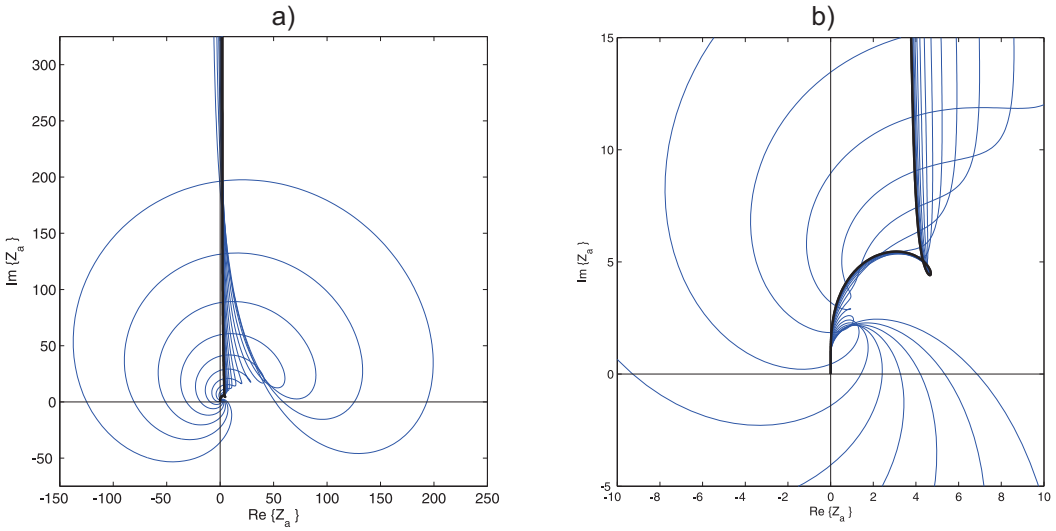

Figure 4.21: Bode plot (a) and Nyquist diagram (b) of the predicted base impedance for closed loop, current controlled actuator for a practical controller response; 0 feedback gain ($solid$), feedback gains between 0.1 and 250 ($faint$).

The controller integrator circuit is assumed to act as a voltage source with infinite input impedance and zero output impedance. The controller amplifier circuit is assumed to act as a current source with infinite input impedance and infinite output impedance. However from this present study it is not completely clear how close the actual controller circuits resemble the ideal input and output impedances. The controller therefore may not enforce an ideal current signal on the actuator voice coil. Further studies should be conducted to understand more fully the interaction between all electrical circuits involved in the control system.

4.4 Summary

In this chapter the results from experimental and simulation studies on the open and closed loop response of control units with electrodynamic proof-mass actuators and accelerometer-sensor pairs has been presented. In contrast to previous work these experimental and simulation studies characterise the control units in terms of the open and closed loop base impedances they exert on panels onto which they are mounted.

- Section 4.1 presented experimental and simulation studies on the actuator blocked force frequency response function.
  - The blocked response of the five actuators are similar in the lower and upper limits of the observed frequency range. Around the actuator fundamental resonance frequency the response of the actuators is dominated by internal damping, which differs between the units. However the actuators can be sufficiently represented by a mean response averaged over all actuators.
  - The blocked force of proof-mass electrodynamic actuators can be readily modelled using a basic electromechanical model with empirically estimated input parameters. However, for frequencies above 5000 Hz the response of the actuators is characterised by mounting resonance effects which are not captured in the electromechanical model.
- Section 4.2 presented experimental studies on the open and closed loop base impedance of a representative control unit.
  - At low frequencies the base impedance of the actuator corresponds to the impedance of the total actuator mass while at high frequencies it converges to the impedance of the actuator base mass. In the transition region the open loop

response of the actuators is non-linear and depends on the base excitation level.

  - The closed loop control unit base impedance shows the same low and high frequency characteristics as in the open loop case. In the transition region, around and above the actuator fundamental resonance frequency, the response of the control unit is dominated by the feedback force generated by the actuator voice coil.

  - Around the actuator fundamental resonance, the control unit base impedance has a negative real part which indicates a negative damping effect. This results in conditional stability of the closed feedback loop.

- Section 4.3 presented simulation studies on the closed loop base impedance of the control units in such a way as to give physical interpretation of the measured control unit responses.

  - The simulated base impedance with ideal controller FRF shows a generally good agreement but fails to capture some of the characteristics that are apparent in the measured responses.

  - The simulated base impedance with practical controller FRF shows a good agreement with the measured base impedance and captures all response characteristics apparent in the measured control unit responses.

  - For frequencies well below the actuator fundamental resonance the control unit base impedance corresponds to that of the total actuator mass. For frequencies around actuator resonance the combined response characteristics of the actuator dynamics and the controller frequency response function result in a dip in the magnitude of the control unit base impedance. For low feedback gains this happens alongside an increase in phase by up to 90°; for higher feedback gains the phase shifts by -360°. For very high feedback gains the simulation studies indicate that this phase shift occurs within an increasingly narrow frequency band and the dip in the magnitude of the base impedance disappears. For increasing frequency the magnitude of the base impedance forms a plateau and the phase is between 90° and 0° or -270° and -360°. This indicates that the closed loop control units produce considerable active damping effects. For high frequencies, for high feedback gains, the phase of the base impedance drops below -360°, which is due to the low pass filter cut-off of the control unit response. At very

high frequencies, for all feedback gains, the base impedance of the closed loop control units converges to that of the actuator base mass.

The basic electromechanical model with controller FRF function readily describes the closed loop control unit base impedance in the frequency range of interest. It can therefore be used to investigate new designs of both electro-mechanical actuator and electrical controller in order to optimise the stability and control performance properties. For example future studies could investigate the implementation of an analogue phase compensator in the controller FRF which would increase the stability of the control unit feedback loops when mounted on flexible panels.

Resonance effects due to the actuator and sensor mounting conditions are not captured by the current model. An extended model should capture these multiple degree of freedom resonance effects to characterise the control unit response at higher frequencies.

The open loop response of the actuators has been found to be non-linear. Further studies could investigate the closed loop control unit response for low base excitation levels and non-flat excitation spectra. However, the effort to measure these responses and to implement non-linearity in the electrodynamic response model may be disproportionate to the benefits since the non-linear characteristics of the response is only specific to the prototype actuator design investigated in this study.

The following chapter presents the results from experimental studies on the control stability and performance of the system with five decentralised control units mounted on a homogeneous aluminium panel and a lightweight honeycomb sandwich panel. Also the results from simulation studies on the control stability and performance are presented where the feedback control loops are modelled using the expressions for control units with current-controlled actuators from Equation (4.3).

Chapter 5

Simulation and experimental studies of practical control set-ups

This chapter presents the results of experimental and simulation work on a thin aluminium panel and a honeycomb sandwich panel with decentralised velocity feedback control. The control system consists of five decentralised control units with proof-mass electrodynamic actuator - accelerometer sensor pairs as described in Chapter 4.

Both the experimental and simulation studies consider the control stability and performance in terms of panel kinetic energy and far field radiated sound power of the two panels. In the experimental study the panels are either excited mechanically by a shaker or by the acoustic field produced by a loudspeaker. In the simulation study these two excitations are modelled as a point force excitation and an acoustic plane wave excitation. The response of the two panels to stochastic acoustic diffuse field (ADF) and turbulent boundary layer (TBL) disturbances is also simulated but not investigated experimentally.

The aluminium panel considered in this study is shown in Figure 5.1(a). The panel is 1.6 mm thick and modelled as a thin homogeneous panel using the same material properties as for the aluminium panel considered in the simulation studies in Chapter 3.

The honeycomb test panel considered in this chapter is shown in Figure 5.1(b). In contrast to the honeycomb panel considered in the theoretical studies in Chapter 3 this panel has a similar mass per unit area to the aluminium test panel but a much higher static stiffness. Moreover, both panels have larger dimensions than the panels considered in Chapter 3. The decision to use a stiffer honeycomb panel was mainly based on the availability of the test specimen. Nevertheless, it is believed that the honeycomb test panel more closely represents

lightweight sandwich panels that could be used in the construction of transportation vehicles. Also the frequency range for the studies in this chapter has been restricted to 6400 Hz, which represents the frequency range of interest for most interior noise control applications.

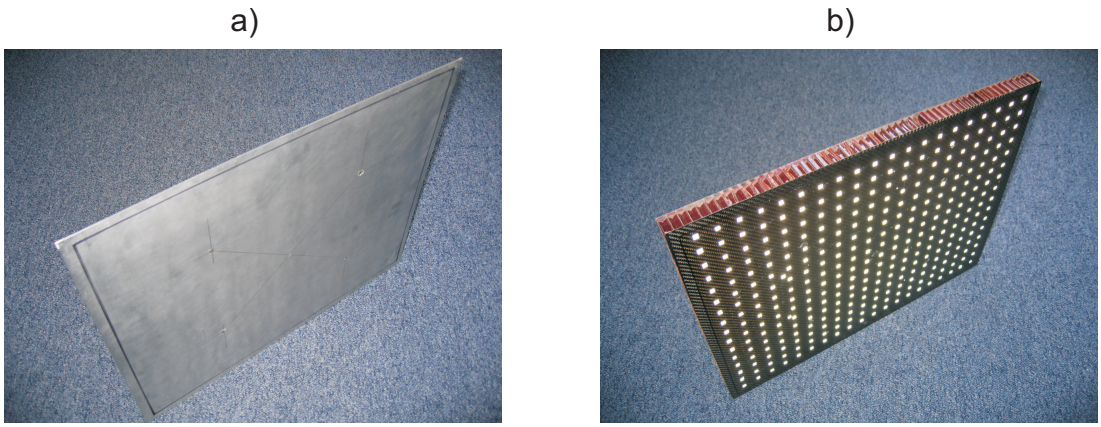

Figure 5.1: Thin homogeneous aluminium test panel (a) and stiff lightweight honeycomb sandwich test panel (b).

This chapter is organized in three main sections:

- Section 5.1 discusses the dynamic characteristics of the two panels. In particular the implication of frequency dependent anisotropic behaviour on the response of the stiff lightweight honeycomb panel is discussed with respect to (a) the wavenumbers of propagating waves, (b) the modal density, (c) the modal overlap factor and (d) both excitation and radiation coincidence effects.

- Section 5.2 presents simulation studies on the implementation of a practical control system with decentralised feedback control units using electrodynamic proof-mass actuators as described in Chapter 4. The model parameters are chosen to replicate approximately the experimental set-ups with the aluminium and honeycomb panels. The control performance and stability of the decentralised control system is assessed for both panels. The control performance is analysed in terms of the time-averaged total kinetic energy and total sound power radiated by the panel, for excitation by (a) a point force, (b) an acoustic plane wave.

- Section 5.3 presents measurements on the two panels without control units and with open and closed loop feedback control units. These are carried out in a sound transmission suite facility. The control performance and stability properties of the decentralised control system are assessed for both panels. Also in this case the control performances are analysed in terms of the-time averaged total kinetic energy and total sound power radiated by the panels when subjected to mechanical excitation via an

electrodynamic shaker and an acoustic field generated by an loudspeaker. With these experiments the simulation results in Section 5.2 can be validated.

In addition

- Appendix D provides background information on the experimental studies for the estimation of the structural parameters of the anisotropic honeycomb test panel, and
- Appendix E provides further details on the sound transmission suite facility and the experimental set-ups.

5.1 Test panel characteristics

This section discusses the dynamic characteristics of the aluminium and the honeycomb test panels. First the panel models are introduced. As in Chapter 3, the specific dynamic characteristics of the two panels are then discussed with respect to (a) the wavenumbers of propagating transverse waves, (b) the modal density, (c) the modal overlap factor and (d) both excitation and radiation coincidence effects.

5.1.1 Panel models

This subsection introduces the dynamic models considered for the modelling of the thin homogeneous and the lightweight honeycomb sandwich test panels used in the simulation studies of this chapter. The honeycomb sandwich panel, considered in this chapter, has a significantly higher static stiffness than the homogeneous aluminium panel. However, both panels have a very similar mass per unit area.

Aluminium test panel: As in Chapter 3, the aluminium test panel has been modelled as a thin homogeneous and isotropic plate. In order to replicate approximately the experimental set-up, it is assumed that all edges are subjected to clamped boundary conditions. The panel dimensions are chosen as l_x=477 mm and l_y=381 mm. This replicates the inner dimensions of the test frame, which is specified in Appendix E. The formulations given in References [47, 48] are used to express the natural frequencies and modeshapes for a clamped panel. These are summarised in Appendix A. The dimensions, cross-section geometry and material properties of the aluminium test panel are summarised in Table 5.1.

Table 5.1: Geometry and physical parameters of the aluminium test panel.

Parameter	Symbol	Value	Unit
x-dimension	l_x	477	mm
y-dimension	l_y	381	mm
Thickness	h	1.6	mm
Mass density	ρ	2720	kg m^{-3}
Young's modulus	E	70	GPa
Poisson's ratio	ν	0.33	–
Modal loss factor	η	0.02	–

Honeycomb sandwich test panel: For practical sandwich panels the transverse dynamic stiffness is often anisotropic with respect to the x and y-axes [61]. The most sensitive structural parameters for an accurate modelling are the out-of-plane shear modulus of the sandwich core G_x and G_y [62]. In contrast to the model used in Chapter 3, the frequency dependent transverse stiffness of the honeycomb sandwich panel is therefore modelled independently in the x- and y-directions using the formulations in Equations (3.3) to (3.6)(b). The anisotropic behaviour of the honeycomb panel is modelled using a formulation given by Blevins [63], where the natural frequencies are expressed with the formula:

$$\omega_{m,n} = \frac{\pi^2}{\sqrt{m''}} \sqrt{D_x \left(\frac{G_m}{l_x}\right)^4 D_y \left(\frac{G_n}{l_y}\right)^4 + \frac{2J_m J_n + 2\nu(H_m H_n - J_m J_n)}{(l_x l_y)^2} \alpha \sqrt{D_x D_y}}. \quad (5.1)$$

In the above equation, the parameters G, J and H depend on the mode order in x and y-directions, denoted by m and n respectively, and the boundary conditions [47, 48] (see Appendix A). The parameter α is adjusted to give good agreement between predicted and measured natural frequency for the [rocking, rocking] mode of the panel when it is freely suspended [61].

As in the simulation studies in Chapter 3, the modeshapes in the $x-$ and y-directions are considered to be those of an equivalent thin homogeneous beam with pinned boundary conditions, which gave the best agreement with the measured responses of the honeycomb panel mounted in the test frame [see Appendix E, Section E.1.2]. For a sandwich panel the bending stiffnesses D_x and D_y are frequency-dependent and need to be evaluated at $\omega = \omega_{m,n}$. A Regular-Falsi root search algorithm [49] is employed to estimate the panel natural frequencies that satisfy the relationship

$$0 = \omega^2 - \frac{\pi^4}{m''}\left(D_x(\omega)\left(\frac{G_m}{l_x}\right)^4 D_y(\omega)\left(\frac{G_n}{l_y}\right)^4 + \frac{2J_mJ_n + 2\nu(H_mH_n - J_mJ_n)}{(l_xl_y)^2}\alpha\sqrt{D_x(\omega)D_y(\omega)}\right). \tag{5.2}$$

The honeycomb sandwich panel considered in this study comprises two face plates which are made from three plies of carbon reinforced resin. The faceplates are bound to the core honeycomb structure, which is made from fibreglass-reinforced Phenolic Honeycomb (HRP) with a cell size of 3/8 inch.

The principal structural parameters of the panel where estimated in an experimental study when the panel was freely suspended in a test frame. A shaker with attached force gauge was used to excite the panel at a corner location. A laser vibrometer was used to measure the panel point mobility and a 24x18 uniform grid of panel transfer mobilities. The test panel response along the x- and y-axis was analysed by identifying isolated beam-like modes from the grid of measured transfer mobilities. This also gave the specific sequence of panel modes. Knowledge of the panel geometry, manufacturer material specifications, experimental natural frequencies and modes allowed to the parameters to be determined using the anisotropic sandwich panel model described above.

The simulated response for a panel with all sides free gave good agreement with the measured structural response of the honeycomb panel in the observed frequency range up to 5000 Hz. Further details on the panel model and the experimental studies on the freely supported honeycomb panel are provided in Appendix D. The cross-section geometry and the material parameters used to model the honeycomb panel are summarised in Table 5.2. The panel dimensions are the same as those of the aluminium panel specified in Table 5.1.

Table 5.2: Cross-section geometry and physical parameters for the honeycomb sandwich test panel.

Parameter	Symbol	Value	Unit
x-dimension	l_x	477	mm
y-dimension	l_y	381	mm
Thickness of face plate	h_f	0.86	mm
Core depth	d	23.09	mm
Mass density face plates	ρ_f	1250	kg m^{-3}
Mass density core	ρ_c	96	kg m^{-3}
Panel mass per unit area[1]	m''	4.28	kg m^{-2}
Young's modulus face-plates x-axis	E_x	48	GPa
Young's modulus face-plates y-axis	E_y	43	GPa
Shear modulus core x-axis	G_x	82	MPa
Shear modulus core y-axis	G_y	155	MPa
Poisson's ratio face plates	ν_f	0.33	–
Poisson's ratio sandwich plate	ν	0	–
Loss factor	η	0.015	–
Anisotropic factor	α	0.035	–

[1] $m'' = 2h_f\rho_f + (d - h_f)\rho_c$

5.1.2 Wavenumbers

Figure 5.2 shows the spectra of the propagating bending wavenumbers of the aluminium panel and the propagating transverse wavenumbers of the honeycomb panel in the x- and y-direction. Figure 5.2 also shows the spectra of the acoustic wavenumber in air and the convective wavenumber for the TBL disturbance, with the parameters specified in Table 2.3. Note that in contrast to Figure 3.3 the results circles and squares do not indicate wavenumber components of structural modes but only indicate the natural frequencies.

At low frequencies the wavenumbers of the honeycomb panel are dominated by the high bending stiffness of the sandwich cross-section and are hence much lower than that of the aluminium panel. At frequencies above 1000 Hz the transverse stiffness of the honeycomb panel is increasingly shear-controlled and the wavenumber in this region converges towards $k_s = \omega(m''/Gd)^{1/2}$ [19].

The acoustic critical frequency, where the acoustic wavelength equals the transverse wavelength of the panels, occurs at about 400 Hz for the honeycomb panel and at 7540 Hz for the aluminium panel. Assuming the TBL excitation with the parameters defined in Table 2.3, the convective coincidence occurs at about 56 Hz for the honeycomb panel (thus at very low audio frequency) and at about 1170 Hz for the aluminium panel (thus at mid audio frequency).

The squares and circles mark the resonance frequencies of the panels, which are estimated from the models described in Section 5.1.1. The fundamental resonance of the clamped aluminium panel occurs at 82 Hz, thus below the acoustic coincidence. Therefore there are many structural modes which do not radiate sound efficiently and which are also not efficiently excited by acoustic fields [19]. The predicted fundamental frequency of the honeycomb panel is 579 Hz and hence above the acoustic coincidence. Thus all structural modes of the honeycomb panel are efficient radiators of sound and are also efficiently excited by acoustic fields.

As discussed in Chapter 3, the response of a finite panel depends on the specific dimensions and boundary conditions (i.e. the specific natural frequencies of resonant modes) in relation to the excitation and radiation coincidence wavenumbers. Therefore all dimensions and boundary conditions are important for the prediction of the narrow band sound transmission through a finite panel. For example, a honeycomb panel with larger dimensions than the panel considered here, may have resonant modes at frequencies below the acoustic critical frequency these would be characterised by lower excitation and radiation efficiencies. However such a panel would also have a higher number of structural modes per unit frequency bandwidth. It is therefore possible that specific modes will resonate around coincidence, which may result in high excitation sensitivity and radiation efficiency in that frequency band, depending on where exactly these modes are.

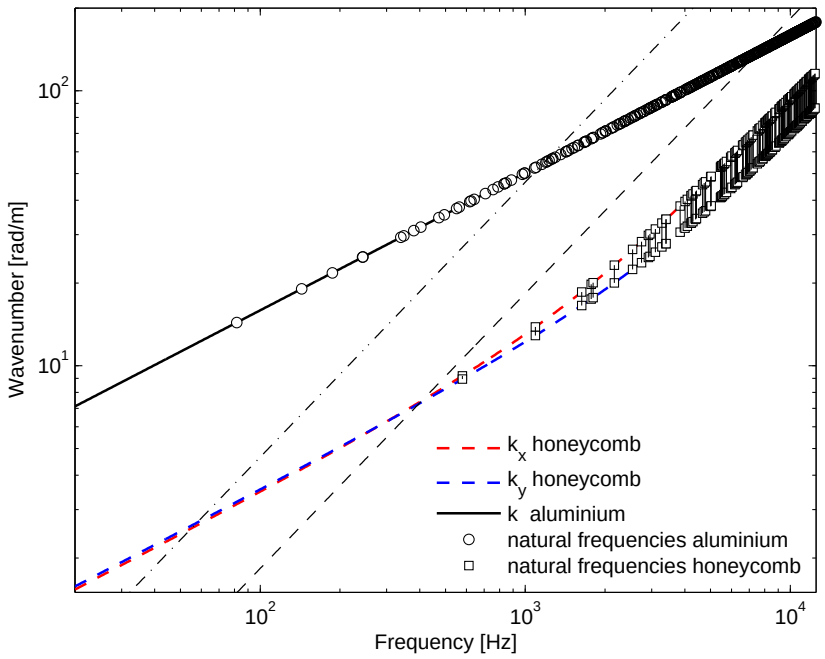

Figure 5.2: Predicted dispersion curves of the propagating transverse wavenumber and resonant frequencies of the aluminium and honeycomb test panels (see legend in graph), acoustic wavenumber in air ($faint-dashed$) and convective wavenumber ($faint-dash-dotted$).

5.1.3 Modal density and modal overlap

As discussed in Chapter 3 the modal density of the thin aluminium panel is constant with frequency as, shown in Figure 5.3(a). Due to the higher panel surface area, the modal density of the aluminium test panel is 0.0362 [per Hz] and therefore 2.66 times higher than that of the aluminium panel considered in the simulation studies in Chapter 3. As for the smaller panel, there is a good general agreement but high variability between the statistical modal density calculated from Equation (3.8) and the specific density of resonant modes along the frequency axis.

As for the sandwich panel considered in Chapter 3, the modal density of the honeycomb test panel, shown in Figure 5.3(b) is frequency-dependent and increases with frequency. This is because above 1000 Hz the response of the honeycomb panel is increasingly shear controlled. However, the modal density of the honeycomb panel remains below that of the aluminium panel over the entire observed frequency range between 0 and 6400 Hz. There is a good agreement between the modal densities estimated from Equations (3.9) and (3.10) and the specific density of resonant modes along the frequency axis. It should be noted that the modal densities of the honeycomb panel were calculated using equivalent isotropic Young's and Shear moduli, $E = \sqrt{E_x E_y}$ and $G = \sqrt{G_x G_y}$ respectively.

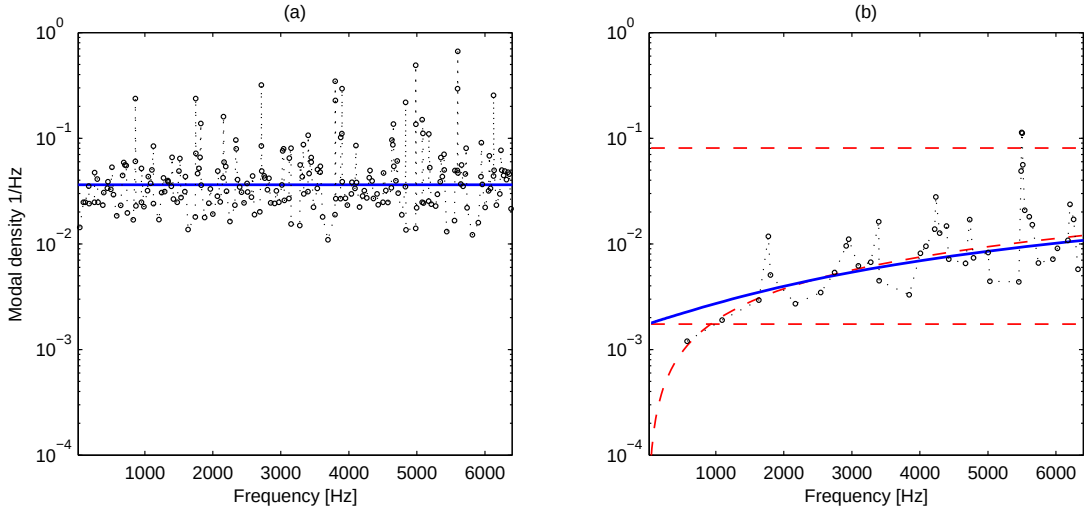

Figure 5.3: Modal density for (a) the thin homogeneous aluminium panel and (b) the honeycomb sandwich panel. Modal density ($solid\ line$), asymptotic limits for sandwich panel ($faint-dashed\ lines$) and specific density of resonant panel modes ($dotted\ line\ with\ circles$).

The modal overlap factor of the two panels is shown in Figure 5.4. The modal overlap factor for the aluminium panel exceeds unity for frequencies above 1390 Hz. At low frequencies, the modal overlap factor for the honeycomb panel is much lower than that of the aluminium panel and only exceeds unity for frequencies above 6290 Hz which is at the upper end of the observed frequency range.

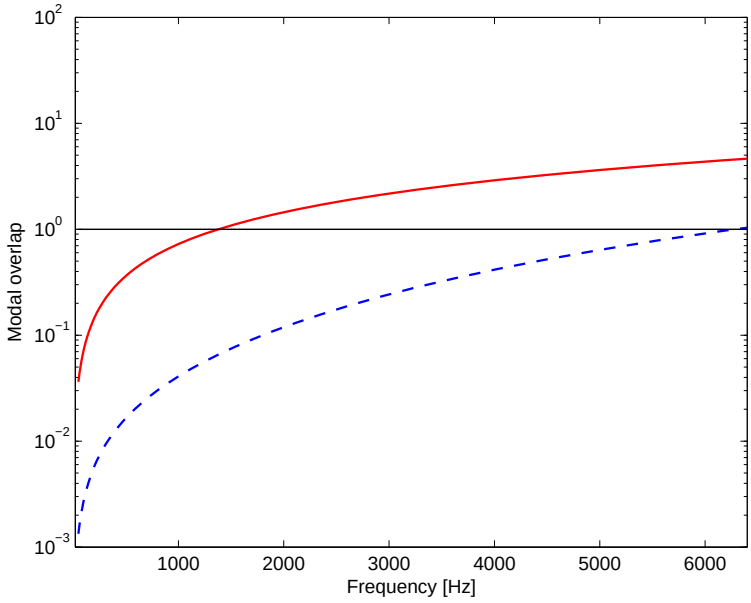

Figure 5.4: Modal overlap factor for the thin homogeneous aluminium panel ($solid$) and for the honeycomb sandwich panel ($dashed$).

5.2 Simulation studies on decentralised velocity feedback AVC with practical control units

This Section presents simulation results for the stability and control performance of a control system with five decentralised velocity feedback loops, as shown in Figure 5.5(a), when installed on the thin aluminium and honeycomb sandwich panels introduced in Section 5.1. The panel response and far field radiated sound power due to a point force excitation and an acoustic plane wave (APW) excitation with θ=45° are estimated using the elemental approach as described in Chapter 2.

As indicated in the block diagram in Figure 5.5(b), the control loops are modelled in terms of the open or closed loop base impedance $\tilde{Z}_a$ which is applied to the structure where the control units are mounted. First the model parameters are specified and then the results of the simulation studies for the two panels are compared with respect to control stability and performance.

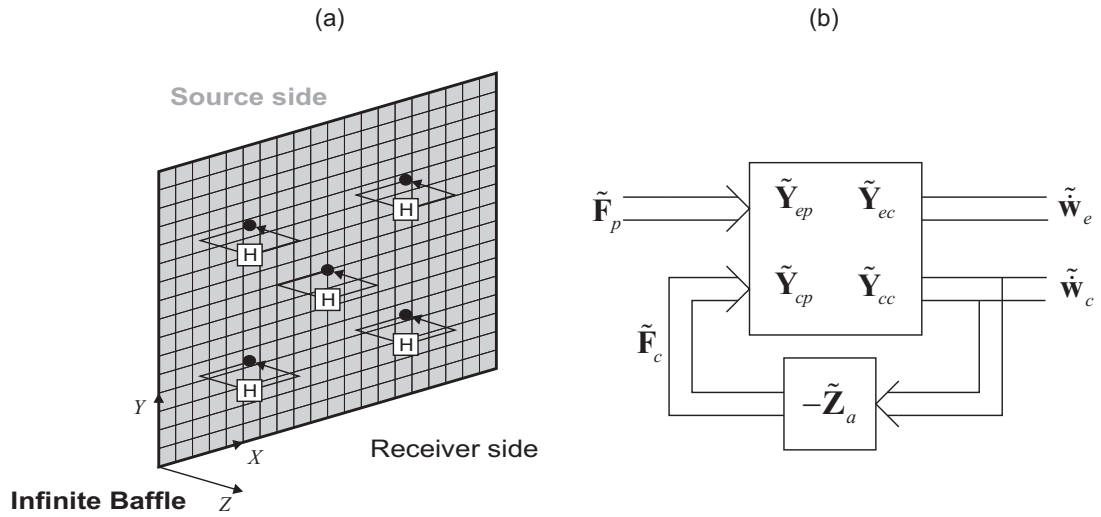

Figure 5.5: (a) Schematic view of the five channel decentralised velocity feedback control system mounted on the panels and (b) corresponding block diagram.

5.2.1 Model parameters

The two panels are modelled using the parameters specified in Section 5.1. As discussed before, the simulations have been carried out assuming that the aluminium panel is clamped on all edges and the honeycomb sandwich panel is pinned on all edges. As shown in Figure 5.6, the element grid was chosen to consist of 20 elements along the x-axis and 16 elements along the y-axis of the panels. This resembles the measurement grid for the laser vibrometer scans in the experimental studies presented in Section 5.3. This grid density satisfies a spatial resolution of at least two elements per transverse wavelength on the panels at the highest frequency of interest, which is 6400 Hz. Simulations with a higher element resolution showed that the chosen grid yields reliable results with a negligible overestimation of the spectra at the upper end of the observed frequency range.

In this study modes with natural frequency up to five times the observed frequency range were considerd in the model of the panels, where modes up to twice the observed frequency range (up to 12.4 kHz) were considered as dynamic modes with their stiffness damping and mass parts and modes between twice and five times the observed frequency (up to 32 kHz) were considered as residual modes with stiffness and damping parts only (see Appendix A). For the aluminium panel a total of 1097 modes were included in the model, 427 dynamic and 670 residual. For the honeycomb panel a total of 955 modes were included in the model, 165 dynamic and 790 residual.

As shown in Figure 5.6, one of the five control loops is placed in the centre of the panel while the other four are arranged symmetrically on the panel diagonals. The exact locations of the control loops and the position of the primary point force excitation are shown in Figure 5.6 and specified in Table 5.3. The control loops are implemented in terms of the open or closed loop base impedances of the control units, which are applied to the structure where the control units are mounted. As indicated in the block diagram in Figure 5.5, the diagonal matrix of base impedances $\tilde{\mathbf{Z}}_a$ replaces the feedback gain matrix $\tilde{\mathbf{H}}$ in the formulations given in Chapter 2. The impedance formulations that describe the response of the feedback loops are those for voltage and current-driven control units with proof-mass electrodynamic actuator and practical feedback controller FRF as specified in Section 4.3. In this study a uniform feedback gain is considered, i.e. the same gain is applied to all five feedback loops.

Table 5.3: Control point (CP) coordinates and primary excitation (PE) location on the test panels.

	PE	CP1	CP2	CP3	CP4	CP5
x [mm]	101	347	347	130	130	238.5
y [mm]	240	277	104	104	277	190.5

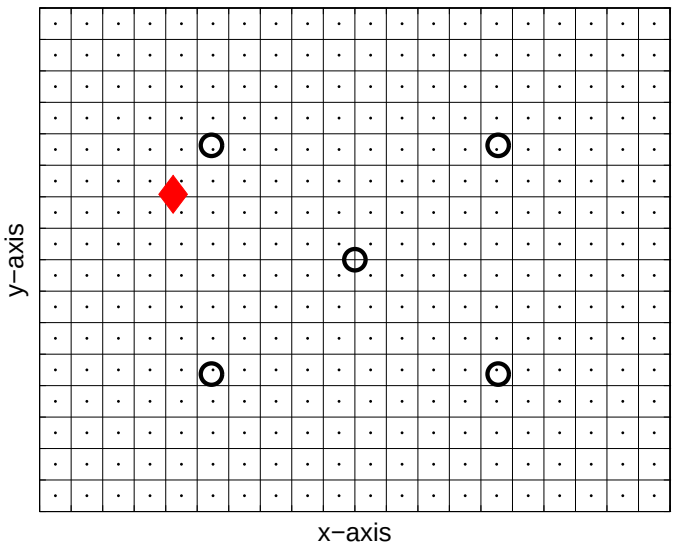

Figure 5.6: Sketch of panel with element grid, control points ($circles$) and primary excitation location ($diamond$).

5.2.2 Stability analysis

Open loop frequency response functions

In order to analyse the stability of the control system, the open loop frequency response functions (OL-FRFs) of the control system are calculated in frequency range between 10 Hz and 25600 Hz. In order to assess the stability of the individual feedback loops, the OL-FRFs $\tilde{H}_{11}$, $\tilde{H}_{22}$, $\tilde{H}_{33}$, $\tilde{H}_{44}$ and $\tilde{H}_{55}$ of the five feedback loops are analysed. The OL-FRFs functions for control units with current-driven control units are given by

$$\tilde{H}_{I_{ii}} = \frac{\tilde{Y}_{c_{ii}}\,\tilde{C}\,\Psi\left(1-\frac{\tilde{Z}_s}{\tilde{Z}_{m_2}+\tilde{Z}_s}\right)}{1+\tilde{Y}_{c_{ii}}\left(\tilde{Z}_s+\tilde{Z}_{m_1}-\frac{\tilde{Z}_s^2}{\tilde{Z}_{m_2}+\tilde{Z}_s}\right)}, \tag{5.3}$$

where g is the applied feedback gain, $\tilde{C}$ is the gain-normalised controller FRF, and Ψ is the voice coil coefficient. Also $\tilde{Z}_s = c_s + k_s/(j\omega)$, $\tilde{Z}_{m_1} = j\omega m_1$ and $\tilde{Z}_{m_2} = j\omega m_2$ are the actuator suspension, base mass and proof mass impedances as before. The corresponding formulation for the OL-FRFs functions for control units with voltage-driven control units are given by

$$\tilde{H}_{U_{ii}} = \frac{\tilde{Y}_{c_{ii}}\,\tilde{C}\,\frac{\Psi}{\tilde{Z}_e}\left(1-\frac{\tilde{Z}_s+\frac{\Psi^2}{\tilde{Z}_e}}{\tilde{Z}_{m_2}+\tilde{Z}_s+\frac{\Psi^2}{\tilde{Z}_e}}\right)}{1+\tilde{Y}_{c_{ii}}\left(\tilde{Z}_s+\tilde{Z}_{m_1}+\frac{\Psi^2}{\tilde{Z}_e}-\frac{\left(\tilde{Z}_s+\frac{\Psi^2}{\tilde{Z}_e}\right)^2}{\tilde{Z}_{m_2}+\tilde{Z}_s+\frac{\Psi^2}{\tilde{Z}_e}}\right)}, \tag{5.4}$$

where $\tilde{Z}_e = R_e + j\omega L_e$ is the electrical impedance of the voice coil. The parameters used to model the actuators were summarised in Table 4.1. These expressions are derived in Appendix C. To guarantee stability for an individual control loop, the OL-FRF must not encircle the Nyquist stability point at (-1,0j) [13].

Aluminium panel: Figures 5.7 and 5.8 show (a) the Bode diagrams and (b) Nyquist plots of the OL-FRFs $\tilde{H}_{11}$ to $\tilde{H}_{55}$ for the feedback control loops on the aluminium panel. Figure 5.7 corresponds to current control and Figure 5.8 to voltage control. Only two curves are visible in each plot because the control positions 1, 2, 3 and 4 are located symmetrically with respect to the centre of the panel, and therefore yield identical simulation results.

Considering first the case of current driven control actuators in Figure 5.7, it can be seen that the control loops are only conditionally stable due to the presence of circles in the left

half-plane. The gain margins for the control loops are limited by the 180° phase shift which is due to the actuator fundamental resonance in combination with the FRF of the feedback controller. At low frequencies this produces a circle on the left half-plane of the Nyquist plot so that the feedback loops would become unstable when the feedback gains are increased beyond the stable gain margin.

Even if small control gains that guarantee stability are implemented, the part of the OL-FRFs that falls within the unit circle around the Nyquist stability point at (-1,0j) results in an enhancement of the structural response in that frequency band. This effect is known as low frequency control spillover [13, 19].

For frequencies above the actuator resonance frequency, the circles of the OL-FRFs migrate into the right half-plane quadrants of the Nyquist plot. This indicates that, for frequencies well above the fundamental resonance frequency of the actuator, the velocity feedback loops reduce the structural response of the panel by means of active damping. The magnitudes of the circles indicate how efficiently the response of the structural modes is attenuated at the corresponding resonance frequencies.

At very high frequencies the circles of the OL-FRFs migrate back into the left half-plane of the Nyquist plot. In this frequency range the magnitudes of the OL-FRFs are very small compared with that of the low frequency circle due to the actuator fundamental resonance; hence these parts of the OL-FRFs do not pose stability limits. Control spillover effects in this high frequency band occur, although they are of smaller amplitude than that around the fundamental resonance of the actuator.

For the case of voltage-driven control actuators in Figure 5.8, the feedback loops are also only conditionally stable. As discussed above, the gain margins for the control loops are limited by the 180° phase shift around the actuator fundamental resonance. The Bode diagram in Figure 5.8(a) shows that compared with the current-controlled feedback loops, the resonant peak around the actuator fundamental resonance frequency is more highly damped due to the back electromotive force (back emf) effect. At very high frequencies the phase and magnitude of the OL-FRFs roll off at a higher rate than those of the current-controlled feedback loops shown in Figure 5.7. Therefore the circles of the OL-FRFs migrate more rapidly back into the left half-plane of the Nyquist plot and multiple loops of the OL-FRFs cross the negative real axis in the frequency range between 3000 and 4000 Hz.

The differences between voltage- and current-driven control units can be readily explained by the differences between the blocked force spectra for voltage- and current-driven control actuators, as discussed in Section 4.1. The blocked force produced by the control actors for 1 V input voltage is considerably lower than that for 1 A input current.

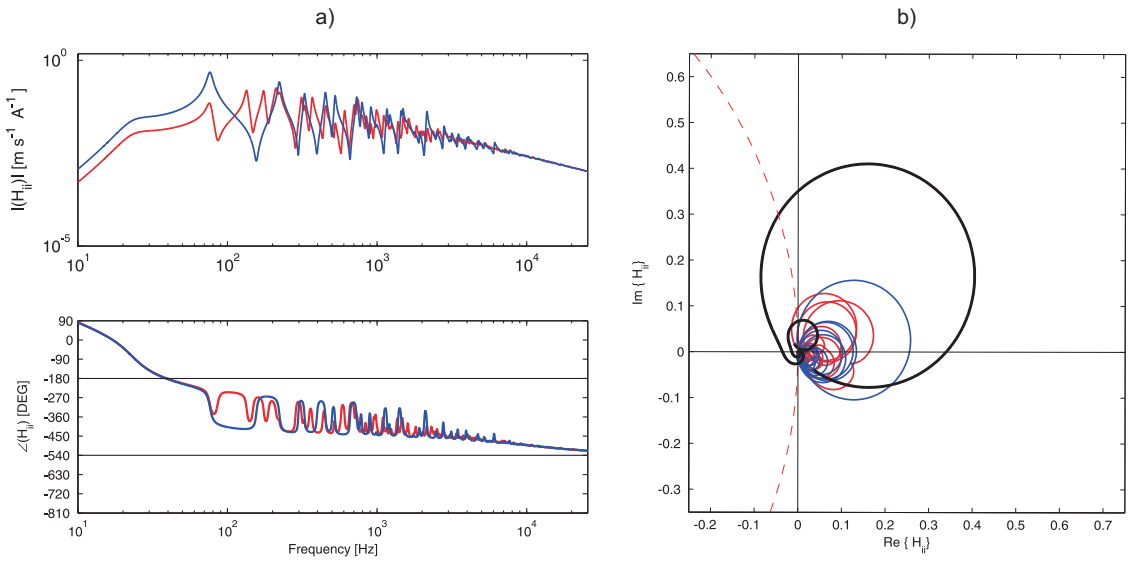

Figure 5.7: Simulated OL-FRFs of the **current**-controlled feedback loops on the **aluminium** panel. Thick solid lines in the Nyquist plot mark the FRFs in the frequency range from 0 Hz to 100 Hz and the (*dashed*) line marks the unit circle around the Nyquist stability point.

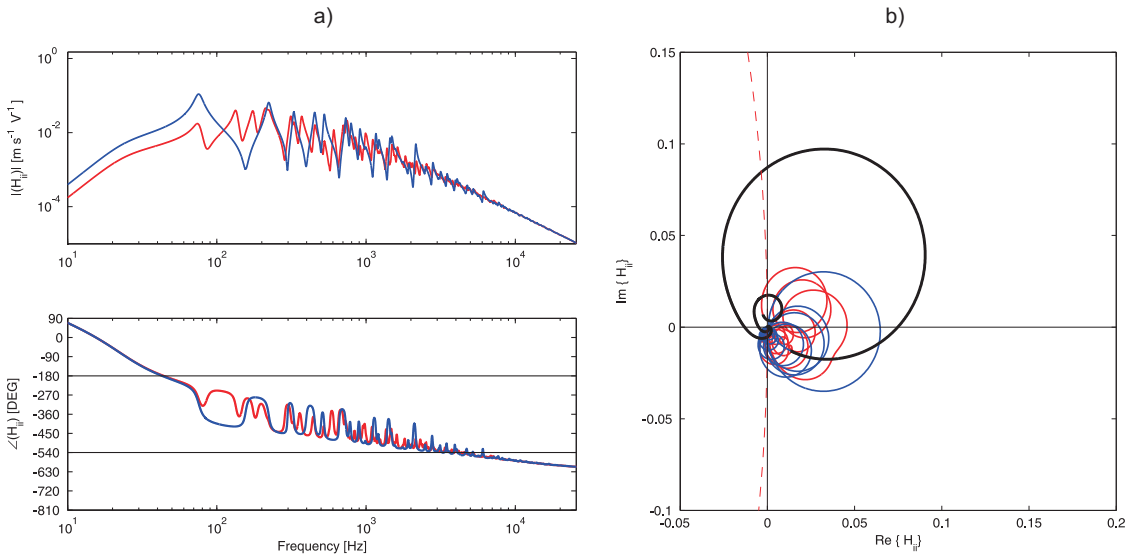

Figure 5.8: Simulated OL-FRFs of the **voltage**-controlled feedback loops on the **aluminium** panel. Thick solid lines in the Nyquist plot mark the FRFs in the frequency range from 0 Hz to 100 Hz and the (*dashed*) line marks the unit circle around the Nyquist stability point.

Honeycomb panel: Figures 5.9 and 5.10 show (a) the Bode diagram and (b) the Nyquist plots of the OL-FRFs $\tilde{H}_{11}$ to $\tilde{H}_{55}$ for the feedback control loops on the honeycomb panel. Considering first the case of current-driven control actuators in Figure 5.9, it can be seen that the OL-FRFs of the feedback loops on the honeycomb panel show the same 180° phase shift around the actuator fundamental resonance frequency and the resulting low frequency circle in the left half-plane of the Nyquist plot. However, compared with the OL-FRFs of the feedback loops on the aluminium panel in Figure 5.9, in this frequency range the magnitudes of the OL-FRFs of the feedback loops on honeycomb panel are very low and hence allow for high gain margins. This is because the first panel mode is much higher in frequency than the actuator resonance.

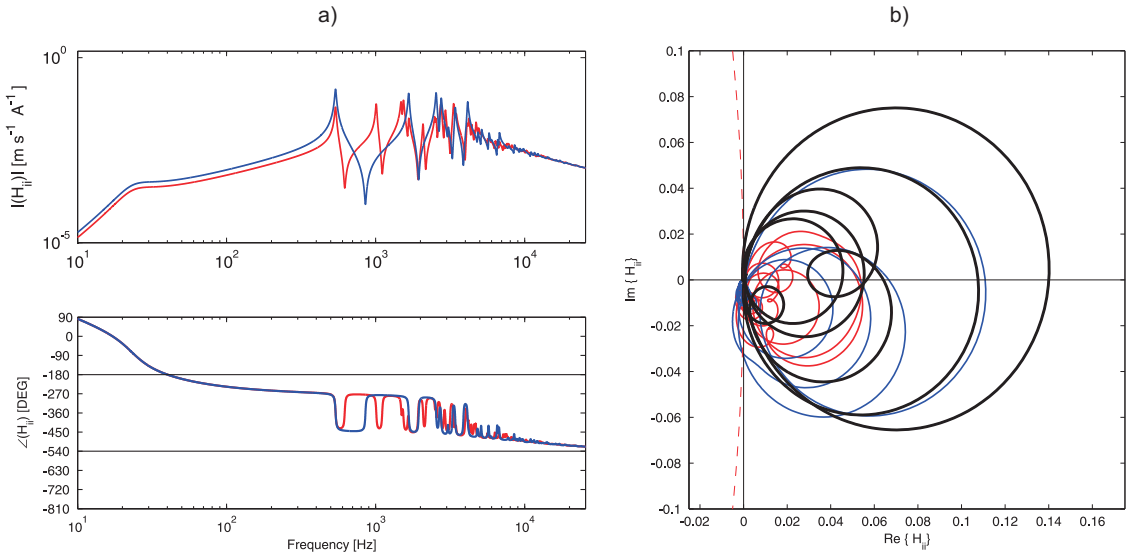

Figure 5.9: Simulated OL-FRFs of the **current**-controlled feedback loops on the **honeycomb** panel. Thick solid lines in the Nyquist plot mark the FRFs in the frequency range from 0 Hz to 2000 Hz and the (*dashed*) line marks the unit circle around the Nyquist stability point.

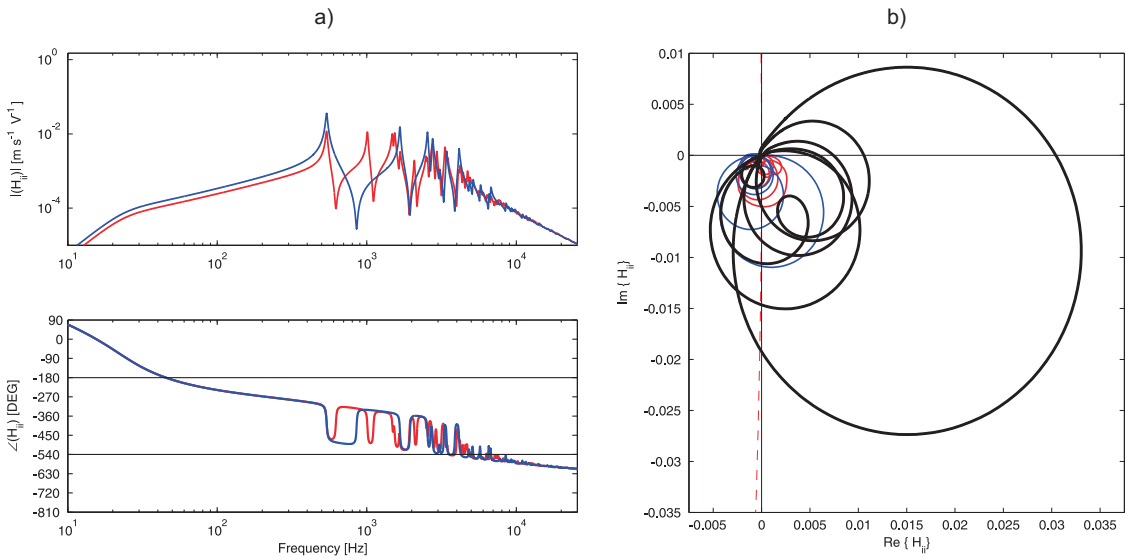

Figure 5.10: Simulated OL-FRFs of the **voltage**-controlled feedback loops on the **honeycomb** panel. Thick solid lines in the Nyquist plot mark the FRFs in the frequency range from 0 Hz to 2000 Hz and the (*dashed*) line marks the unit circle around the Nyquist stability point.

For the case of voltage-driven control actuators in Figure 5.10, the resonant peak around the actuator fundamental resonance frequency is more highly damped due to the back electromotive force (back emf) effect. At very high frequencies the Bode diagram in Figure 5.10(a) shows that the phase and magnitude of the OL-FRFs roll off at a more rapid rate than that of the current-controlled feedback loops. Therefore the circles of the OL-FRFs migrate more rapidly back into the left half-plane of the Nyquist plot and cross the negative real axis in the frequency range between 3000 and 4000 Hz. In this frequency range the magnitude of the OL-FRFs has not yet rolled off significantly since it is controlled by the low order resonant modes of the honeycomb panel. Therefore the maximal stable feedback gain is given by these high frequency circles of the OL-FRFs in the left half-plane of the Nyquist plot.

Table 5.4 summarises the stable gains for the two panels with voltage- and current-driven feedback loops. In the cases where the feedback gain is limited by the actuator resonance, and the resulting low frequency loops in the left half-plane of the Nyquist plots, it is the OL-FRF $\tilde{H}_{55}$ of the feedback loop located in the centre of the panel that limits the maximal feedback gain. This is because the feedback loop of the control unit located in the centre of the panels experiences the highest velocity response of the fundamental bending mode of the panels. For the aluminium panel the maximal stable gain for current-controlled feedback loops is 28 while that for voltage-driven feedback loops is 76. As discussed in Chapter 4, this can be explained by the difference in the blocked force response of the actuator due to input voltage and input current. For the honeycomb panel, the maximal feedback gains are significantly higher than for the aluminium panel. For the current-controlled feedback loops, the maximal gain is 2134. For the voltage controlled feedback loops, the maximal gain is 642, due to the high frequency circles of the OL-FRFs on the left hand side quadrants of the Nyquist plot. The maximal stable feedback gain for the low frequency loop around the actuator fundamental resonance in isolation is 6215 and would therefore be much higher.

Table 5.4: Maximal stable feedback gain of the feedback loop located in the centre of the panels.

Panel	Maximal stable feedback gain	
	Current	Voltage
Aluminium panel	28 *	76 *
Honeycomb panel	2134 *	642** 6215*

* limit due to response around actuators fundamental resonance.

** limit due to high frequency spillover.

System eigenvalues

As discussed by Gonzalez Diaz et al. [45, 33, 34] and Baumann and Elliott [64], the stable gain margin for a feedback control system with multiple proof-mass electrodynamic actuators reduces with increasing number of feedback loops. This is due to cross-talk, i.e. cross excitation effects between the actuators. Hence, to assess the stability of the multiple input multiple output (MIMO) control system with five decentralised control loops, it is necessary to evaluate the eigenvalues of the fully populated [5×5] matrix of OL-FRFs between the output of the five control sensors and the actuator input signals,

$$\begin{bmatrix} \tilde{H}_{1,1} & \tilde{H}_{1,2} & \tilde{H}_{1,3} & \tilde{H}_{1,4} & \tilde{H}_{1,5} \\ \tilde{H}_{2,1} & \tilde{H}_{2,2} & \tilde{H}_{2,3} & \tilde{H}_{2,4} & \tilde{H}_{2,5} \\ \tilde{H}_{3,1} & \tilde{H}_{3,2} & \tilde{H}_{3,3} & \tilde{H}_{3,4} & \tilde{H}_{3,5} \\ \tilde{H}_{4,1} & \tilde{H}_{4,2} & \tilde{H}_{4,3} & \tilde{H}_{4,4} & \tilde{H}_{4,5} \\ \tilde{H}_{5,1} & \tilde{H}_{5,2} & \tilde{H}_{5,3} & \tilde{H}_{5,4} & \tilde{H}_{5,5} \end{bmatrix}. \tag{5.5}$$

Expressions for the OL-FRFs matrices $\tilde{\mathbf{H}}_I$ and $\tilde{\mathbf{H}}_U$ for current- and voltage-control are derived in Appendix C. To guarantee stability, the eigenvalues of the OL-FRF matrix must satisfy the generalised Nyquist stability criterion [13]. For each frequency the eigenvalues of the OL-FRF matrix are calculated using the MatLab command eig. However, this does not yield the matrix eigenvalues in a consistent order, so that it is necessary to sort the resulting eigenvalues with respect to the eigenvectors to yield five consistent open loop frequency eigenvalue functions (OL-FEVF).

Figures 5.11 and 5.12 show (a) the Bode diagrams and (b) the Nyquist plots with the eigenvalues of the fully populated OL-FRF matrices for installation on the aluminium panel. Figure 5.11 shows the results for current-driven feedback loops and Figure 5.12 for voltage driven feedback. In contrast to the plots of the OL-FRF in Figures 5.7 and 5.8, the OL-FEVF exhibit five curves, each representing one of the system eigenvalue functions. The results exhibit similar characteristics to the OL-FRFs for the individual feedback loops. However, the loops are slightly expanded, which results in a decrease in the stable gain margin.

The eigenvalue functions of the control system on the honeycomb panel are shown in Figures 5.13 and 5.14. These also show similar effects to the corresponding OL-FRFs in Figures 5.9 and 5.10. As discussed above, the circles of the OL-FEVFs are inflated which results in lower gain margins.

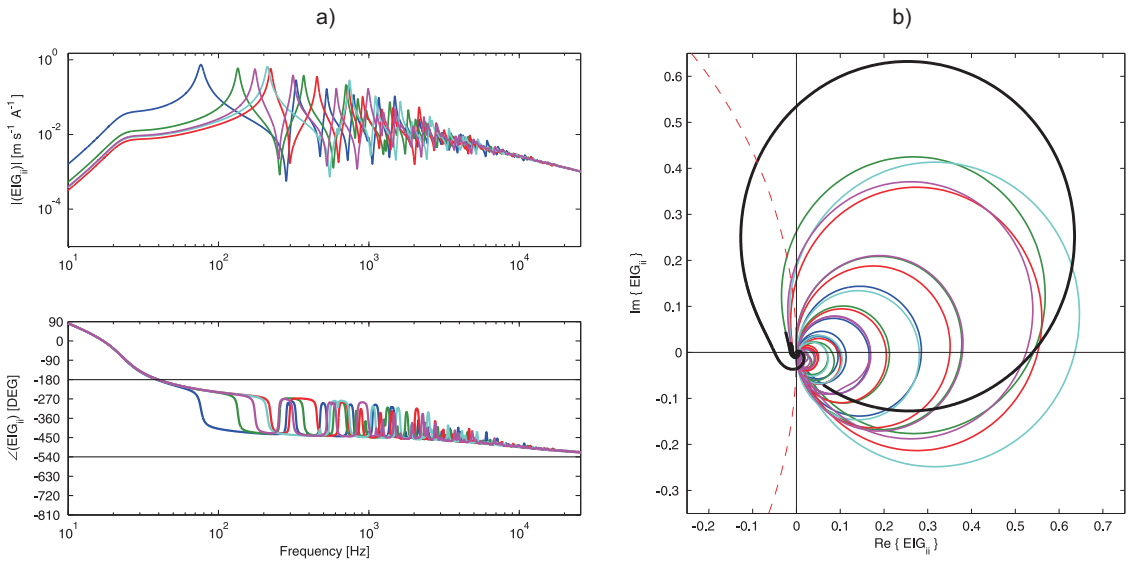

Figure 5.11: Simulated Eigenvalues of the OL-FRFs of the control system with **current**-controlled feedback loops on the **aluminium** panel. Thick solid lines in the Nyquist plot mark the FRFs in the frequency range from 0 Hz to 100 Hz and the (*dashed*) line marks the unit circle around the Nyquist stability point.

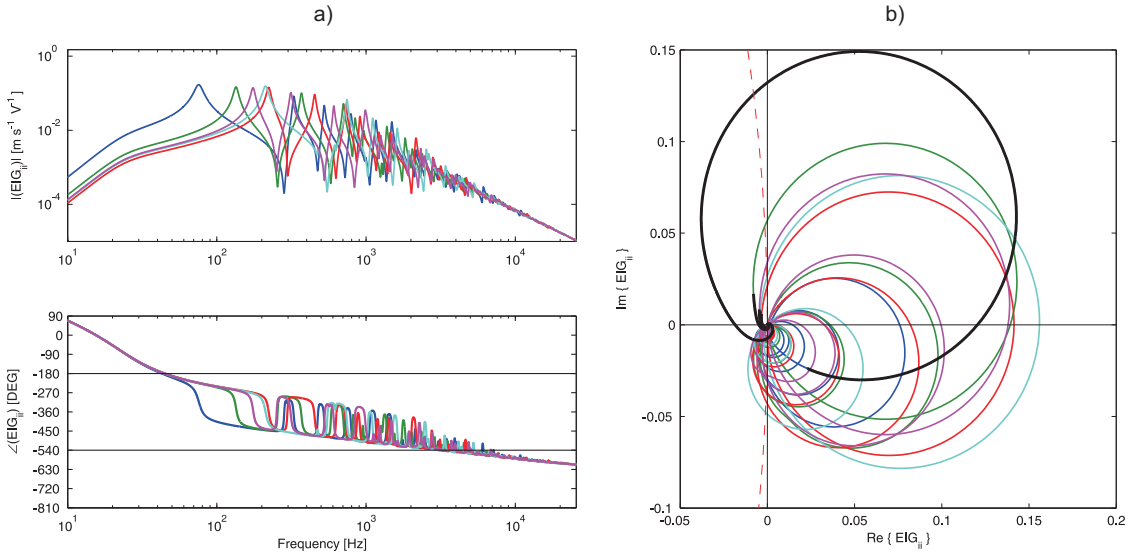

Figure 5.12: Simulated Eigenvalues of the OL-FRFs of the control system with **voltage**-controlled feedback loops on the **aluminium** panel. Thick solid lines in the Nyquist plot mark the FRFs in the frequency range from 0 Hz to 100 Hz and the (*dashed*) line marks the unit circle around the Nyquist stability point.

Table 5.5 summarises the maximal stable gains for the control system on the two panels for both current- and voltage-driven feedback loops. The system stability is limited by the OL-FEVF that forms the largest circle crossing the negative real axis in the Nyquist plot. For the results shown on the aluminium panel the system gain for current-controlled feedback loops is reduced by 28.5% and that for voltage driven feedback loops is reduced by about 30%. For the honeycomb panel the system gain for the current-controlled feedback loops is reduced by 42% and for voltage-controlled feedback loops the gain is reduced by 26.5%, for the high frequency gain limit and by 42% for the low frequency gain limit.

Table 5.5: Maximal stable uniform feedback gains for the control system.

Panel	Maximal stable uniform feedback gain	
	Current	Voltage
Aluminium panel	20 *	53 *
Honeycomb panel	1244*	471** 3620*

* limit due to response around actuators fundamental resonance.

** limit due to high frequency spillover.

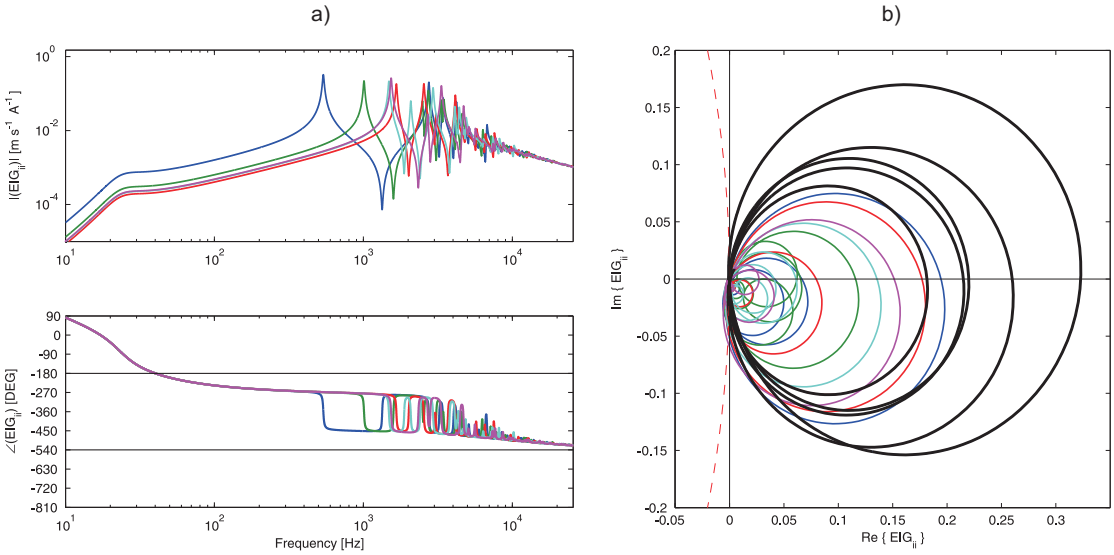

Figure 5.13: Simulated Eigenvalues of the OL-FRFs of the control system with **current**-controlled feedback loops on the **honeycomb** panel. Thick solid lines in the Nyquist plot mark the FRFs in the frequency range from 0 Hz to 2000 Hz and the (*dashed*) line marks the unit circle around the Nyquist stability point.

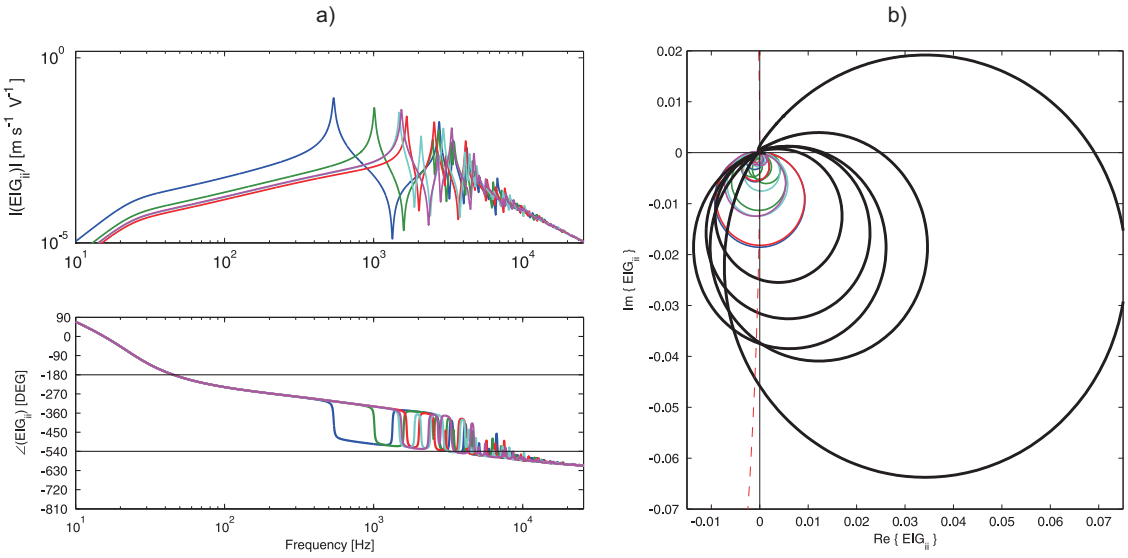

Figure 5.14: Simulated Eigenvalues of the OL-FRFs of the control system with **voltage**-controlled feedback loops on the **honeycomb** panel. Thick solid lines in the Nyquist plot mark the FRFs in the frequency range from 0 Hz to 2000 Hz and the (*dashed*) line marks the unit circle around the Nyquist stability point.

5.2.3 Control performance

The performance of the control system is assessed considering control units with current-driven actuators and a controller with a practical FRF as given in Equation (4.3). This closely represents the practical control system investigated in the experimental study presented in the next part of this chapter. The response of the panel, without control units, to a point force excitation and to a plane wave excitation with θ=45° and φ=45°, is calculated using Equation (2.5). The response with decentralised velocity feedback control units is calculated using Equation (2.43). The panel kinetic energy and total sound power radiated are then calculated using Equations (2.11) and (2.14) respectively. The panel dimensions, control locations and the coordinates of the primary point force excitation are those shown in Figure 5.6 and specified in Table 5.3.

Point force

Figure 5.15 shows the predicted panel kinetic energy and radiated sound power for the aluminium panel (left hand side) and the honeycomb panel (right hand side) for point force excitation. Considering first the plain panels, without control units, the kinetic energy spectra for both panels, shown in Figures 5.15(a) and (b), are characterised by a set of well separated resonances of low order modes of the panels; those of the aluminium panel occur between the fundamental resonance at 82 Hz and about 500 Hz, while those of the honeycomb panel occur between the fundamental resonance at 579 Hz and about 2000 Hz. Above these two frequency bands, the kinetic energies of the two panels are characterised by smoother spectra since, as discussed in Section 5.1.3, the number of modes significantly excited at any one frequency, i.e. the modal overlap factor, increases with frequency. The spectrum of the honeycomb panel kinetic energy shows a dip between 3000 Hz and 3800 Hz, which is due to the location of the force position relative to the edge and also due to the uneven frequency distribution of resonance frequencies of the anisotropic honeycomb panel. For frequencies below 4000 Hz the kinetic energy of the plain aluminium panel is much higher than that of the plain honeycomb panel. Above 4000 Hz the response of aluminium and honeycomb panel are of comparable level.

Considering next the sound radiation from the aluminium and honeycomb plain panels, shown in Figures 5.15(c) and 5.15(d), in contrast to the result for the kinetic energy, above the fundamental resonance frequency at 579 Hz the honeycomb panel sound radiation levels

are slightly higher than those for the aluminium panel. This is due to the fact that, as discussed in Section 5.1, the two panels have significantly different radiation efficiencies for low and mid audio frequencies. The aluminium panel is characterised by many resonant modes at low and mid audio frequencies (the fundamental resonance is at 82 Hz) which, however, poorly radiate sound below the acoustic coincidence frequency at 7544 Hz. In contrast the honeycomb panel is characterised by comparatively fewer modes at low and mid audio frequencies (the fundamental resonance is at 579 Hz), which on the other hand efficiently radiate sound since they all resonate above the acoustic coincidence frequency at around 400 Hz.

Figure 5.15 also shows the predicted responses and sound radiation spectra of the two panels with open and closed loop velocity feedback. The mass effect of the open loop control units shifts down the resonance frequencies of the low order modes of the panels. Also, passive damping effects of the open loop control units reduce the amplitude of the resonant peaks over a wide frequency band. The amplitudes of low order resonances are reduced by up to 15 dB for the aluminium panel and up to 7 dB for the honeycomb panel.

For the aluminium panel, when the feedback loops are closed with progressively higher control gains, 10 to 15 dB additional reductions of both kinetic energy and radiated sound power are predicted in the frequency range from 50 Hz to 300 Hz. In the frequency region between 30 and 50 Hz, as the feedback gains are increased the panel response and radiated sound power are enhanced, since, as discussed in Chapter 4, the control units insert power into the structure rather than absorbing it from the structure. This effect is normally reported as low frequency control spillover. As discussed in Section 5.2.2, the response of the control units around the actuator fundamental resonance frequency results in a conditionally stable MIMO feedback control system, which is stable only up to a maximal feedback gain.

For the honeycomb panel, when the feedback loops are closed with progressively higher control gains, 20 to 30 dB additional reductions of both kinetic energy and radiated sound power are predicted in the frequency range from 400 Hz to 2000 Hz. Below 400 Hz the honeycomb panel response is stiffness-controlled and drops rapidly with decreasing frequency. As a result, there is nearly no low frequency control spillover produced by the actuators.

Figure 5.16 shows the broad-band reductions in panel kinetic energy and radiated sound power for a range of feedback gains, which are set to be uniform over all feedback loops. Both the results for the aluminium and the honeycomb panel show a typical performance curve with a single control optimum [23, 19].

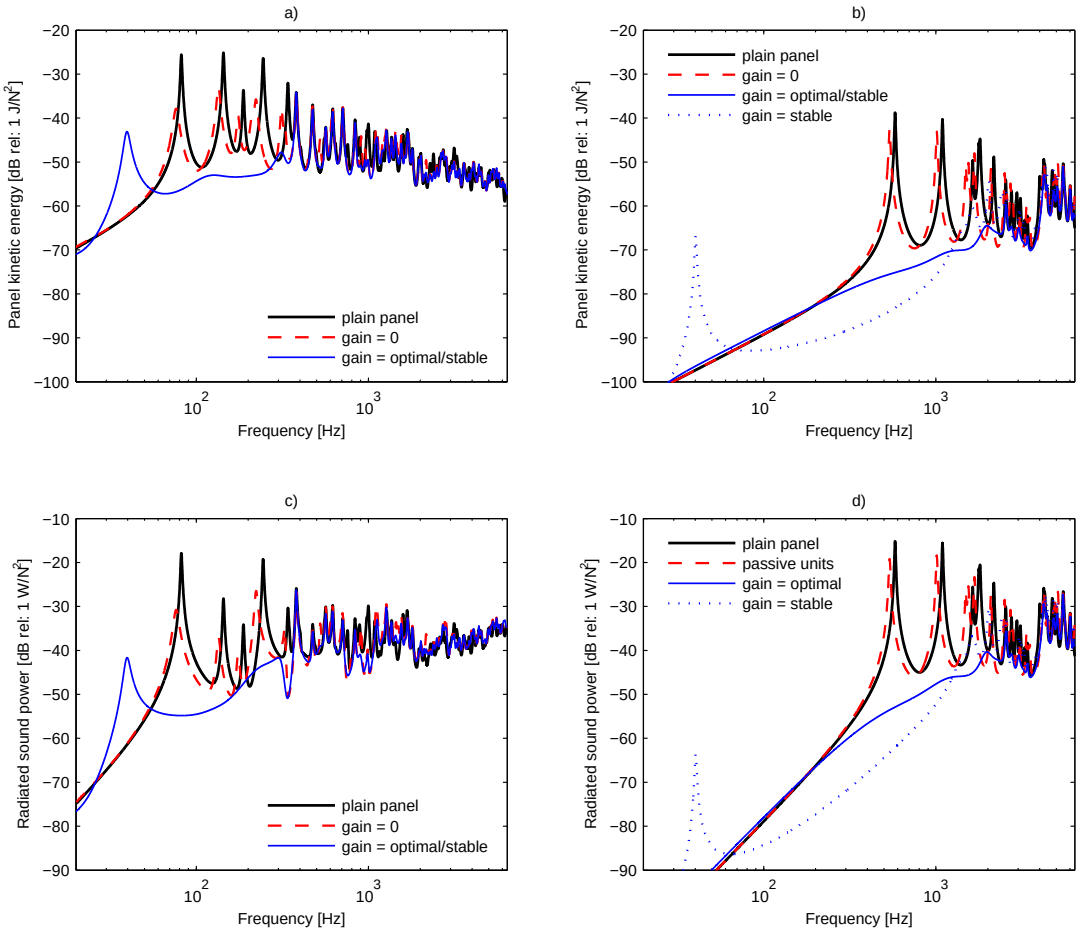

Figure 5.15: Predicted panel responses and radiated sound powers for **point force excitation**. Aluminium panel left hand side, honeycomb panel right hand side; panel kinetic energy top row, radiated sound power bottom row.

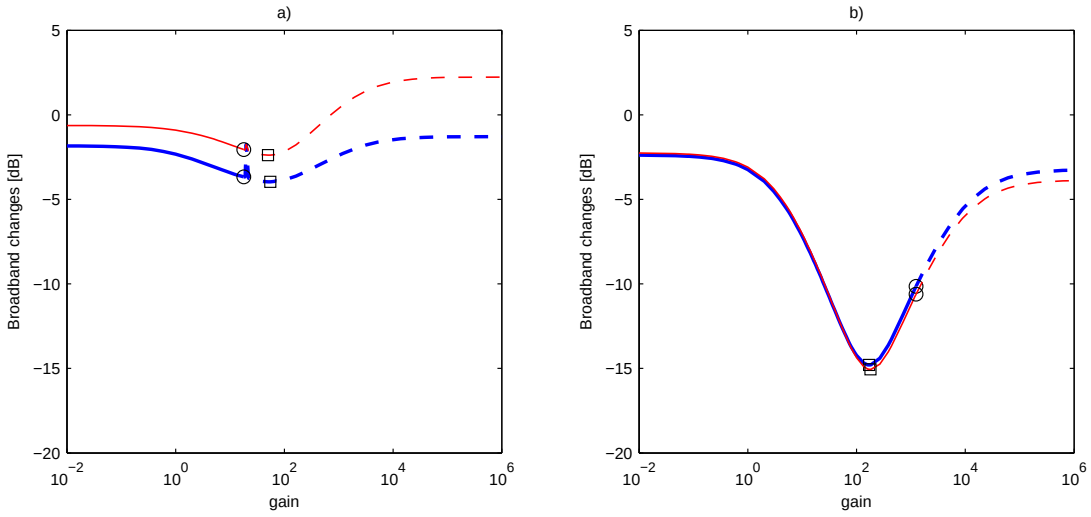

Figure 5.16: Predicted changes in broad band panel responses and radiated sound power for **point force excitation**. (a) aluminium panel and (b) honeycomb panel. Panel kinetic energy ($solid$) and radiated sound power ($faint$). Gain of highest reductions ($squares$) and maximal stable stable gain ($circles$)

The plot in Figure 5.16(a), for the aluminium panel, shows that the reductions achieved in panel kinetic energy are larger than those in radiated sound power. This is because not all resonant modes are efficient radiators of sound. Reduction in the response of non-radiating modes contribute the overall reduction in kinetic energy but not to the reduction of radiated sound power. Also as shown in Figure 5.15(c) the efficiently radiating modes occur at high frequencies where feedback control is not effective.

The results also show that the control system becomes unstable for lower gains than those that would produce optimal control performance. The results in Figures 5.15(a) and (c) are those for the optimal/stable uniform feedback gain of 14 that can be applied to the control units when installed on the aluminium panel. This gain is chosen to be slightly lower than the maximal stable gain, given in Table 5.5, since the control system with maximal stable uniform feedback gain produces already produces high low frequency control spillover.

The plot in Figure 5.16(b), for the honeycomb panel, shows that the broad-band reductions of kinetic energy and radiated sound power produced by the decentralised control system are similar to each other. This is because all modes of the honeycomb panel resonate at frequencies above the acoustic coincidence frequency, so that all resonant modes radiate sound efficiently. A reduction of the response of any mode therefore contributes similarly to the broad-band reduction of kinetic energy and radiated sound power. The plots also show that the control optimum is achieved for feedback gains which are below the maximum stable gain of the control system (see Table 5.5). Therefore in Figures 5.15(b) and (d) the response spectra for both optimal and maximum stable feedback control gains are shown. When the maximum stable feedback control gains are applied, significant low frequency spillover effects are produced by the control system.

For the aluminium panel, only relatively small broad-band reductions of the response and radiated sound power are achieved. This is because the low frequency control spillover between 30 and 50 Hz counter-balances the active control reductions between 50 and 300 Hz. Significantly higher broad-band reductions, up to 15 dB, are achieved on the honeycomb panel since the low frequency spillover effects produced by the control units are small for the optimal gain.

Acoustic plane wave

Figure 5.17 shows the predicted panel kinetic energy and radiated sound power for the aluminium panel (left hand side) and the honeycomb panel (right hand side) excited by an acoustic plane wave with θ=45° and φ=45°. The spectra of the kinetic energy and radiated sound power of the plain panels are similar to those shown in corresponding plots for the point force excitation in Figure 5.15. However, for the aluminium panel the spectra are characterised by a smaller number of well-separated resonances. This is due to the fact that the distributed acoustic field does not efficiently excite all low order modes of the aluminium panel, even modes having a lower radiation efficiency. In contrast all modes of the honeycomb panel are well excited due to its low acoustic coincidence frequency. The spectra for both panels tend to roll off at a higher rate as the frequency rises. This is because the excitation strength of the acoustic wave tends to decrease with rising frequency.

Comparing the plots in Figure 5.15 and Figure 5.17, it is noted that for both panels the narrow-band effects produced by the control units with open and closed feedback loops are very similar for both point force and acoustic plane wave excitations.

Figure 5.18 shows the broad-band reductions of panel kinetic energy and radiated sound power for a range of feedback gains, set uniform for all feedback loops. The results for both the aluminium and the honeycomb panel show a typical performance curve with a single control optimum. In contrast to the broad-band reductions for the point force excitation in Figure 5.18, much higher reductions are achieved for the plain wave excitation, particularly on the aluminium panel. This is because the spectra are dominated by the responses of low order structural modes which are efficiently reduced by means of active damping, produced by the velocity feedback loops.

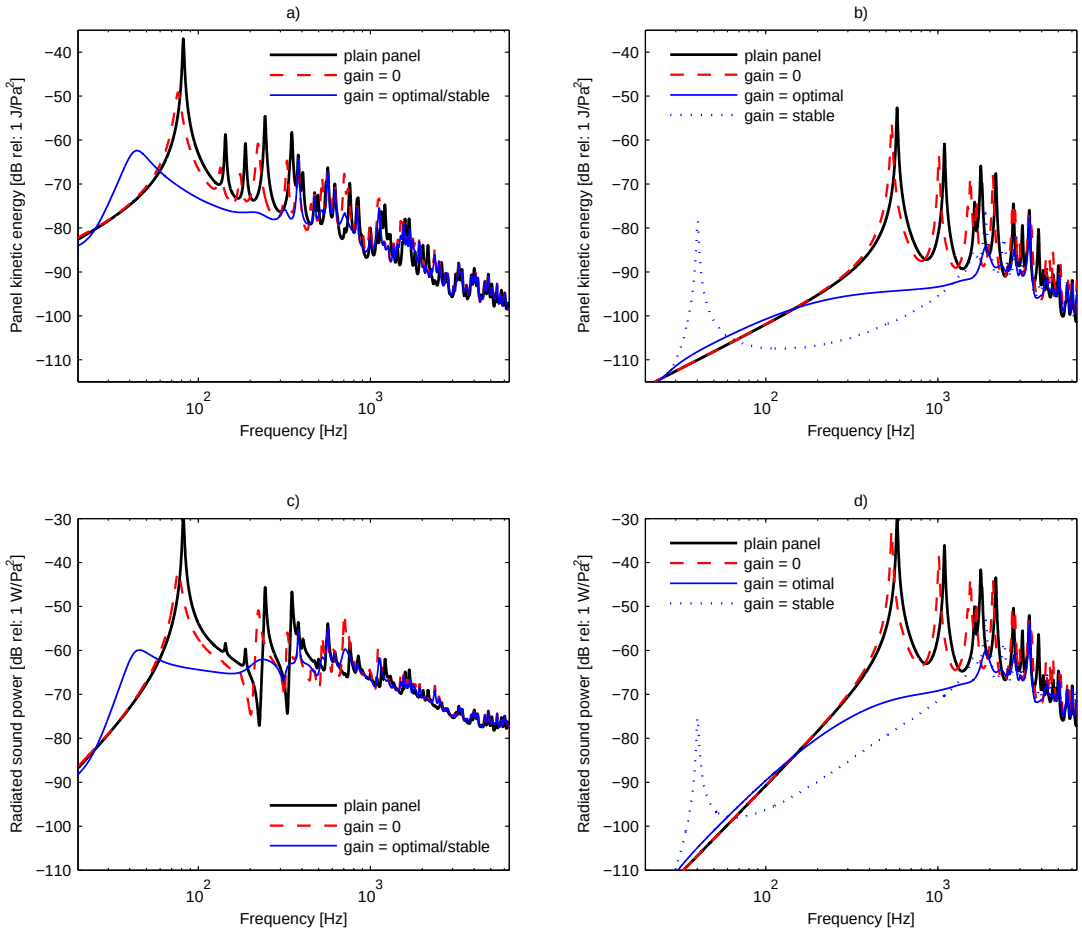

Figure 5.17: Predicted panel responses and radiated sound powers for **APW 45° excitation**. Aluminium panel left hand side, honeycomb panel right hand side; panel kinetic energy top row, radiated sound power bottom row.

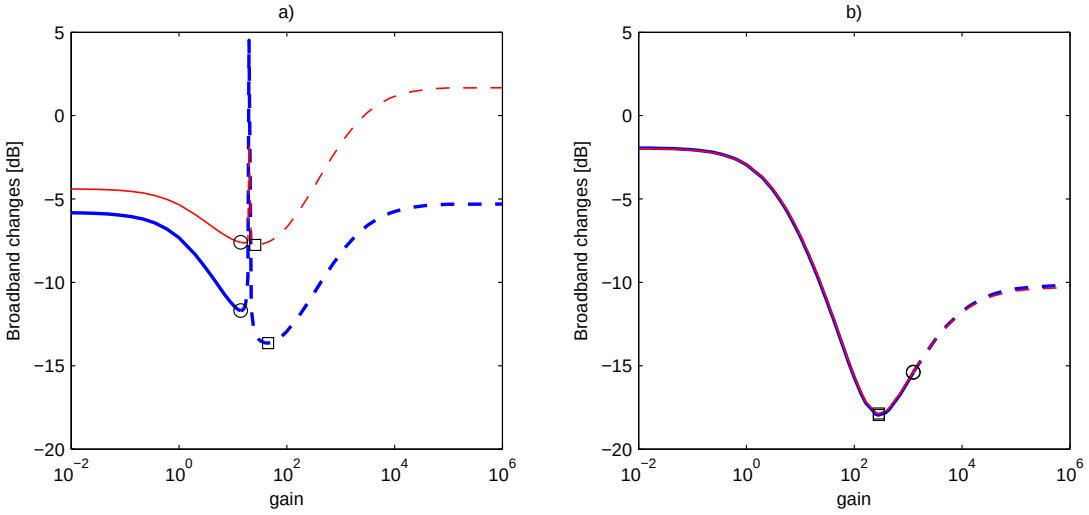

Figure 5.18: Predicted changes in broad band panel responses and radiated sound power for **APW 45° excitation**. (a) aluminium panel and (b) honeycomb panel. Panel kinetic energy ($solid$) and radiated sound power ($faint$). Gain of highest reductions ($squares$) and maximal stable stable gain ($circles$)

Stochastic excitation

Figure 5.19 shows the simulation results for the structural response and radiated sound power of both panels for ADF and TBL stochastic disturbances. For comparison the results for APW, which have been given in Figure 5.17 are also presented in Figures 5.19(a) and (b). The results plotted with continuous lines are those for the plain aluminium and the plain honeycomb panels. The results plotted with dashed lines are those for the panels with closed feedback control loops. The results for the aluminium panel with control are those for optimal/stable feedback gains of 14. The results the honeycomb panel with control for acoustic APW and ADF disturbances are those for feedback gains of 255. The results for the TBL disturbance are those for feedback gains of 180.

The results for the stochastic ADF and TBL disturbances on the honeycomb panel have not been simulated for as many values of feedback gain as the deterministic APW and point force excitations. However, the results presented correspond closely to optimal control performance. It should also be noted that the number of elements in the y-direction of the panel has been increased from 16 to 55 for simulations with TBL excitation. This is to guarantee at least three elements per convective wavelenght at 6400 Hz, i.e. $\Delta_y \leq \lambda_{conv}/3$.

The panel responses and radiated sound power for all types of excitation reflect the specific excitation characteristics discussed in Chapter 3 and also the specific structural dynamics and radiation characteristics of the two test panels discussed in the previous sections of this chapter. The response characteristics of the two panels to acoustic excitation have already been discussed. However, the simulation results for the response of the panels to TBL excitation gives interesting new results.

For the honeycomb panel the convective coincidence frequency occurs at 56 Hz, well below the fundamental resonance frequency at 579 Hz. Therefore none of the structural modes of the panel are excited at coincidence. As shown in Figure 5.19(e), the structural response of the honeycomb panel to TBL excitation is therefore lower than that of the aluminium panel over the entire observed frequency range, particularly around the convective coincidence of the aluminium panel which occurs at 1169 Hz. Above the honeycomb panel fundamental resonance frequency the radiated sound power spectra of the two plain panels, shown in Figure 5.19(f), exhibit relatively similar levels. The results with closed feedback loops indicate that for TBL excitation the panel response and radiated sound power of the honeycomb panel could be significantly reduced below the levels of the aluminium panel over a wide range of mid audio frequencies.

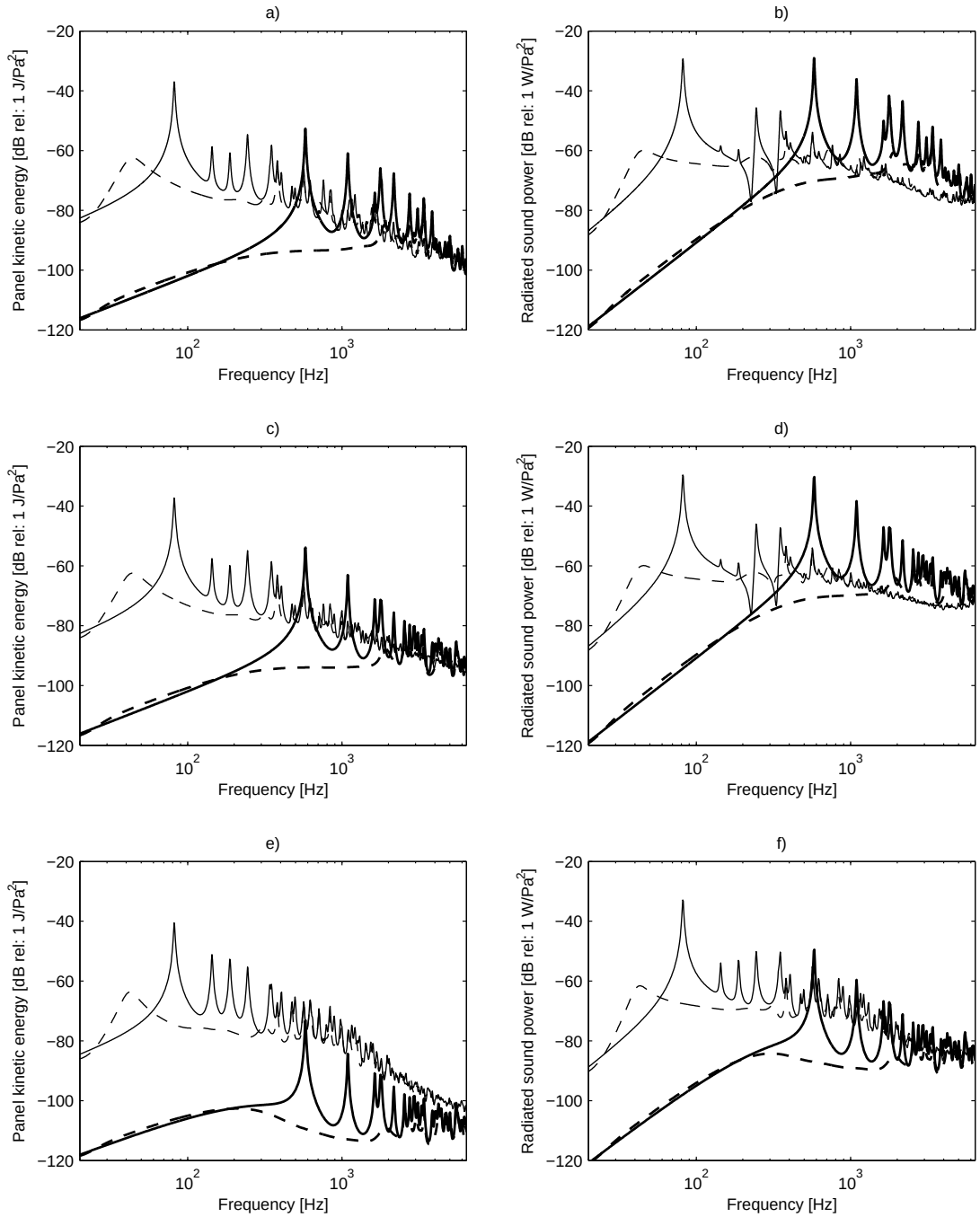

Figure 5.19: Panel kinetic ($left-column$) and radiated sound power ($right-column$) from the aluminium panel ($faint$) and the honeycomb panel ($thick$) without active control ($solid$) and with active control using current controlled actuators and optimal/stable feedback gain ($dashed$). For APW (θ=45°) ($top-row$) , ADF ($centre-row$) and TBL ($bottom-row$) excitation.

The results of this study also highlight that, in contrast to the maximum stable feedback gain, which only depends on the control units and panel coupled dynamics, the optimal control gain is also a function of the specific excitation and radiation characteristics of the panels. As previously discussed in Section 3.4, the optimal feedback gain therefore varies with changes in the excitation characteristics. During operation a vehicle may go through specific operation cycles, e.g. landing, climb, cruise, approach and landing of an aircraft or other variations such as changes in speed. It seems desirable therefore to develop a control

system with adaptive (possibly self-sensing and tuning) feedback loops that can optimise the feedback gain in order to achieve optimal control reductions. This idea seems to be more promising for the application on a stiff honeycomb panel than on a thin aluminium panel since the results in this study indicate that the optimal feedback gain for the control system on the honeycomb panel can be significantly lower than the stability limits.

In addition to the simulations carried out in this study, more investigations should be conducted to investigate the possibility to optimise further the control stability and performance by applying individual non-uniform feedback gains to each feedback loop. Also the possibility should be investigated to enhance the stability of the single feedback loops by modifying the frequency response function of the feedback controller with appropriate compensator circuits that can shift the actuator fundamental resonance towards lower frequencies.

5.3 Experimental studies

This section presents results of experimental studies on the control stability and active control performance when a decentralised velocity feedback control system is mounted on a thin homogeneous aluminium panel and a stiff lightweight honeycomb sandwich panel. The properties of the panels are those described in Section 5.1. The control system is the MIMO decentralised feedback control system with five proof-mass electrodynamic-actuator sensor pairs that is described in Chapter 4.

5.3.1 Experimental set-ups

For the experimental studies, the aluminium and honeycomb panels were clamped in a test frame and placed in the window of a sound transmission suite, as shown in Figure 5.20. The edge dimensions of the panels in the test frame are l_x=477 mm, l_y=381 mm. The resulting boundaries for the honeycomb panel were found to be between pinned and clamped conditions. Also, it has been found that the aluminium panel was affected by in-plane loads due to in-perfect mounting conditions and panel curvature effects which shifted the measured resonance frequencies above those predicted for an ideal flat panel with clamped boundary conditions.

The five control actuators are mounted on the source side of the panels using a thin layer of adhesive wax. The control locations are those specified in Table 5.3. The accelerometer

sensors are mounted in the footprint of the control actuators on the opposite side of the panels (receiving side) also using a thin layer of adhesive wax. Together the five control units (excluding the controller) add a mass of 0.185 kg to the panels with a mass of 0.785 kg, which is an increase by 23.5%.

As shown in Figure 5.20, on the source side, the panels were excited (a) mechanically using a shaker and (b) by the direct acoustic field generated by a loudspeaker placed in front of the panels at about 80 cm distance. The excitation point for the shaker excitation is that specified in Table 5.3. In the case of shaker excitation the input force applied to the panel was measured and used as the reference excitation signal. For the acoustic excitation, the voltage input to the loudspeaker was measured and used as the reference excitation signal. The effects introduced by the loudspeaker and by the source room responses have been considered by correcting the measured responses on the receiver side of the panel with the magnitude of the transfer function between the loudspeaker input voltage and the spatially averaged sound pressure measured in close proximity to the panel surface on the source side.

Figure 5.20: Set-ups for shaker excitation (a) and loudspeaker excitation (b).

As shown in Figure 5.21(a), on the receiver side a laser vibrometer was used to measure the response of the panel on a grid of 16x20 points. The panel kinetic energy and radiated sound power are estimated from these measurement using the formulations for the 'elemental approach' described in Chapter 2. The panel is assumed to be subdivided into a uniform grid of elements and the grid of measured panel velocities represents the velocities at the centres of these elements. The panel kinetic energy and radiated sound power are then estimated using Equations (2.11) and (2.14) respectively.

As shown in Figure 5.21(b), the radiated sound power was also estimated from sound pressure measurements made on a hemispherical array with nine microphones under semi-anechoic conditions in the receiving room. The procedure employed followed those described in the relevant ISO standard [65]; it should be noted however that the receiving room used does not meet the strict standard requirements and that the chosen microphone arrangement is also different from that described in the ISO standard as the microphones are at a distance of only 60 cm from the centre of the panel.

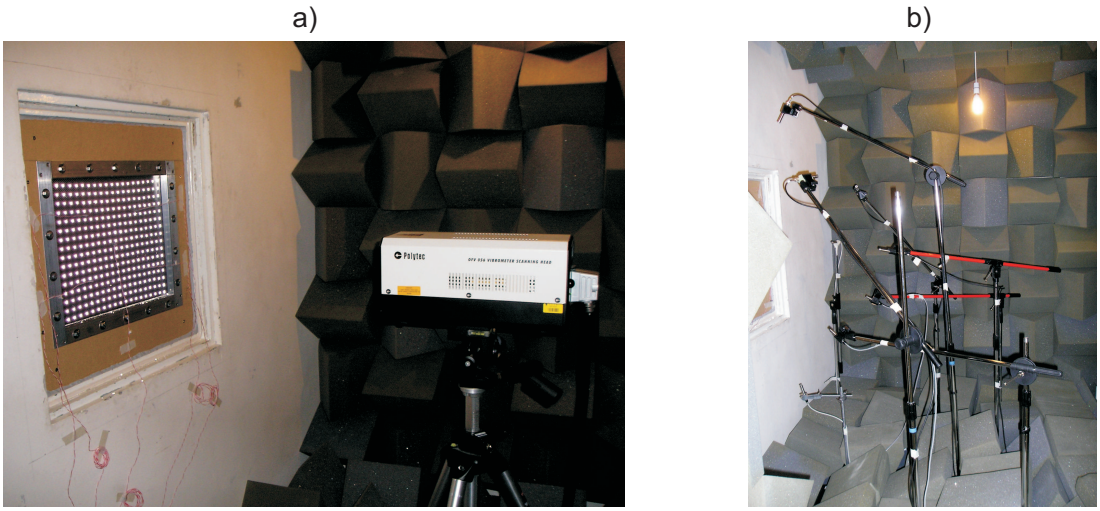

Figure 5.21: Set-up for (a) laser vibrometer measurements and (b) microphone array measurements.

The radiated sound power obtained from the laser vibrometer measurements and from the microphone array measurements were found to be in good agreement with each other. At frequencies below 250 Hz, the acoustic measurements were found to be slightly contaminated by the resonant response of the receiving room. This is an expected effect as the 30 cm deep foam wedges used to treat the surfaces in the receiving room are only efficient above about 250 Hz where the wedge depth exceeds a quarter of the acoustic wavelength. The laser vibrometer measurements are largely independent from any background noise or from the properties of the receiving room. Also the honeycomb panel was found to have a strong radiation directivity so that a sampling using nine microphones may not yield sufficient resolution. For this reason only the results from the laser vibrometer measurements are presented and discussed in the thesis. The results from the microphone measurements are presented in Appendix E, together with a more detailed description of the experimental arrangements.

5.3.2 Stability analysis

The stability of the control system is experimentally investigated by measuring the open-loop frequency response functions (OL-FRFs) between the voltage input to the integrator of each control channel and the five voltage outputs of the sensor signal conditioner. As discussed in Section 5.2.2, in order to guarantee stability of each control loop, the OL-FRF must not encircle the Nyquist instability point at (-1,0j) and to readily assess the stability of the MIMO control system with the five decentralised control loops the eigenvalues of the fully populated [5 $\times$ 5] matrix of OL-FRFs between the five input signals to each control channel and the five sensor output signals must satisfy the Nyquist stability criteria [13].

Open loop response functions:

To assess the stability of the control system, the gain for each control loop is normalised to guarantee a 6 dB gain margin, i.e. they are set to half the maximum stable gain. The OL-FRFs for the five channels of the control system when mounted on the aluminium panel and the honeycomb panel are shown in Figures 5.22 and 5.23 respectively.

As noted in the simulation study presented above, the gain margins for the control loops on the aluminium panel are limited by the actuator fundamental resonance, which for low frequencies produces a circle on the left half-plane of the Nyquist plot in Figure 5.22(b). The parts of the OL-FRFs that fall in the unit circle around the Nyquist stability point at (-1,0j) are expected to result in enhancement of the structural response in that frequency range, i.e. to cause control spillover.

For frequencies above the actuator resonance frequency, the circles of the OL-FRFs migrate into the right half-plane of the Nyquist plot. It is therefore expected that, for frequencies above the fundamental resonance frequency of the actuator, the velocity feedback loops reduce the structural response of the panel by means of active damping. The relatively large magnitudes of the circles in the right half-plane compared with that on the low frequency circle in the left half-plane of the Nyquist plot indicate that the response of low order structural modes of the aluminium panel are attenuated efficiently around their resonance frequencies.

At very high frequencies the circles of the OL-FRFs migrate back into the left half-plane of the Nyquist plot. In this frequency range the magnitudes of the OL-FRFs are very small compared with that of the low frequency circle due to the actuator fundamental resonance; hence these parts of the OL-FRFs do not pose stability limits, but are expected to cause

small control spillover effects at high frequencies.

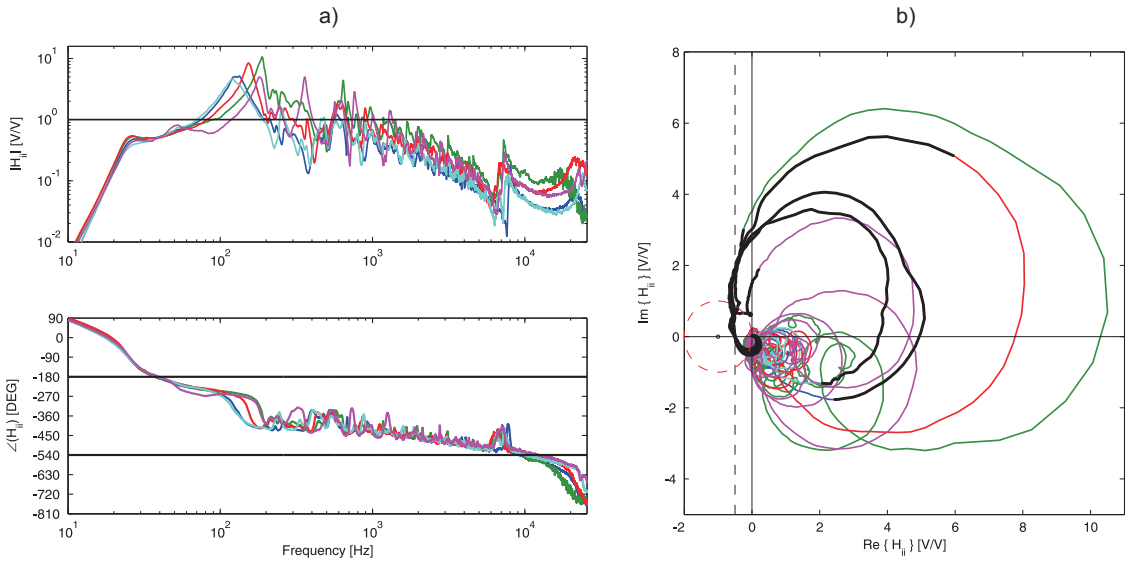

Figure 5.22: Open-loop FRFs of the control units on the aluminium panel. Thick solid lines in the Nyquist plot mark the FRFs in the frequency range from 0 Hz to 150 Hz and the ($dashed - red$) line marks the unit circle around the Nyquist stability point.

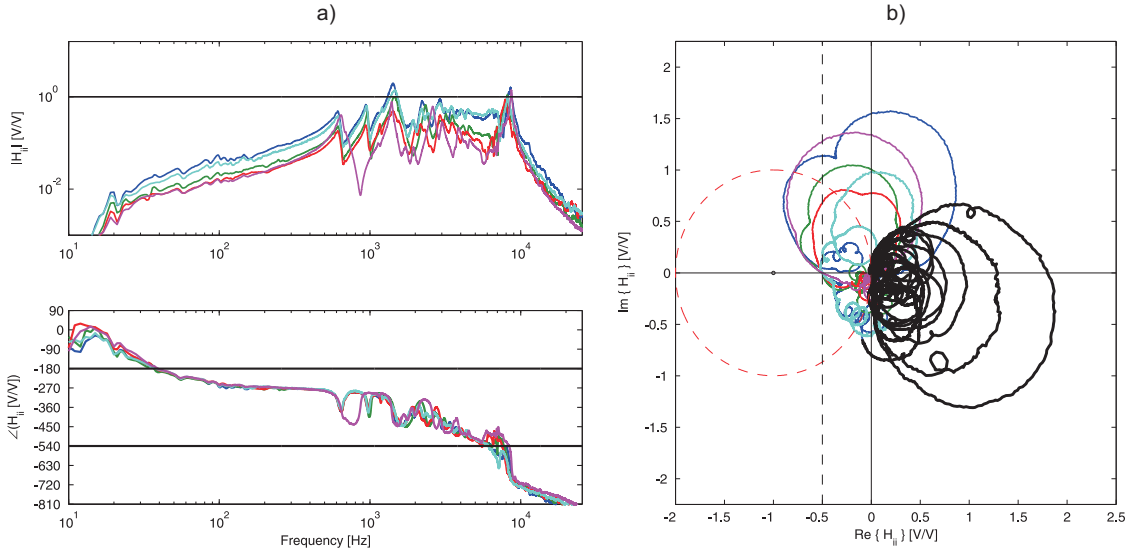

Figure 5.23: Open-loop FRFs of the control units on the honeycomb panel. Thick solid lines in the Nyquist plot mark the FRFs in the frequency range from 0 Hz to 3000 Hz and the ($dashed - red$) line marks the unit circle around the Nyquist stability point.

As noted in the simulation studies, the Nyquist plot of the OL-FRFs of the control loops on the honeycomb panel in Figure 5.23(b) shows the same low frequency circle on the left half-plane as those of the aluminium panel in Figure 5.22(b). The magnitudes of the OL-FRFs in this frequency range are very small and would hence allow for high gain margins. However, for frequencies above about 3000 Hz, the circles of the OL-FRFs with high magnitude migrate onto the left half-plane of the Nyquist plot and pose a more stringent limit on the gain margin of the control loops. Thus higher control spillover effects occur at these high frequencies than around the fundamental resonance of the actuator.

The Bode diagrams in Figures 5.22(a) and 5.23(a) with the OL-FRFs for the control system on both the aluminium and the honeycomb panel show resonance and anti-resonance behaviour in the frequency range between 7 kHz and 9 kHz. Those resonances occur in the same frequency range for both panels; it is therefore assumed that these resonances are specific to the control system. A comparison with measurement results in Chapter 4 strongly suggests that they are due to mounting resonances of the actuator and accelerometer units. For the control system on the honeycomb panel other high frequency problems at high frequencies may occur due to resonances of the honeycomb cross-section [66].

The results in Figures 5.22 and 5.23 correspond well to the simulation results for the control system with current-controlled feedback loops in Figures 5.7 and 5.9 respectively. The panel model with closed loop feedback control seems to capture all important features of the system except the control unit mounting resonances. For the control system on the honeycomb panel it is these mounting resonances that impose the stability limit of the system and for further studies different mounting methods rather than adhesive wax should be investigated.

Eigenvalues of open loop FRF matrix

Figures 5.24 and 5.25 show the eigenvalues of the fully populated OL-FRFs matrices for the control system mounted on the aluminium and honeycomb panels respectively. The results for the control system mounted on the aluminium panel given in the Nyquist plot in Figure 5.24(b) show the same low frequency characteristics as the OL-FRFs for the individual feedback loops in Figure 5.22. However, all circles are slightly inflated and the low frequency circle of one of the system eigenvalues crosses the negative real axis close to the Nyquist stability point. This shows that although all individual control loops have a gain margin of 6 dB, the resulting control system with five decentralised control loops is only just stable.

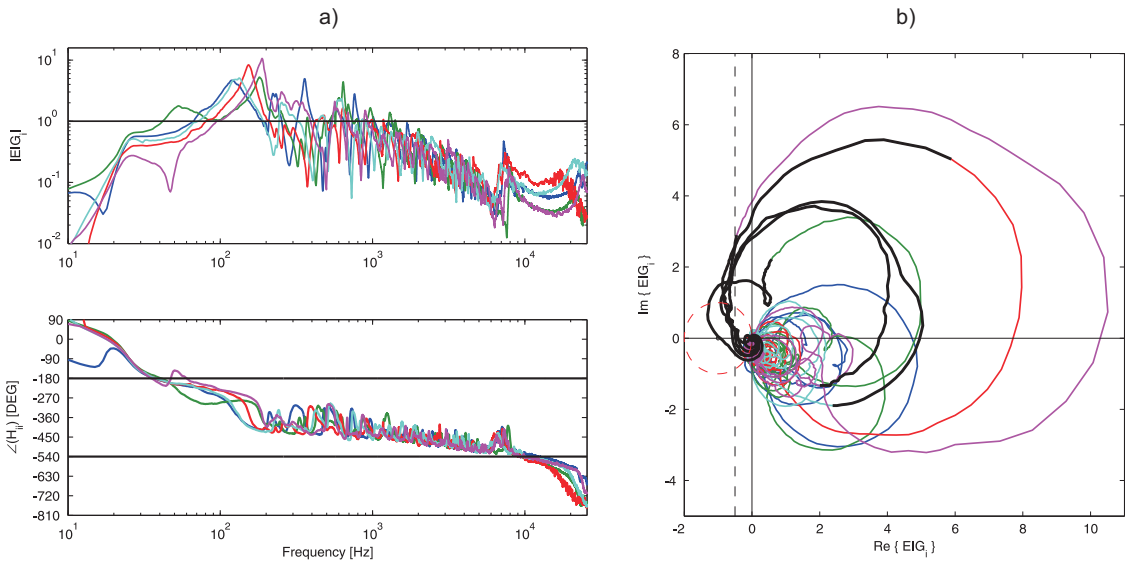

Figure 5.24: Eigenvalues of the open-loop FRF matrix of the control system on the aluminium panel. Thick solid lines in the Nyquist plot mark the FRFs in the frequency range from 0 Hz to 150 Hz and the ($dashed - red$) line marks the unit circle around the Nyquist stability point.

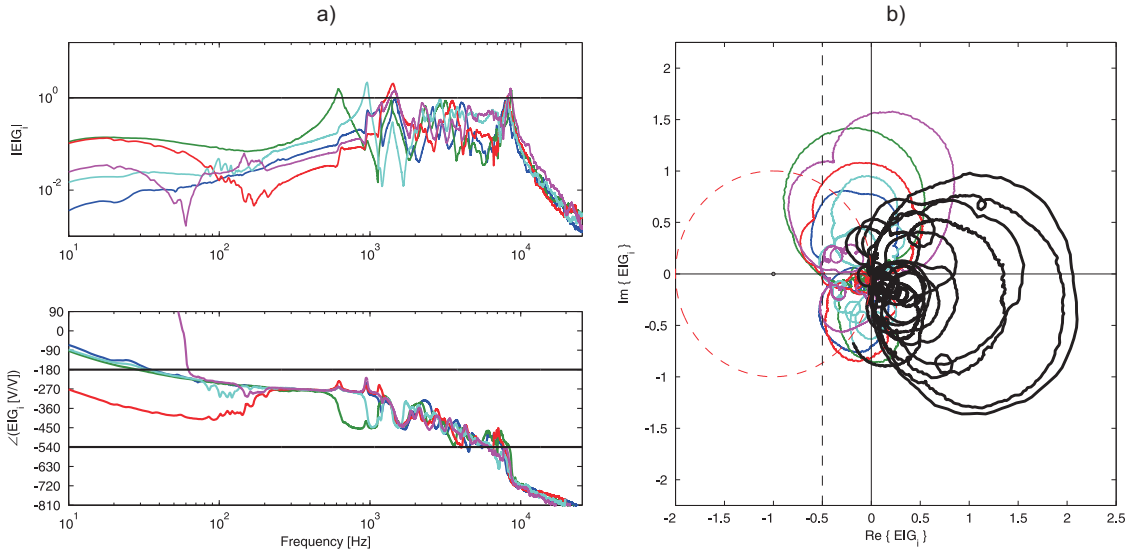

Figure 5.25: Eigenvalues of the open-loop FRF matrix of the control system on the honeycomb panel. Thick solid lines in the Nyquist plot mark the FRFs in the frequency range from 0 Hz to 3000 Hz and the ($dashed - red$) line marks the unit circle around the Nyquist stability point.

The eigenvalues for the control system mounted on the honeycomb panel given in Figure 5.25(b) show similar characteristics to the OL-FRFs for the individual feedback loops in Figure 5.23. The low frequency circles on the left hand side of the Nyquist plot are slightly inflated. However this may be due to numerical instability caused by the low magnitude of the measured OL-FRFs of the control system in this frequency range. As discussed for the OL-FRFs of the individual feedback loops in Figure 5.22, it is the high frequency circles of the system eigenvalues, which limit the gain margin and determine the control spillover. The high frequency circles of the OL-FEVF in the Nyquist plot in Figure 5.25(b) are only very slightly inflated compared with those in Figure 5.23(b), which indicates only little cross-

talk between the individual feedback loops at those high frequencies. Thus the dynamic response of the honeycomb structure tends to mask cross-talk effects between neighbouring actuators so that multiple feedback loops can be implemented with control gains close to those that would implemented if the control units were operating in isolation.

During the experiments it was found that for the control system on the aluminium panel, unstable control gains result in self-excitation of the control loops at low frequencies. For the system on the honeycomb panel excessive control gains resulted in high frequency whistling of control units. This observation is in good agreement with simulated and measured stability properties of the control system on the two test panels.

5.3.3 Control Performance

This section presents the measured narrow-band spectra of the panel kinetic energy and radiated sound power for the aluminium and the honeycomb panel. The results presented are those for the plain panels, the panels with open loop control units and for the active panels with manually tuned feedback control gains. On the aluminium panel the feedback gain for each control unit was individually tuned to the maximum gain that guaranteed the system to be stable. As expected from the stability analysis in Section 5.3.2 unstable feedback gains resulted in self excitation of the control units around the actuator fundamental resonance frequency. On the honeycomb panel, as discussed in Section 5.3.2, the stability of the feedback loops is limit due to conditional stability at high frequencies. Unstable feedback gains resulted in self excitation of the control units, which caused a clearly audible high frequency buzzing sound. The feedback gain were individually tuned to the maximum level for which this buzzing sound was inaudible.

Shaker excitation: The plots in Figure 5.26 show the measured narrow-band spectra of the panel kinetic energy and radiated sound power for the aluminium panel (left hand side) and the honeycomb panel (right hand side) with shaker excitation. Figure 5.27 shows the corresponding changes in panel kinetic energy and radiated sound power in 1/3 octave bands for the panels with passive control units and with closed feedback loops with reference to the spectra of the plain panels. Figure 5.28 shows the differences in panel kinetic energy and radiated sound power between the plain aluminium panel and the honeycomb panel without control system and with open and closed loop feedback control units in 1/3 octave bands.

Considering first the narrow-band kinetic energy spectra for the plain panels under shaker excitation in Figures 5.26(a) and (b), it can be observed that for low and mid frequency bands the spectra for both panels are characterised by a set of well-separated resonances of low order modes; those of the aluminium panel occur between the fundamental frequency of 117 Hz and about 500 Hz, while those of the honeycomb panel occur between the fundamental resonance at 735 Hz and about 2000 Hz.

For higher frequencies, the kinetic energies of the two panels are characterised by more complex spectra resulting from the response of a number of overlapping modes. The kinetic energy spectrum of the honeycomb panel shows a dip between 3000 Hz and 3750 Hz, which is due to the uneven frequency distribution of resonance frequencies of the anisotropic honeycomb panel and the location of the force position, which also occurs in the simulation results. As in the simulations, for frequencies below 3750 Hz the kinetic energy of the plain aluminium panel is much higher than that of the plain honeycomb panel.

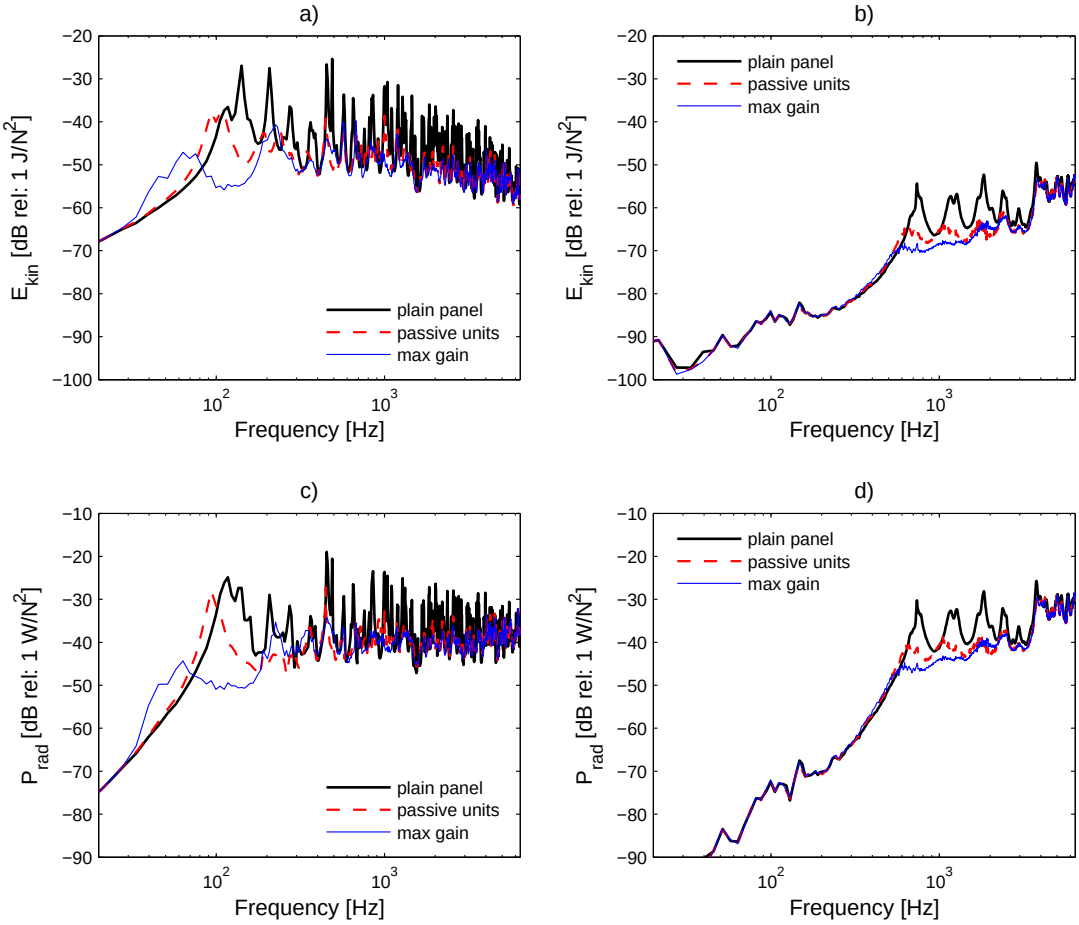

Figure 5.26: Measured response and sound power radiated for **shaker** excitation. Aluminium panel ($left$) and Honeycomb panel ($right$); Panel kinetic energy (top) and radiated sound power ($bottom$).

The measured response of the honeycomb panel in this frequency range is even lower than the simulation result in Figure 5.15. The response of the honeycomb panel indicates considerable structural damping which is introduced by the mounting conditions of the panel in the test frame. Above 3750 Hz the response of aluminium and honeycomb panels approach similar level, which can also be seen from the direct comparison of the 1/3 octave band spectra in Figure 5.28(a).

Moving to the shaker-induced sound radiation spectra shown in Figures 5.26(c) and (d), in contrast to what is found for the kinetic energy, above the fundamental resonance frequency of the honeycomb panel at 735 Hz, both panels show more similar sound radiation levels, which can also be seen from the 1/3 octave band spectra in Figure 5.28(b). This is due to the fact that the two panels have significantly different radiation efficiencies at low and mid audio frequencies, which combined with the different response levels at these frequencies give rise to similar sound radiation levels.

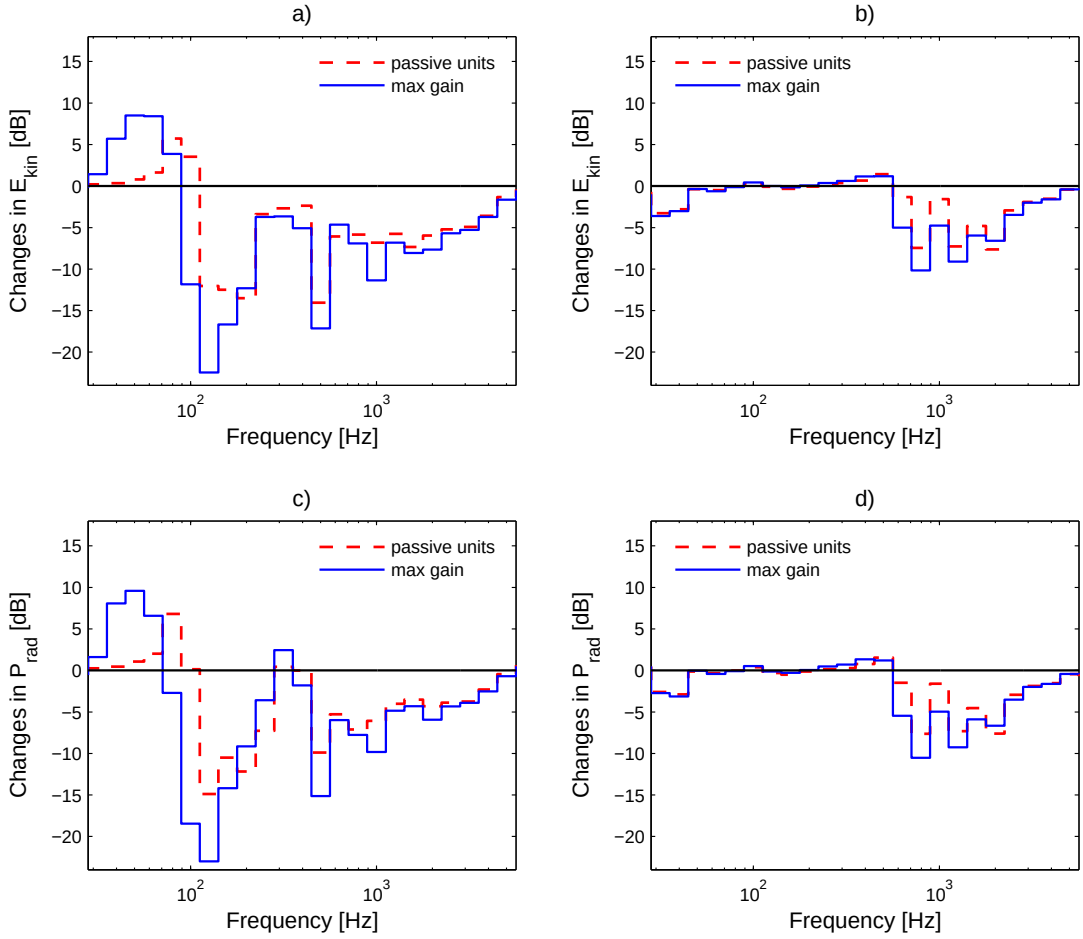

Figure 5.27: Change in the panel kinetic energy and radiated sound power for **shaker** excitation, evaluated in 1/3 octave bands. Aluminium panel ($left$) and Honeycomb panel ($right$); E_{kin} (top) and P_{rad} ($bottom$).

As found in the simulation study presented above, the measured sound radiation spectrum of the aluminium panel is characterised by many resonances peaks and anti-resonances troughs which are due to the superposition of contributions of low order structural modes that poorly radiate sound below the acoustic critical frequency at about 7500 Hz. In contrast at low and mid audio frequencies the sound radiation of the honeycomb panel is characterised by a few well separated low order resonances, which are efficiently radiating modes, since they all resonate above the acoustic critical frequency of about 400 Hz.

The plots in Figure 5.26 also show the measured responses and sound radiation spectra of the two panels with attached open loop and closed loop velocity feedback control units. The passive effects of the open loop control units shift the resonance frequencies of low order modes downwards, due to the added point masses. Also, the amplitudes of the resonant modes are significantly reduced over a wide frequency range due to passive damping effects. Above the fundamental resonance of the actuators, the magnet proof-mass acts as an inertial reference so that both mechanical and electrical damping effects are produced. Mechanical damping is caused by the air being squeezed in and out the ring cavity in the magnet mass by the vibration of the coil. Electric damping is induced by the back e.m.f. effect in the coil. The shift of low frequency resonances and the broad-band damping effects due to the passive action of the control actuators can also be seen in the 1/3 octave band spectra in Figure 5.27.

The simulated responses for panels with open loop control loops in Figure 5.15 do not exhibit considerable high frequency broad-band reductions due to damping effects. It is believed that the high broad-band damping effects measured experimentally may be due to the non-linear response of the open-loop control units as shown in Figure 4.6. The model of the control units does not capture these non-linear effects and further studies on the base response of the control units would be necessary to get a better understanding of this phenomenon.

As shown on the left hand side of Figures 5.26 and 5.27, for the aluminium panel with closed feedback loops, additional reductions of both kinetic energy and radiated sound power are achieved in the frequency range from 80 Hz to 200 Hz. In particular, in the 125 Hz 1/3 octave band containing the panel fundamental resonance frequency, the kinetic energy and radiated sound power is reduced by more than 10 dB to give a total reduction due to active and passive effects of more than 20 dB. In the frequency region between 20 and 63 Hz, feedback control results in enhancement of the panel response and radiated sound power;

particularly in the 50 Hz 1/3 octave band the panel kinetic energy and radiated sound power are increased by about 10 dB. As discussed in Sections 5.2.2 and 5.3.2, this is due to the control spillover effects around the fundamental resonance of the actuators.

As shown on the right hand side of Figures 5.26 and 5.27, for the honeycomb panel with closed-loop feedback control units, additional reductions of both kinetic energy and radiated sound power are achieved in the frequency range between 630 Hz to 1600 Hz. In particular in the 800 Hz 1/3 octave band that contains the panel fundamental resonance frequency, the kinetic energy and radiated sound power are reduced by about 4 dB to give a total reduction, due to passive and active effects, of more than 10 dB. Below 500 Hz the response of the honeycomb panel is stiffness-controlled and drops rapidly as frequency decreases. As discussed in Sections 5.2.2 and 5.3.2, in this case, little low frequency control spillover is produced by the closed-loop control units.

Figure 5.28 shows the difference between the panel kinetic energy and radiated sound power spectra of the plain aluminium panel and of the honeycomb panel with the control units implementing the manually tuned feedback gains. This comparison shows that the honeycomb panel is characterised by much lower kinetic energy at low and mid audio frequencies and much lower radiated sound power at low audio frequencies. The levels of radiated sound power at mid audio frequencies are similar for both plain panels. In this frequency region the radiated sound power of the honeycomb panels is considerably reduced by the feedback control units so that the honeycomb panel with active control radiates less sound than the plain aluminium panel. As shown in Figure 5.27, in the mid audio frequency range the response and radiated sound power of the aluminium panel with control units is also considerably reduced, predominantly due to the control unit passive effects. It can therefore be concluded that for shaker excitation, in the mid audio frequency range, both panels with installed feedback control units radiate similar levels of sound power. Above 4 kHz the honeycomb panel radiates more sound than the aluminium panel for each configuration.

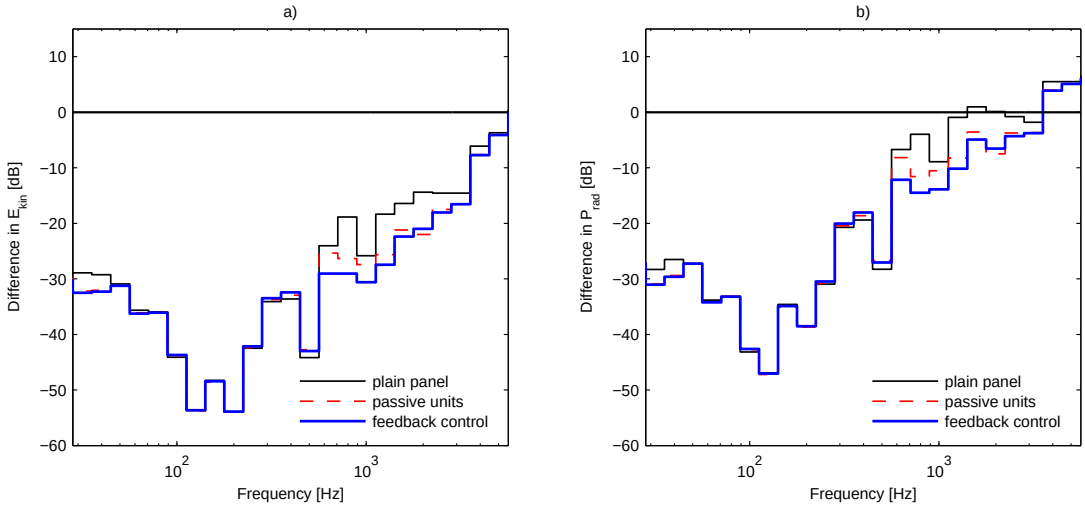

Figure 5.28: Differences in the response of the plain aluminium panel and those of the honeycomb panel without control units ($faint$), with passive control units ($dashed-red$) and with closed loop feedback control ($solid-blue$) for **shaker** excitation, evaluated in 1/3 octave bands. (a) E_{kin} and (b) P_{rad}.

Loudspeaker excitation: The plots in Figure 5.29 show the measured narrow-band spectra of the kinetic energy and radiated sound power for the aluminium panel (left hand side) and the honeycomb panel (right hand side) with loudspeaker excitation. Results are presented for the plain panels, the panels with open loop control units and for the active panels with manually tuned feedback control gains. Figure 5.30 shows the changes in panel kinetic energy and radiated sound power in 1/3 octave bands. Figure 5.31 shows the difference in panel kinetic energy and radiated sound power between the plain aluminium panel and the honeycomb without control system and with open and closed loop feedback control units in 1/3 octave bands.

Considering the narrow-band kinetic energy of the panels for loudspeaker excitation, the spectra in Figures 5.29(a) and (b) show similar characteristics to those for the shaker excitation, although the spectra are characterised by a smaller number of well-separated resonances and also tend to roll off at a higher rate as frequency rises. This is due to the fact that the distributed acoustic field does not efficiently excite all low order modes and also the excitation strength tends to decrease with increasing frequency, which is in good agreement with the simulation results in Figure 5.17. Compared with the results for shaker excitation, below 3750 Hz the kinetic energy of the plain honeycomb panel excited by the loudspeaker is closer to that for the aluminium panel, which can also be seen from the 1/3 octave band difference spectra in Figure 5.31(a). This is because at a given frequency lower order structural modes exist the honeycomb panel which are more efficiently excited by the acoustic field produced by the loudspeaker.

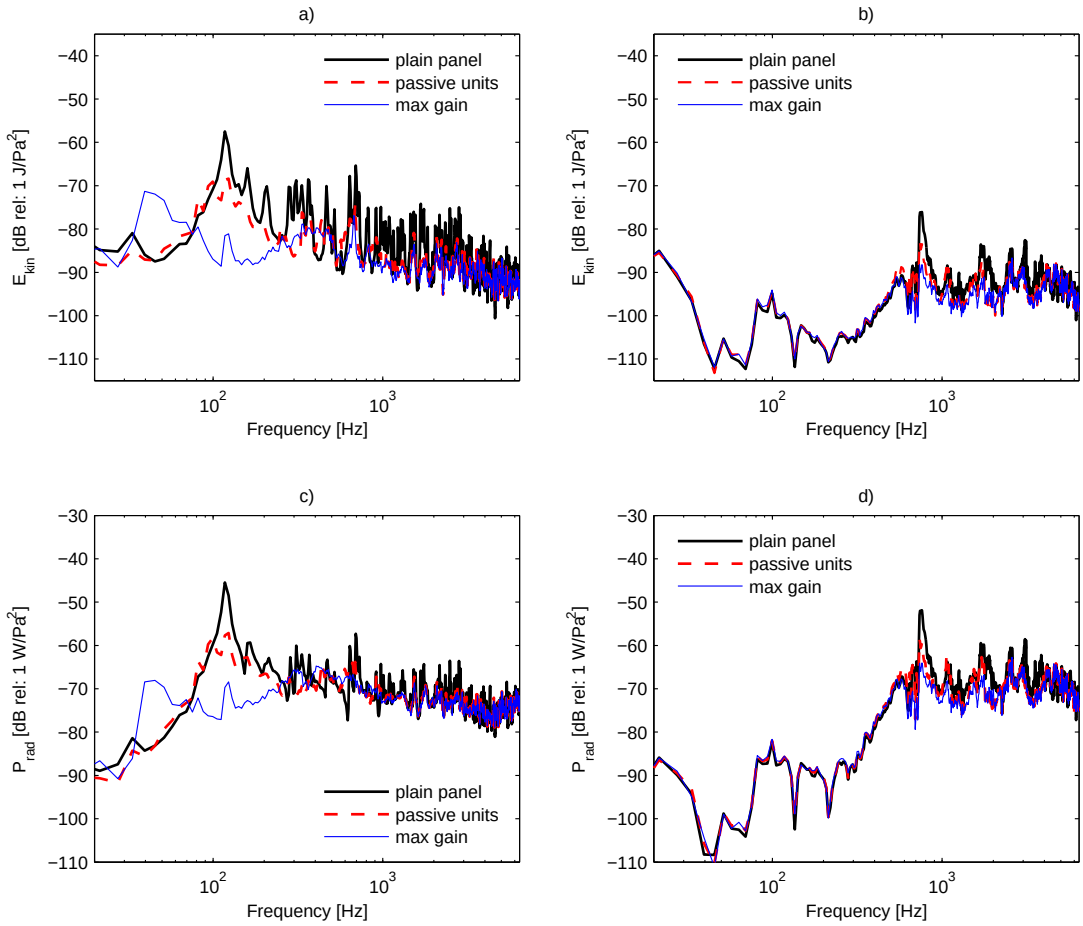

Figure 5.29: Measured response and sound power radiated for **loudspeaker** excitation. Aluminium panel ($left$) and honeycomb panel ($right$); panel kinetic energy (top) and radiated sound power ($bottom$).

The narrow-band radiated sound power spectra for loudspeaker excitation in Figures 5.29 (c) and (d) show that above 735 Hz the radiated sound power of the plain honeycomb panel exceeds that of the aluminium panel. This confirms the predicted combined effect of higher radiation efficiency and higher sensitivity to acoustic disturbance of the honeycomb panel resonant modes.

As shown in Figures 5.29 and 5.30, for loudspeaker excitation, the sound radiation from the aluminium panel above 400 Hz is only marginally changed by the addition of the control unit systems. This is because the radiated sound power spectrum is mass-controlled and not dominated by resonant modes.

The comparison of the changes in kinetic energy and radiated sound power in Figures 5.27 and 5.30 show that the reductions achieved for both types of excitation are otherwise generally very similar. The experimental studies confirm that the reductions achieved depend on the number of modes that are efficiently excited at resonance and, for the sound power, the number the radiate sound efficiently.

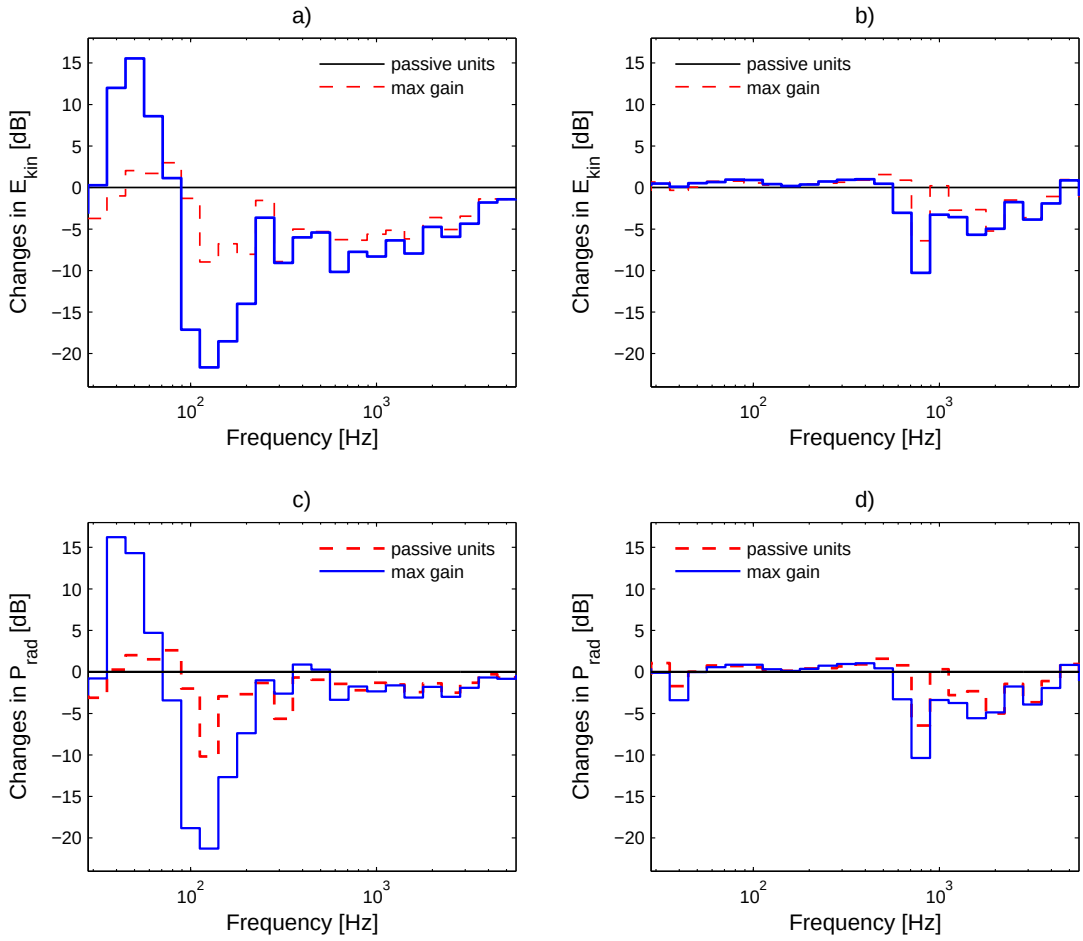

Figure 5.30: Change in the panel kinetic energy and radiated sound power for **loudspeaker** excitation, evaluated in 1/3 octave bands. Aluminium panel ($left$) and Honeycomb panel ($right$); E_{kin} (top) and P_{rad}($bottom$).

Figure 5.31 shows the differences in radiated sound power between the loudspeaker-excited plain aluminium panel and the plain honeycomb panel without control system and with open and closed loop feedback control units. As in the case of shaker excitation, shown in Figure 5.28, this comparison shows that the honeycomb panel is characterised by much lower kinetic energy at low and mid audio frequencies and much lower radiated sound power at low audio frequencies, although the differences are less significant.

In the case of loudspeaker excitation, for frequencies above 800 Hz the radiated sound power from the plain honeycomb panel exceeds that from the plain aluminium panel; particularly in the 800 Hz 1/3 octave band, where it is about 11 dB higher despite having similar mass. The results with open loop control units and closed feedback control loops show that the sound radiation from the honeycomb panel in the frequency range between 800 Hz and 2500 Hz is efficiently reduced to similar levels as those for the plain aluminium panel. As discussed above, in this frequency range, only small reductions due to passive and active effects of the control units are achieved on the aluminium panel. This indicates

that for acoustic excitations the aluminium and honeycomb active panels show a similar performance in the mid audio frequency range between 800 Hz and 2500 Hz, although in this frequency band the sound radiation from the plain honeycomb panel is considerably higher than that from the aluminium panel.

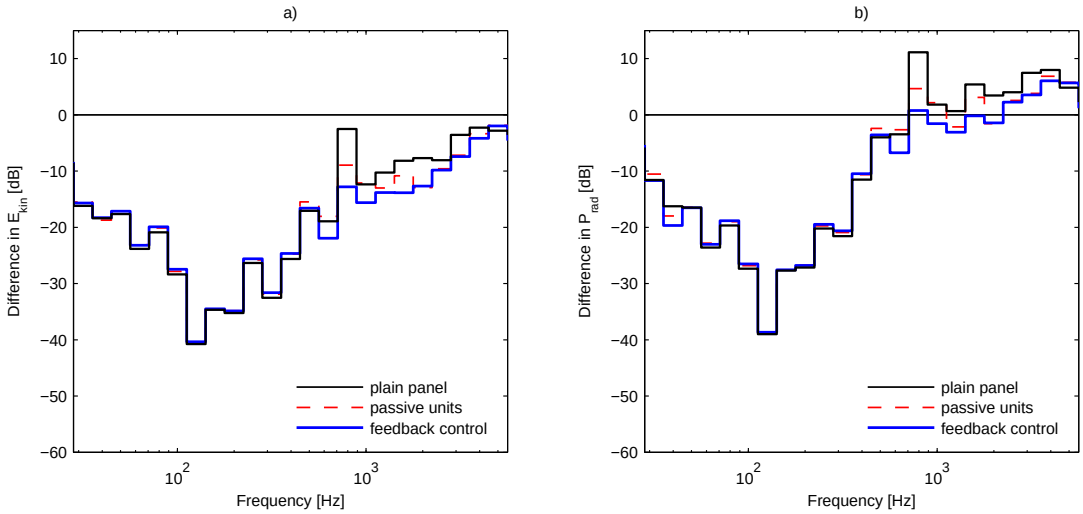

Figure 5.31: Differences in the response of the plain aluminium panel and those of the honeycomb panel without control units ($faint$), with passive control units ($dashed-red$) and with closed loop feedback control ($solid-blue$) for **loudspeaker** excitation, evaluated in 1/3 octave bands. (a) E_{kin} and (b) P_{rad}.

Effect of lumped masses: Additional measurements with lumped masses were conducted in order to contrast the passive inertia effects produced by small blocks of steel and the passive and active effects produced by the control units. The control actuators were replaced with lumped masses of either 11 grams or 35 grams, where the 11 gram masses represent the mounting mass of the actuators including the voice coil and the 35 gram mass represents the total mass of an actuator. The results showed that the added lumped masses shift the resonances of low order structural modes towards lower frequencies but do not introduce damping. At low frequencies this results in a shift of kinetic energy and radiated sound power spectra in frequency. The 1/3 octave band spectra indicate that at higher frequencies the added lumped masses does not produce a significant net reduction of the panel response and radiated sound power. For completeness the results for the measurements with equivalent lumped masses are presented in Appendix E.

5.4 Summary

This chapter presented simulation and experimental results of studies on a thin aluminium panel and a honeycomb sandwich panel with decentralised velocity feedback control. The control system was implemented considering the five decentralised control units with proof-mass electrodynamic actuator - accelerometer sensor pairs as described in Chapter 4.

Simulation and experimental measurements have been carried out in order to assess and compare the control stability and performance, in terms of panel kinetic energy and radiated sound power, of the two panels. In the experimental study the panels were either excited mechanically by a shaker or by the acoustic field produced by a loudspeaker. In the simulation study these two excitations were modelled as point force excitation and an acoustic plane wave excitation. Further simulation results have been presented for the panels excited by random broad-band ADF and TBL disturbances. The two panels are characterised by a very similar mass per unit area, but the honeycomb panel has a much higher bending stiffness than the aluminium panel. This results in considerably different fundamental resonance and acoustic coincidence frequencies.

- It was found in Section 5.1 that the bending wave numbers on the Honeycomb panel are significantly lower than those of the aluminium panel in the entire frequency range of interest. This results in a much lower modal density and lower modal overlap for the honeycomb panel and also in much lower convective and acoustic coincidence frequencies.

- Section 5.2 presented the simulation results for the implementation of a practical control system with decentralised feedback control units as described in Chapter 4, where the model parameters were chosen to replicate the experimental set-up.

  Due to its lower fundamental resonance frequency, the response and radiated sound power of the aluminium panel at low audio frequencies are much higher than those of the honeycomb panel. In the mid audio frequency range, all modes of the honeycomb panel are efficient radiators of sound and are also efficiently excited by an acoustic source, which results in higher levels of radiated sound power than for the aluminium panel.

  The control system on the honeycomb panel performs better in terms of both control stability and also of control performance, which, depending on the type of excitation, allows the response of the honeycomb panel to be controlled in the mid audio

frequency range to similar or even lower levels than those of the aluminium panel.

- Section 5.3 presented the results from experimental studies in a transmission chamber on the two panels with and without AVC system.

  The results show that considerable broad-band reductions of kinetic energy and radiated sound power are produced by the passive and active effects of the control units. For the aluminium panel, significant reductions are achieved in the low audio frequency range between 80 Hz and 250 Hz. For the honeycomb panel, considerable reductions are achieved in the mid audio frequency range between 500 Hz and 1600 Hz.

  The results from the experimental study validated the simulation results. The active panel model used in the simulation study captures all important physical effects. The effects that are not captured in the model are the non-linear actuator dynamics that produce broad-band damping with the open loop control units and also the control unit mounting resonance, which imposes the current stability limits for the control system on the honeycomb panel.

  Further studies are needed to optimise the high frequency stability of the control system on the honeycomb panel and to yield a better understanding of the considerable broad band damping effects of the passive control units.

Chapter 6

Summary, conclusions and recommendations for further work

This final chapter summarises the findings of this thesis, and also emphasises suggestions for future research work on decentralised velocity feedback control. A more detailed summary of the conclusions is provided at the end of each chapter.

6.1 Summary

Chapter 1 provided a brief introduction on motivation and technical background for active vibration control on panels. Also the objectives and structure of this dissertation were outlined and the original contributions of this research were highlighted.

Chapter 2 introduced the general, elemental based, model for the structural response and radiated sound power for passive and active panels with feedback control. The expressions for discrete and distributed deterministic transverse excitation, and distributed stochastic transverse excitation were reviewed. It has been shown that the transmission coefficient of a baffled passive panel derived with the elemental approach is in good agreement with the corresponding simplified analytical solutions.

Chapter 3 presented the simulation studies on decentralised velocity feedback control via ideal sensor actuator pairs for different types of distributed deterministic and stochastic excitation. The objectives of this study were twofold. Firstly, to investigate and contrast the structural response and the sound radiation in the audio frequency range produced by homogeneous and lightweight sandwich panels subject to deterministic and stochastic distributed

excitations. Secondly, to study and compare the control effects produced by an array of idealized velocity feedback control loops on homogeneous and lightweight sandwich panels.

The principal differences between the structural response of thin homogeneous and the sandwich panels were discussed with respect to: (a) the real wavenumber solutions of the governing equations, (b) the modal density, (c) the modal overlap and (d) both excitation and radiation coincidence effects.

Then the structural response and sound radiated of the two panels due to (a) acoustic plane wave, (b) stochastic acoustic diffuse field and (c) turbulent boundary layer disturbances were contrasted.

Simulation studies on the two panels with 16 ideal velocity feedback loops were conducted in order to compare the control effects on both panels and to investigate the intrinsic limitations of decentralised velocity feedback control. In contrast to most previous studies on active panels, the analysis in this study has been extended to the upper end of the audio frequency range.

Chapter 4 presented experimental and simulation studies on the open and closed loop base impedance of practical control units with proof-mass electrodynamic actuator-accelerometer sensor pairs and controller FRF of realistic integrator and amplifier electronic circuits. The experimental studies have been performed on prototype actuators specifically developed for this study.

Experimental studies on the actuator blocked force frequency response function allowed to fit parameters to an electromechanical model that describes the open and closed loop base impedance of the control units.

Experimental and simulation studies on the closed loop base impedance of the control units were conducted to give physical interpretation of the measured closed loop control unit base impedance.

Chapter 5 presented simulation and experimental results of studies on a thin aluminium panel and a honeycomb sandwich panel with decentralised velocity feedback control considering five decentralised control units with proof-mass electrodynamic-actuator accelerometer sensor pairs.

The two panels are characterised by a very similar mass per unit area, but the honeycomb panel has a much higher static bending stiffness than the aluminium panel. This results in

considerably different fundamental resonance and acoustic coincidence frequencies. Both simulation and experimental studies have been carried out for the two panels in order to investigate the stability and performance of the control system.

In the experimental study the panels were either excited mechanically by a shaker or by the acoustic field produced by a loudspeaker. In the simulation study these two excitations were modelled as point force excitation and an acoustic plane wave excitation. The response of the two panels to distributed stochastic ADF and TBL disturbances was also simulated but not investigated experimentally.

The results from the experimental study validated the simulation results. The active panel model used in the simulation study captures all important parameter. The effects that are not captured in the model are the non-linear actuator dynamics that produce the broad band damping with the open loop control units and also the control unit mounting resonance which impose the stability limits for the control system on the honeycomb panel.

6.2 Conclusions

The results in this study show that **decentralised velocity feedback control** of a panel is efficient in controlling the response of low order structural modes at resonance and also in controlling the response of individual modes resonating at acoustic coincidence in the mid and high audio frequency range. Decentralised velocity feedback control is particularly efficient on panels under TBL excitation where the structural response is dominated by low order resonant modes.

The base impedance of the closed loop control units can be readily described by a basic electromechanical model with a controller FRF. Therefore this model can be used to investigate new designs of both electro-mechanical actuator and electrical controller in order to optimise the stability and control performance properties.

It was found that around the actuator fundamental resonance, the control unit base impedance has a negative real part, which indicates a negative damping effect. This results in conditional stability of the closed feedback loop and control spillover effects at frequencies around the fundamental resonance of the actuator. The simulations showed that it is important to include the controller FRF in the model in order to capture the principal characteristics of the base impedance of the closed loop control units.

At high frequencies the response of the actuators is characterised by mounting resonance effects which are not captured in the electromechanical model. It was also found that the response of the actuators built for the experimental studies is non-linear and depends on the amplitude of the excitation at the base of the actuators. These two characteristics are not captured in the model, which assumes a linear response and ideal mounting conditions.

Lightweight sandwich panels comprise a high stiffness-to-weight ratio and therefore exhibit lower modal density and lower convective and acoustic coincidence frequencies than thin homogeneous panels with corresponding mass per unit surface area or corresponding static stiffness. Therefore the structural response and radiated sound power of stiff lightweight sandwich panels is dominated by discrete resonant modes over a wider range of audio frequencies than for thin homogeneous aluminium panels.

The results in this thesis indicate high potential for the application of velocity feedback control to reduce the kinetic energy and radiated sound power of stiff lightweight sandwich panels, which, due to the lower modal density, is efficient up to mid audio frequencies, while for thin aluminium panels it was found to be limited to low audio frequencies.

It has also been demonstrated that the high stiffness-to-weight ratio of the sandwich panels results in an enhancement in both the stability and the control performance of decentralised velocity feedback control systems compared with the case when the control system is implemented on a thin homogeneous aluminium panel.

The results in this thesis suggest that decentralised velocity feedback control is efficient in reducing the structural response and radiated sound power of stiff lightweight sandwich panels in the low and mid audio frequency range. Therefore active control systems could balance the poor sound transmission properties of lightweight sandwich structures to such extent that this would justify the additional expense and additional installed mass of an active control systems.

6.3 Future work

In this section suggestions for future research on decentralised velocity feedback control for panels are summarised. The suggested research includes further experimental and theoretical studies on the improvement of control stability and performance.

6.3.1 Suggested experimental studies

The stability of the velocity feedback control units with proof-mass electrodynamic actuators and accelerometer sensors may be enhanced if more rigid mounting conditions for the control unit components are realised. More rigid mounting conditions will shift the mounting resonance effects further up in frequency and may allow for higher feedback gains when the control units are installed on stiff lightweight honeycomb sandwich panels. This study could also clarify whether the stability of the control system is also affected by the cross-section resonances of the honeycomb panel.

The stability of the velocity feedback control units studied here could be efficiently enhanced by applying an appropriate electrical compensator that cancels out the actuator mechanical resonance. Simulation and experimental studies on the closed loop responses of the actuators should be conducted to development appropriate compensator circuits.

An uncertain factor in the measured OL-FRFs is the difference between the output impedance of the accelerometer signal conditioner and the output impedance of the analyser signal generator. This may have an effect on the output current per unit input voltage of the controller board. This should be further investigated to yield a better understanding of the dynamic interaction of all electric circuits in the control loop.

The open loop response of the prototype actuators used in this study has been found to be non-linear. Further studies could investigate the closed loop control unit response for low base excitation levels and non-flat excitation spectra. However, the effort to measure these responses and to implement non-linearity in the electro-mechanical response model may be disproportionate to the expected benefits since the non-linear characteristics of the response are only specific to the prototype actuator design investigated in this thesis.

The simulation results for TBL excited panels gave interesting results and it would be desirable to design an experimental set-up to simulate TBL primary disturbances. One possibility could be to emulate the pressure field produced by a TBL disturbance using an array of loudspeakers that can reproduce the TBL complex pressure correlation function [54].

The AVC system could also be installed and tested on other types of panels, i.e. different types of honeycomb sandwich panels, and on other structures that more closely represent lightweight car body or fuselage sections.

6.3.2 Theoretical studies

In this thesis a basic model was used to simulate the structural response of sandwich panels. This basic model captures the principal characteristics of a sandwich panel and was found to be suitable in the scope of the presented comparative studies. A more complex model, considering near-field waves and the cross-section dynamics of the sandwich structure, may be needed for more detailed investigations.

In the simulation studies presented in this thesis, the panels were ideally restrained along the edges. For idealised mutually dual and collocated sensor-actuator pairs the feedback control loops are unconditionally stable regardless of the boundary conditions of the structure. This may not be the case for feedback loops with practical actuator-sensor pairs. Further studies should be conducted to investigate the effect of flexible boundary conditions on the stability and control performance of systems with practical actuator sensor-pairs. The implementation of flexible boundaries in the elemental approach is outlined in Reference [46].

For the simulation studies in this thesis the control gains were set to be uniform over all feedback loops. The results showed that for decentralised velocity feedback control with proof-mass electrodynamic actuators the feedback loop of the control unit in the centre of the panel had the lowest gain margin. Further studies should investigate if the stability and performance of the control system can be improved by allowing variations between the gains of the individual feedback loops.

The optimal feedback control gain is a function of the characteristics of the primary disturbance. It should therefore be investigated how-self sensing and self-tuning control units could be implemented in order to design adaptive feedback control systems.

It may also worth studying the optimal actuator placement on the panels in order to investigate how a given number of control units should be distributed, i.e. if they should be positioned randomly or in a regular pattern, if they should be evenly distributed or arranged in clusters.

Future generations of feedback control units with proof-mass electrodynamic actuators may also implement control in more than one degree of freedom. The control performance of simultaneous transverse force and moment feedback could be investigated in simulation studies considering feedback control on thin restrained beams and/or plates.

The above idea of multiple degree of freedom feedback may be particularly appealing for

the implementation of active boundary impedances close to the edges of restrained panels. This type of control system could aim to replicate boundaries that emulate infinite panels with minimal resonant response.

6.3.3 Component development

For further studies, although the non-linear response of the control units have some advantages, it would be beneficial to develop control units with more linear response characteristics. This would require the proof-mass suspension to be redesigned and also the actuator manufacturing tolerances to be reduced.

The size and weight of future feedback control units could be effectively reduced, particularly if microelectronic circuits were to be used for the local controllers and micromechanical technologies were to be used for the sensors and also for specific components of the miniaturised actuators.

Future research should also explore further the possibility of multi-functional control units that can also be used for fatigue monitoring, power harvesting or provide other complementary functional features.

For all of the three points above, the involvement of industrial partners would be beneficial. Firstly these partners could provide specialist know-how in high precision manufacturing of high quality transducers. Secondly they could help to specify industrial requirements for practical control units. This would push the application readiness level of these control units further towards practical industrial implementation.

This is desirable since active panel really are a promising way to deal with interior noise in aircraft and other vehicles particularly in combination with lightweight honeycomb sandwich panels.

Appendix A

Modal formulations for the response of thin rectangular panels

This Appendix summarises the expressions used to derive the natural frequencies, natural modes and point and transfer mobilities of thin homogeneous isotropic panels; it is organised in two sections.

The first section describes how the panel point and transfer mobility terms are derived from finite modal summations considering dynamic and residual modal contributions and how these formulations are cast into vector and matrix expressions to calculate point and transfer mobilities for multiple points on the panel.

The second section gives the formulations for the geometric and dynamic properties of thin homogeneous isotropic panels and summarizes the relevant formulations for the natural frequencies, natural modes, and receptance terms for different boundary conditions as given by Gardonio and Brennan [47].

A.1 Panel mobility derived from finite modal expansion

The structural response of the panel model introduced in Chapter 2 is expressed in terms of point and transfer mobilities $\tilde{Y}_{i,j}(\omega)$ which are derived from finite modal summation [47]. In order to model accurately the response of a panel, the contribution of higher order modes with natural frequencies beyond the observed frequency range must be taken into account. Only then can near-field effects of point forces can be be modelled accurately. This is of particular importance for the modelling of panels with point control forces espe-

cially if high feedback gains are applied such that the contributions of lower order modes is largely cancelled. Simulation studies [23] showed that a large number of modes with natural frequencies up to 50 times the highest observation frequency are required to describe the response of panels with feedback control forces adequately. Preumont [38] suggested that the point and transfer responses on a structure can be calculated from the sum of dynamic and residual terms which implies that the mobility can be expressed as

$$\tilde{Y}_{i,j}(\omega) = j\omega \left(\tilde{G}_{dyn_{i,j}}(\omega) + \tilde{G}_{res_{i,j}} \right), \tag{A.1}$$

where $\tilde{G}_{dyn_{i,j}}$ and $\tilde{G}_{res_{i,j}}$ are the dynamic and residual point and transfer receptances between the panel locations i and j. The expansion formulation for the dynamic receptance is given by

$$\tilde{G}_{dyn_{i,j}}(\omega) = \sum_{r=1}^{N_{dyn}} \frac{\phi_r(x_i, y_i)\, \phi_r(x_j, y_j)}{M\left(\omega_r^2 (1 + j\eta) - \omega^2\right)}, \tag{A.2}$$

where N_{dyn} is the total number of dynamic modes considered in the summation, ω_r is the rth natural frequency and $\phi_r(x_i, y_i)$ and $\phi_r(x_j, y_j)$ are the rth natural mode at the panel locations i and j respectively. Also M is the total mass of the panel. The dynamic receptance is a function of the excitation frequency ω; it is therefore calculated for the entire range of observation frequencies. Hence the computational effort increases with the number of observation frequencies and also with the number of dynamic modes considered in the summation. For modes with natural frequencies well above the highest observation frequency, only the stiffness and damping terms are of importance for the response of the panel, while the mass terms can be neglected. Thus the modal expansion formulation for the residual panel element receptance is given by

$$\tilde{G}_{res_{i,j}} = \sum_{r=N_{dyn}+1}^{N_{res}} \frac{\phi_r(x_i, y_i)\, \phi_r(x_j, y_j)}{M\left(\omega_r^2 (1 + j\eta)\right)}. \tag{A.3}$$

Since the term under the sum in the residual receptance $\tilde{G}_{res_{i,j}}$ is independent of the excitation frequency, it only needs to be computed once for each panel location, which can reduce the computational effort. For convenience the formulations for the velocity response of a number of locations on the panel can be cast into a vector/matrix expression. For example the mobility matrix $\tilde{\mathbf{Y}}_{ee}$ containing point and transfer mobility functions is given by

$$\tilde{\mathbf{Y}}_{ee}(\omega) = j\omega \left(\tilde{\mathbf{G}}_{ee,dyn}(\omega) + \tilde{\mathbf{G}}_{ee,res} \right). \tag{A.4}$$

Considering Equation (A.2), the dynamic receptance matrix $\tilde{\mathbf{G}}_{ee,dyn}(\omega)$ is calculated from the diagonal frequency-dependent matrix $\tilde{\mathbf{\Omega}}_{dyn}(\omega)$ and the fully populated frequency independent $\mathbf{\Phi}_{e,dyn}$ matrix of the dynamic mode shapes at the element centre positions, so that

$$\tilde{\mathbf{G}}_{ee,dyn}(\omega) = \mathbf{\Phi}_{e,dyn} \tilde{\mathbf{\Omega}}_{dyn}(\omega) \mathbf{\Phi}_{e,dyn}^{T}. \tag{A.5}$$

The diagonal matrix $\tilde{\mathbf{\Omega}}_{dyn}(\omega)$ is assembled from the terms

$$\tilde{\Omega}_{r_{dyn}}(\omega) = \frac{1}{M\left(\omega_r^2\left(1 + j\eta\right) - \omega^2\right)}, \tag{A.6}$$

where the mode index r ranges from $r = 1$ to the maximum number of dynamic modes $r = N_{dyn}$. Therefore $\tilde{\mathbf{\Omega}}_{dyn}(\omega)$ is a square diagonal matrix with dimensions $[N_{dyn} \times N_{dyn}]$. The matrix of dynamic natural modes at the element centre locations $\mathbf{\Phi}_{e,dyn}$ is assembled from

$$\Phi_{i,r_{dyn}} = \phi_r\left(x_i, y_i\right), \tag{A.7}$$

where the mode index r ranges from $r = 1$ to the maximum number of dynamic modes $r = N_{dyn}$ and the element index i ranges from $i = 1$ to $i = N_e$ to yield $\mathbf{\Phi}_{e,dyn}$ as a matrix of dimensions $[N_e, N_{dyn}]$. The residual receptance matrix $\tilde{\mathbf{G}}_{ee,res}$ is calculated from the diagonal frequency-independent residual matrix $\tilde{\mathbf{\Omega}}_{res}$ and the fully populated residual modeshape matrix $\mathbf{\Phi}_{e,res}$

$$\tilde{\mathbf{G}}_{ee,res} = \mathbf{\Phi}_{e,res} \tilde{\mathbf{\Omega}}_{res} \mathbf{\Phi}_{e,res}^{T}, \tag{A.8}$$

where the residual matrix $\tilde{\mathbf{\Omega}}_{res}$ is assembled from terms

$$\tilde{\Omega}_{r_{res}} = \frac{1}{M\left(\omega_r^2\left(1 + j\eta\right)\right)}. \tag{A.9}$$

Here the mode index r ranges from $r = (N_{dyn} + 1)$ to the maximum number of residual modes considered $r = N_{res}$. Therefore $\tilde{\mathbf{\Omega}}_{res}$ is a square diagonal matrix of dimensions $[(N_{res} - N_{dyn}) \times (N_{res} - N_{dyn})]$. Analogous to equation (A.7) the natural mode matrix

$\mathbf{\Phi}_{e,res}$ is assembled from the terms

$$\Phi_{i,r_{res}} = \phi_r\left(x_i, y_i\right), \tag{A.10}$$

where the mode index r ranges from $r = (N_{dyn} + 1)$ to the maximum number of residual modes considered $r = N_{res}$ and the element index i ranges from $i = 1$ to N_e to yield $\mathbf{\Phi}_{e,res}$ as a matrix of dimensions $[N_e \times (N_{res} - N_{dyn})]$.

A.2 Formulations for the natural frequencies and modes of thin isotropic panels

In this section the formulations for the natural modes, natural frequencies and modal expansion terms for the point and transfer receptances of thin rectangular panels used in this thesis are summarised [47, 48].

A.2.1 Definition of panel geometric and dynamic properties

The geometric and dynamic properties of the panel are given as:

- Panel surface A_p [m^2]:

$$A_p = l_x l_y, \tag{A.11}$$

- Panel mass per unit area: m'' [kg/m^2]:

$$m'' = \rho h, \tag{A.12}$$

- Panel mass M [kg]:

$$M = A_p m'', \tag{A.13}$$

- and bending stiffness B [N m]:

$$B = \frac{E h^3}{12(1-\nu^2)}, \tag{A.14}$$

where l_x and l_y are the panel dimensions in x and y-direction, h is the panel thickness. Also ρ, E and ν are the mass density, Young's modulus and Poisson ratio of the panel material.

A.2.2 Natural frequencies and modes

The natural frequencies ω_r [rad/s] for rectangular plates for any type of boundary are given by [48]

$$\omega_r(m,n) = \sqrt{\frac{B}{m''}} \left(\frac{\pi}{l_x}\right)^2 q_r(m,n) \tag{A.15}$$

where the factor $q_r(m,n)$ is given by

$$q_r(m,n) = \sqrt{G_m^4 + G_n^4 \left(\frac{l_x}{l_y}\right)^4 + 2\left(\frac{l_x}{l_y}\right)^2 [\nu H_m H_n + (1-\nu) J_m J_n]} \tag{A.16}$$

The constants G, H, J are given in Table A.1. The mass-normalised modeshapes $\phi_r(m,n)$ are given by

$$\phi_r(m,n) = \phi_m \phi_n \tag{A.17}$$

where mass-normalised characteristic beam mode functions ϕ are given in Table A.2. It should be noted that Equation (A.17) is an approximation unless the panel is pinned a at least two opposite edges.

Table A.1: Constants for the the variables G, H and J for plates with pinned, clamped and free boundary conditions on each edge; taken from [47].

Boundary conditions	n	G	H	J
P-P-P-P (all side pinned) $w(0)=0$ $w''(0)=0$ $w(L)=0$ $w''(L)=0$	1,2,3,...	n	n^2	n^2
C-C-C-C (all side clamped) $w(0)=0$ $w'(0)=0$ $w(L)=0$ $w'(L)=0$	1	1.506	1.248	
	$2,3,4...$	$n+\frac{1}{2}$	$\left(n+\frac{1}{2}\right)^2 \times \left[1-\frac{4}{(2n+1)\pi}\right]$	
F-F-F-F (all sides free) $w''(0)=0$ $w'''(0)=0$ $w''(L)=0$ $w'''(L)=0$	even	0	0	0
	rocking	0	0	$12/\pi^2$
	1	1.506	1.248	5.017
	$2,3,4...$	$n+\frac{1}{2}$	$\left(n+\frac{1}{2}\right)^2 \times \left[1-\frac{4}{(2n+1)\pi}\right]$	$\left(n+\frac{1}{2}\right)^2 \times \left[1+\frac{12}{(2n+1)\pi}\right]$

Note that the first values for γ in Table A.2 can be determined using numerical root-finding methods, where it is important to yield results with a high precision. For values larger than 10 the numerical methods can fail to determine the roots correctly. For i greater than 10, γ_i is given by

$$\gamma_i = \frac{(4i+1)\pi}{2} \quad \text{for} \quad \tan\left(\frac{\gamma_i}{2}\right) - \tanh\left(\frac{\gamma_i}{2}\right) = 0, \tag{A.18}$$

and as

$$\gamma_i = \frac{(4i-1)\pi}{2} \quad \text{for} \quad \tan\left(\frac{\gamma_i}{2}\right) + \tanh\left(\frac{\gamma_i}{2}\right) = 0 \tag{A.19}$$

respectively.

Table A.2: Characteristic beam functions for a plate with pinned, clamped and free boundary conditions on all edges; taken from [47].

Boundary conditions	$\phi_{1,3,5...}(x)$ with $i = (n+1)/2$	$\phi_{2,4,6...}(x)$ with $j = (n/2)$
P-P-P-P (all side pinned) $w(0) = 0$ $w''(0) = 0$ $w(L) = 0$ $w''(L) = 0$	$\phi_n(x) = \sqrt{2}\sin\left(\frac{n\pi x}{l_x}\right)$	
C-C-C-C (all side clamped) $w(0) = 0$ $w'(0) = 0$ $w(L) = 0$ $w'(L) = 0$	$\phi_n(x) = \sqrt{2}\left\{\cos\left[\gamma_i\left(\frac{x}{l_x} - \frac{1}{2}\right)\right] + k_n \cosh\left[\gamma_i\left(\frac{x}{l_x} - \frac{1}{2}\right)\right]\right\}$ $k_n = \frac{\sin\left(\frac{\gamma_i}{2}\right)}{\sinh\left(\frac{\gamma_i}{2}\right)}$ with $\tan\left(\frac{\gamma_i}{2}\right) + \tanh\left(\frac{\gamma_i}{2}\right) = 0$	$\phi_n(x) = \sqrt{2}\left\{\sin\left[\gamma_i\left(\frac{x}{l_x} - \frac{1}{2}\right)\right] + k_n \sinh\left[\gamma_i\left(\frac{x}{l_x} - \frac{1}{2}\right)\right]\right\}$ $k_n = -\frac{\sin\left(\frac{\gamma_j}{2}\right)}{\sinh\left(\frac{\gamma_j}{2}\right)}$ with $\tan\left(\frac{\gamma_j}{2}\right) - \tanh\left(\frac{\gamma_j}{2}\right) = 0$
F-F-F-F (all side free) $w''(0) = 0$ $w'''(0) = 0$ $w''(L) = 0$ $w'''(L) = 0$	$\phi_{even}(x) = 1$ $\phi_{rocking}(x) = \sqrt{3}(1 - \frac{2x}{l})$	
	$\phi_n(x) = \sqrt{2}\left\{\cos\left[\gamma_i\left(\frac{x}{l_x} - \frac{1}{2}\right)\right] + k_n \cosh\left[\gamma_i\left(\frac{x}{l_x} - \frac{1}{2}\right)\right]\right\}$ $k_n = -\frac{\sin\left(\frac{\gamma_i}{2}\right)}{\sinh\left(\frac{\gamma_i}{2}\right)}$ with $\tan\left(\frac{\gamma_i}{2}\right) + \tanh\left(\frac{\gamma_i}{2}\right) = 0$	$\phi_n(x) = \sqrt{2}\left\{\sin\left[\gamma_i\left(\frac{x}{l_x} - \frac{1}{2}\right)\right] + k_n \sinh\left[\gamma_i\left(\frac{x}{l_x} - \frac{1}{2}\right)\right]\right\}$ $k_n = \frac{\sin\left(\frac{\gamma_j}{2}\right)}{\sinh\left(\frac{\gamma_j}{2}\right)}$ with $\tan\left(\frac{\gamma_j}{2}\right) - \tanh\left(\frac{\gamma_j}{2}\right) = 0$

Appendix B

Formulations for kinetic energy and radiated sound power

This Appendix gives the formulations for panel kinetic energy and radiated sound power for deterministic and stochastic excitations. The formulations are derived from first principles and then cast into modal and elemental approach formulations.

- Section B.1 introduces the notation for the time-harmonic excitation and vibration velocity response of a rectangular panel.
- Sections B.2 and B.3 derive the panel response and sound radiation for panels under deterministic excitation in terms of total panel kinetic energy and total sound power radiated.
- Sections B.4 and B.5 derive the panel response and sound radiation for panels under stochastic excitation in terms of power spectral densities of total kinetic energy and radiated sound power

B.1 Notations for the time harmonic response of the panel

First the notation for the time-harmonic excitation and vibration velocity response of a rectangular panel, as shown in Figure 2.1 are introduced. This notation is then used to derive the formulations for the panel structural response and sound radiation for time harmonic and stochastic disturbances. Assuming time-harmonic behaviour, of the form $Re\{\exp(j\omega t)\}$, where ω is the angular frequency and $j = \sqrt{-1}$, the transverse force excitation and the

transverse velocity response of a panel can be expressed as

$$f(x,y,t) = Re\left\{\tilde{f}(x,y,\omega)e^{j\omega t}\right\}, \tag{B.1}$$

$$\dot{w}(x,y,t) = Re\left\{\tilde{\dot{w}}(x,y,\omega)e^{j\omega t}\right\}, \tag{B.2}$$

where $\tilde{f}$ and $\tilde{\dot{w}}$ are frequency-dependent complex phasors of the force and the velocity response.

B.1.1 Modal formulation

The time-dependent velocity response, can be expressed in terms of the following infinite modal summation

$$\dot{w}(x,y,t) = Re\left\{\sum_{r=1}^{\infty}\phi_r(x,y)\dot{a}_r(t)e^{j\omega t}\right\}, \tag{B.3}$$

where $\phi_r(x,y)$ is the modeshape of the r-th natural mode and $\tilde{\dot{a}}_r(\omega)$ is the complex modal velocity. Thus the complex frequency-dependent velocity response is given by

$$\tilde{\dot{w}}(x,y,\omega) = \sum_{r=1}^{\infty}\phi_r(x,y)\tilde{\dot{a}}_r(\omega). \tag{B.4}$$

The frequency-dependent complex modal velocities $\tilde{\dot{a}}_r(\omega)$ can be expressed as the product of a resonant term and a modal or generalised excitation term:

$$\tilde{\dot{a}}_r(\omega) = \tilde{\Omega}_r\,\tilde{F}_r(\omega). \tag{B.5}$$

Considering a hysteretic damping model, the mass-normalised resonant term is given by

$$\tilde{\Omega}_r = \frac{j\omega}{M_r\left[\omega_r^2(1+j\eta)-\omega^2\right]} \tag{B.6}$$

where ω_r is the r-th natural frequency, η is the modal damping loss factor and M_r is the modal mass for the r-th natural mode, which is given by

$$M_r = \rho h \int_0^{l_x} \int_0^{l_y} [\phi_r(x,y)]^2 \, dx \, dy, \tag{B.7}$$

where ρ is the panel mass density and h is the panel thickness. If the panel is simply supported, the natural modeshape function $\phi_r(x,y)$ can take the form

$$\phi_r(x,y) = 2 \sin\left(\frac{m_r \pi x}{l_x}\right) \sin\left(\frac{n_r \pi y}{l_y}\right) \tag{B.8}$$

where, m_r is the modal order in the x-direction and n_r is the modal order in the y-direction for the r-th mode. In this case $M_r = \rho h \, l_x \, l_y = M$, where M is the total mass of the panel. The corresponding modal excitation term is given by

$$\tilde{F}_r(\omega) = \int_0^{l_x} \int_0^{l_y} \phi_r(x,y) \, \tilde{f}(x,y,\omega) \, dx \, dy. \tag{B.9}$$

Mode truncation

If the modal summation in Equation (B.4) is truncated to the sum over the first N modal terms, so that

$$\tilde{\dot{w}}(x,y,\omega) \approx \sum_{r=1}^{N} \phi_r(x,y) \tilde{\dot{a}}_r(\omega), \tag{B.10}$$

after substituting Equation (B.5), the velocity at an arbitrary point of the panel can be cast into the following matrix form

$$\tilde{\dot{w}}(x,y,\omega) = \mathbf{\Phi} \, \tilde{\dot{\mathbf{a}}} = \mathbf{\Phi} \, \tilde{\mathbf{\Omega}} \, \tilde{\mathbf{F}}, \tag{B.11}$$

where

$$\tilde{\mathbf{\Omega}} = \begin{bmatrix} \tilde{\Omega}_1 & & \\ & \ddots & \\ & & \tilde{\Omega}_N \end{bmatrix} \tag{B.12}$$

is a diagonal matrix containing the first N resonant terms from Equation (B.6),

$$\mathbf{\Phi} = \left[\begin{array}{cccc} \phi_1(x,y) & \phi_2(x,y) & \cdots & \phi_N(x,y) \end{array} \right], \tag{B.13}$$

is a row vector containing the first N natural modes,

$$\tilde{\dot{\mathbf{a}}} = \left[\begin{array}{cccc} \tilde{\dot{a}}_1 & \tilde{\dot{a}}_2 & \cdots & \tilde{\dot{a}}_N \end{array} \right]^T, \tag{B.14}$$

is a column vector containing the first N modal velocities and

$$\tilde{\mathbf{F}} = \left[\begin{array}{cccc} \tilde{F}_1 & \tilde{F}_2 & \cdots & \tilde{F}_N \end{array} \right]^T \tag{B.15}$$

is a column vector containing the first N modal excitations. Note that the modal formulation involves the evaluation of the spatial integrals in Equation (B.9).

B.1.2 Elemental approach

In the elemental approach the panel surface is subdivided in a uniform grid of N_e panel elements of dimensions $\Delta x \times \Delta y$. The element excitation and response is defined at the element centres. This allows the integration over the panel dimensions in Equation (B.9) to be replaced by a finite sum over element contributions to give

$$\tilde{F}_r(w) \approx \sum_{i=1}^{N_e} \phi_r(x_i, y_i)\, \tilde{f}(x_i, y_i, \omega)\, \Delta x\, \Delta y. \tag{B.16}$$

Therefore a vector of complex element velocities

$$\tilde{\dot{\mathbf{w}}}_e = \left[\begin{array}{cccc} \tilde{\dot{w}}_{e_1} & \tilde{\dot{w}}_{e_2} & \cdots & \tilde{\dot{w}}_{e_{N_e}} \end{array} \right]^T \tag{B.17}$$

can be derived from equation (B.11) as follows

$$\tilde{\dot{\mathbf{w}}}_e(\omega) = \mathbf{\Phi}_e \tilde{\dot{\mathbf{a}}} = \mathbf{\Phi}_e \tilde{\mathbf{\Omega}} \mathbf{\Phi}_e^T \tilde{\mathbf{F}}_e \tag{B.18}$$

where $\mathbf{\Phi}_e$ is a $[N_e \times N]$ matrix with N_e rows each containing the first N natural modes at the centres of the panel elements

$$\mathbf{\Phi}_e = \begin{bmatrix} \phi_1(x_1, y_1) & \cdots & \phi_N(x_1, y_1) \\ \vdots & \ddots & \vdots \\ \phi_1(x_{N_e}, y_{N_e}) & \cdots & \phi_N(x_{N_e}, y_{N_e}) \end{bmatrix} \tag{B.19}$$

and $\tilde{\mathbf{F}}_e$ is the N_e-dimensional vector of discrete excitation forces at the centres of the panel elements

$$\tilde{\mathbf{F}}_e = \begin{bmatrix} \tilde{F}_{e_1} & \tilde{F}_{e_2} & \cdots & \tilde{F}_{e_{N_e}} \end{bmatrix}^T. \tag{B.20}$$

The approximation of the surface integrals in Equation (B.9) by the sum over element contributions simplifies the analysis of panels with arbitrary boundary conditions and arbitrary spatial excitation fields that lead to complex mode functions and complex pressure distribution functions that should be considered in the integral in Equation (B.9).

B.2 Time-averaged total panel kinetic energy

The instantaneous total kinetic energy of the panel is given by the product of the panel mass per unit area and the squared panel velocity integrated over the panel surface [19]:

$$E(t) = \frac{1}{2} \int_0^{l_x} \int_0^{l_y} \rho h \, \dot{w}^2(x, y, t) dx \, dy, \tag{B.21}$$

where l_x and l_y are the dimensions of a rectangular panel in the x and the y-directions, ρh is the panel mass per unit area and $\dot{w}(x, y, t)$ is the transverse panel velocity. Assuming the panel mass per unit area is constant, Equation (B.21) can be rewritten as

$$E(t) = \frac{\rho h}{2} \int_0^{l_x} \int_0^{l_y} \dot{w}^2(x, y, t) dx \, dy. \tag{B.22}$$

The time-averaged total panel energy is given by [67, 68]:

$$\overline{E} = \frac{\rho h}{2} \int_0^{l_x} \int_0^{l_y} \frac{1}{T} \int_0^T \dot{w}^2(x, y, t) dt \, dx \, dy \tag{B.23}$$

where T is a suitable period of time over which the mean square velocity is estimated; e.g. for time-harmonic vibration , T is the period. Assuming time-harmonic vibration as given in Equation (B.2), the time-average integral can be rewritten in terms of the magnitude of the complex panel velocity $\tilde{\dot{w}}(x, y, \omega)$ to give

$$\frac{1}{T}\int_0^T \dot{w}^2(x, y, t)dt = \frac{1}{2}\left|\tilde{\dot{w}}(x, y, \omega)\right|^2, \tag{B.24}$$

which yields the time-averaged total kinetic energy of the panel as

$$\overline{E} = E(\omega) = \frac{\rho h}{4}\int_0^{l_x}\int_0^{l_y}\left|\tilde{\dot{w}}(x, y, \omega)\right|^2 dx\, dy. \tag{B.25}$$

B.2.1 Modal formulation

Using the vector notation for the truncated modal summation of the transverse velocity of the panel given in Equation (B.11), the total panel kinetic energy in Equation (B.25) can be rewritten as

$$\begin{aligned} E(\omega) &= \frac{\rho h}{4}\int_0^{l_x}\int_0^{l_y}\tilde{\dot{\mathbf{a}}}^H(\omega)\,\boldsymbol{\Phi}^T\,\boldsymbol{\Phi}\,\tilde{\dot{\mathbf{a}}}(\omega)\,dx\,dy, \\ &= \frac{\rho h}{4}\,\tilde{\dot{\mathbf{a}}}^H(\omega)\int_0^{l_x}\int_0^{l_y}\boldsymbol{\Phi}^T\,\boldsymbol{\Phi}\,dx\,dy\,\tilde{\dot{\mathbf{a}}}(\omega), \end{aligned} \tag{B.26}$$

where ^{H} denotes the Hermitian transpose. The orthogonality property gives

$$\int_0^{l_x}\int_0^{l_y}\phi_r(x, y)\,\phi_s(x, y)\,dx\,dy = 0, \qquad r \neq s \tag{B.27}$$

and

$$\int_0^{l_x}\int_0^{l_y}\phi_r(x, y)\phi_r(x, y)dx\,dy = l_x l_y, \tag{B.28}$$

where $l_x l_y$ is the total surface area of the panel. Thus the integration over the panel surface

in Equation (B.26) results in

$$
\begin{aligned}
E(\omega) &= \frac{\rho h}{4}\begin{bmatrix} \tilde{\dot{a}}_1^* & \tilde{\dot{a}}_2^* & \cdots & \tilde{\dot{a}}_N^* \end{bmatrix}\begin{bmatrix} \int\int \phi_1\phi_1 & \cdots & \int\int \phi_1\phi_N \\ \vdots & \ddots & \vdots \\ \int\int \phi_N\phi_1 & \cdots & \int\int \phi_N\phi_N \end{bmatrix}\begin{bmatrix} \tilde{\dot{a}}_1 \\ \vdots \\ \tilde{\dot{a}}_N \end{bmatrix} \\
&= \frac{\rho h}{4}\begin{bmatrix} \tilde{\dot{a}}_1^* & \tilde{\dot{a}}_2^* & \cdots & \tilde{\dot{a}}_N^* \end{bmatrix}\begin{bmatrix} l_x l_y & & \\ & \ddots & \\ & & l_x l_y \end{bmatrix}\begin{bmatrix} \tilde{\dot{a}}_1 \\ \vdots \\ \tilde{\dot{a}}_N \end{bmatrix}, \qquad \text{(B.29)}
\end{aligned}
$$

which can be expressed in terms of the modal velocities vector defined in Equation (B.14):

$$
\begin{aligned}
E(\omega) &= \frac{\rho h\, l_x l_y}{4}\begin{bmatrix} \tilde{\dot{a}}_1^* & \cdots & \tilde{\dot{a}}_N^* \end{bmatrix}\begin{bmatrix} \tilde{\dot{a}}_1 \\ \vdots \\ \tilde{\dot{a}}_N \end{bmatrix} \\
&= \frac{M}{4}\,\tilde{\dot{\mathbf{a}}}^H(\omega)\,\tilde{\dot{\mathbf{a}}}(\omega), \qquad \text{(B.30)}
\end{aligned}
$$

where M represents the total mass of the panel.

B.2.2 Elemental approach

In the elemental approach the spatial integral in Equation (B.25) is replaced by a summation over a grid of elements to give

$$
\begin{aligned}
E(\omega) &= \frac{\rho h}{4}\sum_{n=1}^{N_e} A_e\,|\tilde{\dot{w}}(x_n, y_n, \omega)|^2 \\
&= \frac{M_e}{4}\sum_{n=1}^{N_e} |\tilde{\dot{w}}(x_n, y_n, \omega)|^2. \qquad \text{(B.31)}
\end{aligned}
$$

where A_e and M_e the area and mass of a single panel element. Using the matrix notation for the element approach in Section B.1.2, Equation (B.31) can be written as

$$E(\omega) = \frac{M_e}{4} \left[\begin{array}{ccc} \tilde{\dot{w}}_1^* & \cdots & \tilde{\dot{w}}_{N_e}^* \end{array} \right] \left[\begin{array}{c} \tilde{\dot{w}}_1 \\ \vdots \\ \tilde{\dot{w}}_{N_e} \end{array} \right]$$
$$= \frac{M_e}{4} \tilde{\dot{\mathbf{w}}}_e^H(\omega)\, \tilde{\dot{\mathbf{w}}}_e(\omega). \tag{B.32}$$

B.3 Time-averaged total radiated sound power

The instantaneous total sound power radiated is given by the product of panel velocity and acoustic pressure on the panel surface, integrated over the dimensions of the panel [19]:

$$P(t) = \int_0^{l_x} \int_0^{l_y} \dot{w}(x,y,t)\, p(x,y,0,t) dx\, dy, \tag{B.33}$$

where $\dot{w}(x,y,t)$ is the panel velocity and $p(x,y,0,t)$ is the surface sound pressure on the radiating side of the panel. The time-averaged total radiated sound power is given by [67, 68]

$$\overline{P} = \int_0^{l_x} \int_0^{l_y} \frac{1}{T} \int_0^{T} \dot{w}(x,y,t)\, p(x,y,0,t)\, dt\, dx\, dy \tag{B.34}$$

where T is a suitable period of time over which to estimate the mean radiated sound power. Assuming time-harmonic vibration, the time-average integral can be rewritten in terms of the complex panel velocity $\tilde{\dot{w}}(x,y,\omega)$ and complex surface pressure fluctuations $\tilde{p}(x,y,0,\omega)$

$$\overline{P} = P(\omega) = \frac{1}{2} \int_0^{l_x} \int_0^{l_y} Re\left\{ \tilde{\dot{w}}^*(x,y,\omega)\, \tilde{p}(x,y,0,\omega) \right\} dx\, dy. \tag{B.35}$$

The complex surface pressure $\tilde{p}(x,y,0,\omega)$ for time-harmonic vibrations of a planar surface is given by the Rayleigh integral [19]

$$\tilde{p}(x,y,0,\omega) = \frac{j\omega\rho_0}{2\pi}\int_0^{l_x}\int_0^{l_y}\tilde{\dot{w}}(x',y',\omega)\,\frac{e^{-jk_0R}}{R}\,dx'\,dy' \tag{B.36}$$

where $R=\sqrt{(x-x')^2+(y-y')^2}$ is the distance between two points on the panel, k_0 is the acoustic wavenumber in the surrounding medium and ρ_0 is the mass density of the surrounding medium on the radiating side of the panel. Thus substituting Equation (B.36) into Equation (B.35) gives

$$\begin{aligned}
P(\omega) &= \frac{1}{2}Re\left\{\int_0^{l_x}\int_0^{l_y}\tilde{\dot{w}}(x,y,\omega)^*\,\frac{j\omega\rho_0}{2\pi}\int_0^{l_x}\int_0^{l_y}\tilde{\dot{w}}(x',y',\omega)\,\frac{e^{-jk_0R}}{R}\,dx\,dy\,dx'\,dy'\right\}\\
&= \frac{1}{2}Re\left\{\int_0^{l_x}\int_0^{l_y}\int_0^{l_x}\int_0^{l_y}\frac{j\omega\rho_0}{2\pi}\left[\frac{\cos(kR)-j\sin(kR)}{R}\right]\tilde{\dot{w}}^*(x,y,\omega)\,\tilde{\dot{w}}(x',y',\omega)\,dx'\,dy'\,dx\,dy\right\}\\
&= \frac{\omega\rho_0}{4\pi}\int_0^{l_x}\int_0^{l_y}\int_0^{l_x}\int_0^{l_y}\frac{\sin(kR)}{R}\,\tilde{\dot{w}}^*(x,y,\omega)\,\tilde{\dot{w}}(x',y',\omega)\,dx'\,dy'\,dx\,dy\\
&= \frac{\omega^2\rho_0}{4\pi c_0}\int_0^{l_x}\int_0^{l_y}\int_0^{l_x}\int_0^{l_y}\frac{\sin(kR)}{kR}\,\tilde{w}^*(x,y,\omega)\,\tilde{w}(x',y',\omega)\,dx'\,dy'\,dx\,dy
\end{aligned} \tag{B.37}$$

B.3.1 Modal formulation

Substituting the modal expression for the transverse velocity of Equation (B.4) into Equation (B.37) gives

$$\begin{aligned}
P(\omega) &= \frac{\omega^2\rho_0}{4\pi c_0}\int_0^{l_x}\int_0^{l_y}\int_0^{l_x}\int_0^{l_y}\frac{\sin(kR)}{kR}\sum_{r=1}\phi_r(x,y)\tilde{\dot{a}}_r^*\sum_{s=1}\phi_s(x',y')\tilde{\dot{a}}_s\,dx'\,dy'\,dx\,dy\\
&= \sum_{r=1}\sum_{s=1}\tilde{\dot{a}}_r^*\tilde{\dot{a}}_s\frac{\omega^2\rho_0}{4\pi c_0}\int_0^{l_x}\int_0^{l_y}\int_0^{l_x}\int_0^{l_y}\phi_r(x,y)\frac{\sin(kR)}{kR}\,\phi_s(x',y')dx'\,dy'\,dx\,dy
\end{aligned} \tag{B.38}$$

Considering the vector notation for modal truncation to the first N terms in Section B.1.1, Equation (B.38) can be cast in the following matrix formulation [19]

$$
\begin{aligned}
P(\omega) &= \left[\begin{array}{ccc} \tilde{\dot{a}}_1^* \cdots & \tilde{\dot{a}}_N^* \end{array} \right] \left[\begin{array}{ccc} A_{1,1} & \cdots & A_{1,N} \\ \vdots & \ddots & \vdots \\ A_{N,1} & \cdots & A_{N,N} \end{array} \right] \left[\begin{array}{c} \tilde{\dot{a}}_1 \\ \cdots \\ \tilde{\dot{a}}_N \end{array} \right] \\
&= \tilde{\dot{\mathbf{a}}}^H \, \mathbf{A} \, \tilde{\dot{\mathbf{a}}}, \qquad \text{(B.39)}
\end{aligned}
$$

where $\mathbf{A}$ is the power transfer matrix with the elements $A_{r,s}$ given by

$$
A_{r,s} = \frac{\omega \rho_0}{4\pi} \int_0^{l_x} \int_0^{l_y} \int_0^{l_x} \int_0^{l_y} \phi_r(x,y) \, \frac{\sin\left(k_0 R\right)}{R} \, \phi_s(x',y') \, dx' \, dy' \, dx \, dy. \qquad \text{(B.40)}
$$

B.3.2 Elemental approach

In the elemental approach the spatial integrals in Equation (B.37) are replaced by summations over the uniform grid of panel elements. According to the notations defined in Section B.1.2, this gives

$$
P(\omega) = \frac{\omega^2 \rho_0}{4\pi c_0} \sum_{i=1}^{N_e} \sum_{j=1}^{Ne} \frac{\sin(kR_{i,j})}{kR_{i,j}} \, \tilde{\dot{w}}^*(x_i, y_i, \omega) \, \tilde{\dot{w}}(x_j', y_j,' \omega) \, dx' \, dy' \, dx \, dy,
$$

which can be cast in the following matrix expression

$$
\begin{aligned}
P(\omega) &= \left[\begin{array}{ccc} \tilde{\dot{w}}_1^* & \cdots & \tilde{\dot{w}}_{N_e}^* \end{array} \right] \left[\begin{array}{ccc} R_{rad_{1,1}} & \cdots & R_{rad_{1,N_e}} \\ \vdots & \ddots & \vdots \\ R_{rad_{N_e,1}} & \cdots & R_{rad_{N_e,N_e}} \end{array} \right] \left[\begin{array}{c} \tilde{\dot{w}}_1 \\ \vdots \\ \tilde{\dot{w}}_{N_e} \end{array} \right] \qquad \text{(B.41)} \\
&= \tilde{\dot{\mathbf{w}}}_e^{\,H} \, \mathbf{R}_{rad} \, \tilde{\dot{\mathbf{w}}}_e \qquad \text{(B.42)}
\end{aligned}
$$

where $\tilde{\dot{\mathbf{w}}}_e$ denotes the vector of element velocities given in Equation (B.17) and $\mathbf{R}_{rad}$ denotes the element radiation matrix with the elements $R_{rad_{i,j}}(\omega)$ given by [19]:

$$
R_{rad_{i,j}}(\omega) = \frac{\omega^2 \rho_0 A_e^2}{4\pi c_0} \, \frac{\sin\left(k_0 R_{i,j}\right)}{k_0 R_{i,j}}, \qquad \text{(B.43)}
$$

where the diagonal terms of the radiation matrix $R_{i,i}(\omega)$ reduce to

$$R_{rad_{i,i}}(\omega) = \frac{\omega^2 \rho_0 A_e^2}{4\pi c_0}. \tag{B.44}$$

Note that the radiation matrix is proportional to the radiation resistance matrix, i.e. proportional to the real part of the radiation impedance matrix

$$\mathbf{R}_{rad}(\omega) = \frac{A_e}{2} Re\left\{\tilde{\mathbf{Z}}_{rad}\right\}, \tag{B.45}$$

where the elements of the elemental radiation impedance matrix $\tilde{\mathbf{Z}}_{rad}$ are given by

$$\tilde{Z}_{rad_{i,j}}(\omega) = \frac{j\omega\rho_0 A_e}{2\pi} \frac{e^{-jk_0 R_{i,j}}}{R_{i,j}}. \tag{B.46}$$

B.4 Power spectral density of total kinetic energy

It can be demonstrated [11], that the power spectral density of $x(t)$ is given by

$$S_{xx}(\omega) = \lim_{T\to\infty} E\left[\frac{1}{T}\tilde{X}^*(\omega)\tilde{X}(\omega)\right], \tag{B.47}$$

where $\tilde{X}(\omega)$ is the finite Fourier transform of $X(t)$:

$$\tilde{X}(\omega) = \frac{1}{2\pi}\int_0^T X(t)e^{-j\omega t}\,dt \tag{B.48}$$

and $E[\ ]$ denotes the expectation for an infinite sample length. Thus considering the general formulation for the instantaneous total kinetic energy in Equation (B.21), the power spectral density of the total kinetic energy S_E, due to a time and spatial stochastic disturbance over the panel surface, can be written as [67]:

$$S_E(\omega) = \frac{1}{2}\int_0^{l_x}\int_0^{l_y} \rho h \lim_{T\to\infty} E\left[\frac{1}{T}\tilde{\dot{w}}^*(x,y,\omega)\tilde{\dot{w}}(x,y,\omega)\right] dx\,dy, \tag{B.49}$$

B.4.1 Modal formulation

Substituting the modal expression for the transverse velocity of Equation (B.4), into Equation (B.49) gives

$$\begin{aligned} S_E(\omega) &= \frac{1}{2}\int_0^{l_x}\int_0^{l_y} \rho h \lim_{T\to\infty} E\left[\frac{1}{T}\sum_{r=1}^{\infty}\phi_r(x,y)\tilde{\dot{a}}_r^*(\omega)\sum_{s=1}^{\infty}\phi_s(x,y)\tilde{\dot{a}}_s(\omega)\right] dx\,dy \\ &= \frac{1}{2}\int_0^{l_x}\int_0^{l_y} \rho h \sum_{r=1}^{\infty}\sum_{s=1}^{\infty}\phi_r(x,y)\phi_s(x,y) \lim_{T\to\infty} E\left[\frac{1}{T}\tilde{\dot{a}}_r^*(\omega)\tilde{\dot{a}}_s(\omega)\right] dx\,dy. \end{aligned} \quad \text{(B.50)}$$

Assuming ρh=constant and considering the orthogonality conditions in Equations (B.27) and (B.28) results in

$$\begin{aligned} S_E(\omega) &= \frac{1}{2}\rho h \sum_{r=1}^{\infty}\sum_{s=1}^{\infty}\int_0^{l_x}\int_0^{l_y}\phi_r(x,y)\phi_s(x,y)S_{\dot{a}_r\dot{a}_s}dx\,dy \\ &= \frac{1}{2}\rho h \sum_{r=1}^{\infty}\int_0^{l_x}\int_0^{l_y}\phi_r(x,y)^2 dx\,dy\, S_{\dot{a}_r\dot{a}_r} \\ &= \frac{M}{2}\sum_{r=1}^{\infty} S_{\dot{a}_r\dot{a}_r}, \end{aligned} \quad \text{(B.51)}$$

where $S_{\dot{a}_r\dot{a}_r}$ is the power spectral density of modal velocities

$$S_{\dot{a}_r\dot{a}_r}(\omega) = \lim_{T\to\infty} E\left[\frac{1}{T}\tilde{\dot{a}}_r^*(\omega)\tilde{\dot{a}}_r(\omega)\right] = \lim_{T\to\infty} E\left[\frac{1}{T}\left|\tilde{\dot{a}}_r(\omega)\right|^2\right] \quad \text{(B.52)}$$

and M is the mass of the panel. Substituting Equation (B.5) into Equation (B.52) gives

$$\begin{aligned} S_{\dot{a}_r\dot{a}_r}(\omega) &= \lim_{T\to\infty} E\left[\frac{1}{T}\tilde{\Omega}_r^*(\omega)\tilde{F}_r^*(\omega)\tilde{\Omega}_r(\omega)\tilde{F}_r(\omega)\right] \\ &= \lim_{T\to\infty} E\left[\frac{1}{T}\left|\tilde{\Omega}_r(\omega)\right|^2\tilde{F}_r^*(\omega)\tilde{F}_r(\omega)\right] \\ &= \left|\tilde{\Omega}_r(\omega)\right|^2 \lim_{T\to\infty} E\left[\frac{1}{T}\tilde{F}_r^*(\omega)\tilde{F}_r(\omega)\right]. \end{aligned}$$

Substituting the formulation for the modal excitation terms in Equation (B.9) then gives

$$\begin{aligned} S_{\dot{a}_r\dot{a}_r}(\omega) &= \left|\tilde{\Omega}_r(\omega)\right|^2 \lim_{T\to\infty} E\left[\frac{1}{T}\int_0^{l_x}\int_0^{l_y} \phi_r(x,y)\,\tilde{f}^*(x,y,\omega)\,dx\,dy \int_0^{l_x}\int_0^{l_y} \phi_r(x',y')\,\tilde{f}(x',y',\omega)\,dx'\,dy'\right] \\ &= \left|\tilde{\Omega}_r(\omega)\right|^2 \int_0^{l_x}\int_0^{l_y}\int_0^{l_x}\int_0^{l_y} \phi_r(x,y)\,\phi_r(x',y') \lim_{T\to\infty} E\left[\frac{1}{T}\tilde{f}^*(x,y,\omega)\,\tilde{f}(x',y',\omega)\right] dx\,dy\,dx'\,dy' \\ &= \left|\tilde{\Omega}_r(\omega)\right|^2 \int_0^{l_x}\int_0^{l_y}\int_0^{l_x}\int_0^{l_y} \phi_r(x,y)\,\phi_r(x',y')\,\tilde{S}_{ff}(x,y,x',y',\omega)dx\,dy\,dx'\,dy', \end{aligned} \tag{B.53}$$

where $\tilde{S}_{ff}(x,y,x',y',\omega)$ is the cross-spectral density of the stochastic disturbance between positions (x,y) and (x',y'), which can be expressed as the product of the power spectral density $\Psi(\omega)$ and the spatial correlation function $\tilde{C}(x,y,x',y',\omega)$ of the disturbance so that

$$\tilde{S}_{ff}(x,y,x',y',\omega) = \Psi(\omega)\,\tilde{C}(x,y,x',y',\omega). \tag{B.54}$$

Both the power spectral density $\Psi(\omega)$ and spatial correlation function $\tilde{C}(x,y,x',y',\omega)$ are specific properties of the disturbance. Formulations that describe the the spatial correlation functions for ADF and TBL excitation are given in Chapter 2, Section 2.1.2. Substituting Equation (B.53) back into Equation (B.50) gives the final expression for the power spectral density of total kinetic energy due to a disturbance which is stochastic in time and space as

$$S_E(\omega) = \frac{M}{2}\sum_{r=1}^{\infty}\left|\tilde{\Omega}_r(\omega)\right|^2 \int_0^{l_x}\int_0^{l_y}\int_0^{l_x}\int_0^{l_y} \phi_r(x,y)\,\phi_r(x',y')\,\tilde{S}_{ff}(x,y,x',y',\omega)dx\,dy\,dx'\,dy'. \tag{B.55}$$

B.4.2 Elemental approach

According to the notations in Section B.1.2, the spatial integral in Equation (B.49) can be replaced by a summation of element contributions, so that the power spectral density of the total kinetic energy due to time and spatial stochastic disturbances is given by

$$S_E(\omega) = \frac{1}{2}\sum_{i=1}^{N_e} \rho h\, A_e \lim_{T\to\infty} E\left[\frac{1}{T}\tilde{\dot{w}}^*(x_i,y_i,\omega)\,\tilde{\dot{w}}(x_i,y_i,\omega)\right] \tag{B.56}$$

where A_e denotes the area of a single panel element and $\tilde{\dot{w}}(x_i,y_i,\omega)$ is the transverse velocity of the i-th element. Using the vector formulation for the elemental velocities given in Equation (B.18) the expression for the power spectral density becomes

$$\begin{aligned}
S_E(\omega) &= \frac{M_e}{2}\sum_{i=1}^{N_e}\lim_{T\to\infty} E\left[\frac{1}{T}\tilde{\dot{w}}_i^*(\omega)\,\tilde{\dot{w}}_i(\omega)\right] \\
&= \frac{M_e}{2}\,trace\left(\lim_{T\to\infty} E\left[\frac{1}{T}\begin{bmatrix}\tilde{\dot{w}}_1\\ \vdots \\ \tilde{\dot{w}}_{N_e}\end{bmatrix}\begin{bmatrix}\tilde{\dot{w}}_1^* & \cdots & \tilde{\dot{w}}_{N_e}^*\end{bmatrix}\right]\right) \\
&= \frac{M_e}{2}\,trace\left(\lim_{T\to\infty} E\left[\frac{1}{T}\left[\tilde{\dot{\mathbf{w}}}_e\tilde{\dot{\mathbf{w}}}_e^H\right]\right]\right) \\
&= \frac{M_e}{2}\,trace\left(\lim_{T\to\infty} E\left[\frac{1}{T}\left[\mathbf{\Phi}_e\tilde{\dot{\mathbf{a}}}\,\tilde{\dot{\mathbf{a}}}^H\mathbf{\Phi}_e^T\right]\right]\right) \\
&= \frac{M_e}{2}\,trace\left(\mathbf{\Phi}_e\lim_{T\to\infty} E\left[\frac{1}{T}\left[\tilde{\dot{\mathbf{a}}}\,\tilde{\dot{\mathbf{a}}}^H\right]\right]\mathbf{\Phi}_e^T\right) \\
&= \frac{M_e}{2}\,trace\left(\mathbf{\Phi}_e\tilde{\mathbf{S}}_{\dot{a}\dot{a}}(\omega)\mathbf{\Phi}_e^T\right),
\end{aligned} \tag{B.57}$$

where $\tilde{\mathbf{S}}_{\dot{a}\dot{a}}(\omega)$ is the $[N\times N]$ matrix of power and cross-spectral densities of the modal velocities. According to Equation (B.18) the vector of modal velocities is given by

$$\tilde{\dot{\mathbf{a}}} = \tilde{\mathbf{\Omega}}\mathbf{\Phi}_e^T\tilde{\mathbf{F}}_e, \tag{B.58}$$

thus $\tilde{\mathbf{S}}_{\dot{a}\dot{a}}(\omega)$ can be written as

$$\begin{aligned}
\tilde{\mathbf{S}}_{\dot{a}\dot{a}}(\omega) &= \lim_{T\to\infty} E\left[\frac{1}{T}\left[\tilde{\dot{\mathbf{a}}}\,\tilde{\dot{\mathbf{a}}}^H\right]\right] \\
&= \lim_{T\to\infty} E\left[\frac{1}{T}\tilde{\mathbf{\Omega}}^H\mathbf{\Phi}_e^T\tilde{\mathbf{F}}_e\tilde{\mathbf{F}}_e^H\mathbf{\Phi}_e\tilde{\mathbf{\Omega}}\right] \\
&= \tilde{\mathbf{\Omega}}\mathbf{\Phi}_e^T\lim_{T\to\infty} E\left[\frac{1}{T}\tilde{\mathbf{F}}_e\tilde{\mathbf{F}}_e^H\right]\mathbf{\Phi}_e\tilde{\mathbf{\Omega}}^H \\
&= \tilde{\mathbf{\Omega}}\,\mathbf{\Phi}_e^T\,\tilde{\mathbf{S}}_{f_ef_e}(\omega)\,\mathbf{\Phi}_e\,\tilde{\mathbf{\Omega}}^H,
\end{aligned} \tag{B.59}$$

where $\tilde{\mathbf{S}}_{f_e f_e}(\omega)$ is the $[N_e \times N_e]$ matrix containing the power and cross-spectral densities of the element excitation forces, which has the form

$$\tilde{\mathbf{S}}_{f_e f_e} = \begin{bmatrix} \tilde{S}_{f_1,f_1} & \cdots & \tilde{S}_{f_1,f_{N_e}} \\ \vdots & \ddots & \vdots \\ \tilde{S}_{f_{N_e},f_1} & \cdots & \tilde{S}_{f_{N_e},f_{N_e}} \end{bmatrix} \tag{B.60}$$

with the elements

$$\tilde{S}_{f_i f_j}(\omega) = \tilde{S}_{ff}\left(x_i, y_i, x_j, y_j, \omega\right), \tag{B.61}$$

as defined in Equation (B.54). Substituting the final expression in Equation (B.59) back into the Equation (B.57) gives

$$\begin{aligned} S_E(\omega) &= \frac{M_e}{2}\, trace\left(\boldsymbol{\Phi}_e\, \tilde{\boldsymbol{\Omega}}\, \boldsymbol{\Phi}_e^T\, \tilde{\mathbf{S}}_{f_e f_e}(\omega)\, \boldsymbol{\Phi}_e\, \tilde{\boldsymbol{\Omega}}^H\, \boldsymbol{\Phi}_e\right) \\ &= \frac{M_e}{2}\, trace\left(\tilde{\mathbf{Y}}_{ee}\tilde{\mathbf{S}}_{f_e f_e}(\omega)\tilde{\mathbf{Y}}_{ee}^H\right), \end{aligned} \tag{B.62}$$

where $\tilde{\mathbf{Y}}_{ee} = \boldsymbol{\Phi}_e\tilde{\boldsymbol{\Omega}}\boldsymbol{\Phi}_e^T$ is the $[N_e \times N_e]$ matrix of element point and transfer mobilities.

B.5 Power spectral density of total sound power radiated

Considering the general formulation for the instantaneous total radiated sound power given in Equation (B.33) and considering the relationship for the spectral density given in Equation (B.47), the power spectral density of the total sound power radiated due to disturbances which are stochastic in time and space is given by

$$S_P(\omega) = Re\left\{\int_0^{l_x}\int_0^{l_y} \lim_{T\to\infty} E\left[\frac{1}{T}\tilde{\dot{w}}^*(x,y,\omega)\tilde{p}(x,y,0,\omega)\right] dx\, dy\right\}. \tag{B.63}$$

Substituting the Rayleigh integral expression for $\tilde{p}(x,y,0,\omega)$ from Equation (B.36) gives

$$S_P(\omega) = Re\left\{ \frac{j\omega\rho_0}{2\pi} \int_0^{l_x}\int_0^{l_y}\int_0^{l_x}\int_0^{l_y} \frac{e^{-jk_0R}}{R} \lim_{T\to\infty} E\left[\frac{1}{T}\,\tilde{\dot{w}}^*(x,y,\omega)\tilde{\dot{w}}(x',y',\omega)\right] dx'\,dy'\,dx\,dy \right\}. \quad \text{(B.64)}$$

B.5.1 Modal formulation

Substituting the modal expression for the transverse velocity of Equation (B.4) into Equation (B.64) gives

$$\begin{aligned}
S_P(\omega) &= Re\left\{ \frac{j\omega\rho_0}{2\pi} \int_0^{l_x}\int_0^{l_y}\int_0^{l_x}\int_0^{l_y} \frac{e^{-jk_0R}}{R} \lim_{T\to\infty} E\left[\frac{1}{T}\sum_{r=1}^{\infty}\phi_r(x,y)\tilde{\dot{a}}_r^*(\omega)\sum_{s=1}^{\infty}\phi_s(x',y')\tilde{\dot{a}}_s(\omega)\right] dx\,dy\,dx'\,dy' \right\} \\
&= Re\left\{ \frac{j\omega\rho_0}{2\pi} \int_0^{l_x}\int_0^{l_y}\int_0^{l_x}\int_0^{l_y} \sum_{r=1}^{\infty}\sum_{s=1}^{\infty}\phi_r(x,y)\frac{e^{-jk_0R}}{R}\phi_s(x',y') \lim_{T\to\infty} E\left[\frac{1}{T}\,\tilde{\dot{a}}_r^*(\omega)\tilde{\dot{a}}_s(\omega),\right] dx\,dy\,dx'\,dy' \right\} \\
&= \sum_{r=1}^{\infty}\sum_{s=1}^{\infty} Re\left\{ \frac{j\omega\rho_0}{2\pi} \int_0^{l_x}\int_0^{l_y}\int_0^{l_x}\int_0^{l_y} \phi_r(x,y)\,\frac{e^{-jk_0R}}{R}\,\phi_s(x',y')\,\tilde{S}_{\dot{a}_r\dot{a}_s} dx\,dy\,dx'\,dy' \right\}, \quad \text{(B.65)}
\end{aligned}$$

where $\tilde{S}_{\dot{a}_r\dot{a}_s}$ denotes the spectral densities of the the modal velocities. Substituting the formulation for the modal velocities of Equation (B.5) gives

$$\begin{aligned}
S_{\dot{a}_r\dot{a}_s}(\omega) &= \lim_{T\to\infty} E\left[\frac{1}{T}\tilde{\dot{a}}_r^*(\omega)\tilde{\dot{a}}_s(\omega)\right] \\
&= \lim_{T\to\infty} E\left[\frac{1}{T}\,\tilde{\Omega}_r^*(\omega)\tilde{F}_r^*(\omega)\tilde{\Omega}_s(\omega)\tilde{F}_s(\omega)\right] \\
&= \tilde{\Omega}_r(\omega)\tilde{\Omega}_s^*(\omega) \lim_{T\to\infty} E\left[\frac{1}{T}\,\tilde{F}_r^*(\omega)\tilde{F}_s(\omega)\right]. \quad \text{(B.66)}
\end{aligned}$$

Substituting the formulation for the modal excitation terms in Equation (B.9) then gives

$$
\begin{aligned}
S_{\dot{a}_r\dot{a}_s}(\omega) &= \tilde{\Omega}_r(\omega)\tilde{\Omega}_s^*(\omega) \lim_{T\to\infty} E\left[\frac{1}{T}\int_0^{l_x}\int_0^{l_y} \phi_r(x,y)\,\tilde{f}^*(x,y,\omega)\,dx\,dy \int_0^{l_x}\int_0^{l_y} \phi_s(x',y')\,\tilde{f}(x',y',\omega)\,dx'\,dy'\right] \\
&= \tilde{\Omega}_r(\omega)\tilde{\Omega}_s^*(\omega) \int_0^{l_x}\int_0^{l_y}\int_0^{l_x}\int_0^{l_y} \phi_r(x,y)\,\phi_s(x',y') \lim_{T\to\infty} E\left[\frac{1}{T}\tilde{f}^*(x,y,\omega)\,\tilde{f}(x',y',\omega)\right] dx\,dy\,dx'\,dy' \\
&= \tilde{\Omega}_r(\omega)\tilde{\Omega}_s^*(\omega) \int_0^{l_x}\int_0^{l_y}\int_0^{l_x}\int_0^{l_y} \phi_r(x,y)\,\phi_s(x',y')\,\tilde{S}_{ff}(x,y,x',y',\omega)dx\,dy\,dx'\,dy'. \qquad \text{(B.67)}
\end{aligned}
$$

Finally, substituting this expression for the spectral density of the the modal velocities back into Equation (B.65) gives

$$
\begin{aligned}
S_P(\omega) &= \sum_{r=1}^{N}\sum_{s=1}^{N} \tilde{\Omega}_r(\omega)\tilde{\Omega}_s^*(\omega) \\
&\quad \times Re\left\{ \frac{j\omega\rho_0}{2\pi} \int_0^{l_x}\int_0^{l_y}\int_0^{l_x}\int_0^{l_y} \phi_r(x,y)\,\frac{e^{-jk_0R}}{R}\,\phi_s(x',y')\,dx\,dy\,dx'\,dy' \right. \\
&\quad \left. \times \int_0^{l_x}\int_0^{l_y}\int_0^{l_x}\int_0^{l_y} \phi_r(x,y)\,\phi_s(x',y')\,\tilde{S}_{ff}(x,y,x',y',\omega)\,dx\,dy\,dx'\,dy' \right\}. \qquad \text{(B.68)}
\end{aligned}
$$

B.5.2 Elemental approach

Replacing the spatial integrals in Equation (B.64) by a finite summation over all panel elements gives the following expression for the power spectral density of the total sound power radiated due to disturbances which are stochastic in time and space:

$$
\begin{aligned}
S_P(\omega) &= Re\left\{ \frac{j\omega\rho_0 A_e^2}{2\pi} \sum_{i=1}^{N_e}\sum_{j=1}^{N_e} \frac{e^{-jkR_{i,j}}}{R_{i,j}} \lim_{T\to\infty} E\left[\frac{1}{T}\tilde{\dot{w}}^*(x_i,y_i,\omega)\,\tilde{\dot{w}}(x_i,y_i,\omega)\right]\right\} \\
&= 2\lim_{T\to\infty} E\left[\frac{1}{T}\begin{bmatrix} \tilde{\dot{w}}_1^* & \cdots & \tilde{\dot{w}}_{N_e}^* \end{bmatrix} \begin{bmatrix} R_{rad_{1,1}} & \cdots & R_{rad_{1,N_e}} \\ \vdots & \ddots & \vdots \\ R_{rad_{N_e,1}} & \cdots & R_{rad_{N_e,N_e}} \end{bmatrix} \begin{bmatrix} \tilde{\dot{w}}_1 \\ \vdots \\ \tilde{\dot{w}}_{N_e} \end{bmatrix}\right] \\
&= 2\lim_{T\to\infty} E\left[\frac{1}{T}\,\tilde{\dot{\mathbf{w}}}_e^H\,\mathbf{R}_{rad}\,\tilde{\dot{\mathbf{w}}}_e\right], \qquad \text{(B.69)}
\end{aligned}
$$

where $\mathbf{R}_{rad}$ is the elemental radiation impedance matrix as defined in Equations (B.43) to (B.46). Equation (B.69) can be rewritten to give

$$\begin{aligned} S_P(\omega) &= 2\,trace\left(\lim_{T\to\infty} E\left[\frac{1}{T}\,\tilde{\dot{\mathbf{w}}}_e\,\tilde{\dot{\mathbf{w}}}_e^{\,H}\,\mathbf{R}_{rad}\right]\right) \\ &= 2\,trace\left(\lim_{T\to\infty} E\left[\frac{1}{T}\,\boldsymbol{\Phi}_e\,\tilde{\dot{\mathbf{a}}}\tilde{\dot{\mathbf{a}}}^H\,\boldsymbol{\Phi}_e^T\,\mathbf{R}_{rad}\right]\right) \\ &= 2\,trace\left(\boldsymbol{\Phi}_e\,\tilde{\mathbf{S}}_{\dot{a}\dot{a}}\boldsymbol{\Phi}_e^T\,\mathbf{R}_{rad}\right), \end{aligned} \tag{B.70}$$

where the $[N \times N]$ matrix of power and cross-spectral densities of the modal velocities $\tilde{\mathbf{S}}_{\dot{a}\dot{a}}$ is derived in Equation (B.59), so that:

$$\begin{aligned} S_P(\omega) &= 2\,trace\left(\left[\boldsymbol{\Phi}_e\,\tilde{\boldsymbol{\Omega}}\,\boldsymbol{\Phi}_e^T\,\tilde{\mathbf{S}}_{f_e f_e}\,\boldsymbol{\Phi}_e\,\tilde{\boldsymbol{\Omega}}^H\,\boldsymbol{\Phi}_{e,r}^T\right]\mathbf{R_{rad}}\right) \\ &= 2\,trace\left(\left[\tilde{\mathbf{Y}}_{ee}\,\tilde{\mathbf{S}}_{f_e f_e}\,\tilde{\mathbf{Y}}_{ee}^H\right]\mathbf{R_{rad}}\right), \end{aligned} \tag{B.71}$$

where $\tilde{\mathbf{Y}}_{ee}$ is the $[N_e \times N_e]$ matrix of element point and transfer mobilities and $\tilde{\mathbf{S}}_{f_e f_e}$ is the matrix containing the power and cross-spectral densities of the element excitation forces given in Equation (B.60).

Appendix C

Formulations for the base impedance of proof-mass electrodynamic actuators

This Appendix provides the derivation of the open and closed loop base impedance for current- and voltage-driven feedback control units, which they apply to the structure at the point where they are mounted. The open loop response functions for single feedback loops and decentralised multiple input multiple output (MIMO) feedback control systems are then formulated using the expressions for open and closed loop actuator base impedances.

Figure C.1 shows the standard block diagram which is normally used to describe the response of a structure with a multi-channel feedback control system, as discussed in Reference [45] for example. In this block diagram the matrices $\tilde{\mathbf{G}}$ contain frequency response functions between the error/monitor sensors and the control/primary excitations including the control unit passive responses while $\tilde{\mathbf{H}}(g)$ contains solely the control functions.

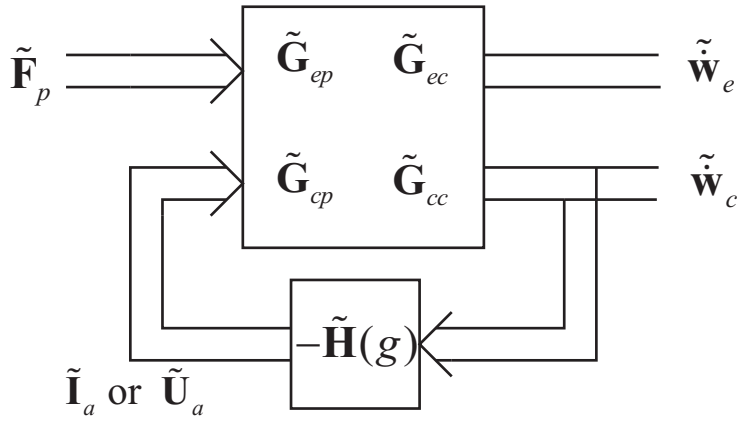

Figure C.1: Block diagram of the multi-channel velocity-feedback control system, with the system plant response $\tilde{\mathbf{G}}$ containing the panel response and also the control unit dynamics.

Figure C.2 shows the alternative block diagram proposed in this study, where the frequency response functions in the matrices $\tilde{\mathbf{Y}}$ do not include the passive effects of the control units which are instead included in the feedback loop via the $\tilde{\mathbf{Z}}_a(g)$ matrix, which contains the open and closed loop base impedance of the control units. This notation gives a better insight into the system dynamics since it formally separates the dynamic properties of the structure under control from the dynamics of the control units.

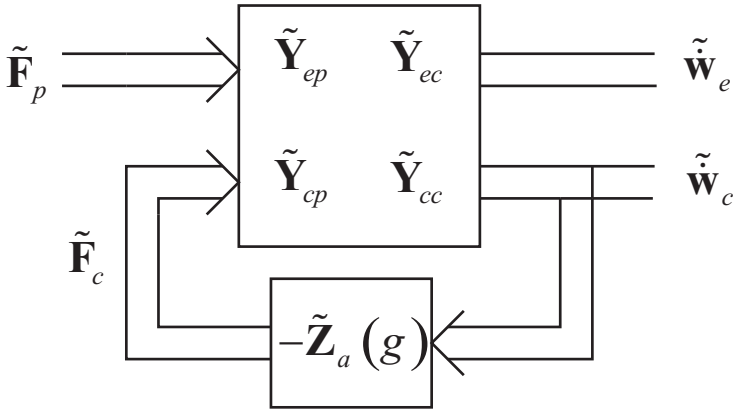

Figure C.2: Block diagram of the multi-channel velocity-feedback control system, with the plant response of the panel $\tilde{\mathbf{Y}}$ and the base impedance $\tilde{\mathbf{Z}}_a(g)$ of the control units.

C.1 Base impedance with general actuator force

The force balance for the control unit shown in Figure C.3 can be expressed by the following set of linear equations

$$\tilde{f}_c = -\left(\tilde{Z}_s + \tilde{Z}_{m_1}\right)\tilde{\dot{w}}_c + \tilde{Z}_s\tilde{\dot{w}}_{m_2} + \tilde{f}_a \tag{C.1}$$

$$\tilde{f}_{m_2} = \tilde{Z}_s\tilde{\dot{w}}_c - \tilde{Z}_s\tilde{\dot{w}}_{m_2} - \tilde{f}_a. \tag{C.2}$$

In these equations $\tilde{Z}_s = c_s + k_s/(j\omega)$ is the actuator suspension impedance, where k_s and c_s are the mechanical stiffness and damping coefficient of the proof-mass suspension. The suspension damping coefficient combines mechanical damping effects, viscous damping effects due to fluid flow in the air gaps and Eddy current damping which is due to the relative velocity between the conductive actuator parts which are attached to the structure and the magnetic field of the actuator permanent magnet. The term $\tilde{Z}_{m_1} = j\omega m_1$ represents the mechanical impedance of the actuator mounting mass m_1 which, in this model, is assumed

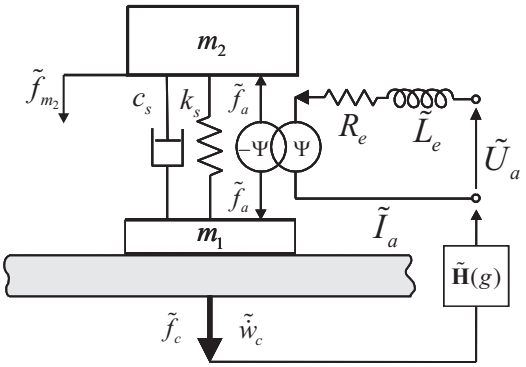

Figure C.3: Actuator schematic view.

to be rigidly attached to the structure and includes both the actuator base mass and the mass of the control sensor. Also, $\tilde{\dot{w}}_c$ is the velocity of the structure at the point where the control unit is mounted and $\tilde{\dot{w}}_{m_2}$ is the velocity of the actuator proof-mass m_2. $\tilde{f}_c$ is the effective control force acting on the structure, $\tilde{f}_{m_2}$ is the force acting on the actuator proof-mass m_2 and $\tilde{f}_a$ is the force developed by the actuator voice coil motor. The velocity of the actuator proof-mass is given by

$$\tilde{\dot{w}}_{m_2} = \tilde{Z}_{m_2}^{-1} f_{m_2}, \tag{C.3}$$

where $\tilde{Z}_{m_2} = j\omega m_2$ is the impedance of the actuator proof-mass. Substituting Equation (C.3) into Equation (C.1) and (C.2) gives

$$\tilde{f}_c = -\left(\tilde{Z}_s + \tilde{Z}_{m_1}\right)\tilde{\dot{w}}_c + \tilde{Z}_s\tilde{Z}_{m_2}^{-1} f_{m_2} + \tilde{f}_a \tag{C.4}$$

$$\tilde{f}_{m_2} = \tilde{Z}_s\tilde{\dot{w}}_c - \tilde{Z}_s\tilde{Z}_{m_2}^{-1} f_{m_2} - \tilde{f}_a. \tag{C.5}$$

The force on the actuator proof-mass can therefore be written as

$$\tilde{f}_{m_2} = \left(1 + \tilde{Z}_s\tilde{Z}_{m_2}^{-1}\right)^{-1}\tilde{Z}_s\tilde{\dot{w}}_c - \left(1 + \tilde{Z}_s\tilde{Z}_{m_2}^{-1}\right)^{-1}\tilde{f}_a. \tag{C.6}$$

Substituting Equation (C.5) into Equation (C.4) yields the control force f_c as

$$\begin{aligned}\tilde{f}_c = \;\; = \;\; & -\left[\left(\tilde{Z}_s + \tilde{Z}_{m_1}\right) - \tilde{Z}_s\tilde{Z}_{m_2}^{-1}\left(1 + \tilde{Z}_s\tilde{Z}_{m_2}^{-1}\right)^{-1}\tilde{Z}_s\right]\tilde{\dot{w}}_c \\ & + \left[1 - \tilde{Z}_s\tilde{Z}_{m_2}^{-1}\left(1 + \tilde{Z}_s\tilde{Z}_{m_2}^{-1}\right)^{-1}\right]\tilde{f}_a. \end{aligned} \tag{C.7}$$

C.2 Control current

In the case of a current-driven voice coil, the force $\tilde{f}_a$ produced by the voice coil motor is given by

$$\tilde{f}_a = \Psi I_a, \tag{C.8}$$

where Ψ is the transducer coefficient of the voice coil-magnet system and I_a is the current through the voice coil. In the case of velocity feedback control this current is given by

$$\begin{aligned}\tilde{I}_a \;\; &= \;\; -\tilde{H}(g)\tilde{\dot{w}}_c, \\ &= \;\; -\tilde{C}g\tilde{\dot{w}}_c, \end{aligned} \tag{C.9}$$

where $\tilde{H}(g) = \tilde{C}g$ is the feedback control function, which is given by the product of the gain-normalised frequency response function (FRF) of the controller $\tilde{C}$ and the feedback gain g. For ideal proportional velocity feedback the controller FRF is unity for all frequencies, for integral feedback (displacement) by $\tilde{C} = 1/(j\omega)$ and for differential feedback (acceleration) by $\tilde{C} = j\omega$. Substituting Equations (C.8) and (C.9) into Equation (C.7), the control force can be expressed in terms of a passive and an active actuator base impedance, so that

$$\begin{aligned}\tilde{f}_c \;\; &= \;\; -\left[\tilde{Z}_{passive,I} + \tilde{Z}_{active,I}\,\tilde{C}g\right]\tilde{\dot{w}}_c \\ &= \;\; -\left[\left(\left(\tilde{Z}_s + \tilde{Z}_{m_1}\right) - \tilde{Z}_s\tilde{Z}_{m_2}^{-1}\left(1 + \tilde{Z}_s\tilde{Z}_{m_2}^{-1}\right)^{-1}\tilde{Z}_s\right)\right. \\ &\quad \left. + \left(\Psi\,\tilde{C}g\left(1 - \tilde{Z}_s\tilde{Z}_{m_2}^{-1}\left(1 + \tilde{Z}_s\tilde{Z}_{m_2}^{-1}\right)^{-1}\right)\right)\right]\tilde{\dot{w}}_c. \end{aligned} \tag{C.10}$$

Rewriting Equation (C.10) gives

$$\tilde{f}_c = -\left[\left(\tilde{Z}_s + \tilde{Z}_{m_1} - \frac{\tilde{Z}_s^2}{\tilde{Z}_{m_2} + \tilde{Z}_s}\right) + \Psi\,\tilde{C}g\left(1 - \frac{\tilde{Z}_s}{\tilde{Z}_{m_2} + \tilde{Z}_s}\right)\right]\tilde{\dot{w}}_c. \tag{C.11}$$

From Equation (C.11) it can be seen that in the limiting case that the proof mass m_2 of the actuator tends to zero, the base impedance of the actuator reduces to the impedance of the actuator mounting mass $\tilde{Z}_{m_1}$

$$\tilde{f}_c\Big|_{\lim m_2 \to 0} = -\tilde{Z}_{m_1}\tilde{\dot{w}}_c. \tag{C.12}$$

Also in the limiting case that the proof-mass tends to infinity, the base impedance of the actuator reduces to

$$\tilde{f}_c\Big|_{\lim m_2 \to \infty} = -\left[\left(\tilde{Z}_s + \tilde{Z}_{m_1}\right) + \Psi\,\tilde{C}g\right]\tilde{\dot{w}}_c. \tag{C.13}$$

With increasing frequency the impedance of the mounting mass m_1 becomes the dominating term in Equation (C.11). This will limit the frequency range over which an active control force can be applied. The mounting mass m_1 of the actuator should therefore be as small as possible. The performance of the actuator increases with increasing actuator proof mass m_2, which should therefore be as large as possible.

C.3 Control voltage

In the case of a voltage-driven voice coil, the force $\tilde{f}_a$ produced by the voice coil motor can be derived from the relationship between the current, the driving voltage and the back electromotive force (back emf), which is generated by the relative motion between the magnet and the coil

$$\tilde{Z}_e I_a = U_a - \Psi(\tilde{\dot{w}}_c - \tilde{\dot{w}}_{m_2}), \tag{C.14}$$

where $\tilde{Z}_e = R_e + j\omega L_e$ is the electrical impedance of the the voice coil motor with the voice coil resistance R_e and inductance L_e. Rearranging Equation (C.14) for $\tilde{I}_a$ and substituting Equation (C.8) gives the force produced by the voice coil motor as

$$\tilde{f}_a = \Psi I_a = \frac{\Psi U_a}{\tilde{Z}_e} - \frac{\Psi^2}{\tilde{Z}_e}(\tilde{\dot{w}}_c - \tilde{\dot{w}}_{m_2}). \tag{C.15}$$

Assuming velocity feedback, the driving voltage is given by

$$U_a = -\tilde{C}g\tilde{\dot{w}}_c, \tag{C.16}$$

so that

$$\tilde{f}_a = -\frac{\Psi\tilde{C}g}{\tilde{Z}_e}\tilde{\dot{w}}_c - \frac{\Psi^2}{\tilde{Z}_e}(\tilde{\dot{w}}_c - \tilde{\dot{w}}_{m_2}). \tag{C.17}$$

Since the force produced by a voltage-driven voice coil motor depends on the back emf force, which is a function of the difference between the control velocity $\tilde{\dot{w}}_c$ and the velocity of the actuator proof mass $\tilde{\dot{w}}_{m_2}$, the force balance in Equations (C.1) and (C.2) is reformulated to give

$$\tilde{f}_c = -\left(\tilde{Z}_s + \tilde{Z}_{m_1}\right)\tilde{\dot{w}}_c + \tilde{Z}_s\tilde{\dot{w}}_{m_2} - \frac{\Psi\tilde{C}g}{\tilde{Z}_e}\tilde{\dot{w}}_c - \frac{\Psi^2}{\tilde{Z}_e}\tilde{\dot{w}}_c + \frac{\Psi^2}{\tilde{Z}_e}\tilde{\dot{w}}_{m_2} \tag{C.18}$$

$$\tilde{f}_{m_2} = \tilde{Z}_s\tilde{\dot{w}}_c - \tilde{Z}_s\tilde{\dot{w}}_{m_2} + \frac{\Psi\tilde{C}g}{\tilde{Z}_e}\tilde{\dot{w}}_c + \frac{\Psi^2}{\tilde{Z}_e}\tilde{\dot{w}}_c - \frac{\Psi^2}{\tilde{Z}_e}\tilde{\dot{w}}_{m_2}. \tag{C.19}$$

Substituting the expression for the velocity of the actuator proof mass in Equation (C.3) in to (C.18) gives

$$\tilde{f}_c = -\left(\tilde{Z}_s + \tilde{Z}_{m_1}\right)\tilde{\dot{w}}_c + \tilde{Z}_s\tilde{Z}_{m_2}^{-1}f_{m_2} + \frac{\Psi\tilde{C}g}{\tilde{Z}_e}\tilde{\dot{w}}_c - \frac{\Psi^2}{\tilde{Z}_e}\tilde{\dot{w}}_c + \frac{\Psi^2}{\tilde{Z}_e}\tilde{Z}_{m_2}^{-1}f_{m_2} \tag{C.20}$$

$$\tilde{f}_{m_2} = \tilde{Z}_s\tilde{\dot{w}}_c - \tilde{Z}_s\tilde{Z}_{m_2}^{-1}f_{m_2} + \frac{\Psi\tilde{C}g}{\tilde{Z}_e}\tilde{\dot{w}}_c + \frac{\Psi^2}{\tilde{Z}_e}\tilde{\dot{w}}_c - \frac{\Psi^2}{\tilde{Z}_e}\tilde{Z}_{m_2}^{-1}f_{m_2}. \tag{C.21}$$

The force acting on the actuator proof mass can therefore be written as

$$
\begin{aligned}
\tilde{f}_{m_2} &= \left(1+\tilde{Z}_s\tilde{Z}_{m_2}^{-1}+\frac{\Psi^2}{\tilde{Z}_e}\tilde{Z}_{m_2}^{-1}\right)^{-1}\tilde{Z}_s\dot{\tilde{w}}_c \\
&\quad+\left(1+\tilde{Z}_s\tilde{Z}_{m_2}^{-1}+\frac{\Psi^2}{\tilde{Z}_e}\tilde{Z}_{m_2}^{-1}\right)^{-1}\frac{\Psi\tilde{C}g}{\tilde{Z}_e}\tilde{w}_c \\
&\quad+\left(1+\tilde{Z}_s\tilde{Z}_{m_2}^{-1}+\frac{\Psi^2}{\tilde{Z}_e}\tilde{Z}_{m_2}^{-1}\right)^{-1}\frac{\Psi^2}{\tilde{Z}_e}\tilde{w}_c. \qquad \text{(C.22)}
\end{aligned}
$$

Substituting Equation (C.22) into Equation (C.20) yields the control force f_c as

$$
\begin{aligned}
\tilde{f}_c &= -\left(\tilde{Z}_s+\tilde{Z}_{m_1}\right)\dot{\tilde{w}}_c \\
&\quad+\tilde{Z}_s\tilde{Z}_{m_2}^{-1}\left(1+\tilde{Z}_s\tilde{Z}_{m_2}^{-1}+\frac{\Psi^2}{\tilde{Z}_e}\tilde{Z}_{m_2}^{-1}\right)^{-1}\tilde{Z}_s\dot{\tilde{w}}_c \\
&\quad+\tilde{Z}_s\tilde{Z}_{m_2}^{-1}\left(1+\tilde{Z}_s\tilde{Z}_{m_2}^{-1}+\frac{\Psi^2}{\tilde{Z}_e}\tilde{Z}_{m_2}^{-1}\right)^{-1}\frac{\Psi\tilde{C}g}{\tilde{Z}_e}\tilde{w}_c \\
&\quad+\tilde{Z}_s\tilde{Z}_{m_2}^{-1}\left(1+\tilde{Z}_s\tilde{Z}_{m_2}^{-1}+\frac{\Psi^2}{\tilde{Z}_e}\tilde{Z}_{m_2}^{-1}\right)^{-1}\frac{\Psi^2}{\tilde{Z}_e}\tilde{w}_c \\
&\quad-\frac{\Psi\tilde{C}g}{\tilde{Z}_e}\dot{\tilde{w}}_c \\
&\quad-\frac{\Psi^2}{\tilde{Z}_e}\tilde{w}_c \\
&\quad+\frac{\Psi^2}{\tilde{Z}_e}\tilde{Z}_{m_2}^{-1}\left(1+\tilde{Z}_s\tilde{Z}_{m_2}^{-1}+\frac{\Psi^2}{\tilde{Z}_e}\tilde{Z}_{m_2}^{-1}\right)^{-1}\tilde{Z}_s\dot{\tilde{w}}_c \\
&\quad+\frac{\Psi^2}{\tilde{Z}_e}\tilde{Z}_{m_2}^{-1}\left(1+\tilde{Z}_s\tilde{Z}_{m_2}^{-1}+\frac{\Psi^2}{\tilde{Z}_e}\tilde{Z}_{m_2}^{-1}\right)^{-1}\frac{\Psi\tilde{C}g}{\tilde{Z}_e}\tilde{w}_c \\
&\quad+\frac{\Psi^2}{\tilde{Z}_e}\tilde{Z}_{m_2}^{-1}\left(1+\tilde{Z}_s\tilde{Z}_{m_2}^{-1}+\frac{\Psi^2}{\tilde{Z}_e}\tilde{Z}_{m_2}^{-1}\right)^{-1}\frac{\Psi^2}{\tilde{Z}_e}\tilde{w}_c. \qquad \text{(C.23)}
\end{aligned}
$$

Rearranging Equation (C.23) and combining the passive and the active terms, which contain the feedback control function, results in

$$
\begin{aligned}
\tilde{f}_c &= -\left[\tilde{Z}_{passive,U} + \tilde{Z}_{active,U}\,\tilde{C}g\right]\tilde{\dot{w}}_c \\
&= -\left[\left(\tilde{Z}_s + \tilde{Z}_{m_1} + \frac{\Psi^2}{\tilde{Z}_e} - \frac{\left(\tilde{Z}_s + \frac{\Psi^2}{\tilde{Z}_e}\right)^2}{\tilde{Z}_{m_2} + \tilde{Z}_s + \frac{\Psi^2}{\tilde{Z}_e}}\right)\right. \\
&\quad \left. + \tilde{C}g\,\frac{\Psi}{\tilde{Z}_e}\left(1 - \frac{\tilde{Z}_s + \frac{\Psi^2}{\tilde{Z}_e}}{\tilde{Z}_{m_2} + \tilde{Z}_s + \frac{\Psi^2}{\tilde{Z}_e}}\right)\right]\tilde{\dot{w}}_c. \qquad \text{(C.24)}
\end{aligned}
$$

For the limiting case that the proof mass m_2 of the actuator tends to zero, the base impedance of the actuator reduces to the impedance of the actuator mounting mass $\tilde{Z}_{m_1}$ which is the same as in Equation (C.12). In the limiting case that the proof mass tends to infinity, the base impedance of the actuator reduces to

$$
\tilde{f}_c\Big|_{\lim m_2 \to \infty} = -\left[\left(\tilde{Z}_s + \tilde{Z}_{m_1} + \frac{\Psi^2}{\tilde{Z}_e}\right) + \tilde{C}g\,\frac{\Psi}{\tilde{Z}_e}\right]\tilde{\dot{w}}_c. \qquad \text{(C.25)}
$$

To produce a control voltage signal from a voltage sensor signal it is necessary to use a voltage amplifier. An ideal amplifier of this type has an infinite input impedance and a zero output resistance.

C.4 Open loop response function for single channel control

The open loop response function for a single control channel can be derived from the velocity response at the control position in absence of primary excitation

$$
\tilde{\dot{w}}_c = \tilde{Y}_c \tilde{f}_c \qquad \text{(C.26)}
$$

where $\tilde{Y}_c$ is the point mobility of the structure at the control position. The control force $\tilde{f}_c$ is given by

$$
\tilde{f}_c = -\tilde{Z}_{passive}\tilde{\dot{w}}_c - \tilde{Z}_{active}\,\tilde{C}\,g\,\tilde{\dot{w}}_c \qquad \text{(C.27)}
$$

Substituting Equation (C.27) into Equation (C.26) gives

$$\tilde{\dot{w}}_c = -\tilde{Y}_c \tilde{Z}_{passive} \tilde{\dot{w}}_c - \tilde{Y}_c \tilde{Z}_{active}\, \tilde{C}\, g\, \tilde{\dot{w}}_c \tag{C.28}$$

As discussed previously, both passive and active impedance functions depend on the type of control signal that is used, i.e. if current or voltage is supplied to the voice coil motor. Assuming an input current proportional to velocity $\tilde{I}_a = -\tilde{C}\, g\, \tilde{\dot{w}}_c$, Equation (C.28) gives

$$\tilde{\dot{w}}_c = -\tilde{Y}_c \tilde{Z}_{passive_I} \tilde{\dot{w}}_c + \tilde{Y}_c \tilde{Z}_{active_I} \tilde{I}_a. \tag{C.29}$$

The open loop frequency response function $\tilde{H}_I$ for a single current-controlled feedback loop with unit feedback is given by

$$\tilde{H}_I = \frac{\tilde{\dot{w}}_c\, \tilde{C}}{\tilde{I}_a} = \frac{\tilde{Y}_c \tilde{Z}_{active_I}\, \tilde{C}}{1 + \tilde{Y}_c \tilde{Z}_{passive_I}}, \tag{C.30}$$

which is

$$\tilde{H}_I = \frac{\tilde{Y}_c\, \tilde{C}\, \Psi \left(1 - \frac{\tilde{Z}_s}{\tilde{Z}_{m_2} + \tilde{Z}_s}\right)}{1 + \tilde{Y}_c \left(\tilde{Z}_s + \tilde{Z}_{m_1} - \frac{\tilde{Z}_s^2}{\tilde{Z}_{m_2} + \tilde{Z}_s}\right)}. \tag{C.31}$$

Similarly assuming a velocity proportional input voltage, $\tilde{U}_a = -\tilde{C}\, g\, \tilde{\dot{w}}_c$ the open loop response function for a single feedback loop is given by

$$\tilde{H}_U = \frac{\tilde{\dot{w}}_c \tilde{C}}{\tilde{U}_a} = \frac{\tilde{Y}_c \tilde{Z}_{active_U} \tilde{C}}{1 + \tilde{Y}_c \tilde{Z}_{passive_U}}, \tag{C.32}$$

which is

$$\tilde{H}_U = \frac{\tilde{Y}_c\, \tilde{C}\, \frac{\Psi}{\tilde{Z}_e} \left(1 - \frac{\tilde{Z}_s + \frac{\Psi^2}{\tilde{Z}_e}}{\tilde{Z}_{m_2} + \tilde{Z}_s + \frac{\Psi^2}{\tilde{Z}_e}}\right)}{1 + \tilde{Y}_c \left(\tilde{Z}_s + \tilde{Z}_{m_1} + \frac{\Psi^2}{\tilde{Z}_e} - \frac{\left(\tilde{Z}_s + \frac{\Psi^2}{\tilde{Z}_e}\right)^2}{\tilde{Z}_{m_2} + \tilde{Z}_s + \frac{\Psi^2}{\tilde{Z}_e}}\right)}. \tag{C.33}$$

C.5 Open loop response for multi-channel control

The open loop response function for a decentralised multi-channel control system can be derived from the velocity responses at all control positions in the absence of primary excitation

$$\dot{\tilde{\mathbf{w}}}_c = \tilde{\mathbf{Y}}_{cc}\tilde{\mathbf{f}}_c \tag{C.34}$$

where $\tilde{\dot{\mathbf{w}}}_c$ is the $[N_c \times 1]$ vector of control point velocities, $\tilde{f}_c$ is the $[N_c \times 1]$ vector of feedback control forces and $\tilde{\mathbf{Y}}_{cc}$ is the $[N_c \times N_c]$ matrix of point and transfer mobilities between the control points. The vector of control forces can be expressed as

$$\tilde{\mathbf{f}}_c = -\tilde{\mathbf{Z}}_{passive}\tilde{\dot{\mathbf{w}}}_c - \tilde{\mathbf{Z}}_{active}\,\tilde{\mathbf{C}}\,\mathbf{g}\,\tilde{\dot{\mathbf{w}}}_c \tag{C.35}$$

where $\tilde{\mathbf{Z}}_{passive}$ is the $[N_c \times N_c]$ diagonal matrix containing the passive actuator impedance terms, $\tilde{\mathbf{Z}}_{active}$ is the $[N_c \times N_c]$ diagonal matrix containing the active actuator base impedance terms, $\tilde{\mathbf{C}}$ is the $[N_c \times N_c]$ diagonal matrix controlling the Controller FRFs and $\mathbf{g}$ is the $[N_c \times N_c]$ diagonal matrix containing the feedback control gains. Substituting Equation (C.35) into Equation (C.34) gives

$$\tilde{\dot{\mathbf{w}}}_c = -\tilde{\mathbf{Y}}_{cc}\tilde{\mathbf{Z}}_{passive}\tilde{\dot{\mathbf{w}}}_c - \tilde{\mathbf{Y}}_{cc}\tilde{\mathbf{Z}}_{active}\,\tilde{\mathbf{C}}\,\mathbf{g}\,\tilde{\dot{\mathbf{w}}}_c \tag{C.36}$$

Setting the matrix of drive currents to $\tilde{\mathbf{I}}_a = -\tilde{\mathbf{C}}\,\mathbf{g}\,\tilde{\dot{\mathbf{w}}}_c$ gives

$$\tilde{\mathbf{H}}_I = \tilde{\dot{\mathbf{w}}}_c\,\tilde{\mathbf{C}}\,\tilde{\mathbf{I}}_a^{-1} = \tilde{\mathbf{Y}}_{cc}\tilde{\mathbf{Z}}_{active_I}\,\tilde{\mathbf{C}}\,\left(\mathbf{I} + \tilde{\mathbf{Y}}_{cc}\tilde{\mathbf{Z}}_{passive_I}\right)^{-1}, \tag{C.37}$$

where $\mathbf{I}$ is the $[N_c \times N_c]$ identity matrix and $\tilde{\mathbf{H}}_I$ is the fully populated $[N_c \times N_c]$ matrix containing the control system open loop frequency response functions for the current-controlled actuators. Similarly, for voltage control, setting the matrix of driving voltages to $\tilde{\mathbf{U}}_a = -\tilde{\mathbf{C}}\,\mathbf{g}\,\tilde{\dot{\mathbf{w}}}_c$ gives

$$\tilde{\mathbf{H}}_U = \tilde{\dot{\mathbf{w}}}_c\,\tilde{\mathbf{C}}\,\tilde{\mathbf{U}}_a^{-1} = \tilde{\mathbf{Y}}_{cc}\tilde{\mathbf{Z}}_{active_U}\,\tilde{\mathbf{C}}\,\left(\mathbf{I} + \tilde{\mathbf{Y}}_{cc}\tilde{\mathbf{Z}}_{passive_U}\right)^{-1}, \tag{C.38}$$

where $\tilde{\mathbf{H}}_U$ is the fully populated $[N_c \times N_c]$ matrix containing the control system open loop frequency response functions for the voltage controlled actuators.

Appendix D

Parameter estimation for honeycomb test panel

This Appendix presents the initial experimental tests carried out on the structural response of the honeycomb test panel. These studies have been conducted to estimate the principal structural parameters of the panel which are then used to model the panel response.

- Section D.1 gives the test panel geometry, material specification and the structural parameters which are estimated from fitting the model for an anisotropic sandwich panel to the experimentally determined panel response.
- Section D.2 gives the formulations used to model an anisotropic sandwich panel with free boundary conditions on all edges.
- Section D.3 describes the experimental set-up and also presents the experimental and corresponding simulation results.

D.1 The honeycomb panel

The honeycomb test panel has the dimensions $l_x \approx 500$ mm and $l_x \approx 400$ mm. According to the manufacturer both face plates are made of carbon reinforced resin with three plies and an overall thickness of $h_f = 0.86$ mm and were manufactured in an out-of-autoclave process. The honeycomb core is made of phenolic resin material (HRP) with 3/8 inch (9.5 mm) cell width and a thickness of 7/8 inch (22.2 mm). The panel has a total mass of 0.856 kg. The mass per unit area is 4.28 kg/m^{-2} which corresponds to that of a homogeneous

aluminium panel of 1.6 mm thickness. The estimated structural parameters are summarised in Table D.1. The determination of these parameters is described further below.

Table D.1: Cross section geometry and physical properties for the honeycomb sandwich test panel.

Parameter	Symbol	Value	Unit
Thickness of face plate	h_f	0.86	mm
Core depth	d	23.09	mm
Mass density face plates	ρ_f	1250	kg m^{-3}
Mass density core	ρ_c	96	kg m^{-3}
Panel mass per unit area[1]	m''	4.28	kg m^{-2}
Young's modulus face-plates x-axis	E_x	48	GPa
Young's modulus face-plates y-axis	E_y	43	GPa
Shear modulus core x-axis	G_x	82	MPa
Shear modulus core y-axis	G_y	155	MPa
Poisson's ratio face plates	ν_f	0.33	–
Poisson's ratio sandwich plate	ν	0	–
Loss factor	η	0.015	–
Anisotropic factor	α	0.035	–

[1] $m'' = 2h_f\rho_f + (d - h_f)\rho_c$

D.2 Model for anisotropic sandwich panel

The transverse bending stiffness of honeycomb sandwich panels is frequency-dependent [19, 58] and anisotropic with respect to the x- and y-axes [61]. The principal material properties of the core are the out-of-plane shear moduli G_x and G_y [62].

The frequency-dependent dynamic response of the composite sandwich panel is modelled using a basic theory [19, 58] which considers pure undistorted bending of the cross-section and the face-plates and pure undistorted transverse shear of the core. The relationship between the transverse wavenumber k and the wavenumbers corresponding to pure bending and to pure shear of a sandwich panel is given by

$$1 + \left(\frac{k_s}{k_b}\right)^2 \left(\frac{k}{k_b}\right)^2 - \left(\frac{k}{k_b}\right)^4 - \left(\frac{k_b}{k_{bf}}\right)^4 \left(\frac{k_s}{k_b}\right)^2 \left(\frac{k}{k_b}\right)^6 = 0, \tag{D.1}$$

where k_s is the shear wavenumber in the absence of transverse bending forces, k_b is the overall cross-section bending wavenumber in the absence of shear distortion and k_{bf} is the bending wavenumber for face-plate bending alone. These wavenumbers are given as

$$\text{(a)}\ k_s^2 = \frac{m''\omega^2}{G\,d}, \qquad \text{(b)}\ k_b^4 = \frac{m''\omega^2}{D_1}, \qquad \text{(c)}\ k_{bf}^4 = \frac{m''\omega^2}{2\,D_2}, \tag{D.2}$$

where m'' is the total panel mass per unit area, G is the transverse core shear modulus and, as shown in Figure D.1, d is the distance between the face-plates neutral axis, which assuming that d is much larger than the thickness of the face-plates is also used to represent the core thickness. D_1 is the bending stiffness of the cross-section and D_2 is the bending stiffness of an individual face-plate. These flexural stiffness terms are given by

$$\text{(a)}\ D_1 = \frac{Ed^2 h_f}{2\left(1-\nu_f^2\right)}, \qquad \text{(b)}\ D_2 = \frac{Eh_f^3}{12\left(1-\nu_f^2\right)}. \tag{D.3}$$

where $h_f << d$ is the face-plate thickness.

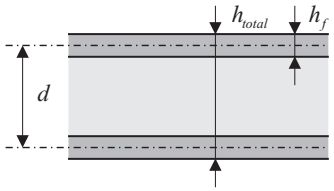

Figure D.1: Sketch of sandwich panel cross section geometry.

Equation (D.1) has one real and two imaginary pairs of axi-symmetric solutions. For simplicity the mode shapes of the honeycomb panel in the x- and y-directions are assumed to be those of a corresponding thin beam with free boundary conditions and it is assumed that the equivalent flexural rigidity D, is given by

$$D = \frac{\omega^2\, m''}{k^4}, \tag{D.4}$$

where the wavenumber k in Equation (D.4) is the real wavenumber solution of Equation (D.2), which corresponds to travelling waves. The imaginary wavenumber solutions to Equation (D.1) correspond to decaying near-field waves, which are neglected in the model. According to References [61, 63] the natural frequencies of an anisotropic rectangular panel can be estimated as

$$\omega_{m,n} = \frac{\pi^2}{\sqrt{m''}}\sqrt{D_x\left(\frac{G_m}{l_x}\right)^4 D_y\left(\frac{G_n}{l_y}\right)^4 + \frac{2J_mJ_n + 2\nu(H_mH_n - J_mJ_n)}{(l_x l y)^2}\alpha\sqrt{D_xD_y}}, \tag{D.5}$$

In the above equation the parameters G, J and H depend on the mode order in x- and y-directions, m and n, and the boundary conditions, which for this study are chosen as those for free boundary conditions [47, 48] (compare Appendix 2, Section A.2). The parameter α

is adjusted to give good agreement between predicted and measured natural frequencies for the [rocking, rocking] mode of the panel [61]. For a sandwich panel the bending stiffnesses D_x and D_y are frequency-dependent and need to be evaluated at $\omega = \omega_{m,n}$. A Regular-Falsi root search algorithm [49] is employed to estimate the panel natural frequencies that satisfy the relationship

$$0 = \omega^2 - \frac{\pi^4}{m''}\left(D_x(\omega)\left(\frac{G_m}{l_x}\right)^4 D_y(\omega)\left(\frac{G_n}{l_y}\right)^4 + \frac{2J_mJ_n + 2\nu(H_mH_n - J_mJ_n)}{(l_xly)^2}\alpha\sqrt{D_x(\omega)D_y(\omega)}\right). \tag{D.6}$$

D.3 Experimental and simulation studies

D.3.1 The experimental set-up

For this study the honeycomb panel was vertically supported in a steel frame using two flexible hangers to simulate free boundary conditions. As shown in Figure D.2, the panel was hanging with the longer panel edge parallel to the floor. The panel was excited at one of the lower edge corners using an LDS type V201 electro-dynamic shaker. The excitation force was measured using a B&K type 8001 impedance head. A B&K type 4375 accelerometer and a Polytec laser vibrometer were used to measure the panel response on the opposite side of the panel.

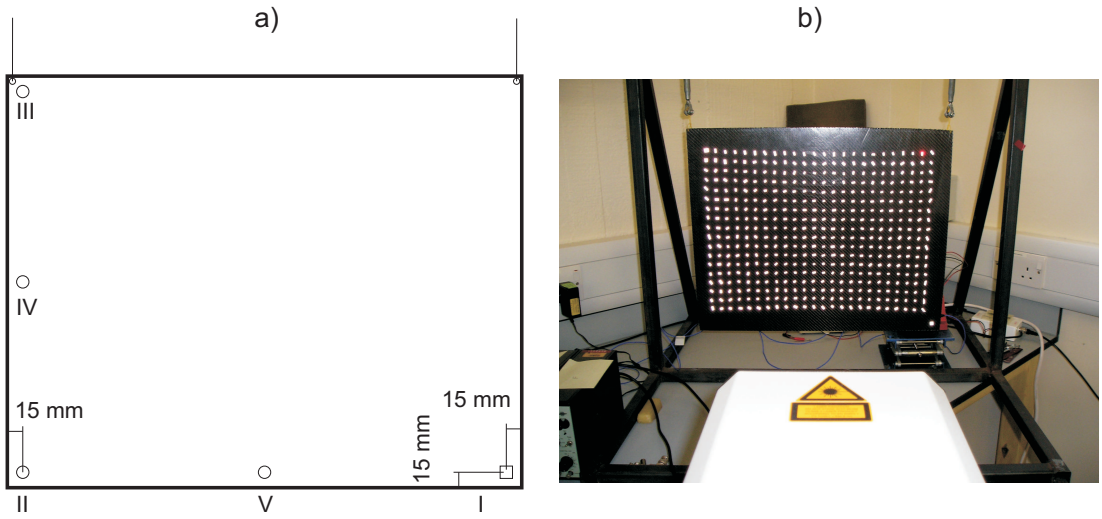

Figure D.2: a) Schematic view of freely supported honeycomb panel, excitation point and point mobility measurement point I ($square$), transfer mobility measurement points II to V ($circles$), b) Experimental set-up, honeycomb panel supported in a steel frame to approximate free boundary conditions with reflective grid used for laser vibrometer measurements.

D.3.2 Experimental and simulation results

Point and transfer mobilities: Figures D.3 and D.4 show the measured and simulated point mobilities at point I as defined in Figure D.2. The simulation parameters were manually fitted to yield a good agreement between measured and simulated results over a wide frequency range. The natural frequencies and modal loss factors were manually estimated from the measured point mobility using a circle fitting method [69].

Since no beam samples of the panel were available, it was not possible to measure the modal response of the panel in x- and y-directions in isolation. Therefore the laser vibrometer head was used to measure a 24x18 uniform grid of panel transfer mobilities. The visualisations of the panel velocity normalised by the excitation force panel from the vibrometer scans were used to associate the natural frequencies with the corresponding modeshapes of the panel, which also gives the specific sequence of panel modes. The test panel response along the x- and y-axes was analysed by identifying isolated beam-like modes from the grid of measured transfer mobilities.

Table D.2: Measured and simulated natural frequencies of the freely supported Honeycomb panel

Experimental		**Simulation**	
Mode order	Natural frequency [Hz]	Mode order	Natural frequency [Hz]
		-1, -1	0
		-1, 0	0
		0, -1	0
0, 0	373.9	0, 0	374.9
1, -1	**597.3**	1, -1	607.9
1, 0	860.9	1, 0	864.3
-1, 1	**939.9**	-1, 1	945.4
0, 1	1086	0, 1	1107.8
2, -1	**1292**	2, -1	1305.6
2, 0	1463	2, 0	1485.3
		1, 1	1492.8
2, 1	2019	2, 1	1986.3
		3, -1	2028.8
-1, 2*	**2151**	-1, 2	2106.5
		3, 0	2159.8
		0, 2	2190.7
1, 2	2426	1, 2	2428.3
3, 1	2580	3, 1	2551.4
4, -1	**2717**	4, -1	2743.4
		2, 2	2770.3
4, 0	2860	4, 0	2845.7
		4, 1	3160.5

* not clearly identifiable

Table D.2 gives the experimentally determined and simulated natural frequencies and corresponding modal identification, where mode orders of -1 correspond to whole body transverse modes, mode orders of 0 correspond to rigid body rocking modes and mode orders of 1 and above correspond to bending modes. In the x-direction three isolated modes, [1,-1] at 597.3 Hz, [2,-1] at 1292 Hz and [4,-1] at 2717 [Hz] were identified. Equation 5.1 was used to fit the panel parameters in the x-direction to the measured natural frequencies. In the y-direction only one isolated mode, [-1,1] at 939.9 Hz was clearly identifiable; the natural frequency at 2151 Hz is assumed to correspond to the [-1,2] mode but could not be clearly identified. The combined information of sequential mode order and isolated modes allowed the model parameters to be chosen to yield a reasonably good agreement between measured and predicted response. Knowledge of the panel geometry, manufacturer material specifications, experimental natural frequencies and modes allowed a set of model parameters to be determined that yield good agreement between predicted and measured structural response of the honeycomb panel used in the experimental study, which are given in Table D.1.

For verification the transfer mobilities between the force at point I and the response at II, III, IV and V (see Figure D.2) were measured using a B&K type 4375 accelerometer and compared with the results of the prediction model. Both the measured and simulated transfer mobilities are shown in Figure D.5. One should note that the locations of the points IV and V in the simulation were chosen to be slightly offset from the panel centre in the $x-$ and $y-$directions in order to capture the response of the [0,0] mode. All four transfer mobilities show a good general agreement between measured and simulated results and indicate that the sandwich composite model and chosen model parameters yield reliable results in the observed frequency range.

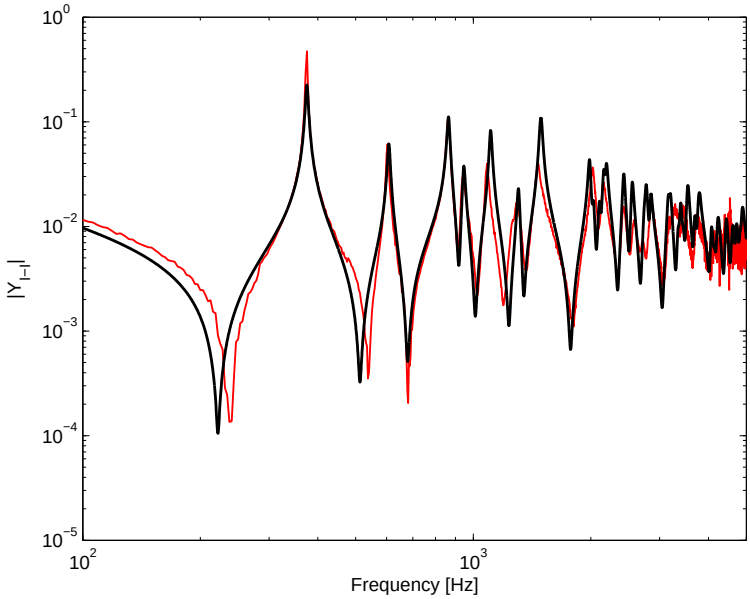

Figure D.3: Measured ($faint$) and simulated ($solid$) point mobility for the freely supported honeycomb test panel on logarithmic frequency scale.

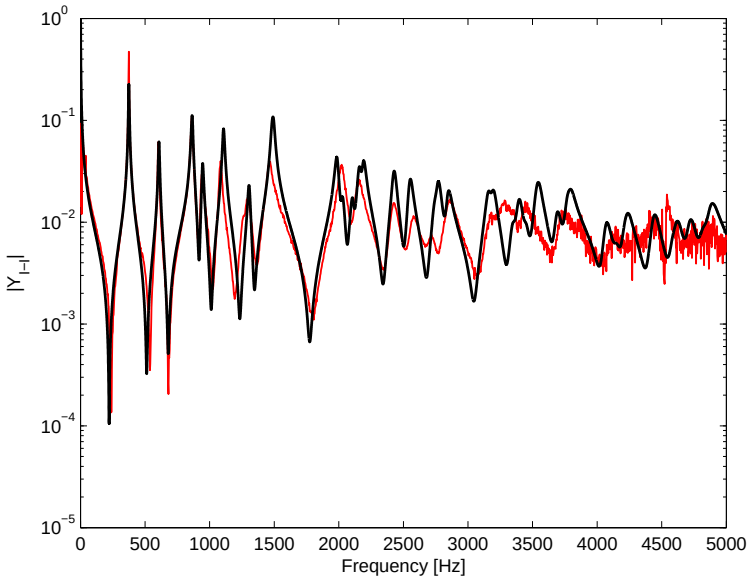

Figure D.4: Measured ($faint$) and simulated ($solid$) point mobility for the freely supported honeycomb test panel on linear frequency scale.

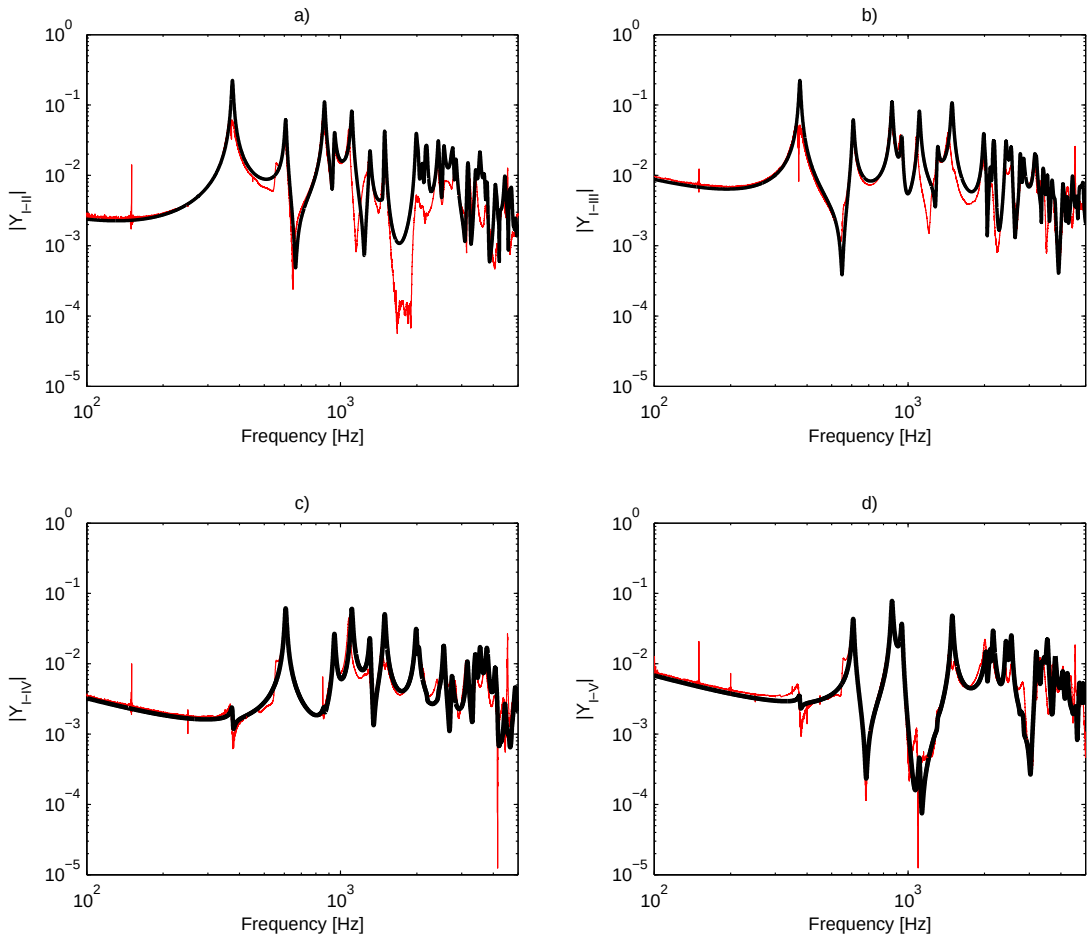

Figure D.5: Measured ($faint$) and simulated ($solid$) point mobilities for the freely supported composite honeycomb panel; (a)I-II; (b) I-III, (c) I-IV and (d) I-V.

Bending stiffness: Figure D.6 shows the simulated equivalent bending stiffness of the honeycomb panel in x and y-directions. For low frequencies the bending stiffnesses are nearly constant and correspond to the bending stiffness of the cross-section. For increasing frequency the equivalent bending stiffness in both directions drops due to core shear effects. It is interesting to note that D_x and D_y cross over at about 290 Hz, which together with the test panel geometry results in the specific modal order observed in the experimental studies. For frequencies well above 10 kHz the bending stiffness in both dimensions of the panel converges towards a constant value which corresponds to pure face-plate bending.

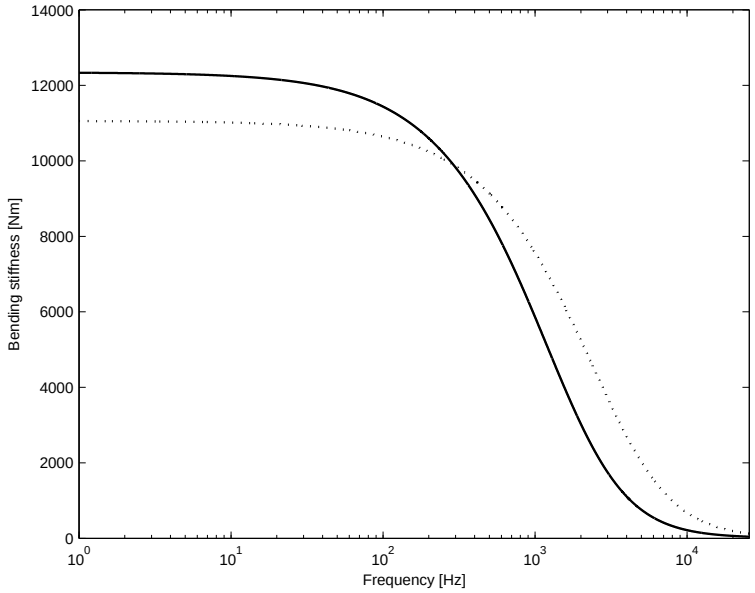

Figure D.6: Simulated frequency dependent equivalent bending stiffness of the honeycomb composite panel in x-direction ($solid$) and y-direction ($dashed$).

Correlation method: The measured 24x18 uniform grid of panel transfer mobilities has also been used in an attempt to identify the panel transverse wavenumbers using a correlation method. In Cartesian coordinates the two-dimensional discrete correlation function for a single frequency is given by Ferguson *et al* [70]

$$C(k_x, k_y) = \int_{-\infty}^{\infty} \int_{-\infty}^{\infty} \tilde{\dot{w}}(x, y) e^{-ik_x x} e^{-ik_y y} dx dy. \tag{D.7}$$

Due to the discrete sampling of data points, the coordinates, (x, y) in Equation (D.7) become discrete coordinates (x_i, y_j) and the double integral is replaced by a double sum. The discretisation of equation (D.7) therefore yields

$$C(k_x, k_y) = \frac{L_x L_y}{N_x N_y} \sum_{i=1}^{N_x} \sum_{j=1}^{N_y} \tilde{\dot{w}}(x_i, y_j) e^{-ik_x x_i} e^{-ik_y y_j}. \tag{D.8}$$

The wavenumbers in the x- and y-directions k_x and k_y for a specific observation frequency are estimated by identifying the maximum of $C(k_x, k_y)$. Note that the increase in computational effort limits the resolution of the correlation grid in k_x and k_y. The correlation method also has certain limitations with respect to the measured data. The spatial density of the measurement grid must guarantee at least two points per wavelength in order to avoid spatial aliasing and for reliable results at least one complete bending wavelength should be

sampled. In the x-direction this is only satisfied above 1290 Hz and in the y-direction this is only satisfied above 2150 Hz (compare Table D.2). Also for a specimen with dimensions of approximately 500 mm the lower wavenumber limit for reliable estimates is therefore $k > 4\pi$ i.e. $k > 12.5$ rad/m.

Figure D.7 shows the simulated wavenumbers of propagating waves of the honeycomb test panel in the x and y-directions and the experimentally estimated wavenumbers from the correlation method. Also the dash-dotted line shows the wavenumbers that correspond to the static bending stiffness $D_1 = \sqrt{D_{1_x} D_{1_y}}$ as a reference. For frequencies below 2000 Hz the results from the correlation method do not give satisfactory results due to the limitations in the test panel dimensions. Above 2000 Hz the results are also not satisfactory but support the trends in the simulated wavenumbers which increase more rapidly with frequency than the wavenumber that corresponds to pure cross-section bending. The results also support the predicted divergence between the wavenumbers in the x- and y-directions with increasing frequency which is a result of the different transverse shear moduli in the two panel directions.

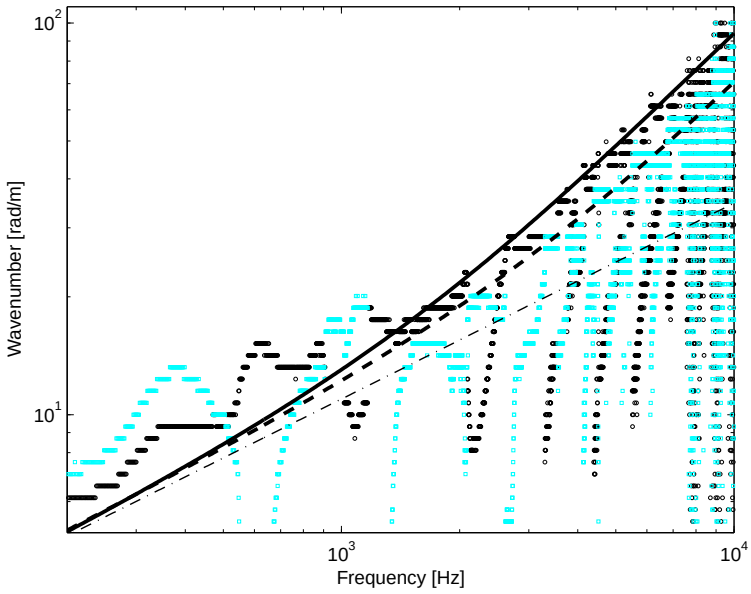

Figure D.7: Experimentally estimated and simulated bending wavenumbers of the honeycomb test panel. Experimental x-direction ($black - circles$), y-direction ($cyan - squares$); Simulated x-direction ($solid - line$), y-direction ($dashed - line$) and wavenumber for constant static stiffness D_1 ($dash - dotted - line$).

Appendix E

Transmission chamber experimental arrangements and complementary experimental results

This appendix provides further background information on the transmission chamber experimental set-ups and also complementary experimental results from microphone measurements. Also it provides experimental results for the panels with lumped point masses in place of the control units. This appendix is therefore organised in two sections:

- Section E.1 describes the experimental set-up, the transmission chamber, the test frame and the excitation and measurement arrangements used in the transmission chamber experimental studies.
- Section E.2 then presents the radiated sound power for the panels without control units and with open and closed loop control units, measured using a grid of microphones. These results are in good agreement with the laser vibrometer measurement experimental results, which are presented and discussed in Chapter 5.

  Finally complementary studies on the panels with lumped point masses are presented. The results show that the control unit mass effects alone do not produce broad-band reductions. The predominant effect of the lumped masses is to shift the resonance frequencies of low order modes.

E.1 Transmission chamber experimental arrangement

Past experimental studies on active panels were conducted at the ISVR [32, 34], using a Perspex box set-up that allowed the measurement of sound radiation into a hemi-anechoic room. The experimental measurements presented in this thesis have instead been carried out in a sound transmission suite, located in the ISVR teaching laboratory (room 13/4060 and 13/4062).

The schematic ground plan of the transmission chamber, shown in Figure E.1, gives the overall dimension of the two chambers. Previous studies indicated that the two rooms of the transmission suite do not satisfy reverberant field assumptions for frequencies below 800 Hz and also reported concerns about flanking transmissions [71]. It was therefore decided to transform the receiving room (13/4060) into a hemi-anechoic chamber which satisfies free-field conditions down to about 250 Hz. It was also decided to increase the amount of acoustic absorption in the source room (13/4062) in order to reduce resonant effects.

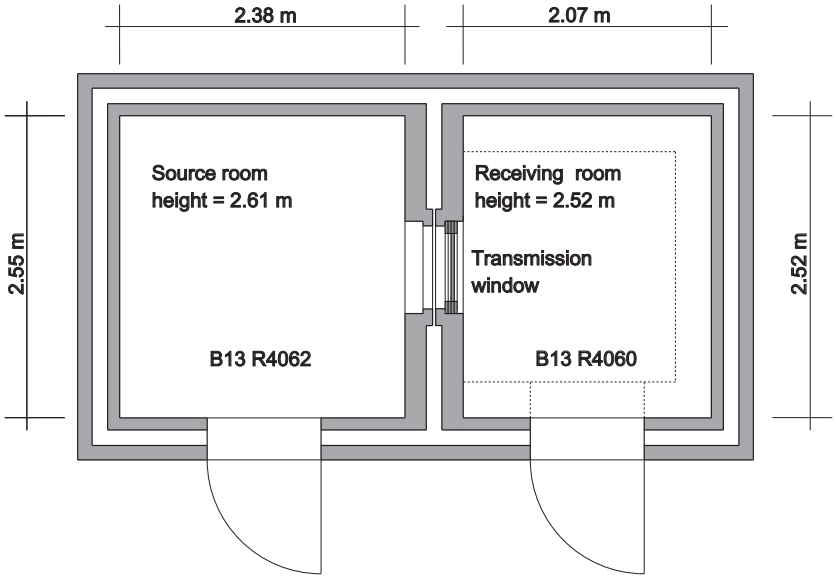

Figure E.1: Schematic ground plan of the transmission chamber in the ISVR teaching Lab (13/4060 and 13/4062).

For the conversion to a hemi-anechoic chamber the back and side walls, the ceiling and the floor of the receiving room (13/4060) were fitted with acoustic absorbent foam wedges. In order to be able easily to convert the room back into reverberant conditions it was decided to mount the foam wedges using adhesive Velcro pads (walls and ceiling only), where the hook pads were stuck to the chamber surfaces and the eye pads were stuck to the back of the foam wedges. The foam wedges are 30 cm deep and should therefore provide a high absorption coefficient above 250 Hz where the wedge depth is equal or large than a quarter of an acoustic wavelength.

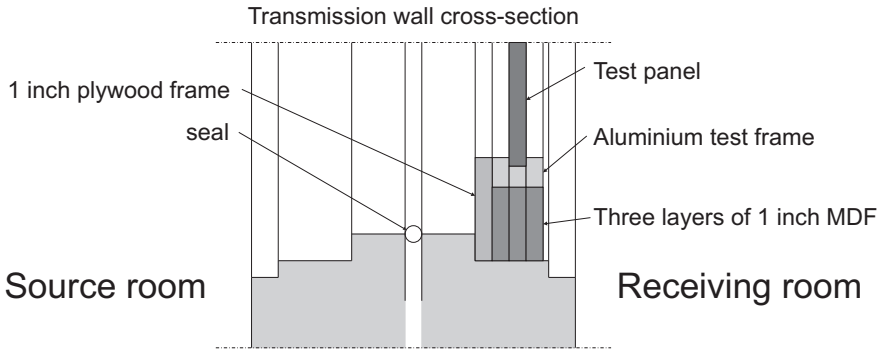

Figure E.2: Schematic cross-sectional view of the transmission chamber separating wall and transmission window with test frame.

As shown in the schematic cross-section view of the separating wall, in Figure E.2, a heavy wooden mounting frame was designed to mount the aluminium test frame in the transmission window and avoid unwanted flanking transmissions. Note that the panel is not perfectly flush mounted on the receiving room side. It was also necessary to modify the cable ducts between the inside and the outside of the source and receiving rooms in order the fit the high number of connecting cables and also the plug of the laser vibrometer data cable which needed to be routed into the receiving room. After all cables were fitted, the inside and outside wall openings of the cable ducts were sealed using removable permanent plastic sealant material (Teroson Terostat-IX).

E.1.1 Test frame

The test frame, schematically shown in Figures E.3 and E.4, is constructed from three individual frame sections made from solid aluminium bars of one inch (25.4 mm) thickness. The base frame section has a width of 7/4 inch (44.5 mm) and has 14 threaded holes that allow the frame to be mounted onto the plywood frame as shown in Figure E.2 and also 18 threaded holes that allow the three frame sections to be assembled together. The brace frame section has a width of 5/4 inch (31.8 mm) and 18 through holes, and as shown in Figure E.4 (a), is only needed when the honeycomb panel is mounted in the frame. The cover frame has a width of 7/4 inch (44.5 mm) and has 18 through holes that allow for a friction-locked connection to the base frame section. Figure E.3 shows the schematic front view of the test frame with the frame dimensions and the locations of the primary shaker excitation point and the control point locations viewed from the source room.

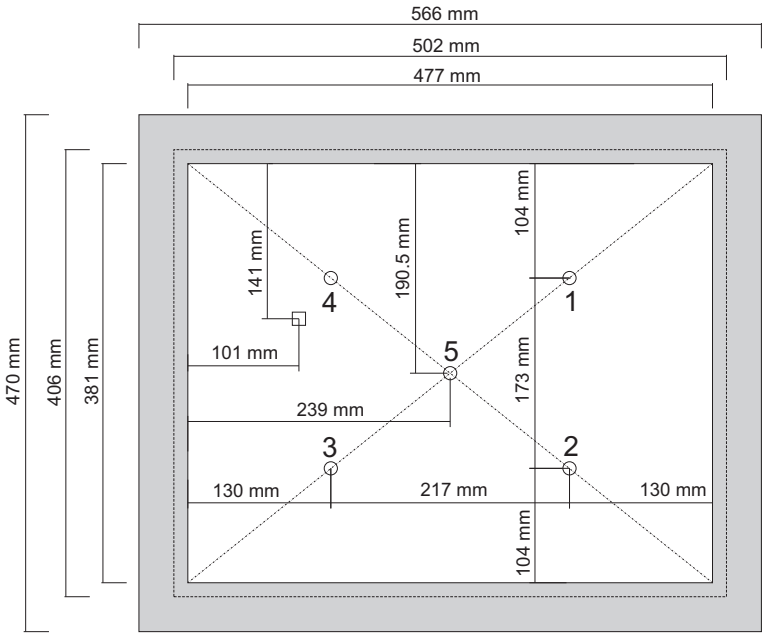

Figure E.3: Schematic front view of the aluminium test frame from the source room side, where the square indicates the excitation point and circles mark the location of the control units.

Figure E.4 shows the schematic of the test frame cross-section with mounting of (a) the honeycomb panel and (b) aluminium panel. The honeycomb panel is clamped between the base and the cover frame sections which are separated by the brace frame. To clamp the honeycomb panel in the test frame without putting extensive stresses on the outer edges, rubber bands were inserted along the panel perimeter. The aluminium panel is directly clamped between the base and the cover frame. As indicated in Figure E.4(b) the aluminium panel only overlaps with the test frame sections by about 1/2 inch (12.7 mm) along each edge unfortunately. This caused uneven stress distribution in the test frame when the base and cover frame were friction-locked by tightening the 18 screws. This introduced uneven in-plane loading on the aluminium panel.

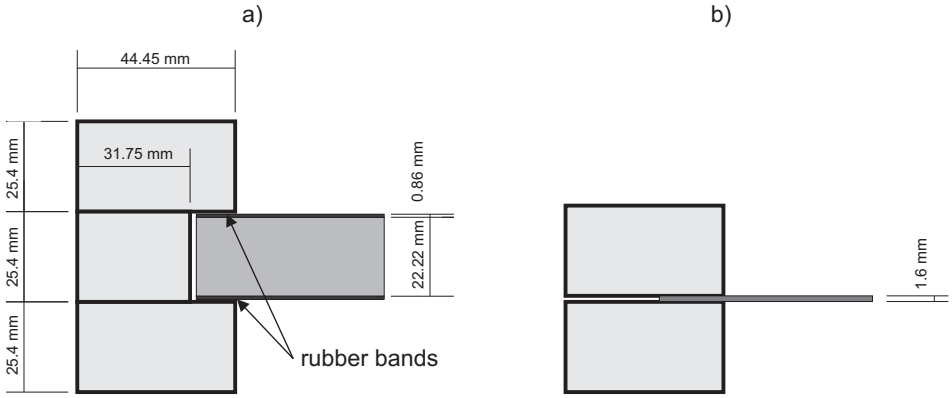

Figure E.4: Schematic view of the aluminium frame cross-section with (a) honeycomb panel and (b) the aluminium panel.

For future experimental studies, thin panels that are directly clamped between the base and cover frame should be fabricated to the frame outside dimensions and fitted with 18 through holes so that an even stress distribution in the friction-locked test frame is guaranteed. For further tests on sandwich panels with a thickness between 0 and 1/2 inch (12.7 mm) an additional height-adjustable inner frame has been designed but not yet assembled.

E.1.2 Panel boundary conditions

Figure E.5 shows the experimental results for the plain honeycomb panel when mounted in the test frame for shaker excitation. Also shown are the simulation results for the honeycomb panel assuming pinned or clamped boundary conditions on all edges, for point force excitation. The measured results fall between the predicted responses for pinned and clamped boundary conditions but are closer to pinned. For simplicity pinned edges are therefore used in the simulations. The magnitude of the resonant responses are also lower than those from the simulation results, which use the structural loss factor that has been estimated from the experimental studies on the freely supported honeycomb panel (see Appendix D). This indicates that the in-situ mounting conditions of the honeycomb panel introduce additional structural damping.

Figure E.6 shows the experimental results for the plain aluminium panel when mounted in the test frame for shaker excitation. Also shown are the simulation results for the aluminium panel assuming pinned or clamped boundary conditions on all edges, for point force excitation. The natural frequencies for the aluminium panel were higher than those predicted for pinned boundaries and also higher than those for clamped boundary conditions. The measured results therefore suggests that the response of the aluminium panel is affected by in-plane loads due to non-perfect mounting conditions. Also the aluminium panel was slightly curved due to the manufacturing process and storage conditions, which is expected to shift the panel resonances towards higher frequencies. With a thickness of 1.6 mm the aluminium panel has a considerable transverse stiffness, therefore it is problematic to straighten existing static deformations of the panel. At the time of the measurements it was not clear how the mounting conditions of the existing aluminium panel could be improved. It was therefore decided to accept the initial in-situ boundary conditions and to represent it in the simulations using clamped boundaries.

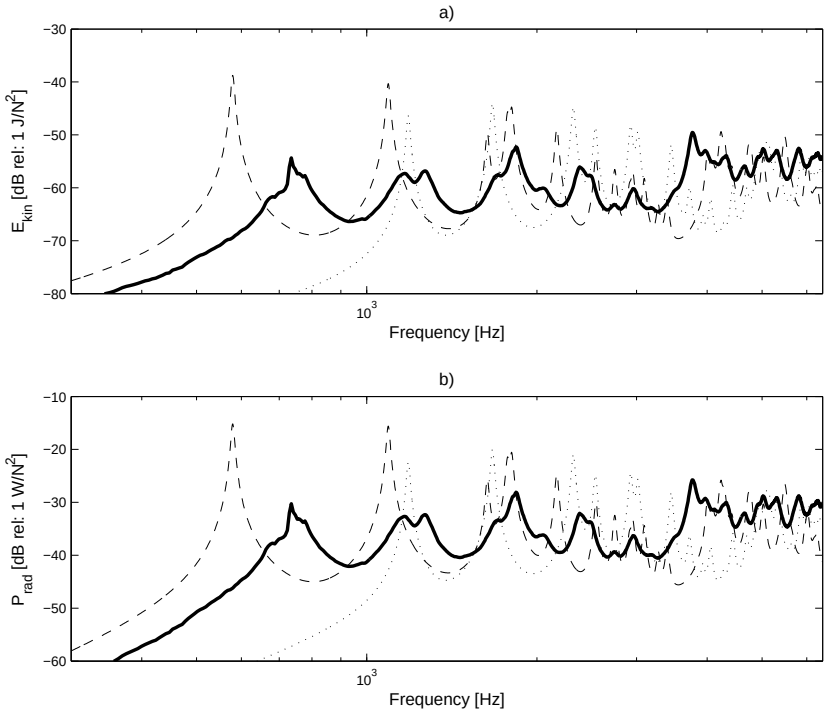

Figure E.5: a) Measured and predicted panel kinetic energy and b) radiated sound power for the **honeycomb panel** due to point force excitation; measured with laser vibrometer ($solid$); simulated for pinned boundary conditions ($dashed$) and predicted for clamped boundary conditions ($dotted$).

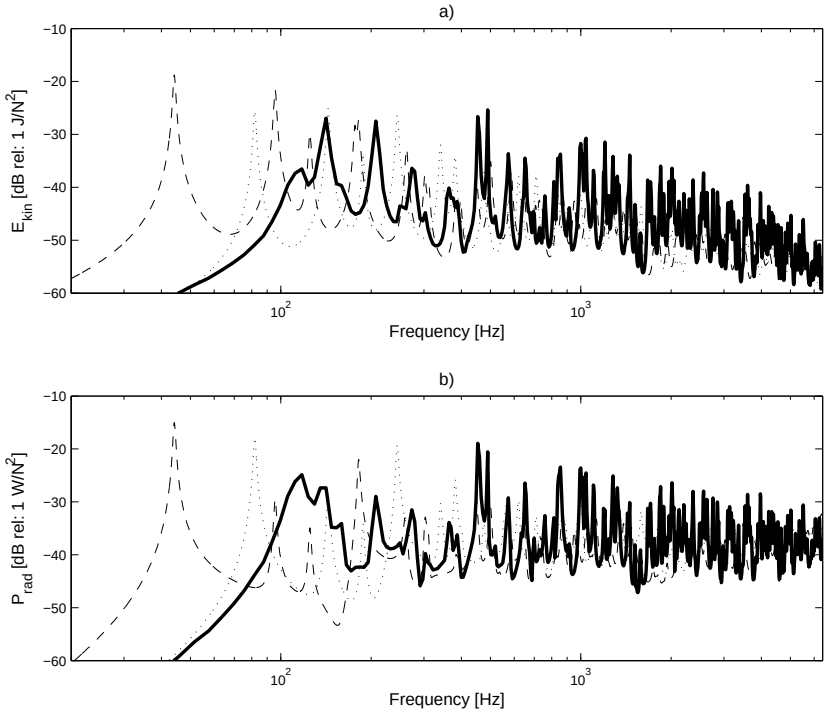

Figure E.6: a) Measured and predicted panel kinetic energy and b) radiated sound power for the **aluminium panel** due to point force excitation; measured with laser vibrometer ($solid$); simulated for pinned boundary conditions ($dashed$) and predicted for clamped boundary conditions ($dotted$).

E.1.3 Excitation arrangements

Shaker excitation

To investigate the performance of the control system for panels excited by a single point force, an electrodynamic shaker was attached to the panels via a force gauge, where the location of the force excitation is defined in Figure E.3. As shown in Figure E.7 the shaker was mounted on a wooden brace, which was attached to a heavy steel framed stand. A force gauge is used to measure the force input into the panel which is used as the reference excitation signal.

Figure E.7: Pictures of the shaker arrangement on the source side of the panel.

Loudspeaker excitation

To investigate the performance of the control system for acoustically excited panels, a loudspeaker was placed in the source room at about 80 cm from the panel surface so that the panels were predominantly excited by the loudspeaker direct field. As shown in Figure E.8, the loudspeaker was resiliently mounted on a stand with a height of 1.04 m, where the front of the loudspeaker was slightly elevated to tilt in the vertical plane. The loudspeaker was then placed in front of the transmission window with angle of 30° to the plane of the test panel. The aim of the loudspeaker arrangement shown in Figure E.8 was to expose the panels to the direct acoustic field produced by the loudspeaker and to realise a non-normal incidence angle for the acoustic waves.

For the loudspeaker excitation, the voltage input to the loudspeaker was measured and used as the reference excitation signal. The effects introduced by the loudspeaker and by the source room responses have been considered by correcting the measured responses on the

receiver side of the panel with the magnitude of the transfer function between the loudspeaker input voltage and the spatially averaged sound pressure measured in close proximity to the panel surface on the source side. These correction spectra are shown in Figure E.9; they roughly resemble the inverse of the loudspeaker frequency response characteristics.

The transfer function between the loudspeaker input voltage and the sound pressure in close proximity (2 to 5 cm distance) to the panel surface was measured at 18 randomly distributed points for both panels. The correction terms for both panels are very similar so that it can be assumed that the contribution of back-radiated sound from the panels is negligible compared with the incident sound pressure field.

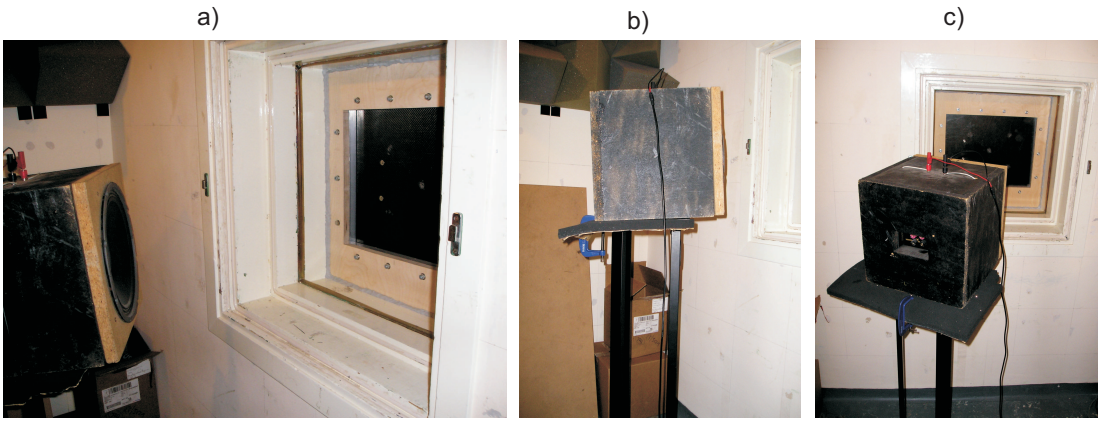

Figure E.8: Pictures of the loudspeaker arrangement in the source room.

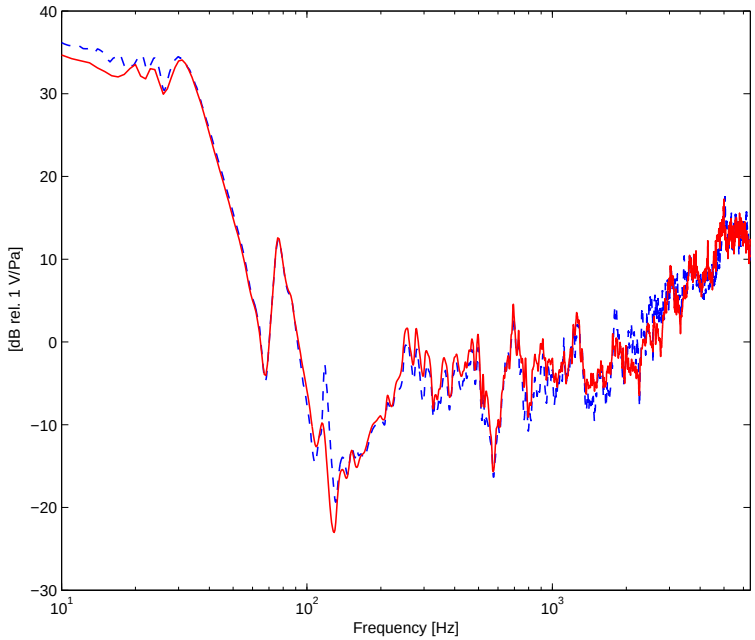

Figure E.9: Spectra of the correction term for loudspeaker excitation. Measured for the honeycomb panel ($solid - red$) and results measured for the aluminium panel ($dashed - blue$).

E.1.4 Measurement arrangements

Laser vibrometer measurements

As shown in Figure E.10(b), on the receiver side a laser vibrometer was used to measure the response of the panel on a grid of 16x20 points. The panel kinetic energy and radiated sound power are estimated using the formulations for the 'elemental approach' described in Chapter 2. The panel is assumed to be subdivided into a uniform grid of elements and the grid of measured panel velocities represents the velocities at the centres of the elements. The panel kinetic energy and radiated sound power are then estimated using Equations (2.11) and (2.14) respectively. This methodology of estimating the radiated sound power from panels has previously been demonstrated by Bai and Tsao [72].

Figure E.10(a), gives the relative location and orientation of the laser vibrometer head with respect to the test panel surface. The laser vibrometer head was arranged such that the laser neutral axis was perpendicular to the plane of the panel at the panel centre.

A critical issue for laser vibrometer measurements is the signal quality of the reflected laser beam. To guarantee high signal quality it was necessary to treat the panel surfaces in order to improve the light scattering properties. For the aluminium panel the light scattering properties were improved by sanding the receiving side surface with very fine sandpaper. The carbon texture of the honeycomb panel surface gave relatively poor signal quality so that it was necessary to improve the scattering properties of the surface on the 16x20 point measurement grid using using small patches of reflective tape as shown in Figure E.10.

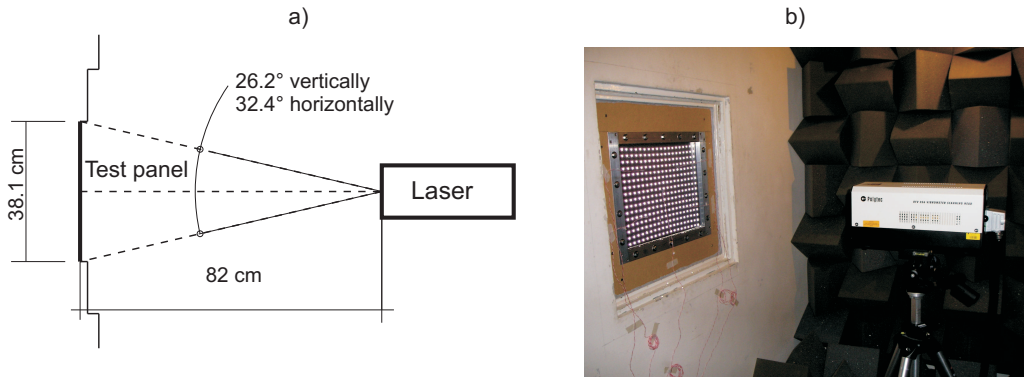

Figure E.10: Laser vibrometer set-up; (a) schematic view of laser and panel geometry and (b) picture of laser vibrometer arrangement in the receiving room.

The benefit of the laser vibrometer measurements is that they allow the estimation of both the panel kinetic energy and the radiated sound power. Also the measurements are relatively

insensitive to background noise and flanking sound transmission. The main drawback is the high number of measurement points that need to be sampled to optain the response accurately, particularly if measurements are conducted up to mid and high audio frequencies. This results in long measurement times and a large amount of measurement data.

Microphone measurements

As shown in Figure E.11, the radiated sound power was also estimated from sound pressure measurements using a hemispherical grid of nine microphones, assuming hemi-anechoic conditions in the receiving room. The procedure employed followed those described in the relevant ISO standard [65]; it should be noted however that the receiving room used does not meet the strict standard requirements and that the chosen microphone arrangement, shown in Figure E.11 (a), is also different from that described in the ISO standard.

The main benefit of the microphone measurements is the relatively short time needed to conduct an individual measurement. This benefit is counterbalanced by the relatively high effort to set up the measurement grid and microphone channels. Also the microphone measurements only allow the estimation of the radiated sound power but not that of the panel kinetic energy. The measurement results are sensitive background noise and flanking sound transmission and therefore pose stringent requirements on the receiving room acoustics and the efficient suppression of possible flanking paths. Further limitations of the accuracy of the results may arise from the small finite number of microphones used in the grid. This is particularly an issue for panels that exhibit distinctive non-uniform radiation characteristics.

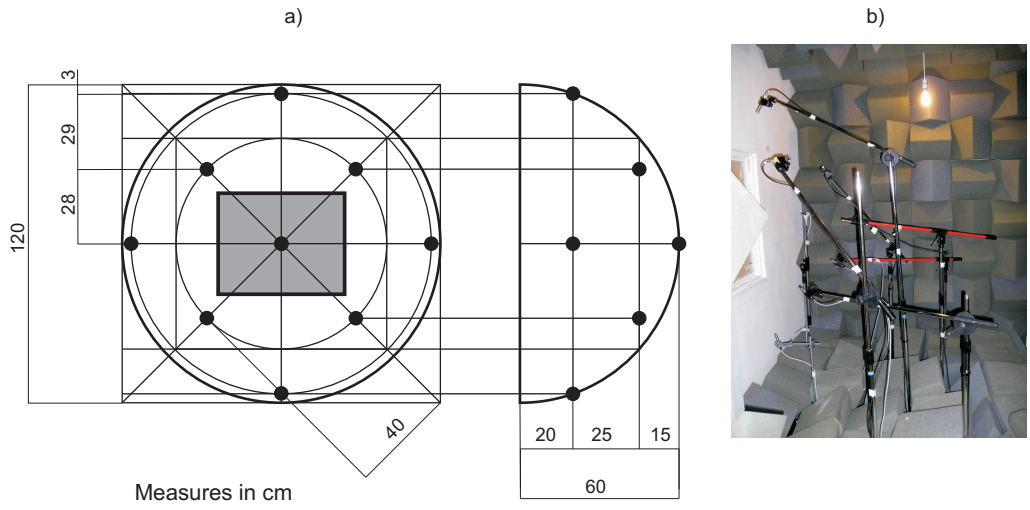

Figure E.11: Microphone array set-up; (a) schematic view of microphone array geometry and (b) picture of microphone arrangement in the receiving room ISVR (13/4060).

Figure E.12 shows good agreement between the radiated sound power obtained from the laser vibrometer measurements and from the microphone measurements. At frequencies below 250 Hz, the acoustic measurements were found to be slightly contaminated by the resonant response of the receiving room and possible also by low frequency flanking sound transmission. This is an expected effect as the 30 cm deep foam wedges used to treat the surfaces in the receiving room only start efficient absorb sound above 250 Hz where the wedge depth exceeds a quarter of the acoustic wave length. Also the honeycomb panel was found to have a strong radiation directivity so that a sampling via nine microphones may not yield sufficient results.

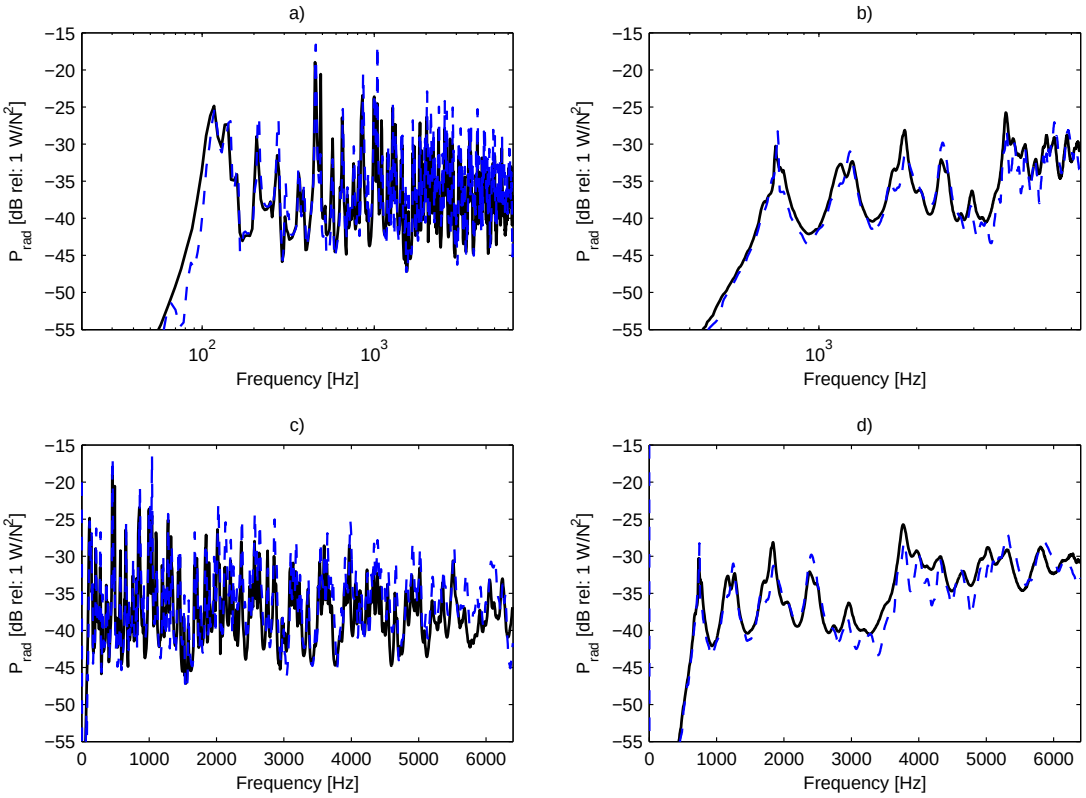

Figure E.12: Radiated sound power for shaker excited panels; radiated sound power from the aluminium panel ($left$) and radiated sound power from the honeycomb panel ($right$) on a linear frequency scale (top) and logarithmic frequency scale ($bottom$); Laser measurements ($solid$) and Microphone array measurements ($dashed$).

E.2 Complementary measurement results

E.2.1 Results from microphone measurements

This section presents the microphone experimental results for the radiated sound power of the panels without control units and with open and closed loop control units. As discussed above, the results generally are in good agreement with the laser vibrometer experimental results, which are presented and discussed in Chapter 5.

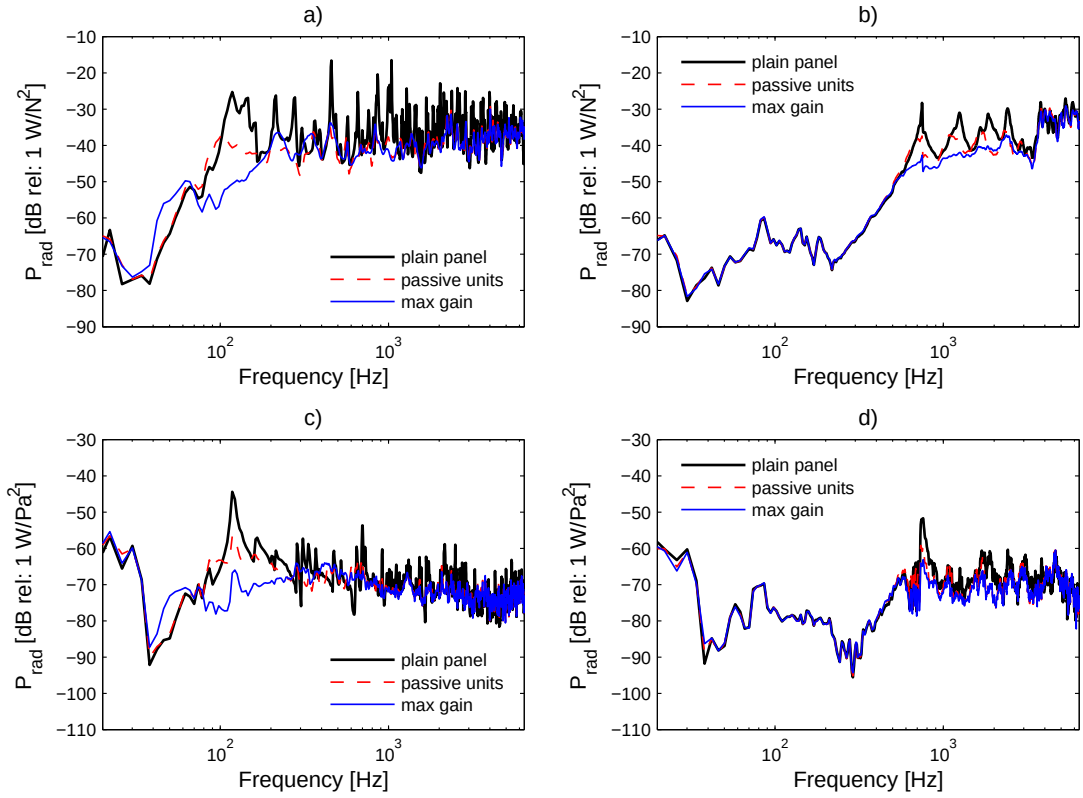

Figure E.13: Radiated sound power measured using a grid of microphones. Aluminium panel ($left$) and honeycomb panel ($right$), shaker excitation (top) and loudspeaker excitation ($bottom$).

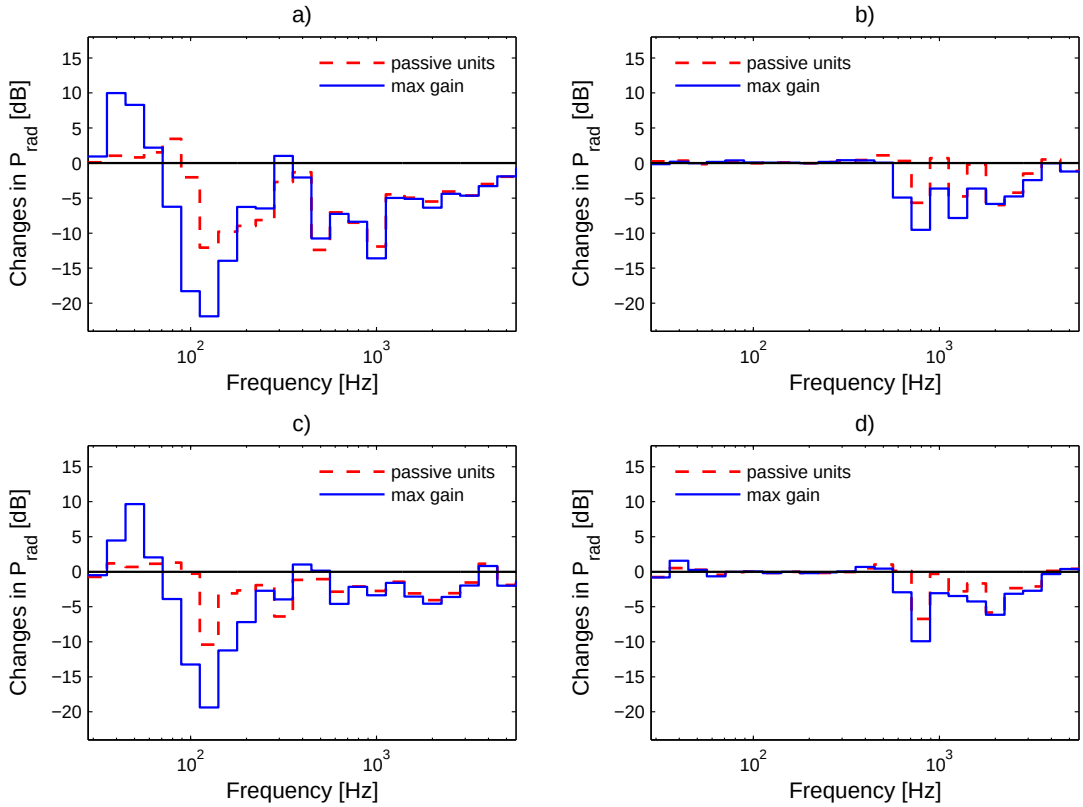

Figure E.14: Change in the radiated sound power measured using a grid of microphones. Aluminium panel ($left$) and honeycomb panel ($right$); shaker excitation (top) and loudspeaker excitation ($bottom$).

E.2.2 Results for panels with lumped point masses

Additional measurements with lumped masses were conducted in order to compare the passive inertia effects produced by small blocks of steel, shown in Figure E.15, and the passive and active effects produced by the control units with equivalent mass. In this study the control actuators were replaced with lumped masses of either 11 grams or 35 grams, where the 11 gram masses represent the mounting mass of the actuators including the voice coil and the 35 gram mass represents the total mass of the actuators. The accelerometer sensors on the opposite side of the panel remained in place to account accurately for the total base mass of the actuators. The results for panel kinetic energy and radiated sound power presented here were measured using the laser vibrometer.

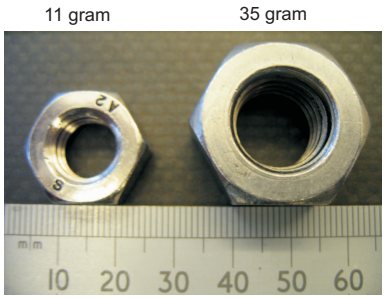

Figure E.15: Equivalent lumped masses

Figures E.16 and E.18 show the measured narrow-band panel kinetic energies and radiated sound power for the plain panels and the panels fitted with the 11 gram and 35 gram equivalent lumped masses. Figures E.17 and E.19 show the changes in kinetic energy and radiated sound power in 1/3 octave band spectra. The results indicate that the added lumped masses shift the resonances of low order structural modes towards lower frequencies but do not introduce damping. At low frequencies this results in a shift of kinetic energy and radiated sound power spectra between frequency bands. The 1/3 octave band spectra indicate that at higher frequencies the added lumped masses do not produce a significant net broad-band reduction of the panel response and radiated sound power. As discussed in Chapter 4, well below the actuator fundamental resonance, the base impedance of the control units corresponds to that of the total lumped mass of the actuators. However, the actuator fundamental resonance is well below the fundamental resonances of both of the panels so that the 35 gram lumped mass does not give a good representation of the control unit inertia effects in the mid and high audio frequency range. For high frequencies the base impedance of the control units converges to the impedance of the actuator base mass. Therefore the 11 gram lumped masses give a good representation of the actuator inertia effects at higher audio frequencies.

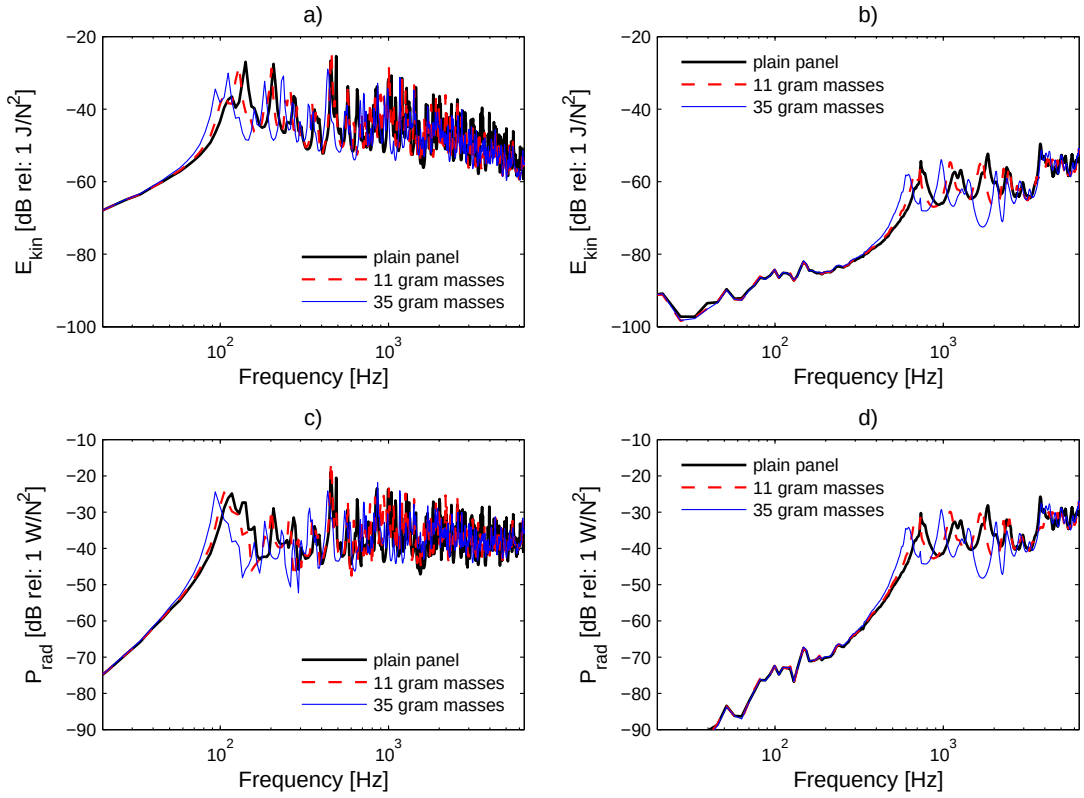

Figure E.16: Measured response and sound power radiated for **shaker** excitation. Aluminium panel ($left$) and Honeycomb panel ($right$); Panel kinetic energy (top) and radiated sound power ($bottom$).

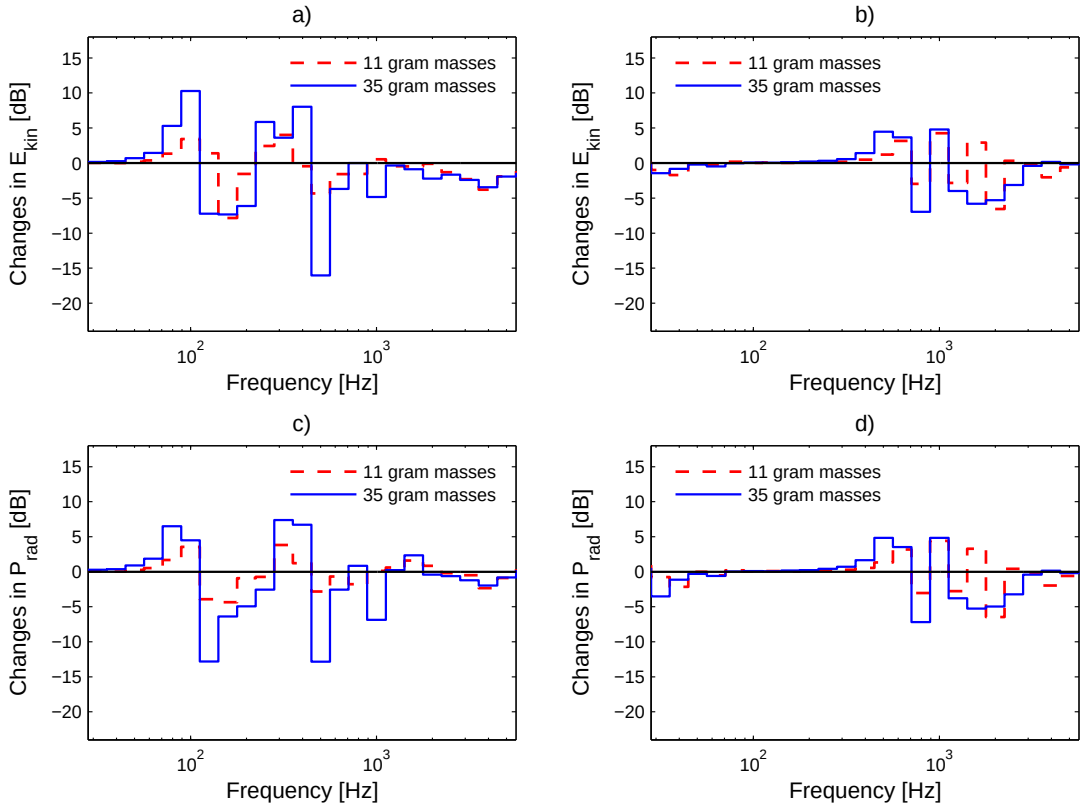

Figure E.17: Change in the panel kinetic energy and radiated sound power for **shaker** excitation, evaluated in 1/3 octave bands. Aluminium panel ($left$) and honeycomb panel ($right$); E_{kin} (top) and P_{rad}($bottom$).

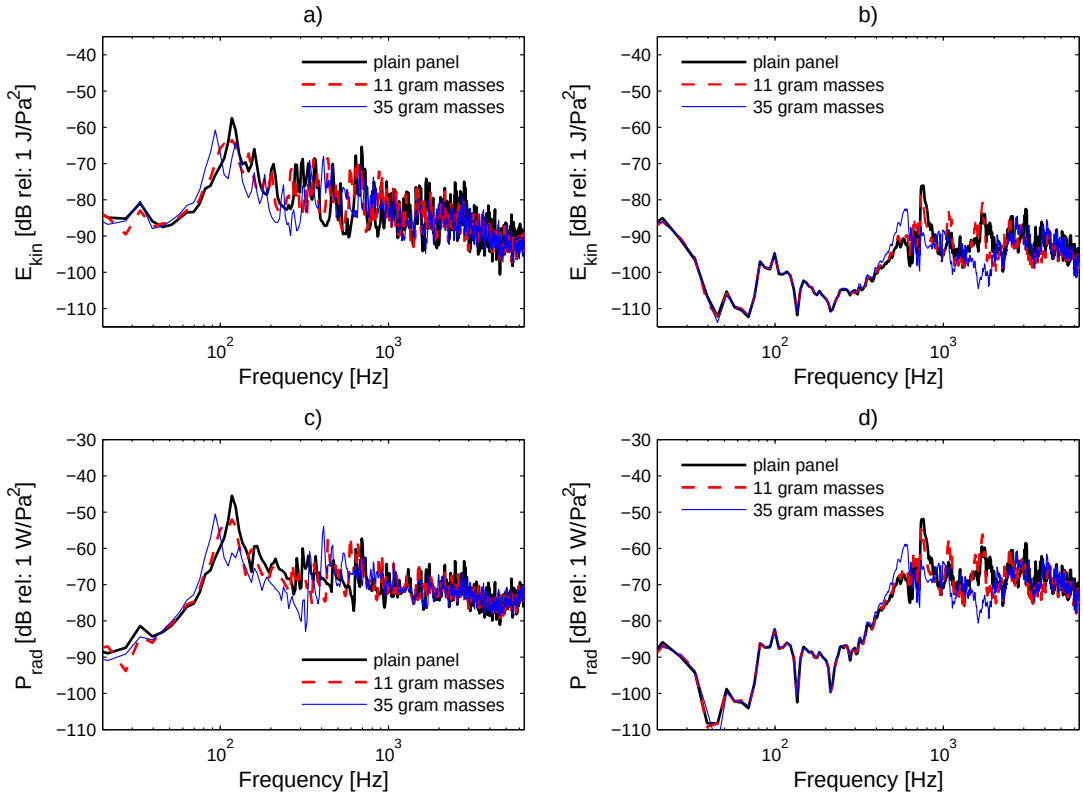

Figure E.18: Measured response and sound power radiated for **loudspeaker** excitation. Aluminium panel ($left$) and Honeycomb panel ($right$); Panel kinetic energy (top) and radiated sound power ($bottom$).

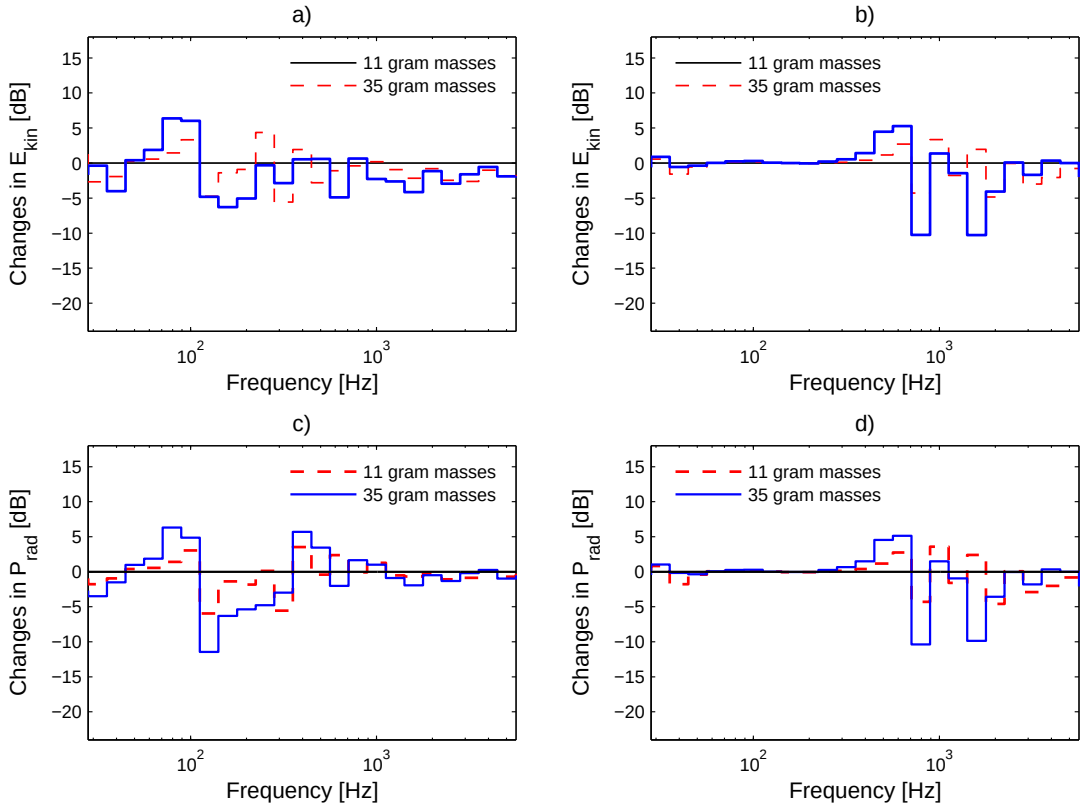

Figure E.19: Change in the panel kinetic energy and radiated sound power for **loudspeaker** excitation, evaluated in 1/3 octave bands. Aluminium panel ($left$) and honeycomb panel ($right$); E_{kin} (top) and P_{rad}($bottom$).

References

[1] D.J. Thompson and J. Dixon. *Vehicle Noise, Chapter 6 in Advanced Applications in Acoustics, Noise and Vibration*. edited by F.J. Fahy and J.G. Walker. E & FN Spon, London and New York, 2004.

[2] J.S. Mixson and J.S. Wilby *Interior Noise, Chapter 16 in Aeroacoustics of Flight Vehicles, Theory and Practice*. edited by H.H. Hubbard. NASA Langley Research Center, Hampton, Virginia, 1995.

[3] J.F. Wilby. Aircraft interior noise. *Journal of Sound and Vibration*, 190(3):545 – 564, 1996.

[4] P. Gardonio. Review of active techniques for aerospace vibro-acoustic control. *Journal of Aircraft*, 39(2):206 – 214, 2002.

[5] F.J. Fahy. *Fundamentals of noise and vibration control, chapter 5 in Fundamentals of noise and vibration*. edited by F.J. Fahy and J.G. Walker. E & FN Spon, London, 1998.

[6] M.J. Brennan and N.S. Ferguson. *Vibration Control, Chapter 12 in Advanced Applications in Acoustics, Noise and Vibration*. edited by F.J. Fahy and J.G. Walker. E & FN Spon, London and New York, 2004.

[7] D.J. Mead. *Passive Vibration Control*. John Wiley, Chichester, UK, 1998.

[8] M.K. Bull. Wall-pressure fluctuations beneath turbulent boundary layers: some reflections on forty years of research. *Journal of Sound and Vibration*, 190(3):299 – 315, 1996.

[9] Y.F. Hwang, W.K. Bonness and S.A. Hambric. Comparison of semi-empirical models for turbulent boundary layer wall pressure spectra. *Journal of Sound and Vibration*, 319(1-2):199 – 217, 2009.

[10] C.R. Fuller, J.P. Maillard, M. Mercadal and A.H. von Flotow. Control of aircraft interior noise using globally detuned vibration absorbers. *Journal of Sound and Vibration*, 203(5):745 – 761, 1997.

[11] P.A. Nelson and S.J. Elliott. *Active Control of Sound*. Academic Press, London and San Diego, 1993.

[12] C.F. Ross and M.R. Purver. Active cabin noise control. *Proceedings of The International Symposium on Active Control of Sound and Vibration ACTIVE 97, Budapest, Hungary*, pages XXXIX–XLVI, 1997.

[13] S.J. Elliott. *Signal processing for active control*. Academic press, London, 2001.

[14] B. Bingham, M.J. Atalla and N.W. Hagood. Comparison of structural-acoustic control designs on an active composite panel. *Journal of Sound and Vibration*, 244(5):761 – 778, 2001.

[15] K.D. Frampton. Distributed group-based vibration control with a networked embedded system. *Smart Materials and Structures*, 14(2):307 – 314, 2005.

[16] K.D. Frampton. Vibro-acoustic control with a distributed sensor network. *Journal of the Acoustical Society of America*, 119(4):2170 – 2177, 2006.

[17] C.R. Fuller, S.J. Elliott and P.A. Nelson. *Active Control of Vibration*. Academic Press, London, 1st edition, 1996.

[18] R.L. Clark, W.R. Saunders and G.P. Gibbs. *Adaptive Structures, Dynamics and Control*. Wiley-Intersience, New York, NY, 1st edition, 1998.

[19] F.J. Fahy and P. Gardonio. *Sound and Structural Vibration, radiation, transmission and response*. Academic Press, Oxford, 2nd edition, 2007.

[20] S.J. Elliott and M.E. Johnson. Radiation modes and the active control of sound power. *Journal of the Acoustical Society of America*, 94(4):2194 – 204, 1993.

[21] J.M. Sullivan, J.E. Hubbard Jr. and S.E. Burke. Distributed sensor/actuator design for plates: Spatial shape and shading as design parameters. *Journal of Sound and Vibration*, 203(3):473 – 493, 1997.

[22] M.E. Johnson and S.J. Elliott. Active control of sound radiation using volume velocity cancellation. *Journal of the Acoustical Society of America*, 98(4):2174 – 86, 1995.

[23] P. Gardonio and S.J. Elliott. Smart panels for active structural acoustic control. *Smart Materials and Structures*, 13(6):1314 – 36, 2004.

[24] M.J. Balas. Direct velocity feedback control of large space structures. *Journal of Guidance, Control, and Dynamics*, 2(3):252 – 253, 1979.

[25] J.Q. Sun. Some observations on physical duality and collocation of structural control sensors and actuators. *Journal of Sound and Vibration*, 194(5):765 – 770, 1996.

[26] K.D. Frampton, O.N. Baumann and P. Gardonio. A comparison of decentralised, distributed and centralised vibro-acoustic control. *Accepted for publication in the Journal of the Acoustical Society of America*.

[27] S.J. Elliott, P. Gardonio, T.C. Sors and M.J. Brennan. Active vibroacoustic control with multiple local feedback loops. *Journal of the Acoustical Society of America*, 111(2):908 – 15, 2002.

[28] P. Gardonio E. Bianchi and S.J. Elliott. Smart panel with multiple decentralized units for the control of sound transmission. part iii: Control system implementation. *Journal of Sound and Vibration*, 274(1-2):215 – 232, 2004.

[29] P. Gardonio, E. Bianchi and S.J. Elliott. Smart panel with multiple decentralized units for the control of sound transmission. part ii: Design of the decentralized control units. *Journal of Sound and Vibration*, 274(1-2):193 – 213, 2004.

[30] P. Gardonio, E. Bianchi and S.J. Elliott. Smart panel with multiple decentralized units for the control of sound transmission. part i: Theoretical predictions. *Journal of Sound and Vibration*, 274(1-2):163 – 192, 2004.

[31] Y. Aoki, P. Gardonio and S.J. Elliott. Modelling of a piezoceramic patch actuator for velocity feedback control. *Smart Materials and Structures*, 17(1):1–13, 2008.

[32] Y. Aoki, P. Gardonio and S.J. Elliott. Rectangular plate with velocity feedback loops using triangularly shaped piezoceramic actuators: Experimental control performance. *Journal of the Acoustical Society of America*, 123(3):1421 – 1426, 2008.

[33] C. González Díaz, C. Paulitsch and P. Gardonio. Active damping control unit using a small scale proof mass electrodynamic actuator. *Journal of the Acoustical Society of America*, 124(2):886 – 897, 2008.

[34] C. González Díaz, C. Paulitsch and P. Gardonio. Smart panel with active damping units. implementation of decentralized control. *Journal of the Acoustical Society of America*, 124(2):898 – 910, 2008.

[35] N. Alujevic, P. Gardonio and K.D. Frampton. Smart double panel with decentralized active dampers for sound transmission control. *AIAA Journal*, 46(6):1463 – 1475, 2008.

[36] N. Alujevic, P. Gardonio and K.D. Frampton. Stability and performance of a smart double panel with decentralized active dampers. *AIAA Journal*, 46(7):1747 – 1756, 2008.

[37] P. Gardonio. Sensor-actuator transducers for smart panels. *Proceedings of The International Symposium on Active Control of Sound and Vibration ACTIVE 2006, Adelaide, Australia, 18-20 September 2006*.

[38] A. Preumont. *Vibration Control of Active Structures*, volume 96 of *Solid Mechanics and its Applications*. Kluwer Academic Publisher, Dordrecht / Boston / London, 2 edition, 2002.

[39] P. Gardonio, Y.-S. Lee, S.J. Elliott and S. Debost. Analysis and measurement of a matched volume velocity sensor and uniform force actuator for active structural acoustic control. *Journal of the Acoustical Society of America*, 110(6):3025 – 3031, 2001.

[40] C. Hong and S.J. Elliott. Local coupling between actuator and sensor pairs in light honeycomb structures. *Journal of Sound and Vibration*, 302(1-2):117 – 137, 2007.

[41] C. Hong and S.J. Elliott. Local feedback control of light honeycomb panels. *Journal of the Acoustical Society of America*, 121(1):222 – 233, 2007.

[42] C. Paulitsch. *Vibration Control with Electrodynamic Actuators*. PhD thesis, University of Southampton, published as Fortschritt-Berichte VDI Reihe 11 Schwingungstechnik Nr. 329, VDI Verlag, Düsseldorf, 2005.

[43] C. Paulitsch, P. Gardonio and S.J. Elliott. Active vibration control using an inertial actuator with internal damping. *Journal of the Acoustical Society of America*, 119(4):2131 – 2140, 2006.

[44] C. Paulitsch, P. Gardonio and S.J. Elliott. Active vibration damping using an inertial, electrodynamic actuator (detc2005-84632). *Journal of Vibration and Acoustics, Transactions of the ASME*, 129(1):39 – 47, 2007.

[45] C. González Díaz and P. Gardonio. Feedback control laws for proof-mass electrodynamic actuators. *Smart Materials and Structures*, 16(5):1766 – 1783, 2007.

[46] J. Rohlfing and P. Gardonio. Active control of sound transmission through panels with flexible boundaries under detreministic and stochastic excitation. Technical report, University of Southampton, Institute of Sound and Vibration Research, ISVR Technical Memorandum No. 977, 2007.

[47] P. Gardonio and M.J. Brennan. *Mobility and impedance methods in structural dynamics, Chapter 9 in Advanced Applications in Acoustics, Noise and Vibration*. edited by F.J. Fahy and J.G. Walker. Spon Press, 2004.

[48] G.B. Warburton. The vibration of rectangular plates. *Proceedings of the Institution of Mechanical Engineers*, 168:371–384, 1954.

[49] J.J. Tuma and R.A. Walsh. *Engeneering Mathematics Handbook*. McGraw-Hill, New York, NY, 4th edition, 1997.

[50] B.-T. Wang, C.R. Fuller and E.K. Dimitriadis. Active control of noise transmission through rectangular plates using multiple piezoelectric or point force actuators. *Journal of the Acoustical Society of America*, 90(5):2820–2830, 1991.

[51] F.J. Fahy. *Sound and Structural Vibration; radiation, transmission and response*. Academic press, London, UK, 1985.

[52] D.J. Thompson, P. Gardonio and J. Rohlfing. Can a transmission coefficient be greater than unity? *Applied Acoustics*, 70(5):681 – 688, 2009.

[53] P.J. Shorter and R.S. Langley. On the reciprocity relationship between direct field radiation and diffuse reverberant loading. *Journal of the Acoustical Society of America*, 117(1):85 – 95, 2005.

[54] C. Maury, S.J. Elliott and P. Gardonio. Turbulent boundary-layer simulation with an array of loudspeakers. *AIAA Journal*, 42(4):706 – 13, 2004.

[55] S.J. Elliott, C. Maury and P. Gardonio. The synthesis of spatially correlated random pressure fields. *Journal of the Acoustical Society of America*, 117(3):1186 – 201, 2005.

[56] G.M. Corcos. The resolution of pressures in turbulence. *Journal of the Acoustical Society of America*, 35:192–199, 1963.

[57] G. Cousin. Sound from TBL induced vibrations. Technical report, trita-fkt 1999:35, Royal Institute of Technology KTH, Stockholm. Department of Vehicle Engineering, The Marcus Wallenberg Laboratory for Sound and Vibration Research MWL, 1999.

[58] G. Kurtze and B.G. Watters. New wall design for high transmission loss or high damping. *Journal of the Acoustical Society of America*, 31(6):739–748, 1959.

[59] R.J.M. Craik. *Sound Transmission Through Buildings: Using Statistical Energy Analysis*. Gower Publishing Limited, Aldershot, UK and Brookfield, Vermont, USA, 1996.

[60] B.L. Clarkson and M.F. Ranky. Modal density of honeycomb plates. *Journal of Sound and Vibration*, 91:103–118, 1983.

[61] E. Nilsson and A.C. Nilsson. Prediction and measurement of some dynamic properties of sandwich structures with honeycomb and foam cores. *Journal of Sound and Vibration*, 251(3):409 – 430, 2002.

[62] C.W. Schwingshackl, G.S. Aglietti and P.R. Cunningham. Determination of honeycomb material properties: Existing theories and an alternative dynamic approach. *Journal of Aerospace Engineering*, 19(3):177 – 183, 2006.

[63] R.D. Blevins. *Formulas for natural frequency and mode shape*. Robert E. Krieger, Malabar, Florida, 1984.

[64] O.N. Baumann and S.J. Elliott. The stability of decentralized multichannel velocity feedback controllers using inertial actuators. *Journal of the Acoustical Society of America*, 121(1):188 – 196, 2007.

[65] BS EN ISO 3745:2003, acoustics - determination of sound power levels of noise sources using sound pressure - precision methods for anechoic and hemi-anechoic rooms.

[66] C. Hong. *Active Control of Resiliently-Mounted Flexible Structures*. PhD thesis, University of Southampton, 2005.

[67] S.H. Crandall and W.D. Mark. *Random Vibration in Mechanical Systems*. Academic Press Inc. New York and London, 1963.

[68] D.E. Newland. *Random vibrations, spectral and wavelet analysis*. Longman Singapore Publishers Pte Ltd, 1993.

[69] D.J. Ewins. *Modal Testing: Theory, Practice and Application*. John Wiley & Sons Ltd, Bognor Regis, UK, 2000.

[70] N.S. Ferguson, C.R. Halkyard, B.R. Mace and K.H. Heron. The estimation of wavenumbers in two-dimensional structures. In *Proceedings of the 2002 International Conference on Noise and Vibration Engineering*, pages 799 – 806, Leuven, Belgium, 2002.

[71] H. Hopper. Final report on studies in the ISVR level 4 teaching lab transmission chamber. Technical report, ISVR, third year B.Sc. project, 2008.

[72] M.R. Bai and M. Tsao. Estimation of sound power of baffled planar sources using radiation matrices. *Journal of the Acoustical Society of America*, 112(3):876 – 83, 2002.